

Random Matrix Theory for Stochastic and Quantum Many-Body Systems



Dissertation zur Erlangung des akademischen Grades
Doctor rerum naturalium (Dr. rer. nat.)

vorgelegt von
Goran Nakerst
geboren am 01. Januar 1994 in Menden

Professur für Theoretische Festkörperphysik
Institut für Theoretische Physik, Fakultät Physik
Technische Universität Dresden

19.04.2024

Betreuer Dr. Masudul Haque
1. Gutachter Prof. Dr. Matthias Vojta
2. Gutachter Prof. Dr. Paul McClarty

Datum der Abgabe: 23.04.2024
Datum der Disputation: 04.09.2024

Für Mama

Abstract

Random matrix theory (RMT) is a mathematical framework that has found profound applications in physics, particularly in the study of many-body systems. Its success lies in its ability to predict universal statistical properties of complex systems, independent of the specific details. This thesis explores the application of RMT to two classes of many-body systems: quantum and stochastic many-body systems.

Within the quantum framework, this work focuses on the Bose-Hubbard system, which is paradigmatic for modeling ultracold atoms in optical traps. According to RMT and the Eigenstate Thermalization Hypothesis (ETH), eigenstate-to-eigenstate fluctuations of expectation values of local observables decay rapidly with the system size in the thermodynamic limit at sufficiently large temperatures. Here, we study these fluctuations in the classical limit of fixed lattice size and increasing boson number. We find that the fluctuations follow the RMT prediction for large system sizes but deviate substantially for small lattices. Partly motivated by these results, the Bose-Hubbard model on three sites is studied in more detail. On few sites, the Bose-Hubbard model is known to be a mixed system, being neither fully chaotic nor integrable. We compare energy-resolved classical and quantum measures of chaos, which show a strong agreement. Deviations from RMT predictions are attributed to the mixed nature of the few-site model.

In the context of stochastic systems, generators of Markov processes are studied. The focus is on the spectrum. We present results from two investigations of Markov spectra. First, we investigate the effect of sparsity on the spectrum of random generators. Dense random matrices previously used as a model for generic generators led to very large spectral gaps and therefore to unphysically short relaxation times. In this work, a model of random generators with adjustable sparsity — number of zero matrix elements — is presented, extending the dense framework. It is shown that sparsity leads to longer, more physically realistic relaxation times. Second, the generator spectrum of the Asymmetric Simple Exclusion Process (ASEP), a quintessential model in non-equilibrium statistical mechanics, is analyzed. We investigate the spectral

boundary, which is characterized by pronounced spikes. The emergence of these spikes is analyzed from several points of view, including RMT.

The results presented in this thesis contribute to the understanding of the applicability of RMT to many-body systems. This thesis highlights successes such as the explanation of “ETH fluctuations” in Bose-Hubbard models, the improvement of random matrix descriptions by introducing sparsity, and the emergence of spikes in the spectral boundary of the ASEP. The latter is a notable case where RMT provides insights even though the ASEP is a Bethe-integrable system. Furthermore, this thesis shows examples of the limits of RMT, exemplified by the results presented for the Bose-Hubbard model with a few sites.

List of Publications and Preprints

- G. Nakerst, J. Brennan, and M. Haque
Gradient descent with momentum — to accelerate or to super-accelerate?
arXiv:2001.06472
- G. Nakerst, and M. Haque
Eigenstate thermalization scaling in approaching the classical limit
Phys. Rev. E **103**, 042109 (2021).
- G. Nakerst, and M. Haque
Chaos in the three-site Bose-Hubbard model: Classical versus quantum
Phys. Rev. E **107**, 024210 (2023).
- G. Nakerst, S. Denisov, and M. Haque
Random sparse generators of Markovian evolution and their spectral properties
Phys. Rev. E **108**, 014102 (2023).
- P. C. Burke, G. Nakerst, and M. Haque
Assigning temperatures to eigenstates
Phys. Rev. E **107**, 024102 (2023).
- P.C. Burke, G. Nakerst, and M. Haque
Structure of the Hamiltonian of mean force
Phys. Rev. E **110**, 014111 (2024).
- G. Nakerst, T. Prosen, and M. Haque
The spectral boundary of the asymmetric simple exclusion process: Free fermions, Bethe ansatz, and random matrix theory
Phys. Rev. E **110**, 014110 (2024).

Table of contents

1	Introduction	1
1.1	Random matrices	3
1.1.1	Ensembles of random matrices	4
1.1.2	Spectral densities	9
1.1.3	Eigenvalue correlations	14
1.1.4	Eigenstates	20
1.1.5	The graph framework	22
1.2	Quantum many-body systems	24
1.2.1	Quantum chaos	24
1.2.2	The Eigenstate Thermalization Hypothesis	25
1.2.3	The Bose-Hubbard model	29
1.3	Stochastic many-body systems	34
1.3.1	Generators of Markov processes	35
1.3.2	The Asymmetric Simple Exclusion Process (ASEP)	36
1.3.3	Random generators of Markov processes	41
1.4	Outline and summary of main results	45
2	“Eigenstate thermalization” in the classical limit	49
2.1	Eigenstate expectation value (EEV) fluctuations	50
2.2	EEV fluctuations for random Gaussian states	52
2.2.1	General trace expressions	52
2.2.2	Quadratic observables	54
2.2.3	Scaling in the classical limit	55
2.3	EEV fluctuations for Bose-Hubbard eigenstates	56
2.4	Non-reasons for anomalous scaling	60
2.4.1	Participation ratios	61
2.4.2	Non-identical distribution of eigenstate coefficients	63
2.4.3	Eigenstate correlations	63

2.5	Discussion	67
3	Classical and quantum chaos in a mixed many-body system	71
3.1	Main results for the three site Bose-Hubbard model	72
3.2	Classical Lyapunov exponents	75
3.2.1	Preliminaries	75
3.2.2	The three site case	78
3.2.3	More chaotic cases	79
3.2.4	Magnitudes of Lyapunov exponents as chaos indicator	80
3.3	Eigenvalue statistics	82
3.3.1	Level spacing ratio distribution	82
3.3.2	Average of level spacing ratios	84
3.4	Eigenstate statistics	85
3.5	Scaling of EEV fluctuations	88
3.6	Discussion	89
4	An ensemble of sparse random generators of Markov processes	91
4.1	Motivation	92
4.2	Defining the ensemble	94
4.3	Bulk spectrum	96
4.3.1	Position	97
4.3.2	Horizontal width	98
4.3.3	Ratio of mean and horizontal width	100
4.4	Spectral gap	101
4.4.1	Numerical results	101
4.4.2	Gap as the minimum of the diagonal	102
4.4.3	Extreme value theory	104
4.4.4	Summary	108
4.5	Complex spacing ratios	108
4.6	Discussion	111
4.7	Appendix	113
4.7.1	Analytical results for the bulk spectrum	113
4.7.2	Bound of the spectral gap for symmetric generators	116
4.7.3	Stochastic systems presented in Figure 4.1	117
5	The spectral boundary of the ASEP	121
5.1	The generator as interacting fermions	122

5.1.1	Periodic boundary conditions (pbc)	122
5.1.2	Open boundary conditions (obc)	123
5.1.3	Spectrum	125
5.2	The “non-interacting” ASEP with pbc	127
5.2.1	Single-body spectrum	127
5.2.2	Rotational invariance	128
5.2.3	Spectral boundary	129
5.2.4	Quantification of spikes	131
5.3	The “non-interacting” TASEP with obc	133
5.3.1	Rotational symmetry	133
5.3.2	Single- and many-body spectrum	134
5.3.3	Spectral boundary	138
5.4	The TASEP with pbc by Bethe ansatz	140
5.4.1	Coordinate Bethe ansatz	141
5.4.2	Solving the Bethe equations numerically	147
5.4.3	Structure of the Bethe roots	149
5.4.4	Structure of the many-body spectrum	151
5.4.5	“Thermodynamic limit”	153
5.5	The random matrix picture	154
5.5.1	From TASEP to graphs	154
5.5.2	Cycles of TASEP	155
5.5.3	Random graph model	155
5.6	Discussion	157
6	Summary	159
References		161

Chapter 1

Introduction

Many-body systems in theoretical physics represent an extensive and intricate domain, where the focus is on understanding the collective behavior of systems composed of many interacting components. The term “body” can refer to anything from atoms in a solid or electrons in a conductor to stars in a galaxy. Many-body systems are not just a simple extrapolation of single-particle physics; they exhibit unique and often unexpected behaviors emerging from the interactions between the many constituents of the system.

The study of many-body systems presents several challenges. Real world systems are often so complex that the terms and values for the interactions used to represent them are unknown. Even with precise knowledge of these parameters, the explicit analysis of many-body systems remains challenging. In interacting many-body systems, the state space expands rapidly with the number of particles, making exact solutions infeasible for all but the smallest systems. In addition, strong interactions preclude treatment as small perturbations, necessitating non-perturbative techniques.

The use of random matrix theory (RMT) in many-body systems addresses these challenges. The first application of RMT in physics, specifically to many-body systems, dates back to the 1950s by Eugene Wigner. He showed that statistical correlations in the energy spectra of highly excited heavy nuclei align with eigenvalue correlations in large random matrices. As quantum mechanical many-body systems, heavy nuclei are modeled by Hamiltonians that are represented by large matrices. The exact calculation of high-energy eigenvalues in such complex systems is impractical. Wigner circumvented this by shifting the focus to the statistical properties of energy levels and replacing the Hamiltonian with large matrices having random entries.

The physical properties of the Hamiltonian impose constraints on the ensemble of random matrices to be considered. The microscopic time-evolution of the physical

system is unitary, so the random matrix should be Hermitian. Additionally, the ensemble should adhere to the symmetries of the system, such as time-reversal symmetry. Wigner demonstrated that only these general characteristics, rather than the intricate details of the model, affect the correlations among energy eigenvalues.

In his application of RMT to the high-energy correlations in large nuclei, Wigner demonstrated its utility in analyzing many-body systems. The RMT method starts by pinpointing key structural aspects like symmetries and conservation laws. It then assumes the system is a typical representation of a random distribution that adheres to the identified structures.

In doing so, RMT parallels the principles of statistical mechanics, where emphasis is shifted from detailed microstates to the aggregate macroscopic and statistical behaviors. Unlike statistical mechanics, which requires understanding of the microscopic laws governing interactions, RMT presupposes no specific knowledge of these laws but adopts a probability distribution of all possible interactions. As Freeman Dyson stated in the 1960s, RMT represents “a new kind of statistical mechanics, in which we renounce exact knowledge not of the state of a system but of the nature of the system itself” [1]. This approach makes RMT a fundamental yet comprehensive model for many-body systems with complex or unknown interactions, capturing their essential features without detailed microscopic insights.

In this thesis, we explore the applications of RMT to two classes of many-body systems: quantum many-body systems and stochastic many-body systems. Despite their distinct nature, these two classes can be mathematically modeled similarly. Both are characterized by dynamics driven by linear operators, to which RMT can be applied. In quantum mechanics, the state of a system is encapsulated by a wavefunction within a Hilbert space, with its evolution governed by the Hamiltonian. Probabilistic systems are characterized by probability distributions over microstates. For Markovian (memory-less) systems the temporal change of these probability distributions is determined by a linear generator known as the Kolmogorov operator.

In the quantum context, two major contributions of RMT are particularly relevant to this thesis. First, RMT has been instrumental in bridging classical and quantum chaos. Quantum systems with classical chaotic limits share features with random matrices, including correlations among eigenvalues and the delocalization of eigenstates. This led to classifying quantum systems, which mirror the behavior of random matrices, as quantum chaotic. Second, RMT significantly aids in the understanding of thermalization in isolated quantum many-body systems. Especially, a generalization of an RMT-ansatz to eigenstates of these systems lead to the Eigenstate Thermalization Hypothesis (ETH).

The ETH predicts that in large, generic systems, eigenstate-to-eigenstate fluctuations of expectation values of observables are sufficiently small, allowing these expectation values to attain their equilibrium value in the long time limit.

In this thesis, these two RMT insights are investigated for a specific quantum many-body system — the Bose-Hubbard model which captures the physics of ultracold atoms in optical lattices. We analyze different quantum chaos metrics and contrast them with chaos indicators of its classical counterpart, the discrete nonlinear Schrödinger or Gross-Pitaevskii equation. Furthermore, we explore the “ETH-fluctuations” of local observables in the classical limit of the quantum model.

In our analysis of stochastic many-body systems, we focus on the spectrum of Markov generators. This spectrum, particularly the spectral gap, indicates relaxation times of the systems to their steady state. By studying random Markov generators, we identify the sparsity — many zero matrix elements — of generators as the significant structure that leads to physically realistic relaxation times. This is in contrast to previously studied dense random generators which yield non-physical relaxation times. Additionally, we analyze the generator spectrum of a paradigmatic stochastic many-body system, the Asymmetric Simple Exclusion Process (ASEP). We derive in detail the origin of spikes in the spectral boundary and link it to random matrices with higher-order correlations between entries and random graphs with specific cycle structures.

The remainder of the introduction to this thesis is divided into four sections. Section 1.1 provides an introduction to RMT, with focus on spectral densities and correlations of nearby eigenvalues. Additionally, we briefly discuss random matrix eigenstates and the connection between matrices and graphs. Section 1.2 introduces the concepts of quantum chaos and the ETH, as well as the Bose-Hubbard model and its classical limit, the Gross-Pitaevskii equation. In Section 1.3, we introduce generators of Markov processes and random (dense) generators. We present the ASEP as a paradigmatic many-body Markov process. In Section 1.4, we outline the content of this thesis and provide a summary of the main results.

1.1 Random matrices

This section introduces random matrices, with a focus on properties that are relevant to the application of RMT to many-body systems. An introduction to RMT specifically for physicists is provided by Livan, Nivanen and Vivo [2]. Thorough treatments of the fundamentals, history and applications of random matrices are given in the books of Mehta [3], Forrester [4], and Akemann et al [5] and the review by Edelman and Rao [6].

This is only a short and personally motivated list of the extensive literature on the topic of random matrices.

This introduction to RMT is organized as follows: In Section 1.1.1, we introduce the Hermitian Gaussian ensembles and their non-Hermitian counterparts, the Ginibre ensembles, and comment on their spectral decomposition. Further, we present more general ensembles, which are relevant to this thesis. Section 1.1.2 focuses on the spectral density in the limit of large matrix size. We present Wigner’s semicircle law for Hermitian matrices and the circular law for non-Hermitian matrices. The latter is generalized to the elliptic and hypotrochoidic law. The non-Hermitian spectral densities are relevant for discussing the spectrum of random Kolmogorov operators in Chapter 4 and the ASEP in Chapter 5. Section 1.1.3 addresses correlations among eigenvalues, with focus on the nearest and next-nearest neighbor correlations. We present results for Hermitian matrices, relevant for our analysis of the Bose-Hubbard model, and results for non-Hermitian matrices, which are important for discussing random Kolmogorov operators. In Section 1.1.4, we comment on eigenstates of Hermitian random matrices. These considerations are relevant in our analysis of the “ETH-fluctuations” and chaos in the Bose-Hubbard model in Chapters 2 and 3. We conclude with presenting the connection between matrices and graphs in Section 1.1.5. This relation is relevant for discussing sparse matrices in Chapters 4 and 5.

1.1.1 Ensembles of random matrices

Gaussian ensembles

When Wigner [7] compared the energy correlations of heavy nuclei to random matrix ensembles he considered the simplest ensemble of random matrices obeying the global properties of the considered physical systems: Gaussian random ensembles. In Gaussian random matrices, up to global constraints, all matrix entries are independent random variables, with a common Gaussian distribution. The constraints on the matrix entries ensure Hermiticity and possible symmetries like time-reversal symmetry.

In the Gaussian Orthogonal Ensemble (GOE), the matrices H are characterized by their elements H_{ij} , which are distributed according to

$$H_{ij} \sim \begin{cases} \mathcal{N}(0, 1), & \text{for } i = j, \\ \mathcal{N}\left(0, \frac{1}{2}\right), & \text{for } i < j, \end{cases} \quad (1.1)$$

where $\sim \mathcal{N}(\mu, \sigma^2)$ denotes equality in probability to a Gaussian distribution with mean μ and variance σ^2 . The lower triangular matrix elements are defined via the symmetry condition $H_{ij} = H_{ji}$, which ensures the Hermitian nature of the matrix. Apart from this condition of Hermiticity, the matrix elements are mutually independent.

The designation “orthogonal” in the GOE relates to the invariance of the ensemble under orthogonal transformations. This is most evident when considering the probability density $P(H)$ of the GOE with respect to the Lebesgue measure $dH = \prod_{1 \leq i \leq j \leq D} dH_{ij}$ with dH_{ij} denoting the standard Lebesgue measure in \mathbb{R} and D the matrix size. This density is given by

$$P(H)dH = \frac{1}{Z} \exp\left(-\frac{1}{2} \operatorname{tr} H^2\right) dH, \quad (1.2)$$

where Z is a normalization constant ensuring that Eq. (1.2) integrated over $\mathbb{R}^{D(D+1)/2}$ equals 1. The additional factor of 2 relating the variances of the diagonal and off-diagonal matrix elements in Eq. (1.1) is crucial in deriving Eq. (1.2). When transforming H via $H \rightarrow O^T H O$ for an orthogonal matrix O , the trace term $\operatorname{tr}(H^2)$ remains unchanged. Furthermore, the Lebesgue measure dH is invariant under linear transformations that satisfy $|\det(O)| = 1$, a well-established result in measure theory [8]. Therefore, the GOE is invariant under orthogonal transformations.

The GOE, along with the Gaussian Unitary Ensemble (GUE) and the Gaussian Symplectic Ensemble (GSE), form the triad of classical Hermitian Gaussian ensembles. Each ensemble is defined by a unique symmetry: the GOE exhibits invariance under orthogonal, the GUE under unitary, and the GSE under symplectic transformations. In contrast to the real matrix elements of the GOE, the GUE and GSE are characterized by matrix elements following complex and quaternionic Gaussian distributions, respectively. A common feature across these ensembles is Hermiticity and, beyond this constraint, the mutual independence of all matrix elements. The Gaussian measure, as specified in Eq. (1.2), is the same for all three ensembles, except for the Lebesgue measure. It operates over the complex numbers in the GUE case and over the quaternions in the GSE case, with the constraint that diagonal elements are real.

Symmetries imply nature of matrix elements

The three Gaussian ensembles emerged from symmetry considerations of quantum Hamiltonians, known as Dyson’s three-fold way [9, 10]. This approach aims to classify the fundamental properties of a Hamiltonian H , which either exhibits or lacks time-reversal symmetry \mathcal{T} . The Hamiltonians H not invariant under \mathcal{T} are most generally expressed through Hermitian matrices with complex entries. If H is invariant under \mathcal{T} ,

two cases emerge: $\mathcal{T}^2 = +1$ or $\mathcal{T}^2 = -1$. When $\mathcal{T}^2 = +1$, H is equal to its elementwise complex conjugate, $H = H^*$, making H real symmetric. When $\mathcal{T}^2 = -1$, the matrix elements of H are quaternionic. These are Dyson's three symmetry classes. They are commonly enumerated by the Dyson index β , which denotes the number of real components of the matrix entries: $\beta = 1$ for real, $\beta = 2$ for complex, and $\beta = 4$ for quaternionic matrix entries. The Gaussian measure given by Eq. (1.2) on these three symmetry classes then leads to the GOE, GUE and GSE. In this thesis, we will consider other measures on these symmetry classes as well.

We remark that Dyson's three-fold way has been generalized into a broader framework, the ten-fold way, which classifies, among other things [11], topological insulators and superconductors [12–18, 10].

Spectral decomposition of Gaussian ensembles

With the application to physical systems in mind, understanding the eigenvalues and eigenstates of random matrices is crucial. In quantum systems, eigenvalues represent observable outcomes, with corresponding eigenstates indicating post-measurement system states. In stochastic Markovian systems, eigenvalues are related to relaxation timescales, while the stationary eigenstate encodes long-term microstate occupancies. Therefore, rather than dealing with the distribution $P(H)$ of matrix elements, we will discuss the joint distribution $P(\lambda_1, \dots, \lambda_D, U)$ of the unordered eigenvalues $\lambda_1, \dots, \lambda_D$ and a matrix U encapsulating the eigenstates as its columns.

The transition from $P(H)$ to $P(\lambda_1, \dots, \lambda_D, U)$ represents a change of variables. The trace term $\exp(-\frac{1}{2} \text{tr } H^2)$ is independent of the eigenstates and equals $\exp(-\frac{1}{2} \sum_{j=1}^D \lambda_j^2)$. Consequently, the Gaussian measure in terms of the eigenvalues λ_j and the eigenstates in U is expressed as

$$P(H)dH \propto e^{-\frac{1}{2} \sum_{j=1}^D \lambda_j^2} |\det \text{Jac}(H \rightarrow (\lambda_1, \dots, \lambda_D, U))| \left(\prod_{j=1}^D d\lambda_j \right) dU, \quad (1.3)$$

where \propto omits any normalizing constant Z and $\text{Jac}(H \rightarrow (\lambda_1, \dots, \lambda_D, U))$ is the Jacobian of the transformation. The measure dU is the uniform (Haar) measure of the orthogonal, unitary, or symplectic group, corresponding to the GOE, GUE, or GSE, respectively. Here dU is a probability measure, which samples each matrix in the corresponding invariant group equally likely. For the orthogonal or unitary groups, such samples can be constructed by the Gram-Schmidt process applied to Ginibre matrices, which will be introduced later.

The Jacobian in Eq. (1.3) can be calculated as

$$|\det \text{Jac}(H \rightarrow (\lambda_1, \dots, \lambda_D, U))| = \prod_{1 \leq j < k \leq D} |\lambda_j - \lambda_k|^\beta, \quad (1.4)$$

where β is the Dyson index; $\beta = 1$ for GOE, $\beta = 2$ for GUE, and $\beta = 4$ for GSE. Notably, the Jacobian term does not depend on U . The joint probability density function (JPDF) of eigenvalues and eigenvectors of the Gaussian ensembles is thus

$$P(H)dH \propto e^{-\frac{1}{2} \sum_{j=1}^D \lambda_j^2} \prod_{1 \leq j < k \leq D} |\lambda_j - \lambda_k|^\beta \left(\prod_{j=1}^D d\lambda_j \right) dU. \quad (1.5)$$

The dependence of the Gaussian ensemble on eigenstates solely arises from the Haar measure dU , which greatly simplifies the study of the eigenstates in Section 1.1.4. By integrating out dU the JPDF of eigenvalues of Gaussian matrices is obtained,

$$P(\lambda_1, \dots, \lambda_D) \propto e^{-\frac{1}{2} \sum_{j=1}^D \lambda_j^2} \prod_{1 \leq j < k \leq D} |\lambda_j - \lambda_k|^\beta. \quad (1.6)$$

The eigenvalue distribution of Gaussian matrices has an interesting physical interpretation [1, 19, 20, 2]. By rescaling $\lambda \rightarrow \lambda/\sqrt{\beta} = \tilde{\lambda}$ the eigenvalue JPDF can be recast into a Boltzmann weight

$$P(\tilde{\lambda}_1, \dots, \tilde{\lambda}_D) \propto e^{-\frac{\beta}{2} \sum_{j=1}^D \tilde{\lambda}_j^2 + \frac{\beta}{2} \sum_{j \neq k} \log |\tilde{\lambda}_j - \tilde{\lambda}_k|} = e^{-\beta \mathcal{H}(\tilde{\lambda}_1, \dots, \tilde{\lambda}_D)}, \quad (1.7)$$

where the Hamiltonian $\mathcal{H}(\tilde{\lambda}_1, \dots, \tilde{\lambda}_D) = \frac{1}{2} \sum_{j=1}^D \tilde{\lambda}_j^2 - \frac{1}{2} \sum_{j \neq k} \log |\tilde{\lambda}_j - \tilde{\lambda}_k|$ characterizes a 2D Coulomb gas, due to the logarithmic interaction, restricted to a 1D line in a harmonic potential. In this model, the harmonic potential confines the particles, while the logarithmic interaction induces repulsion among them. Such models are commonly referred to as “log-gas” models [4]. Eq. (1.7) elucidates the interpretation of the Dyson index β as analogous to an inverse temperature. A diagrammatic representation of this log-gas model is depicted in Figure 1.1(b).

Non-Hermitian Ginibre ensembles

The random Gaussian matrices introduced so far are all Hermitian. However, applying RMT to generators of stochastic many-body systems necessitates understanding of non-Hermitian matrices. This leads us to the introduction of the Ginibre ensembles, which are derived from the Gaussian ensembles by dropping the Hermiticity constraint and letting *all* matrix elements be independent random variables. This implies the

absence of any additional factor between the diagonal and off-diagonal matrix entries, in contrast to Eq. (1.1). The so formed random matrix ensembles are the GinOE, GinUE, and GinSE, with real, complex and quaternion matrix entries, respectively. The Gaussian densities of the Ginibre ensembles can be expressed as

$$P(H)dH = \frac{1}{Z} \exp\left(-\frac{1}{2} \operatorname{tr} HH^\dagger\right) dH, \quad (1.8)$$

where Z is a normalization constant ensuring that $P(H)$ is a probability density. The notation H^\dagger varies across ensembles, indicating the Hermitian adjoint for the GinUE, the transpose for the GinOE, and a specific symplectic form for the GinSE. The Ginibre ensembles retain invariance under orthogonal, unitary, and symplectic transformations, respectively, analogous to their Hermitian counterparts.

Similar reasoning as for the Hermitian Gaussian ensembles applies to the spectral decomposition of the Ginibre ensembles. But there are some differences. A key distinction is that the eigenvalues of the Ginibre ensembles are generally complex, and their (left and right) eigenstates are typically not orthogonal.

The GinUE JPDF can be expressed as [21]

$$P(\lambda_1, \dots, \lambda_D) \propto e^{-\frac{1}{2} \sum_{j=1}^D |\lambda_j|^2} \prod_{1 \leq j < k \leq D} |\lambda_j - \lambda_k|^2. \quad (1.9)$$

This formulation bears a direct correspondence to the eigenvalue density of the GUE, as denoted in Eq. (1.6) with $\beta = 2$. For the GinOE and GinSE, the situation diverges from this correspondence. A notable feature of their eigenvalues is the presence of an additional symmetry: eigenvalues are real or come in complex conjugate pairs. For GinOE, a further complication arises due to the non-negligible probability of encountering real eigenvalues [22]. This typically necessitates the exclusion of these real eigenvalues in finite matrix size analyses.

More general ensembles

The Gaussian and Ginibre ensembles have been extended in various ways. Generalizations relevant to this thesis are presented in the following.

First, the Gaussian distribution of matrix elements has been generalized to arbitrary distributions, maintaining the overall nature of independent and identically distributed (iid) matrix elements. In the Hermitian case, these matrices are referred to as Wigner matrices [23]. In the non-Hermitian case, they are referred to as non-Gaussian Ginibre or simply Ginibre matrices. Both, Hermitian and non-Hermitian generalizations,

typically inherit desirable properties of Gaussian matrices like a deterministic spectral density and universal eigenvalue correlations in the limit of large matrix size D as well as delocalized eigenstates. These aspects will be elaborated on in the following Sections 1.1.2, 1.1.3 and 1.1.4.

Second, the quadratic term $\text{tr}(H^2)$ in the probability density of Gaussian matrices given by Eq. (1.2) has been extended to more general functions $V(H)$. The probability densities for these ensembles are generally expressed as

$$P(D)dH = \frac{1}{Z} \exp(-\text{tr } V(H))dH, \quad (1.10)$$

where V represents an even degree polynomial and dH denotes an appropriate Lebesgue measure. The even degree polynomial ensures that, with a finite normalization Z , $P(D)dH$ constitutes a valid probability measure. The Gaussian scenario is the specific case with harmonic potential $V(x) = \frac{1}{2}x^2$. These ensembles are called invariant ensembles, as they are like their Gaussian counterparts, invariant under the transformations of the classical groups. For these invariant ensembles, the joint probability density of eigenvalues is straightforwardly given by

$$P(\lambda_1, \dots, \lambda_D) \propto e^{-\sum_{j=1}^D V(\lambda_j)} \prod_{1 \leq j < k \leq D} |\lambda_j - \lambda_k|^\beta, \quad (1.11)$$

and admits a similar log-gas interpretation as the Gaussian case where the harmonic potential is replaced by V .

Third, the parameter β , previously limited to the integers 1, 2, and 4, has been extended to any positive value, $\beta \geq 0$. These β -ensembles are realized through specific tridiagonal matrix models [24]. They facilitate the exploration of eigenvalue correlations, varying from strong correlation for large β to complete independence as β approaches zero. As discussed in Section 1.2, the transition from correlated to uncorrelated eigenvalues is in the same spirit as the crossover from integrability to chaos in quantum systems. The β -ensembles have been directly applied in investigations of such transitions [25, 26].

1.1.2 Spectral densities

So far we have examined the JPDF $P(\lambda_1, \dots, \lambda_D)$ for eigenvalues $\lambda_1, \dots, \lambda_D$, which, outside of specific cases, generally lacks explicit formulations. However, with the application of RMT to physical many-body systems in mind, the joint probability of all eigenvalues for some finite matrix size D is of less importance than its marginal

distributions in the limit of large D , such as the (average) spectral density or two point correlations of nearby eigenvalues. This section focuses on the limiting behavior of the spectral density, while Section 1.1.3 addresses correlations in form of spacings between neighboring eigenvalues.

For a random matrix H , the spectral density $\rho_D(\lambda)$ is the normalized eigenvalue counting function

$$\rho_D(\lambda) = \frac{1}{D} \sum_{i=1}^D \delta(\lambda - \lambda_i), \quad (1.12)$$

where λ_i are the eigenvalues of H , and δ is the Dirac delta function. The dependence of ρ_D on H is implicit through the eigenvalues λ_i . The average eigenvalue counting function equals the one-parameter marginal of the eigenvalue JPDF

$$\langle \rho_D(\lambda) \rangle = \int_{\mathbb{R}^{D-1}} P(\lambda, \lambda_2, \dots, \lambda_D) d\lambda_2 \dots \lambda_D, \quad (1.13)$$

where $\langle \dots \rangle$ denotes the average over the random matrix ensemble. As the eigenvalues λ_j of H are unordered, the position of λ in P of Eq. (1.13) is arbitrary.

If ρ_D admits, in an appropriate mathematical sense, a well defined limit of large matrix size D we denote this limit as the limiting spectral density,

$$\rho(\lambda) = \lim_{D \rightarrow \infty} \rho_D(\lambda). \quad (1.14)$$

This limiting density, in principle, might still be random, but as we will see shortly, it typically takes a deterministic form. Consequently, in the limit of large D , the spectral density ρ_D concentrates around its average $\langle \rho_D \rangle$, meaning a single large random matrix represents the spectral density of its entire ensemble, $\rho_D \approx \langle \rho_D \rangle \approx \rho$. This concentration result goes under the name of “self-averaging”.

Hermitian matrices - Wigner’s semicircle law

Wigner matrices (Hermitian matrices with iid entries), which have a non-exotic distribution of matrix elements, have, properly rescaled, a common, deterministic limiting spectral density - the Wigner semicircle distribution [23, 27]. Specifically, for matrix distributions with zero mean and finite variance the limiting spectral density is given by

$$\rho_{sc}(\lambda) = \frac{1}{2\pi} \sqrt{4 - \lambda^2}, \quad (1.15)$$

where $\rho_{sc}(\lambda) = 0$ for λ outside of the interval $[-2, 2]$. The rescaling ensures that the limiting distribution is supported on the interval $[-2, 2]$ and, in the case of Gaussian

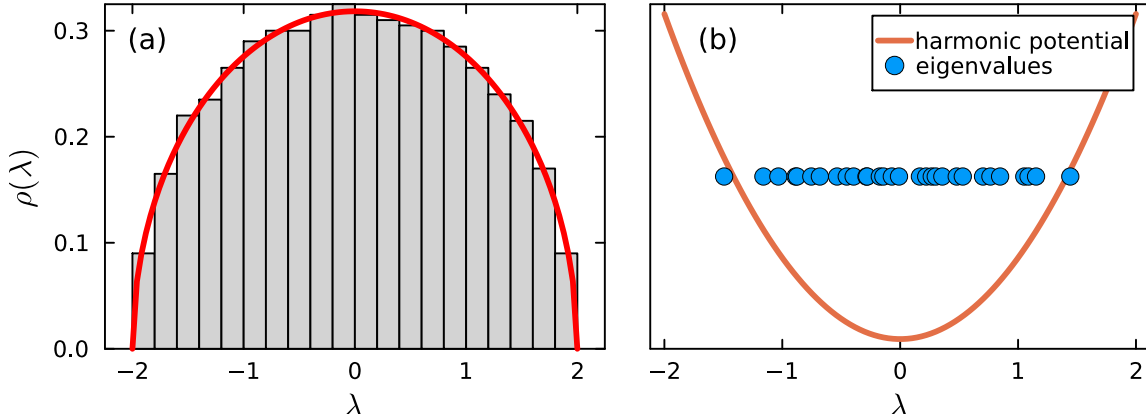


Fig. 1.1 (a) The estimated eigenvalue density of a single 1000×1000 GUE matrix. The red solid line denotes the Wigner semicircle density. (b) Log-gas picture. The orange solid line denotes a harmonic potential and the blue markers are eigenvalues of a single 30×30 GOE matrix.

matrices, is given by $\lambda \rightarrow \sqrt{2}\lambda/\sqrt{\beta D}$. The alignment between the spectral density of a single $D \times D$ GUE matrix with $D = 1000$ and the semicircle distribution is depicted in Figure 1.1(a), with the semicircle distribution (red solid line) serving as an accurate approximation for the spectral density. This exemplifies the self-averaging nature of the spectral density in sufficiently large Wigner matrices.

In the Gaussian case, the limiting spectral distribution can be obtained by a technique common in statistical mechanics. By considering the log-gas picture of the eigenvalue JPDF in Eq. (1.7), Wigner's semicircle distribution emerges in the limit of $D \rightarrow \infty$ by minimizing the free energy corresponding to the partition function $Z = \int d\lambda \tilde{e}^{-\beta \mathcal{H}(\lambda)}$ with \mathcal{H} given as in Eq. (1.7) [4, 2, 28].

The property of a common distribution of matrix entries can be relaxed in terms of more general conditions [27]. Exceptions of the Wigner law occur for random matrices with additional structure like Markov matrices [27, 29], sparse matrices with few non-zero entries or sharply peaked matrix element distributions [30, 31], and banded matrices with small bandwidth [32–42].

Non-Hermitian matrices - circular, elliptic and hypotrochoidic law

We turn to limiting spectral densities of non-Hermitian random matrices, which are important in our analysis of random Kolmogorov and ASEP generator spectra in Chapters 4 and 5. A distinction from the Hermitian case is that eigenvalues are complex, hence, limiting spectral densities are defined within the complex plane.

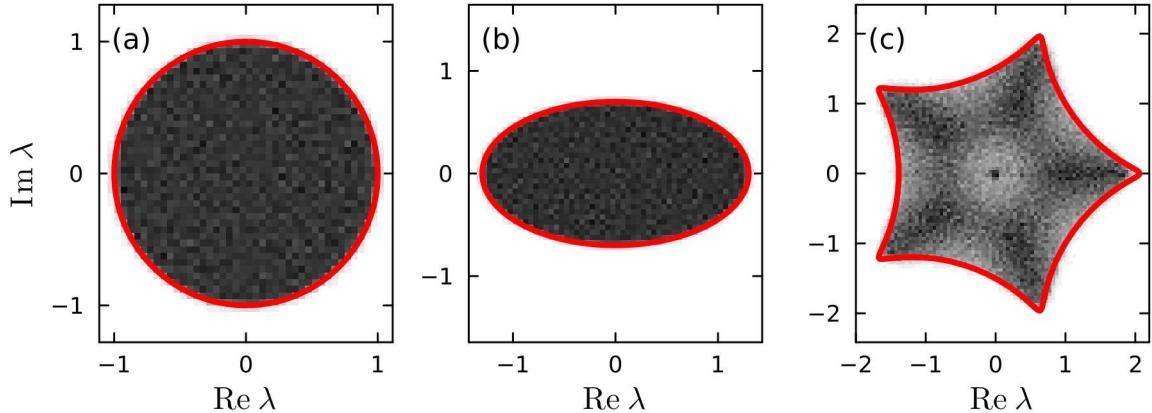


Fig. 1.2 The estimated eigenvalue density of the (a) GinUE, (b) elliptic ensemble with $\tau = 0.3$ and (c) random graphs with cycle length ≥ 5 . Darker color indicates higher density. Matrices are of size 1000×1000 and averages are over 200 samples. The red solid curves denote the boundary of the Girko disc (a), an ellipse with axes $1 \pm \tau$ (b), and a hypotrochoid curve (c), respectively.

The spectral densities of Ginibre matrices (iid entries) with non-exotic matrix element distributions conform to a common, deterministic limiting spectral density. This distribution is uniform on a disk centered at the origin of the complex plane [43, 44]. Due to the simple shape of the support, the limiting law is called the circular law. In honor to Girko, who first derived it in a general setting [43], it is also known as Girko law. In this thesis, we will alternate between the two notions.

Figure 1.2(a) illustrates the computed spectral density of $D \times D$ random GinUE matrices with $D = 1000$. It shows a concentration predominantly within the Girko disc, where it appears uniform. The GinUE matrices are rescaled by $\lambda \rightarrow \lambda/\sqrt{D}$ resulting in the Girko disc having unit radius. The minor variances noted in Figure 1.2(a) are attributable to finite sample effects, derived from a dataset of 100 samples. We note that due to the self-averaging of the spectral density, similar results to Figure 1.2(a) would be obtained for a single realization of the GinUE with $D \approx 10^5$.

The Girko disc is the limiting spectral density of random matrices with independent entries. To investigate the spectral boundary of the ASEP in Chapter 5 from the RMT perspective, it is advantageous to consider random matrices with correlated entries.

Let us first focus on random matrices with two-point correlations between opposite off-diagonal matrix entries

$$\langle H_{ij} H_{ji} \rangle = \tau/D, \quad (1.16)$$

where $\langle \dots \rangle$ denotes the averaging over the random matrix ensemble. Random matrices of such ensembles have a uniform limiting spectral density, which is supported on the

ellipse centered at 0 with semi-major and -minor axis $1 + \tau$ and $1 - \tau$, respectively [45, 46]. This density transitions from the Girko disk at $\tau \rightarrow 0$ to Wigner's semicircle at $\tau \rightarrow 1$. An ensemble of matrices H_{ell} following this elliptic law is constructed by mixing matrices H_1 and H_2 , which adhere to the semicircle law, as

$$H_{ell} = \frac{1}{\sqrt{2}} \left(\sqrt{1 + \tau} H_1 + \sqrt{1 - \tau} i H_2 \right). \quad (1.17)$$

Figure 1.2(b) displays the elliptic law, illustrating the limiting spectral distribution of Eq. (1.17) with $\tau = 0.3$, where $H_{1,2}$ are distributed according to the GUE. The boundary of the support, marked by a red curve, corresponds to an ellipse with axes $1 \pm \tau$.

We note that the two-point correlations given by Eq. (1.16) imply $\frac{1}{D} \langle \text{tr}(H^2) \rangle = \tau$. In this form, matrices adhering to the elliptical law are naturally generalized to matrices with higher-order correlations by considering powers $k \geq 2$,

$$\frac{1}{D} \langle \text{tr}(H^k) \rangle = \tau. \quad (1.18)$$

In the large matrix size limit, the spectral boundary of ensembles with such correlations of matrix entries takes the form of a hypotrochoid, a curve generated by a point on a smaller disk rolling inside a larger circle. The limiting density is thus called the hypotrochoidic law [47]. For $k = 2$ the elliptic law and for $k = 1$ the Girko law are recovered. We note that the limiting spectral density is not flat for $k > 2$, as evident in Figure 1.2(c) for $k = 5$.

The hypotrochoid characterizing the spectral boundary can be parametrized as

$$e^{-it}(\gamma_1 + \gamma_2 e^{ikt}) \quad (1.19)$$

with t running from 0 to 2π . The real constants $\gamma_{1,2}$ depend on the matrix ensemble [47] and their ratio adjusts the “spikiness” of the boundary. In the limit of $\gamma_2 \rightarrow 0$, the circular law is recovered, resulting in a non-spiky boundary. For $0 \ll \gamma_2 \approx \gamma_1/k$ the spectral boundary appears spiky, as shown in Figure 1.2(c). This adjustability of the spikiness in the parametrization of the hypotrochoid is relevant to our analysis of the spectral boundary of the ASEP in Chapter 5.

An ensemble conforming to the hypotrochoidic law are adjacency matrices of random directed graphs [47]. For these matrices to satisfy Eq. (1.18), the associated graphs must predominantly contain cycles of length k . The relationship between the cycle length of graphs and the trace powers, given by Eq. (1.18), will be detailed at the end

of this introduction to RMT in Section 1.1.5. A modification of this graph ensemble will be compared to the ASEP in Chapter 5.

Figure 1.2(c) displays the spectral density of adjacency matrices of random sparse directed graphs, specifically designed without cycles shorter than length 5. These graphs are formed by adding 400 cycles of length 5 to an initially empty graph with $D = 1000$ vertices, ensuring no cycles of length < 5 exist. The resulting adjacency matrices exhibit average trace correlations τ , as defined by Eq. (1.18), with $\tau = 0$ for $k < 5$ and $\tau \approx 2.2$ for $k = 5$. While cycles longer than length 5 are present in this ensemble, their correlations are less dominant. In this graph ensemble, the edge count (2000) is comparable to the vertex count, resulting in significant spectral weight at zero, which is not depicted in Figure 1.2(c).

1.1.3 Eigenvalue correlations

This section discusses correlations between adjacent eigenvalues, quantified by level spacings and level spacing ratios. First, we will address the Hermitian case, where eigenvalues are real. The eigenvalue correlations of Hermitian random matrices are an important signature of quantum chaos. Level spacing ratios will be calculated for the Bose-Hubbard model and compared to the RMT prediction in Chapter 3. Second, we will focus on the non-Hermitian case, where eigenvalues are complex. We introduce complex spacing ratios, which will be used in analyzing spectral correlations of random Kolmogorov operators in Chapter 4. Third, we present level spacings and level spacing ratios of uncorrelated random values. These are important for demarcating chaotic from non-chaotic quantum systems in Chapter 3.

Real level spacings

Correlations of nearby real eigenvalues can be measured in terms of the spacing between them. Let us consider ordered eigenvalues $\lambda_j < \lambda_{j+1}$. Given two adjacent energy levels λ_j and λ_{j+1} the level spacing is defined as $s_j = \lambda_{j+1} - \lambda_j$.

For random matrix ensembles, where the JPDF of eigenvalues is known, the distribution of the level spacings s can in principle be obtained by integrating out all but two neighboring eigenvalues. This turns out to be a difficult task and closed form expressions are up-to-date not known, even for the Gaussian ensembles. Nevertheless, from the eigenvalue JPDF of the Gaussian ensembles given by Eq. (1.6), we should infer some information on the level spacing distribution. For example, the power β of the Euclidean distance between two eigenvalues suggests that the density for small spacing

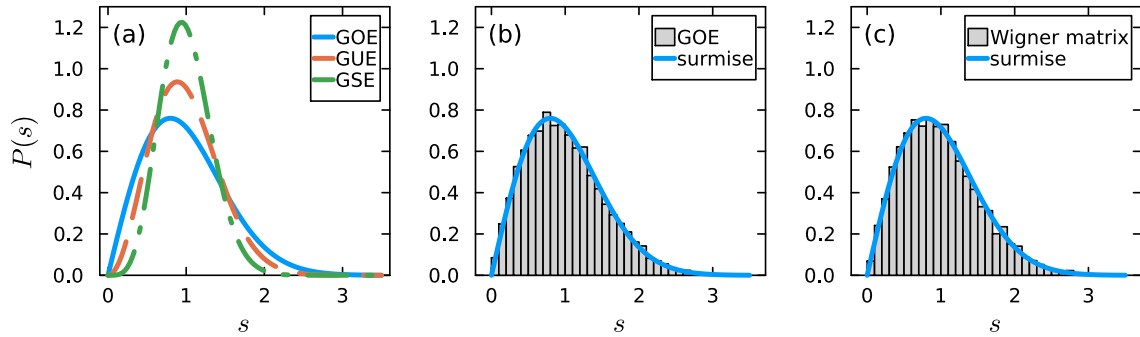


Fig. 1.3 (a) Wigner’s surmise of the level spacing distribution for GOE, GUE and the GSE (bottom to top at peak). (b,c) Unfolded spacing distribution of a single random matrix with dimension $D = 10,000$ from the (b) GOE and (c) Wigner ensemble with uniform entries between ± 1 . Both distributions are well approximated by the corresponding Wigner surmise.

s should vanish proportional to s^β , while the density should vanish exponentially for large s due to the confining harmonic potential.

These heuristic guesses from the form of the eigenvalue JPDF are confirmed in the case of matrix dimension $D = 2$, where the density of the only spacing $s = \lambda_2 - \lambda_1$ is given by

$$P(s) = \frac{1}{Z_\beta} s^\beta e^{-c_\beta s^2}, \quad (1.20)$$

with Z_β a normalization constant and c_β another constant. The functional form of Eq. (1.20) confirms the expected power-law vanishing of s for small s and exponential vanishing for large s . This is displayed in Figure 1.3(a).

Surprisingly, the spacing distribution of 2×2 Gaussian matrices is a good approximation of the spacing distribution of large D Gaussian matrices. This is known as Wigner’s surmise [7]. In Figure 1.3(b), the level spacing density of a single GOE matrix with dimension $D = 10,000$ is displayed and agrees well with the Wigner surmise for $\beta = 1$ given by Eq. (1.20).

Similar to the Wigner law governing the limiting spectral density, the Gaussian level spacing distribution applies to a broader class of matrices beyond the Gaussian ensembles. Specifically, random matrices that share the same moments of matrix elements with the Gaussian ensembles exhibit identical level spacing distributions [44, 48]. Typically, matching the first two moments — the mean and variance — is sufficient [49]. This phenomenon is known as the universality of level spacing distributions. The symmetry class ($\beta = 1$ real, $\beta = 2$ complex or $\beta = 4$ quaternionic

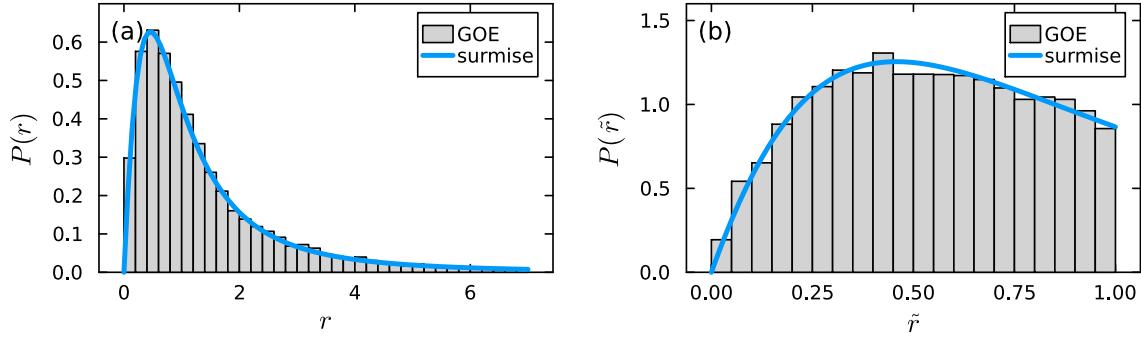


Fig. 1.4 Distribution of level ratios (a) r and (b) \tilde{r} of a single GOE matrix with dimension $D = 10,000$; in both cases well approximated by the GOE Wigner-like surmise Eq. (1.23).

matrix entries) of a Hermitian random matrix, irrespective of whether the measure is Gaussian or not, determines the level spacing distribution.

This universality is highlighted in Figure 1.3(c) where the spacing distribution of a Wigner matrix with uniformly distributed matrix elements between -1 and $+1$ is displayed. As the matrix entries are real, the spacing distribution is well approximated by the Wigner surmise with $\beta = 1$.

Real level spacing ratios

When considering differences between eigenvalues in terms of level spacings, we ignored the overall scale of the differences. The level spacings depend on the local eigenvalue density. A comparison of the level spacing distribution originating from different sources (different parts of the spectrum or different random ensembles) is only meaningful with a common local eigenvalue density. Unifying the local eigenvalue density is known as unfolding of the spectrum.

In Eq. (1.20) as well as in Figure 1.3, the eigenvalue density in the form of Wigner's semicircle distribution was taken into account already, resulting in an average level spacing of 1. This is evident in Figure 1.3, where the peak of the densities given by Wigner's surmise is located close to 1.

Unfolding the spectrum can be cumbersome, especially, when the (limiting) spectral density is not known. This might not so much be an issue for random matrix ensembles, which typically obey Wigner's semicircular law, but can be problematic for physical many-body systems. It has therefore become common to investigate instead of s_j the

distribution of spacing ratios [50, 51]

$$r_j = \frac{s_{j+1}}{s_j}. \quad (1.21)$$

Studying the ratio distribution bypasses the need to unfold the spectrum as the dependence of s_j on the spectral density cancels in the numerator and denominator. Using the quantity

$$\tilde{r}_j = \min \left(r_j, \frac{1}{r_j} \right) = \frac{\min(s_j, s_{j+1})}{\max(s_j, s_{j+1})} \quad (1.22)$$

has the additional benefit of \tilde{r}_j having bounded support, $\tilde{r}_j \in [0, 1]$. This is an advantage in numerical simulations, where only finitely many samples are available and densities are approximated by histograms. The two ratio distributions are related by $P(\tilde{r}) = 2P(r)\Theta(1-r)$, where Θ denotes the Heaviside function [51].

The level ratio distributions of r and \tilde{r}_j are not known in closed form, just like the level spacing distribution. Similar to Wigner's surmise, an approximation to the level spacing ratio distribution is known [51] and given by

$$P(r) = \frac{1}{Z_\beta} \frac{(r+r^2)^\beta}{(1+r+r^2)^{1+3\beta/2}}, \quad (1.23)$$

where Z_β is the normalization constant. For \tilde{r} instead of r , Eq. (1.23) has an additional factor of 2 and is confined to the interval $[0, 1]$. The spacing ratio distributions of Gaussian random matrices with large matrix dimension D is well approximated by the Wigner-like surmise in Eq. (1.23) [51].

In Figure 1.4, the spacing ratio distribution of r in (a) and \tilde{r} in (b) are shown for a single GOE matrix with $D = 10,000$. The Wigner-like surmise with $\beta = 1$ given by Eq. (1.23) is well approximating in both cases. The surmise for the spacing ratio distribution has similar features to the Wigner surmise of the level spacings given by Eq. (1.20). Both densities vanish for decreasing argument as power-law with power β . This enables either to distinguish between the universality classes.

Complex level spacing ratios

Let us now turn to eigenvalue correlations of non-Hermitian matrices. Eigenvalues of such matrices are in general complex and do not follow a natural ordering. Nonetheless, every eigenvalue λ_j has a nearest neighbor eigenvalue λ_j^{NN} and a next-nearest eigenvalue λ_j^{NNN} , which are closest and second closest in Euclidean distance, respectively.

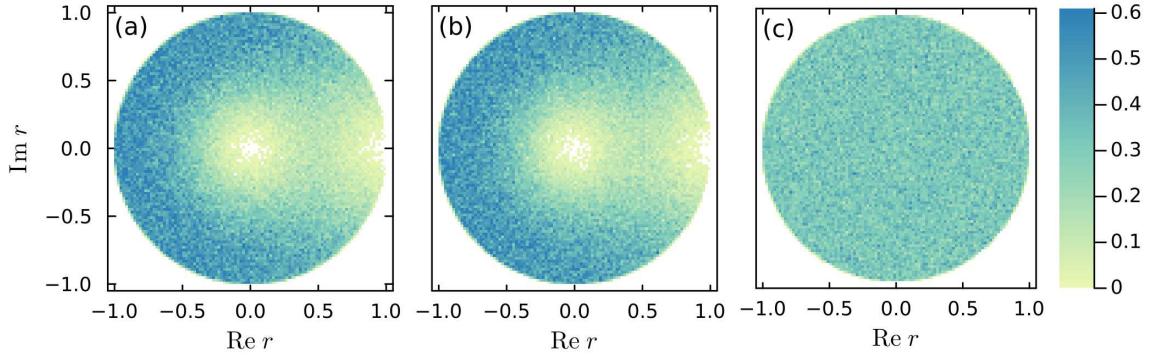


Fig. 1.5 Distribution of complex spacing ratios r of the (a) GinUE, (b) random ensemble with complex entries uniformly distributed in $[-1, 1]^2$ and (c) uncorrelated complex normal variables. (a,b) Densities are estimated by $200 D \times D$ matrices with $D = 1000$ and (c) 10^5 independent random variables.

Following the work by Ref. [52] we denote the complex spacing ratio (CSR) as

$$r_j = \frac{\lambda_j^{NN} - \lambda_j}{\lambda_j^{NNN} - \lambda_j}. \quad (1.24)$$

The CSR is in general complex valued with absolute value bounded by 1. We note that this definition of a CSR does not reduce to the definition of the real spacing ratio for real eigenvalues λ , as it stills carries a sign. Taking the absolute value $|r|$ results in the real spacing ratio \tilde{r} for real eigenvalues.

We first consider the CSR distribution of the GinUE. In Figure 1.5(a) we present the CSR distribution of $D \times D$ GinUE matrices with $D = 1,000$ obtained from 200 samples. The CSR displays vanishing density at 0 and 1. Both are a consequence of eigenvalue repulsion, evident from the eigenvalue JPDF of the GinUE presented in Eq. (1.9) of Section 1.1.1. Vanishing density at 0 results from repulsion of λ_j and λ_j^{NN} , while repulsion of λ_j^{NN} and λ_j^{NNN} implies vanishing density at 1.

Similar to the Hermitian case, the correlations of non-Hermitian Ginibre ensembles do not depend on the details of the matrix element distribution. Ginibre matrices, with matching first four moments of matrix element distributions, have common eigenvalue correlations [53]. As an example we show the CSR density of Ginibre matrices with uniformly distributed entries in $[-1, 1]^2 \subset \mathbb{C}$ in Figure 1.5(b). The estimated densities in panels (a) and (b) of Figure 1.5 only differ by finite size and sample fluctuations.

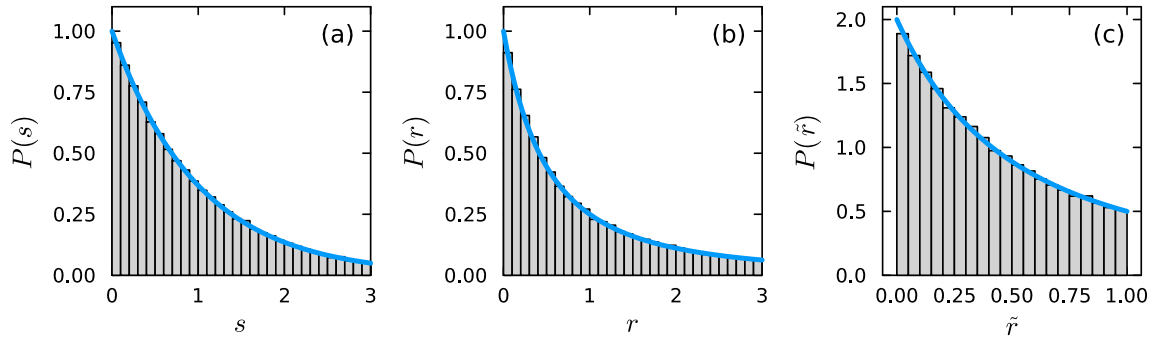


Fig. 1.6 (a) Estimated densities of level spacings and (b,c) level ratios for 10^5 uncorrelated Gaussian random variables. The solid blue lines correspond to the analytical expressions in Eq. (1.26) and Eq. (1.27).

Uncorrelated random variables

This section so far has been concerned with correlated random variables typical for eigenvalues of random matrices. Following, we present the level spacings and ratios of uncorrelated random variables. This discussion is motivated by quantum chaos distinctions: chaotic systems have correlated eigenvalues like random matrices, whereas non-chaotic systems have eigenvalues resembling uncorrelated variables.

Let us consider D uncorrelated, ordered values $\lambda_j < \lambda_{j+1}$, which are distributed according to some common distribution. After unfolding one can assume without loss of generality that the λ 's are distributed uniformly in $[0, D]$. This choice of an interval ensures an average spacing of 1. The independence of the values λ is not altered by the unfolding procedure. It is well known that ordered samples of the uniform distribution follow the Beta-distribution and so do their increments [54]. Especially, the cumulative distribution function F of the spacing s is given by

$$F(s) = 1 - \left(1 - \frac{s}{D}\right)^D. \quad (1.25)$$

The corresponding density $P(s) = \frac{d}{ds}F(s)$ in the limit of large D becomes the density of the exponential distribution with mean 1,

$$P_{\text{Poi}}(s) = e^{-s}. \quad (1.26)$$

Uncorrelated values are referred to as Poisson distributed, since the order statistics of the unfolded values correspond to arrival times of a Poisson process [54]. The distribution of spacings in Eq. (1.26) is therefore referred to as “Poisson level spacings”.

Unlike the correlated eigenvalues of random matrices, the spacing distribution for uncorrelated values, P_{Poi} , approaches 1 at vanishing spacing $s \rightarrow 0$. This is illustrated in Figure 1.6(a), which shows the level spacings for uncorrelated random variables. This distinctive feature is often employed when distinguishing between correlated and uncorrelated nearest-neighbor levels.

Similarly to the level spacing distribution, the distribution of spacing ratios can also be derived analytically,

$$P_{\text{Poi}}(r) = \frac{1}{(r+1)^2}, \quad (1.27)$$

with an additional factor of 2 for \tilde{r} instead of r . For uncorrelated random variables both spacing ratios r and \tilde{r} are shown in Figure 1.6(b) and (c), respectively. Like the level spacing, the level spacing ratio densities do not vanish for $r \rightarrow 0$ ($\tilde{r} \rightarrow 0$). Hence, both level spacing and level spacing ratios are able to demarcate between correlated and uncorrelated random variables.

A similar line of reasoning can be applied to the case of complex uncorrelated values. The corresponding CSR distribution r is flat in the unit circle [52]. This is in contrast to the CSRs of random matrix eigenvalues, which show vanishing density at 0 and 1. The CSR distribution of uncorrelated complex normal variables is depicted in Figure 1.5(c). Up to finite size and sample fluctuations the CSR density appears flat inside the unit circle with value π^{-1} .

1.1.4 Eigenstates

In this section, we present the distribution of eigenstates of random matrices. We focus on eigenstates of Hermitian random matrices with real coefficients. Understanding of such states is important for motivating the Eigenstate Thermalization Hypothesis (ETH) in Section 1.2.2 and deriving random matrix eigenstate-to-eigenstate fluctuations of bosonic operators in Chapter 2. Additionally, in Chapter 3, the (de-)localization of eigenstates is used to demarcate chaos from integrability in the Bose-Hubbard model. The random matrix eigenstate is the typical chaotic state.

For this thesis, it is sufficient to consider eigenstates of the GOE. As depicted in Eq. (1.5), the density of the GOE depends on the eigenstates solely through the Haar measure dU defined on the orthogonal group. The invariance of the Haar measure under actions of this group implies that eigenstates are also invariant. Consequently, normalized eigenstates of the GOE are uniformly distributed on the $(D-1)$ -dimensional unit sphere S^{D-1} in \mathbb{R}^D . In fact, all ensembles invariant under the orthogonal group have such distributed eigenstates.

The invariant distribution on high-dimensional spheres is somewhat elusive. Its approximation for large D is more convenient to deal with. Specifically, eigenstates of invariant ensembles are closely approximated by a D -dimensional Gaussian distribution with independent entries, zero mean, and variance D^{-1} [55, 56]. The variance D^{-1} ensures approximate normalization of such states.

The D -dimensional Gaussian states are likely to be delocalized, with their eigenvector coefficients evenly spread across the entire basis. This is in contrast to localized eigenvectors where only a few coefficients are significantly non-zero.

Effective measures for assessing this (de-)localization are the inverse participation ratio (IPR) and the kurtosis κ . Both concepts are important for our analysis of eigenstates in Chapters 2 and 3. For a normalized eigenstate $v = (v_1, \dots, v_D)$, where $\|v\|_2^2 = \sum_{j=1}^D v_j^2 = 1$, the IPR is defined as

$$\text{IPR} = \sum_{j=1}^D v_j^4. \quad (1.28)$$

Given the normalization of the eigenstate v , the IPR ranges from D^{-1} to 1. An IPR of D^{-1} indicates a fully delocalized state (where $v_j = D^{-1/2}$ for all j), while an IPR of 1 signifies a completely localized state (where $v_j = \delta_{jk}$ for some $1 \leq k \leq D$).

A measure closely related to the IPR is the kurtosis of an eigenstate. It estimates the standardized fourth moment of a distribution with samples v_j . The kurtosis of a state v is defined as

$$\kappa = D \frac{\sum_{j=1}^D (v_j - \bar{v})^4}{\left(\sum_{j=1}^D (v_j - \bar{v})^2\right)^2}, \quad (1.29)$$

where $\bar{v} = \frac{1}{D} \sum_{j=1}^D v_j$ denotes the average coefficient. For vanishing average, $\bar{v} = 0$, the kurtosis κ and the IPR are related by $\kappa = D \times \text{IPR}$.

For large D , the kurtosis κ of a Gaussian state is $\kappa = 3$ with probability approaching 1. Consequently, Gaussian states have an IPR of $3D^{-1}$, which is close to a completely delocalized state. However, the inherent randomness in the Gaussian states inhibits such states from reaching an IPR of D^{-1} , which is characteristic of the deterministic, completely delocalized state. Nevertheless, states with kurtosis close to 3 (or IPR close to $3D^{-1}$) are considered delocalized.

Eigenstates of more general random matrix ensembles than the GOE, for example Wigner matrices with non-exotic matrix element distributions, are typically delocalized [57, 58]. Deviations appear in random banded matrices with small band width and in adjacency matrices of sparse graphs with low connectivity [34, 30, 31, 59].

1.1.5 The graph framework

In this section, we present the connection between matrices and graphs. Specifically, we discuss adjacency and Laplacian matrices of graphs and how their spectra relate to graph properties. Additionally, random graph ensembles and their sampling methods will be briefly touched upon. The correspondence between matrices and graphs is important for discussing Markov generators in Chapters 4 and 5. The relation between graphs and matrices has already been used for presenting an ensemble of random matrices, obeying the hypotrochoidic law in Section 1.1.2.

Graphs are composed of vertices, labeled $1, \dots, D$, and edges (i, j) linking these vertices. The degree of a vertex i denotes the number of edges connecting to i . In this thesis, we deal exclusively with graphs without multiple edges connecting the same pair of vertices. Consequently, graphs are one-to-one with the adjacency matrices A . Their matrix entries, A_{ij} , equal 1 if there is an edge (i, j) between vertices i and j , and 0 if not. This constitutes the standard definition of adjacency matrices. In this thesis, the definition is expanded to include arbitrary real or complex values A_{ij} . These are referred to as the weights of the edges (i, j) . A weight of $A_{ij} = 0$ always signifies the absence of an edge from vertex j to i . In Chapters 4 and 5, graphs with general edge weights will be discussed.

The graph Laplacian matrix $L = \mathcal{D} - A$ offers an alternative matrix representation to the adjacency matrix. Here, \mathcal{D} is the degree matrix with each diagonal element \mathcal{D}_{ii} representing the degree of vertex i . This Laplacian is related to the discrete approximation of the continuous Laplace operator $\Delta = \nabla^2$ by finite differences. The negative Laplacian $-L$ serves as a generator for continuous-time Markov processes on finite state spaces, as detailed in Section 1.3.1.

Graphs can be undirected or directed. In undirected graphs, edges lack orientation, allowing traversal between vertices i and j in both directions. Conversely, directed graphs have unidirectional edges, where an edge from vertex i to j does not necessarily imply a reciprocal edge from j to i . For undirected graphs, both adjacency and Laplacian matrices are symmetric with a real spectrum. In directed graphs, these matrices are typically asymmetric, leading to a complex spectrum.

Spectra and graph structure

The spectra of the adjacency matrix A and the Laplacian L are deeply connected to the properties and structure of the graph itself [60].

One relation between the spectrum of the adjacency matrix and graph properties has already been used at the end of Section 1.1.2 to construct an ensemble of random adjacency matrices following the hypotrochoidic law. The sum of the k th powers of eigenvalues of A , $\sum_i \lambda_i^k$, equals $\text{tr}(A^k)$, which in turn represent the total number of closed walks of length k . The latter follows from considering the entry $(A^k)_{ij}$ which counts the distinct k -step walks between vertices j and i . The diagonal elements $(A^k)_{ii}$ and $\text{tr}(A^k)$, respectively, count the unique closed walks of length k starting at vertex i , and the total number of such walks graph-wide. A cycle is defined as a closed walk without repeated edges. If $\text{tr}(A^k) = 0$, the graph lacks closed walks of length k , and consequently, cycles of that length. Hence, the adjacency matrices of the graph ensemble discussed in Section 1.1.2 exhibit zero trace correlations as per Eq. (1.18) for $k < 5$, while these correlations become dominant when $k = 5$.

Like the spectra of adjacency matrices, the spectra of Laplacians are also related to properties of the corresponding graph. By definition, the Laplacian spectrum resides in the right half of the complex plane. The eigenvalue with the smallest real part is $\lambda_1 = 0$. Its multiplicity reflects the connectivity of the graph. Specifically, if λ_1 has a multiplicity of one, the graph is connected. In undirected graphs, this implies that every vertex is accessible from any other vertex. In directed graphs, connectivity means that all vertices are reachable from each other when edge directions are disregarded, allowing bidirectional traversal. A directed graph where each vertex is accessible from every other vertex, respecting the directed nature of the edges, is termed strongly-connected.

The spectral gap, defined as the real part of the second-smallest (by magnitude of the real part) eigenvalue λ_2 of the Laplacian, provides further information about the connectivity of the graph [61, 62]. In a nutshell, a large spectral gap in a (strongly) connected graph implies “severe connectivity”, requiring the removal of numerous vertices to disconnect it. In contrast, a small spectral gap makes the graph easily disconnected by removing few vertices. For instance, a fully connected graph exhibits a maximal spectral gap and remains connected despite removal of any number of vertices. A one-dimensional line graph has a minimal spectral gap and becomes disconnected with the removal of just one non-boundary vertex.

Random ensembles

Random graph ensembles can be defined by specifying properties (such as number of vertices and edges, average degree, connectivity, or edge weight distributions) and then considering a distribution, typically the uniform distribution, across all graphs meeting these criteria. Sampling from these ensembles often involves starting with

a deterministic graph, such as an empty or fully connected graph, and iteratively modifying vertices and edges randomly.

The random matrices introduced in Section 1.1 are adjacency matrices of random graph ensembles. Matrices with iid elements correspond to fully connected graphs with random iid edge weights. In Section 1.1.2, the random matrix ensemble, following the hypotrochoidic law, can be represented by adjacency matrices of graphs that are not fully connected but rather sparse. The random graph ensemble was constructed by iteratively adding cycles of length $k = 5$ to an initially empty graph, ensuring that each addition of a cycle into the graph did not create cycles with length shorter than 5. This process was continued until the graph contained a sufficient number of edges. Samples created this way are expected to be approximately uniform over all graphs with fixed number of vertices and edges and the property that no cycles with length smaller than 5 are present in the graph.

More examples of random graph ensembles will be presented in Chapters 4 and 5.

1.2 Quantum many-body systems

This section provides some relevant background related to quantum many-body systems, underpinned by Random Matrix Theory (RMT). Section 1.2.1 presents the interplay between classical and quantum chaos, emphasizing the impact of RMT on quantum chaos. In Section 1.2.2, we discuss the development of the Eigenstate Thermalization Hypothesis (ETH) from RMT. In Chapters 2 and 3, the classical-quantum chaos correspondence and statistical aspects related to the ETH are studied for the Bose-Hubbard model. We introduce this many-body system in Section 1.2.3.

1.2.1 Quantum chaos

The concept of chaos in quantum systems has been a subject of debate since the emergence of quantum mechanics [63]. While dynamics of classical chaotic systems exhibit sensitivity to initial conditions [64], applying these ideas to quantum mechanics is challenging due to its linear nature. This linearity contrasts with the non-linear characteristics of classical chaos. Consequently, the principles of classical chaos do not directly translate to the quantum realm.

The adoption of random matrices to describe complex quantum systems significantly advanced the field of quantum chaos [65–67]. It was observed first in single particle systems, particularly in quantized billiards where a single particle is confined by rigid

walls, that high-energy level correlations follow RMT predictions when their classical counterparts are chaotic. Conversely, when the classical system is (Liouville-) integrable, possessing sufficient integrals of motion, the energy levels behave like uncorrelated variables. This led to the hypothesis that quantum systems with a classically chaotic limit should follow RMT level statistics [68, 69], while those with classical integrability display Poisson level statistics [70].

Convincing evidence supporting the conjectures has been found in quantum systems with classical limits other than billiards, such as coupled rotors or coupled tops [71–75], bosonic systems [76–78], the Dicke model and other spin-boson systems [79–89], the Sherrington-Kirkpatrick model [90], and spin systems [91–94]. A common theme is that, for spin systems or systems with angular momentum, the large-spin or large angular momentum limit is the classical limit. For bosonic systems, the classical limit is attained for large number of bosons. In Section 1.2.3, we detail this for the Bose-Hubbard model.

Besides the correlation of eigenvalues, other properties of quantum systems have been used to distinguish between chaotic and non-chaotic systems. In quantum many-body systems, RMT eigenvalue correlations typically coincide with delocalization of eigenstates, with near-Gaussian distributed coefficients [95–104]. In contrast, non-chaotic systems are characterized by imperfectly delocalized states, typically with markedly non-Gaussian coefficient distributions [105, 95, 96, 99].

Other measures of chaos are based on the dynamics of quantum systems, such as the out-of-time-ordered correlator (OTOC) [106–109]. It describes the averaged evolution of quantum operators at different times. In the classical limit of quantum chaotic many-body systems, the OTOC typically grows for short times exponentially [110, 93, 83–85, 111, 112]. Although there are some exceptions [113]. This growth rate is related to Lyapunov exponents of the classical limit. Consequently, the OTOC has been identified as a quantum version of the classical Lyapunov exponent. In classical systems, Lyapunov exponents indicate the sensitivity of dynamics to small perturbations of initial conditions. They measure the exponential rate at which nearby trajectories diverge. Lyapunov exponents will be discussed in Chapter 3.

1.2.2 The Eigenstate Thermalization Hypothesis

In the past decades, significant research efforts have been devoted to elucidating the mechanisms by which isolated quantum systems undergo relaxation and thermalization. Theoretical foundations of thermalization in closed quantum systems trace back to work of von Neumann [114]. But recent advancements in ultra-cold atom and trapped ion

experiments, enabling effective isolation of these systems over experimentally relevant time-scales, have revitalized interest in this area [115]. A major challenge for the emergence of thermalization is the unitary and reversible nature of time-evolution in isolated quantum systems, echoing the difficulties encountered in linking classical and quantum chaos.

A way to address this problem emerged in the 1990s, when Deutsch and Srednicki introduced the Eigenstate Thermalization Hypothesis (ETH) [116–119], which has since become pivotal in understanding thermalization in isolated quantum systems [120–124]. In much the same way that RMT has been instrumental in advancing our understanding of quantum chaos, it has similarly played a key role in addressing the question of thermalization in these systems. Moreover, the ETH is strongly related to eigenstates of random matrices (introduced in Section 1.1.4). Following Ref. [124], we will present the progression from eigenstates of random matrices to the formulation of the ETH. This not only highlights the relevance of RMT for the ETH and the thermalization of isolated quantum systems, but also builds intuition for our analyses of “ETH fluctuations” in Chapter 2.

From random matrix eigenstates to the ETH

We consider an isolated quantum system governed by the Hamiltonian H and an observable of interest A . Let us denote the energy eigenvalues of H by E_m and the corresponding eigenstate by $|E_m\rangle$. For simplicity, we assume that energy levels are non-degenerate. This is typical for generic Hamiltonians, which have repulsive energy correlations, akin to random matrices. The matrix elements of A in the eigenstate basis of H are denoted by A_{mn} . Let us consider an initial state $|\psi\rangle = \sum_{m=1}^D c_m |E_m\rangle$, which evolves unitarily according to H . Then the observable A evolves as

$$A(t) = \langle \psi(t) | A | \psi(t) \rangle = \sum_{m=1}^D |c_m|^2 A_{mm} + \sum_{m \neq n} c_m c_n^* e^{i(E_n - E_m)t} A_{nm}. \quad (1.30)$$

The dependence of the expression on the initial state for all times t , via c_n , raises the question of how thermalization can occur independently of the initial state. One explanation is derived by assuming that the eigenstates $|E_m\rangle$ resemble those of random matrices, being independent D -dimensional Gaussian states with mean 0 and variance

D^{-1} . Under this assumption, the operator elements satisfy

$$\langle A_{mn} \rangle = \begin{cases} \frac{1}{D} \text{tr}(A) & \text{for } m = n, \\ 0 & \text{for } m \neq n, \end{cases} \quad (1.31)$$

where the average $\langle \dots \rangle$ is over the distribution of eigenstates. Thus the ensemble averaged $A(t)$ is

$$\langle A(t) \rangle = \langle A_{mm} \rangle \sum_{m=1}^D |c_m|^2 = \frac{1}{D} \text{tr}(A), \quad (1.32)$$

where we use the normalization of the initial state $|\psi\rangle$. Consequently, averaging over the randomness of the eigenstates implies that the observable A attains a time-independent value, represented by the mean of all possible values that A can assume.

The fluctuations of $A(t)$ around its average value are crucial in determining the utility of the average as a reliable indicator of $A(t)$. For eigenstates $|E_m\rangle$ that exhibit RMT characteristics, these fluctuations decay in the limit of large Hilbert space size D . For Gaussian states, the diagonal variance are given by [124]

$$\langle A_{mm}^2 \rangle - \langle A_{mm} \rangle^2 = \frac{2}{D} \frac{\text{tr}(A^2)}{D}. \quad (1.33)$$

This as well follows from a more general expression, derived in Chapter 2. Similarly, the off-diagonal ($m \neq n$) variance is [124]

$$\langle A_{mn}^2 \rangle - \langle A_{mn} \rangle^2 = \frac{1}{D} \frac{\text{tr}(A^2)}{D}. \quad (1.34)$$

Consequently, the matrix elements of the operator can be approximated by

$$A_{mn} \approx \frac{\text{tr}(A)}{D} \delta_{mn} + \frac{1}{\sqrt{D}} \sqrt{\frac{\text{tr}(A^2)}{D}} R_{mn}, \quad (1.35)$$

where R_{mn} represents a D -independent random variable with a variance of $O(1)$. If the terms $\frac{\text{tr}(A)}{D}$ and $\frac{\text{tr}(A^2)}{D}$ are independent of D , the fluctuations of A_{mn} decay as $D^{-1/2}$ and, after some initial dynamics, the observable $A(t)$ fluctuates around $\frac{\text{tr}(A)}{D}$.

Note that Eq. (1.35) does not have any direct dependence on the eigenvalues of H . Hence, the random matrix picture should be only accurate at high energies, close to an “infinite temperature” state. A more physically reasonable version of Eq. (1.35) should include some energy dependence. Moreover, since relaxation times depend on the

observable, the matrix elements A_{mn} in physical systems include information beyond the RMT prediction in Eq. (1.35).

The generalization of Eq. (1.35) to describe observables in physical systems is the ETH. In terms of the operators elements $A_{mn} = \langle E_m | A | E_n \rangle$, where $|E_m\rangle$, $|E_n\rangle$ are the eigenstates of H , the ETH predicts that

$$A_{mn} = f_A(\bar{E})\delta_{mn} + e^{-S(\bar{E})/2}g_A(\bar{E}, \omega)R_{mn}, \quad (1.36)$$

where S is the thermodynamic entropy, with $e^{S(\bar{E})}$ being the density of states at energy $\bar{E} = (E_n + E_m)/2$, and $\omega = E_m - E_n$. The functions f_A and g_A are smooth functions, and R_{mn} is a (pseudo) random variable with zero mean and unit variance. The RMT eigenstate ansatz, Eq. (1.35), is recovered by specializing $f_A = \frac{\text{tr}(A)}{D}$, $g_A = \sqrt{\frac{\text{tr}(A^2)}{D}}$ and $e^S = D$, which are all energy (eigenvalue) independent quantities.

The ETH in many-body systems

Evidence from a large number of numerical studies strongly suggests that the ETH is satisfied for eigenstates from the bulk of the spectrum of quantum-chaotic many-body systems and for physical observables [120, 125–141, 124, 142, 143, 95, 144–151, 97, 152, 153].

In contrast, the ETH is typically violated by integrable systems [125, 133, 154, 155, 135, 156, 138, 157, 158, 150, 159, 152], strongly localized systems [140, 160], and by many-body scar states [161–163].

Quantifying if a system obeys the ETH or not involves finite size scaling analysis of the fluctuations of matrix elements A_{mn} around the averages given by f and g . For many-body systems with finite Hilbert space dimension D , the entropy in the bulk of the spectrum typically increases as $S \sim \log D$, implying $e^{-S/2} \sim D^{-1/2}$. Fluctuations of operator elements A_{mn} obeying the ETH thus decrease as $D^{-1/2}$. This decrease of A_{mn} fluctuations has been examined in several studies [133, 154, 155, 135, 137, 138, 156–158, 143, 146, 149, 164, 165, 150, 151, 97, 152, 166].

For many-body systems, the Hilbert space dimension D is typically increasing exponentially with the system size L . Therefore, fluctuations of A_{mn} obeying the ETH decrease exponentially fast with increasing L . This exponential decay contrasts sharply with integrable systems, which do not obey the ETH scaling $D^{-1/2}$. The fluctuations of diagonal matrix elements A_{mm} generally decrease as a power-law in L (logarithmically in D) [154, 155, 135, 156–158, 150, 152], and the off-diagonal matrix elements generally have a non-Gaussian distribution [138, 150, 159].

The ETH is an ansatz of how observables in isolated quantum systems reach a thermal value. Consequently, the finite size scaling analyses are conducted in the thermodynamic limit. For systems with conserved particle number N , this typically is the limit of both increasing L and N , keeping the particle density $\rho = N/L$ fixed. Here, the particle density ρ should not be confused with the spectral density $\rho(\lambda)$ of random matrices. In Chapter 2, we investigate the fluctuations of A_{mn} in the classical instead of the usual thermodynamic limit. The Bose-Hubbard system will serve as a test model for this task.

1.2.3 The Bose-Hubbard model

The Bose-Hubbard model is a cornerstone in the study of quantum many-body systems, particularly in the context of ultracold atoms in optical lattices. Originating from the Hubbard model, which was initially formulated to describe electrons in solids, the Bose-Hubbard model adapts the framework to bosonic particles. The model is described by a Hamiltonian that includes two primary terms: the kinetic term, which accounts for the tunneling of bosons between adjacent lattice sites, and the interaction term, which describes the on-site interaction between bosons. This Hamiltonian H is commonly denoted as

$$H = -\frac{J}{2} \sum_{\langle j,l \rangle} (a_j^\dagger a_l + \text{H.c.}) + \frac{U}{2} \sum_j n_j(n_j - 1) - \mu \sum_j n_j. \quad (1.37)$$

Here, $J > 0$ is the tunneling amplitude, $U > 0$ is the on-site interaction strength, μ is the chemical potential, a_j^\dagger and a_j are the bosonic creation and annihilation operators at site j , and $n_j = a_j^\dagger a_j$ is the number operator. The bosonic creation and annihilation operators fulfill the usual commutation relations $[a_j, a_l^\dagger] = \delta_{jl}$. Throughout this thesis we set $\hbar = 1$. The sum $\langle j, l \rangle$ runs over nearest-neighbor pairs of lattice sites.

Due to its conceptual simplicity and computational tractability, the Bose-Hubbard model has been used to study phenomena in condensed matter physics, such as superfluid and Mott insulating phases [167–169]. In this thesis, the Bose-Hubbard model serves as a many-body system to investigate the relation between classical and quantum chaos and “ETH fluctuations” in the classical limit. For these studies, we slightly modify the Hamiltonian in Eq. (1.37). Namely, we will consider Bose-Hubbard systems restricted to open-boundary chains of length L , given by

$$H = -\frac{1}{2} \sum_{\langle j,l \rangle} J_{j,l} a_j^\dagger a_l + \frac{U}{2} \sum_{j=1}^L n_j(n_j - 1). \quad (1.38)$$

Compared to Eq. (1.37) we relax the condition of constant tunneling rate J per site to a site-dependent, symmetric tunneling coefficient $J_{j,l} = J_{l,j}$. In the remainder of this thesis, we let $J_{1,2} = 1.5$ and $J_{j,l} = 1$ for $j, l \geq 2$. This breaks the reflection symmetry of the model. It will simplify the analyses conducted in Chapters 2 and 3, but qualitative results are independent of breaking this symmetry.

Further, we set the chemical potential $\mu = 0$. The corresponding term $\sum_j n_j$ in Eq. (1.37) is the number operator and is conserved by H . Thus a change in the chemical potential results in a shift in the energy spectrum, which we can ignore without loss of generality for the analyses presented in this thesis.

The Bose-Hubbard model consists of N indistinguishable bosonic particles distributed across L sites. Because bosons are not restricted by the Pauli principle the total Hilbert space dimension D is $D = \binom{N+L-1}{L-1}$. The Hilbert space size grows exponentially in the thermodynamic limit of increasing L and N and fixed particle density $\rho = N/L$. In the classical limit of fixed L and increasing N the Hilbert space size grows polynomially in N as $D \sim N^{L-1}$.

Classical limit of the Bose-Hubbard model

The Bose-Hubbard model has a classical limit for increasing particle number $N \rightarrow \infty$ and fixed system size L . For this limit to be well-defined, both the tunneling and the interaction terms in the quantum Hamiltonian Eq. (1.38) need to have the same scaling with N . For fixed number of sites L , the bandwidth of the hopping term $a_j^\dagger a_l$ increases as $\sim N$, while the bandwidth of the on-site potential $n_j(n_j - 1)$ increases as $\sim N^2$. The faster increase of the on-site interaction term is absorbed into an interaction parameter

$$\Lambda = UN, \quad (1.39)$$

which is kept constant in the limit of $N \rightarrow \infty$ and L fixed. The Bose-Hubbard Hamiltonian in terms of the renormalized interaction strength Λ is given by

$$H = -\frac{1}{2} \sum_{\langle j,l \rangle} J_{j,l} a_j^\dagger a_l + \frac{\Lambda}{2} \frac{1}{N} \sum_{j=1}^L n_j(n_j - 1). \quad (1.40)$$

To attain the classical limit, we have to renormalize the creation and annihilation operators $a^{(\dagger)} \rightarrow a^{(\dagger)}/\sqrt{N} = \bar{a}^{(\dagger)}$. In terms of \bar{a} and \bar{a}^\dagger , the renormalized Hamiltonian

\bar{H} is expressed as

$$\bar{H} = H/N = -\frac{1}{2} \sum_{\langle j,l \rangle} J_{j,l} \bar{a}_j^\dagger \bar{a}_l + \frac{\Lambda}{2} \sum_j \bar{n}_j (\bar{n}_j - 1/N), \quad (1.41)$$

where $\bar{n} = \bar{a}^\dagger \bar{a}$. The renormalization of the bosonic operators makes the commutator $[\bar{a}_j, \bar{a}_j^\dagger] = 1/N$ vanish in the limit of $N \rightarrow \infty$. Hence, in this limit, the renormalized operators \bar{a} and \bar{a}^\dagger can be replaced by complex numbers ψ and ψ^* , respectively. Here, ψ^* is the complex conjugate of ψ . The so obtained Hamiltonian \mathcal{H} is classical and expressed as

$$\mathcal{H} = -\frac{1}{2} \sum_{\langle j,l \rangle} J_{j,l} \psi_j^* \psi_l + \frac{\Lambda}{2} \sum_j |\psi_j|^4. \quad (1.42)$$

The dynamics of $\psi(t)$ and $\psi^*(t)$ are given by Hamilton's equations of motion

$$i \frac{\partial}{\partial t} \psi_j = \frac{\partial \mathcal{H}}{\partial \psi_j^*} = -\frac{1}{2} \sum_{\langle j,l \rangle} J_{j,l} \psi_l + \Lambda |\psi_j|^2 \psi_j, \quad (1.43)$$

where the index j runs from 1 to L and l runs over all neighbors of j . Eq. (1.43) is also known as the discrete nonlinear Schrödinger equation (DNLS), or the discrete Gross-Pitaevskii equation [170–173]. By identifying the complex plane \mathbb{C} with the real plane \mathbb{R}^2 the L complex equations in Eq. (1.43) become $2L$ real equations. Using Cartesian coordinates proves to be computationally advantageous. Defining $x = \text{Re } \psi$ and $y = \text{Im } \psi$, Hamilton's equations of motion can be expressed as

$$\frac{\partial}{\partial t} x_j = \frac{1}{2} \frac{\partial \mathcal{H}}{\partial y_j} = -\frac{1}{2} \sum_{\langle j,l \rangle} J_{j,l} y_l + \Lambda (x_j^2 + y_j^2) y_j \quad (1.44)$$

$$\frac{\partial}{\partial t} y_j = -\frac{1}{2} \frac{\partial \mathcal{H}}{\partial x_j} = \frac{1}{2} \sum_{\langle j,l \rangle} J_{j,l} x_l - \Lambda (x_j^2 + y_j^2) x_j. \quad (1.45)$$

Conserved quantities of the quantum Bose-Hubbard model impose constraints on the classical dynamics. Specifically, the conservation of energy in the quantum Hamiltonian directly corresponds to the conservation of the classical energy \mathcal{H} of the dynamics given by Eq. (1.43). Furthermore, the preservation of the total particle number N in the quantum system implies that

$$\sum_j |\psi_j|^2 = 1, \quad (1.46)$$

thereby limiting the phase space of the classical model to the real hyper-sphere S^{2L-1} within \mathbb{R}^{2L} . This can be derived by taking the time derivative of Eq. (1.46) and applying Eq. (1.43).

The formal replacement of operators \bar{a} and \bar{a}^\dagger by complex numbers ψ and ψ^* can be justified more rigorously by a semiclassical approximation of the quantum mechanical propagator [174–176]. The propagator is expressed in terms of a path integral and a stationary phase approximation is applied. The large parameter of the stationary phase approximation is $1/\hbar_{eff} = N$ and the saddle-point conditions are Hamilton's equation of motion in Eq. (1.43). This has led to a widespread use of the Bose-Hubbard model as a testbed for semi-classical methods [177–195, 110, 196, 197], and the quantum model has been compared to that of the DNLS [198, 76, 199, 200, 77, 201, 78, 103, 202–204]. In Chapter 3, we will, in similar spirit, compare several properties of the Bose-Hubbard model related to quantum and classical measures of chaos.

Chaos and integrability

The competition between tunneling and interaction terms generally makes the Bose-Hubbard model chaotic. The remainder of this section aims to provide some intuition for which parameters L and Λ the model shows chaos and for which it does not.

Let us first focus on $L = 2$ sites. In this special case, the Bose-Hubbard model is integrable for all Λ . In the quantum case, eigenvalues and eigenstates are expressible by a Bethe ansatz [205–207], making this system Bethe-integrable. In such systems, eigenvalue correlations typically follow Poisson statistics. The methodology connecting Bethe-integrability to Poisson statistics will be discussed for the ASEP generator in Section 1.3.2. Despite the non-Hermiticity of the the ASEP generator, the underlying reasoning holds for the Hermitian Bose-Hubbard system as well. In the classical case, dynamics happen in $2L = 4$ real dimensions. This system has two integrals of motion: energy and the norm of (ψ_1, ψ_2) stated in Eq. (1.46). These are sufficiently many integrals of motion to qualify the Bose-Hubbard model as Liouville-integrable.

For arbitrary system size L , both the quantum and the classical systems are integrable in the limits of $\Lambda \rightarrow 0$ and $\Lambda \rightarrow \infty$. We first discuss the classical case. If $\Lambda = 0$ then Eq. (1.42) reduces to a free particle Hamiltonian. If $\Lambda \rightarrow \infty$ then, effectively, J can be neglected. Hence, the equations of motion presented in Eq. (1.43) decouple. In both limits, the classical Hamiltonian has sufficient integrals of motion to be considered Liouville-integrable. In the quantum case, Eq. (1.38) becomes a free particle Hamiltonian in the limit of $\Lambda \rightarrow 0$. For $\Lambda \rightarrow \infty$, the Hamiltonian given by Eq. (1.38) is diagonal in the computational basis of mutual eigenstates of n_j . In

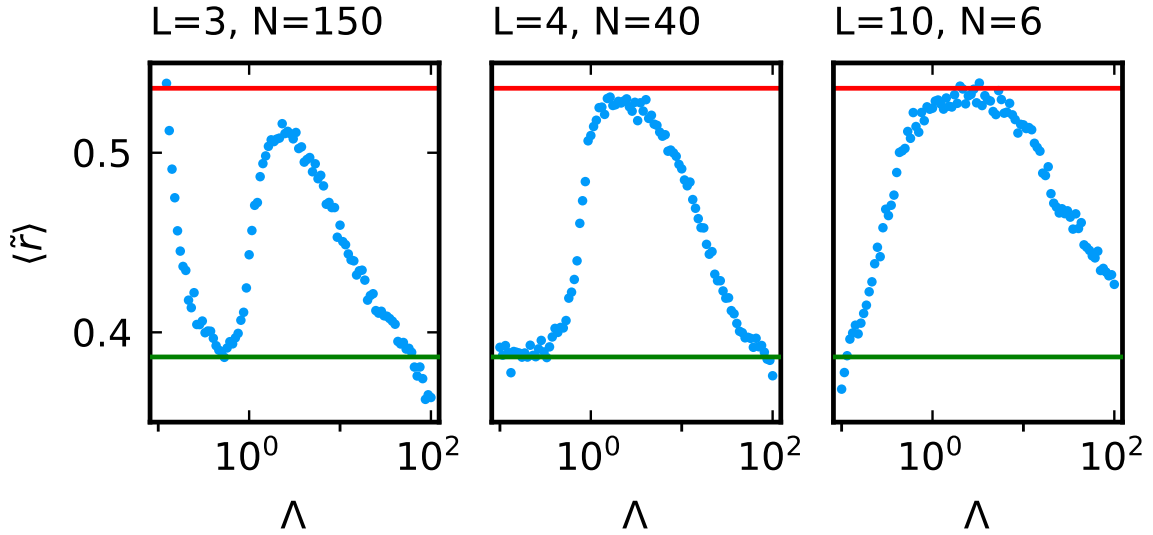


Fig. 1.7 Level ratios \tilde{r} averaged over the whole spectrum, as a function of interaction strength $\Lambda = UN$, shown in the range $\Lambda \in (0.1, 100)$. The horizontal lines are $\langle \tilde{r} \rangle_{\text{Poi}}$ (lower green) and $\langle \tilde{r} \rangle_{\text{GOE}}$ (upper red).

both limits, the many-body eigenvalues of the quantum model are given by sums of single particle eigenvalues. Consequently, they do not repel, which is a signature of non-chaotic models.

For finite Λ , $0 < \Lambda < \infty$, the Bose-Hubbard model on $L \geq 3$ sites is known to be non-integrable [208, 209, 77, 210, 103]. Despite being non-integrable, for $L = 3$ and to some extent for $L = 4$ the system is not strongly chaotic but rather highly mixed, showing signatures of chaotic and integrable models [180, 211, 199, 212–216, 78, 204, 217–219]. This mixed behavior of the Bose-Hubbard model, especially of the three site case, will be discussed in Chapter 3.

To visually underline the parameter ranges under what the Bose-Hubbard model is integrable or chaotic we present averaged spacing ratios of energy eigenvalues (of the quantum model) in Figure 1.7 and compare with the prediction by RMT and uncorrelated random variables. Similar figures have appeared in Refs. [211, 209, 217].

The Bose-Hubbard model belongs to the RMT-symmetry class of the GOE, as the Hamiltonian in Eq. (1.38) is invariant under elementwise complex conjugation. Hence, level statistics should be compared to those of the GOE. The corresponding average level spacing ratio is $\langle \tilde{r} \rangle_{\text{GOE}} \approx 0.54$ [51]. Conversely, an uncorrelated distribution of random values leads to an average ratio of $\langle \tilde{r} \rangle_{\text{Poi}} \approx 0.39$ [51].

Figure 1.7 displays the average ratio $\langle \tilde{r} \rangle$ as a function of Λ for different system sizes L . It shows the transition of the system from integrable for small Λ to chaotic

at intermediate Λ and back to integrable for large Λ . Notably, for small L , the level ratio distributions deviate from both GOE and Poisson statistics at extreme Λ values. This occurs because the Bose-Hubbard model transitions to free fermions as $\Lambda \rightarrow 0$ and becomes diagonal in the computational basis when $\Lambda \rightarrow \infty$. Consequently, the eigenvalues are highly structured and do not adhere to any random sequence.

Furthermore, in small L systems, $\langle \tilde{r} \rangle$ peaks below the GOE value of approximately 0.54, even in highly chaotic regimes. This aligns with the mixed characteristics of the Bose-Hubbard model for $L = 3$ and $L = 4$ sites. The peak approaches the GOE value as L increases, indicating enhanced chaotic behavior in systems with larger L .

1.3 Stochastic many-body systems

The stochastic many-body systems considered in this thesis are placed within the framework of continuous-time Markov chains (CTMCs). CTMCs are (continuous-time) Markov processes that operate on finite state spaces. The characterizing property of a Markov process is that future states depend solely on the present state, independent of past states.

CTMCs provide a popular framework to model stochastic dynamics of many-body systems in diverse fields ranging from physics, chemistry, and biology [220–223] to economics [224, 225] and game theory [226, 227]. For example, they simulate chemical reactions [228–234], gene regulation processes [235–239], quantum dynamics (approximated by rate equations) [240–244], evolutionary game dynamics [227, 245, 246], and many other processes. CTMCs are also the key element of such celebrated models of statistical physics as contact processes [247–249], zero-range processes [250, 251] and exclusion processes like the ASEP [250, 220, 252–258]. In some fields, CTMCs are known under the names “classical Markovian master equations” or “rate equations” or “Pauli rate/master equations”.

In this thesis, we consider generators of CTMCs and their spectra. We introduce the generator of CTMCs in Section 1.3.1. In Section 1.3.2, we present the ASEP as a prominent example of a stochastic many-body system modeled by a CTMC. In Section 1.3.3, we introduce random (dense) generators of CTMCs and revisit their spectral theory.

1.3.1 Generators of Markov processes

For every time point $t \geq 0$, a CTMC is described via a probability vector $P(t)$. The coefficients $P_j(t)$ denote the probability to be in state j at time t . We note that the defining properties for a vector P to be a valid probability vector are that its coefficients are non-negative, $P_j \geq 0$, and sum to one, $\sum_j P_j = 1$. Throughout this thesis, the total number of states is denoted by D . Consequently, $P(t)$ is a D -dimensional (probability) vector.

The generator \mathcal{K} of a CTMC represents the infinitesimal change of the probability vector $P(t)$. Due to the Markovian nature of CTMCs the infinitesimal change is given by a linear first-order differential equation [259], the (Markovian) master equation,

$$\frac{d}{dt}P(t) = \mathcal{K}P(t). \quad (1.47)$$

The generator \mathcal{K} is known as Kolmogorov operator or Kolmogorov generator [260]. Since $P(t)$ is a D -dimensional probability vector, \mathcal{K} is a $D \times D$ -matrix. We choose $P(t)$ to be a column vector, so \mathcal{K} acts in Eq. (1.47) on $P(t)$ from the left. Moving forward, we will use calligraphic letters (e.g., \mathcal{K}) to denote matrices related to generators of CTMCs, and standard letters (e.g., K_{ij}) for their matrix elements.

To be a valid Kolmogorov operator, a matrix \mathcal{K} must satisfy two conditions:

- (i) all its off-diagonal elements have to be real and non-negative, $K_{ij} \geq 0$, $i \neq j$,
- (ii) the sum over every column should be zero, $\sum_i K_{ij} = 0$.

The first condition implies that K_{ij} can be interpreted as transition rate between states i and j . Together with the second condition, it ensures that $P(t)$ remains a probability vector at all times t , given that $P(0)$ is a probability vector [261]. The sum in the second condition is over the columns, since \mathcal{K} is acting from the left in Eq. (1.47).

Due to the first condition the second condition is only met by defining all diagonal elements K_{jj} of \mathcal{K} as

$$K_{jj} = - \sum_{i \neq j} K_{ij}. \quad (1.48)$$

Consequently, any Kolmogorov operator can be expressed by a matrix \mathcal{M} , with real, non-negative elements $M_{ij} \geq 0$ for $i \neq j$ and zero diagonal $M_{ii} = 0$, as

$$\mathcal{K} = \mathcal{M} - \mathcal{J}, \quad (1.49)$$

where \mathcal{J} is a diagonal matrix with diagonal elements $J_{jj} = \sum_i M_{ij}$. This separation into an off-diagonal matrix \mathcal{M} and a diagonal matrix \mathcal{J} will be useful throughout this

thesis. We note that the diagonal of \mathcal{M} can be modified arbitrarily without changing \mathcal{K} , as any diagonal element M_{ii} is canceled by subtracting \mathcal{J} .

In Chapters 4 and 5, we study the spectrum of \mathcal{K} . As \mathcal{K} is in general non-Hermitian, its spectrum is typically complex. Further, the matrix elements of \mathcal{K} are real, so eigenvalues are either real or come in complex conjugated pairs. Following the Gershgorin circle theorem, all eigenvalues are located in the left complex plane [262].

The spectrum of \mathcal{K} is related to the dynamics of the system. For an initial probability vector $P(0)$, the master equation has the formal solution

$$P(t) = e^{t\mathcal{K}}P(0). \quad (1.50)$$

Consequently, the real part of eigenvalues (which is ≤ 0) relates to the relaxation times of eigenmodes, while the imaginary part contributes to the oscillatory timescales of the system.

Since the columns of \mathcal{K} sum to zero, the spectrum contains at least one eigenvalue $\lambda_1 = 0$. All coefficients of the corresponding left eigenvector are equal. Corresponding right eigenvectors are called steady or stationary states. These are attained in the limit of infinite time $t \rightarrow \infty$. If the graph corresponding to \mathcal{K} is strongly connected, the steady state is unique [263, 264, 261]. The relation between the (graph) Laplacian, $-\mathcal{K}$, and the corresponding graph has been discussed in Section 1.1.5.

Of special importance are the eigenvalues λ of \mathcal{K} with the smallest absolute, non-zero real part $|\operatorname{Re} \lambda|$. Their absolute real part equals the so-called spectral gap γ_* . The spectral gap is inverse to the timescale of relaxation of initial probability vectors $P(0)$ to the stationary state.

1.3.2 The Asymmetric Simple Exclusion Process (ASEP)

Before continuing with generic Kolmogorov generators it is instructive to consider a paradigmatic example of a CTMC — the Asymmetric Simple Exclusion Process (ASEP). In the following, we will overview the ASEP, formulate its generator in terms of Pauli spin matrices, present phases of the stationary state and show the spiky spectral boundary as an intriguing feature of its spectrum. Additionally, we highlight the Bethe-integrability of ASEP and that eigenvalues are uncorrelated according to the CSR distribution.

The ASEP is a paradigmatic stochastic many-body model in the realm of nonequilibrium statistical mechanics and mathematical physics [250, 220, 252–258, 265]. It was initially introduced to study kinetics of biopolymerization on nucleic acid templates

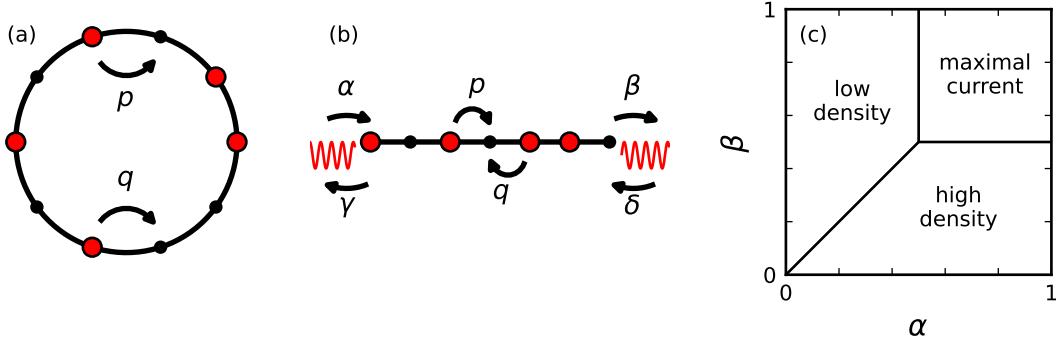


Fig. 1.8 Sketches of the ASEP with (a) $L = 10$ sites (black dots), $N = 5$ particles (red markers), and pbc and (b) $L = 7$ sites and obc. In (c) phase diagram of TASEP ($p = 1$ and $q = \gamma = \delta = 0$) with obc.

[266, 267] but soon extended its reach to other fields, modeling phenomena such as traffic flow [268, 269], biological transport mechanisms [266, 267, 270–272], and surface growth [273–276], just to name a few. Over the years, ASEP has served as a testing ground for theoretical tools and methods in nonequilibrium statistical mechanics, such as the matrix product ansatz [277–279] and the Bethe ansatz [276, 254, 280, 281, 257]. The ASEP consists of interacting particles on a lattice, where each particle can hop to a neighboring site subject to the exclusion principle, which prohibits more than one particle from occupying the same site at any given time. The process is termed “asymmetric” due to the unequal probabilities for particle movement in different directions, leading to a directional bias and a net current of particles even in the steady state. This distinguishes it from its equilibrium counterpart, the symmetric simple exclusion process, where particles are equally likely to move in either direction, resulting in no net flow in the steady state.

In this thesis, we consider the ASEP on one-dimensional chains of length L with both periodic boundary conditions (pbc) and open boundary conditions (obc). In the pbc case, particles move along a ring, depicted in Figure 1.8(a) with the rate to move clockwise p and counterclockwise q . In the obc case, particles move along a one-dimensional chain, with particles entering and exiting at the ends of the chain (site 1 and L) from reservoirs. This is sketched in Figure 1.8(b). Similar to the pbc case, the rate to hop right and left inside the chain is denoted by p and q , respectively. At the ends of the chain, α and γ correspond to the entry and exit rates of particles at the left end (site 1), while β and δ are associated with the exit and entry of particles at the right end (site L).

The ASEP is a continuous time process; the dynamical parameters are rates. For an infinitesimal time step dt the probability for a particle to hop right or left is $p dt$ or $q dt$, respectively. Without loss of generality, we let $p + q = 1$ unless explicitly stated otherwise.

In the case that particles can only hop in one direction, the process is called the Totally Asymmetric Simple Exclusion Process (TASEP). For pbc, the TASEP parameters are $p = 1, q = 0$ and $p = 0, q = 1$. For obc, in addition, the entry and exit rates of particles at the end of the chain are set accordingly. If $p = 1$ ($q = 0$), then $\gamma = \delta = 0$, only leaving α and β as free parameters. The case of $q = 1$ ($p = 0$) is analogous.

The microscopic dynamics of ASEP with particles moving randomly only constrained by the exclusion principle makes this stochastic process Markovian. This, together with the finite size of the chain, puts the ASEP in the framework of CTMCs. Next, we will discuss its (Kolmogorov) generator, the stationary state and the spectrum of the generator.

The Kolmogorov generator \mathcal{K}

The number of particles in the chain is denoted by N and the particle density by $\rho = N/L$. This should not be confused with $\rho(\lambda)$, which denotes the spectral density of random matrices. We note that the particle number N (and so ρ) is conserved for pbc, while it varies for obc.

The Kolmogorov generator $\mathcal{K} = \mathcal{M} - \mathcal{J}$ of ASEP can be formulated in terms of Pauli spin-1/2 matrices. The spin-up state is interpreted as a particle present, while the spin-down state is interpreted as a particle absent. For pbc, the off-diagonal matrix \mathcal{M} is given by

$$\mathcal{M} = \sum_{j=1}^L (p\sigma_{j+1}^+ \sigma_j^- + q\sigma_j^+ \sigma_{j+1}^-) \quad (1.51)$$

and the diagonal matrix \mathcal{J} is given by

$$\mathcal{J} = \frac{1}{4} \sum_{j=1}^L (\sigma_j^z \sigma_{j+1}^z - 1). \quad (1.52)$$

Here, σ^\pm denote spin raising and lowering operators, while σ^z denotes the z -direction of the spin. We identify σ_{L+1} as σ_1 . The off-diagonal matrix \mathcal{M} encodes the transition rates of particles hopping in the ring, while \mathcal{J} is fully determined by \mathcal{M} and ensures that \mathcal{K} is a valid Kolmogorov operator.

Exchanging p and q in Eq. (1.51) corresponds to taking the transpose of \mathcal{M} and so of \mathcal{K} . This in particular implies that the spectrum of \mathcal{K} is invariant under exchanging p and q .

For obc, particles are allowed to enter and exit the chain at the boundaries. Thus, the matrix \mathcal{M} can be denoted as

$$\mathcal{M} = \sum_{j=1}^{L-1} (p\sigma_{j+1}^+ \sigma_j^- + q\sigma_j^+ \sigma_{j+1}^-) + \alpha\sigma_1^+ + \gamma\sigma_1^- + \beta\sigma_L^- + \delta\sigma_L^+, \quad (1.53)$$

while the diagonal \mathcal{J} is given by

$$\begin{aligned} \mathcal{J} = & -\frac{1}{4} \sum_{j=1}^{L-1} (\sigma_j^z \sigma_{j+1}^z - 1) - \frac{1}{2} \left[\left(\frac{p-q}{2} - \alpha + \gamma \right) \sigma_1^z + \left(\frac{q-p}{2} - \delta + \beta \right) \sigma_L^z \right] \\ & + \frac{1}{2} [\alpha + \beta + \gamma + \delta]. \end{aligned} \quad (1.54)$$

In this expression, the bulk term of \mathcal{M} remains consistent with that for pbc. The sources and sinks of particles at the end of the chain are modeled by single spin-flip operators. As for pbc, the diagonal matrix \mathcal{J} is determined by \mathcal{M} to ensure that \mathcal{K} is a valid Kolmogorov operator.

Stationary state

The ASEP as a CTMC converges in the long time limit to a stationary state. This stationary state is a non-equilibrium state with non-zero particle current whenever $p \neq q$ [282, 254].

In the obc case, the asymmetry of probabilities gives rise to nonequilibrium phase transitions [283, 284, 279]. Already the TASEP, with $p = 1$ and $q = \gamma = \delta = 0$, leaving only α and β as free parameters, presents a rich and intricate phase diagram, depicted in Figure 1.8(c). This diagram illustrates the different steady-state behaviors of the system under varying rates of particle entry (α) and exit (β) and is typically divided into three primary phases: low-density, high-density, and maximal current phases. Each phase is characterized by distinct particle densities $\rho = \frac{1}{L} \sum_{j=1}^L \langle n_j \rangle$ and flux strengths $J = \langle \sigma_i^+ \sigma_{i+1}^- \rangle$, where the brackets $\langle \dots \rangle$ denote the expectation with respect to the stationary state. These phases have to be understood in the limit of $L \rightarrow \infty$.

In the low-density phase, the determining factor is the particle entry rate α , subject to $\alpha < \min(\beta, 1/2)$. This results in a bulk density $\rho = \alpha$ below $1/2$, with particle current $J = \alpha(1 - \alpha)$. In the high-density phase, constrained by $\beta < \min(\alpha, 1/2)$, the exit rate β becomes crucial, leading to a bulk density $\rho = 1 - \beta$ above $1/2$ and a

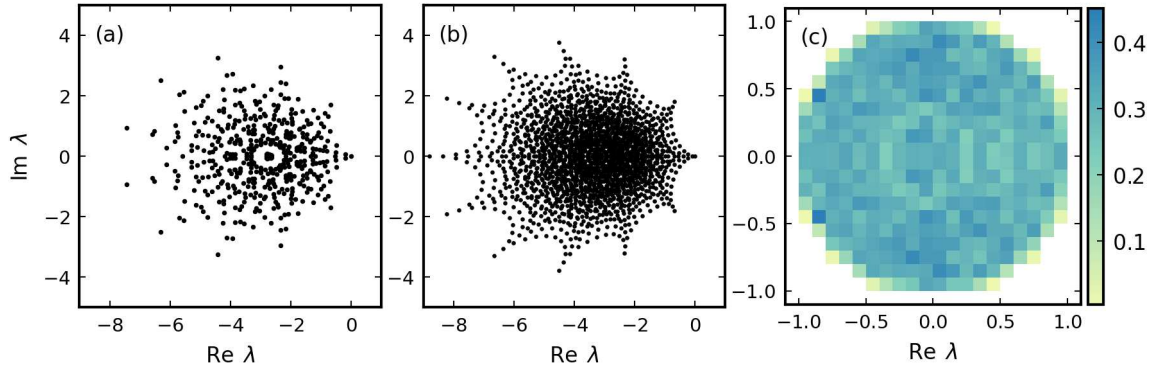


Fig. 1.9 Many-body spectrum of TASEP on $L = 11$ sites with (a) pbc and $N = 5$ particles and (b) obc. Both cases show pronounced spikes. In (c), the distribution of complex spacing ratios of TASEP with pbc and $L = 17$ and $N = 8$ is flat ($\equiv \pi^{-1}$) with finite size fluctuations. This reflects the integrability of the model.

particle current $J = \beta(1 - \beta)$. The maximal current phase occurs when both α and β are larger than $1/2$. Here, the bulk density is $\rho = 1/2$, and the particle current is maximal, $J = 1/4$, irrespective of α and β values. This phase is interesting as it maximizes system throughput, with internal dynamics rather than boundary conditions primarily influencing the system.

Spectrum of the generator

The steady state, while significant, is not the sole point of interest. The spectrum of the Kolmogorov generator \mathcal{K} also holds considerable importance. For example, the spectral gap, the inverse of the timescale of relaxation to the steady state, decreases in the limit of large L as $L^{-3/2}$ [276, 285–287]. The exponent $3/2$ is the same as the dynamical exponent of the Kardar-Parisi-Zhang equation in one dimension [274].

The spectrum of \mathcal{K} has another captivating aspect. Figure 1.9 presents its spectrum in the totally asymmetric case for $L = 11$ with pbc and $N = 5$ in panel (a), and obc in panel (b). Notably, it exhibits distinct spikes: $L = 11$ in the pbc case and $L + 1 = 12$ for obc. Spectra of the ASEP generator, which showed similar spikes, have been presented in Refs. [288, 289]. The mechanism behind the emergence of the spikes, together with its relation to RMT, will be explored in Chapter 5 of this thesis.

Bethe-integrability of the generator

The spectrum of the ASEP generators can be obtained by Bethe ansatz [276, 280, 257]. In the following, we will briefly discuss the coordinate Bethe ansatz [290], applied to

the pbc case. Bethe equations for an extension (deformation) of the ASEP will be derived in detail in Chapter 5.

The coordinate Bethe ansatz is a generalization of the plane-wave ansatz for single-particle systems, in which eigenstates are linear combinations of plane-waves with momenta k_j . This ansatz assumes that an eigenstate $|\psi\rangle$ of the Kolmogorov operator \mathcal{K} with eigenvalue λ is a combination of plane-waves with “generalized momenta” $k_j^{(\lambda)}$, which are typically complex valued and depend on λ . Specifically, the coordinate Bethe ansatz is formulated as

$$\langle x_1, \dots, x_N | \psi \rangle = \sum_{\tau \in S_N} A(\tau) \prod_{j=1}^N e^{ik_{\tau(j)}^{(\lambda)} x_j}, \quad (1.55)$$

where $|x_1, \dots, x_N\rangle$ denotes the state with particles at position $x_1 < \dots < x_N$, $A(\tau)$ are complex amplitudes determined by the eigenvalue equations and the sum runs over all permutations τ of $\{1, \dots, N\}$. The logarithms of the generalized momenta are called Bethe roots $z_j^{(\lambda)} = e^{ik_j^{(\lambda)}}$ and are solutions of recurrent relations, known as Bethe equations. They determine the eigenstate $|\psi\rangle$ via Eq. (1.55) up to a phase. With this ansatz, every eigenvalue λ of the ASEP is a sum of $z_j = z_j^{(\lambda)}$ and its reciprocal,

$$\lambda = \sum_{j=1}^N (pz_j^{-1} + qz_j - 1). \quad (1.56)$$

Nearest neighbor eigenvalues λ and λ^{NN} of the bulk spectrum typically stem from sets of very different Bethe roots $\{z_j^\lambda\}$ and $\{z_j^{\lambda^{NN}}\}$. Consequently, the eigenvalues λ and λ^{NN} are statistically uncorrelated. We numerically confirm this for TASEP on $L = 17$ sites with $N = 8$ particles by presenting the complex spacing ratio (CSR) distribution. In Figure 1.9(c), the CSR distribution appears flat over its support to very good approximation with minor fluctuations. These are attributed to the finite size of the system. The flat CSR distribution is akin to the CSRs of uncorrelated values (panel (c) of Figure 1.5).

A similar relation of the eigenvalues and Bethe roots holds for the obc case as well [291–293, 280] and by the same argument the eigenvalues of the generator are statistically uncorrelated.

1.3.3 Random generators of Markov processes

Following Wigner’s approach with random Hamiltonians, we model the Markovian evolution of complex systems by random Kolmogorov operators.

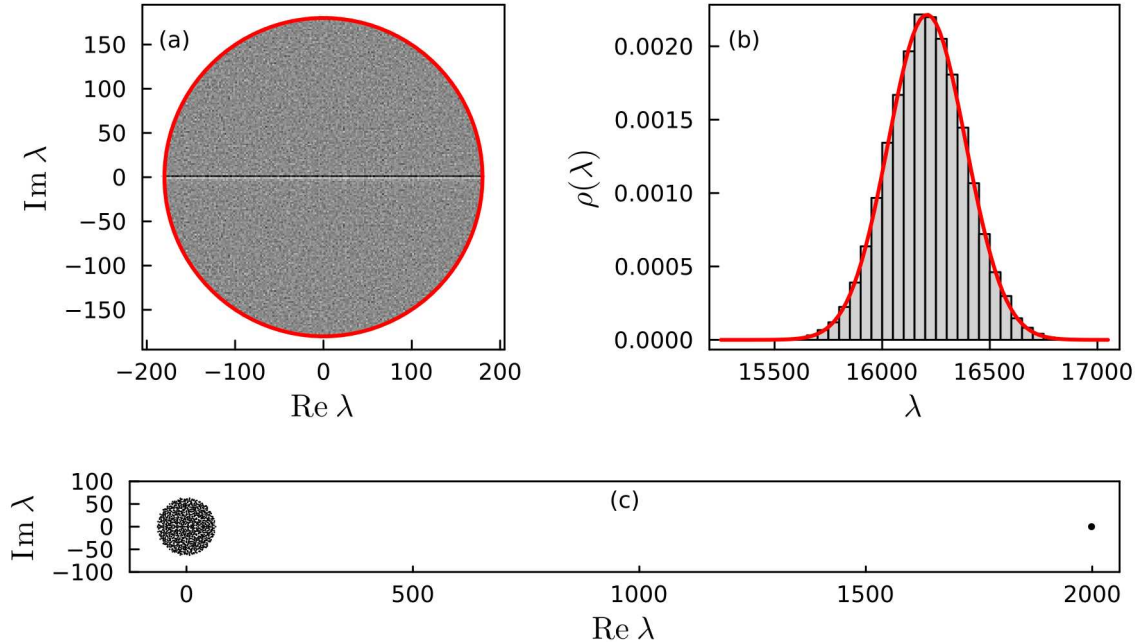


Fig. 1.10 Spectral density of (a) the Ginibre ensemble with χ^2 distributed elements modeling \mathcal{M} and (b) the diagonal matrix \mathcal{J} , whose entries are the sums of columns of \mathcal{M} . Matrix sizes are $D = 8104$ with 100 samples. In (c) the spectrum of a single realization of \mathcal{M} with $D = 1000$.

A generic random Kolmogorov operator must satisfy the conditions to be a valid generator of CTMCs, yet remain as general as possible. Such a generic model can be stated in terms of Eq. (1.49), where any Kolmogorov operator \mathcal{K} is expressed as the difference of two matrices $\mathcal{K} = \mathcal{M} - \mathcal{J}$. In the following, we do not require that the diagonal of \mathcal{M} is non-zero. Hence, the only constraint on the matrix \mathcal{M} is that its matrix elements are real and non-negative. Following [294, 295, 260], the most generic random matrix ensembles fulfilling this constraint are Ginibre ensembles with non-negative element distributions. These ensembles are non-Hermitian and all matrix elements are iid. Thus, the limiting spectral density is expected to adhere to Girko's law and, after appropriate rescaling, becomes uniform in the unit circle.

The matrix elements of \mathcal{K} , and so of \mathcal{M} , are the transition rates. Their magnitudes are related to the timescales of dynamics; hence, have physical relevance. Therefore, we do not rescale the matrix elements, but explicitly consider their mean μ_0 and variance σ_0^2 . The spectral density of the (unscaled) random matrix \mathcal{M} is, in the large D limit, well approximated by the disk of radius $\sqrt{D}\sigma_0$ centered at 0.

In Figure 1.10(a), we present the estimated spectral density of Ginibre matrices with matrix elements distributed according to a χ_2^2 distribution. The χ_k^2 distribution is the sum of k squared, independent standard Gaussians [296]. The special case of $k = 2$ is the distribution of the squared absolute value of a complex Gaussian. The χ_2^2 distribution has mean $\mu_0 = 2$ and variance $\sigma_0^2 = 4$. The matrix size of \mathcal{K} in Figure 1.10(a) is $D = 8104$. Consequently, the radius of the spectral density is $\sqrt{D}\sigma_0 \approx 180$, indicated by the red circle in panel (a).

As discussed in Section 1.1, the fact that matrix elements of \mathcal{M} are real implies that the eigenvalues are either real or come in complex conjugate pairs. As in the case of the GinOE with Gaussian-distributed matrix elements, this implies substantially many real eigenvalues, visible as the dark line on the real axis in Figure 1.10(a). Note that this is not violating Girko's law, as the real line is a Lebesgue-measure zero set in the complex plane.

In contrast to the non-Hermitian Ginibre matrices considered in Section 1.1, the matrix elements of \mathcal{M} have a non-zero mean μ_0 . After subtracting the means,

$$\tilde{\mathcal{M}} = \mathcal{M} - D\mu_0|1\rangle\langle 1|, \quad (1.57)$$

where $|1\rangle = D^{-1/2}(1, \dots, 1)^t$ is the normalized 1-vector, the matrix $\tilde{\mathcal{M}}$ fulfills the requirements of Section 1.1 and adheres to Girko's law. The difference between \mathcal{M} and $\tilde{\mathcal{M}}$ is a rank-1 perturbation $D\mu_0|1\rangle\langle 1|$. This implies that the spectrum of \mathcal{M} is concentrated at the Girko disc, with a single outlier eigenvalue around $\mu_0 D$ [297]. This outlier is a Lebesgue-measure zero set, so \mathcal{M} still obeys Girko's law. As eigenvalues are real whenever they do not come in a complex conjugated pair, the outlier is real. In panel (c) of Figure 1.10, the spectrum of a single realization of \mathcal{M} with χ_2^2 -distributed matrix elements and matrix dimension $D = 1000$ is shown. Besides the Girko disc centered at zero, the single outlier around $D\mu_0 = 2000$ is well recognizable.

Let us now turn to \mathcal{J} . The elements of the diagonal matrix \mathcal{J} are the sums of the columns of \mathcal{M} . All elements of \mathcal{M} are iid. Hence, in the limit of large D , the central limit theorem implies that the elements J_{ii} can be approximated with Gaussian-distributed random variables having mean $D\mu_0$ and variance $D\sigma_0^2$. For $D = 8104$ the distribution of J_{ii} is shown in Figure 1.10(b) for M_{ij} distributed according to the χ_2^2 distribution. The J_{ii} density is well approximated by a corresponding Gaussian density.

Comprehension of the spectra of \mathcal{M} and \mathcal{J} enables us to understand the spectrum of \mathcal{K} . In Figure 1.11, we present spectra of random \mathcal{K} -generators with matrix size $D = 8104$ and χ_2^2 element distribution. In panel (a) we show the spectrum of a single sample. It consists of a bulk spectrum at $-D\mu_0$ and a single outlier at exactly 0,

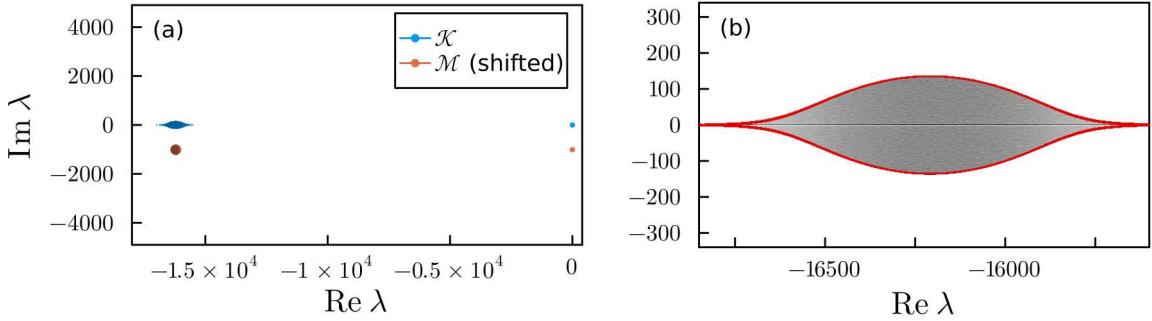


Fig. 1.11 Spectrum of random dense Kolmogorov operators with matrix size $D = 8104$ and off-diagonal elements distributed according to a χ^2_2 distribution. In (a) a single realization and in (b) the bulk density of 100 realizations.

which is the stationary state eigenvalue. The bulk is concentrated in relation to the distance to the zero eigenvalue. This feature is inherited from \mathcal{M} . For comparison, the spectrum of a single realization of \mathcal{M} is shown in Figure 1.11(a). It is shifted in the real direction by $-D\mu_0$ and in the imaginary direction by $-D/8$. The bulk spectra of $\mathcal{M} - D\mu_0$ and \mathcal{K} are of the same order, while the outliers (around 0) are nearly indistinguishable [297].

In panel (b) of Figure 1.11, we present the spectral density of the bulk without the zero eigenvalue outlier. This density is bounded by a spindle-like curve (red). Without going into the details of its derivation [298], it is plausible that this form of the bulk spectrum emerges from a “combination” of the disk in panel (a) and the Gaussian distribution in panel (b) of Figure 1.10.

One of the goals of modeling Kolmogorov operators by random matrices is to understand more about the spectrum of physical generators of Markov processes, like the ASEP. Comparing the spectrum of the ASEP in Figure 1.9(a-b) with the spectrum of Kolmogorov operators in Figure 1.11(a) reveals a big difference between these two: the spectral gap between the bulk and the stationary eigenvalue 0 is large for random generators compared to the gap of the ASEP generators. In Chapter 4, we will argue that the spectral gap is, typically, small for physical systems. This hints essential missing structure in the model of random generators presented so far. In Chapter 4, a model of random Kolmogorov operators will be investigated, generalizing the \mathcal{K} -generators based on Ginibre \mathcal{M} matrices. This ensemble has additional structure in form of sparsity. We will show that sparse random generators have a small spectral gap akin to physical generators like the ASEP.

1.4 Outline and summary of main results

The remainder of this thesis is divided into five chapters. Chapters 2 and 3 investigate several RMT-related properties of the Bose-Hubbard model. Chapters 4 and 5 concern generators of continuous-time Markov chains (CTMCs), with focus on random sparse generators in Chapter 4 and the Asymmetric Simple Exclusion Process (ASEP) in Chapter 5. We conclude in Chapter 6.

The following paragraphs provide a summary of the main results of each chapter and reference associated publications. The last paragraph remarks on the author's publications and preprints that are not part of this thesis.

Chapter 2: *"Eigenstate thermalization" in the classical limit*

The results of this chapter have mostly appeared in [299]

G. Nakerst, and M. Haque, Eigenstate thermalization scaling in approaching the classical limit, *Phys. Rev. E* **103**, 042109 (2021).

In Chapter 2, we investigate the eigenstate-to-eigenstate fluctuations of expectation values (EEV fluctuations) of local observables in the Bose-Hubbard model. As outlined in Section 1.2.2, the Eigenstate Thermalization Hypothesis (ETH) predicts that these fluctuations should decrease as $D^{-1/2}$ in the thermodynamic limit of increasing lattice size L and particle number N with fixed density $\rho = N/L$. This has been confirmed by several studies. Instead of the thermodynamic limit, we study the classical limit of increasing N and constant L . We derive expressions for the expected scaling of EEV fluctuations, assuming eigenstates are RMT-like. After an appropriate rescaling of the local observables, the RMT-decrease of EEV fluctuations agrees with the ETH prediction $D^{-1/2}$. Numerical analyses reveal that EEV fluctuations of Bose-Hubbard mid-spectrum eigenstates decrease as a power-law in D . For large L , the exponent of this power-law agrees with the RMT prediction $-1/2$, while for small L , EEV fluctuations decrease with a different exponent. We investigate several possible reasons for this anomalous scaling. We show that ansätze of uncorrelated and two-point correlated eigenstate coefficients result in an exponent of $-1/2$. Therefore, the anomalous scaling must be due to some more subtle higher-order correlations of eigenstate coefficients.

Chapter 3: *Classical and quantum chaos measures in a mixed many-body system*

The results of this chapter have mostly appeared in [300]

G. Nakerst, and M. Haque, Chaos in the three-site Bose-Hubbard model: Classical versus quantum, *Phys. Rev. E* **107**, 024210 (2023).

In Chapter 3, we present the comparison of classical and quantum chaos measures in the three-site Bose-Hubbard model. On three sites, the Bose-Hubbard model is neither

integrable nor strongly chaotic, but shows a mixture of both behaviors. In the quantum model, we investigate the level ratio distribution, (de-)localization of eigenstates and the decay of EEV fluctuations and compare to the corresponding RMT predictions. Chaos in the classical system, the discrete non-linear Schrödinger equation (DNLS), is quantified in terms of Lyapunov exponents. These capture the exponential sensitivity to perturbations of initial conditions. As a function of energy and interaction strength, we demonstrate a strong overall correspondence between all four measures of chaos.

Chapter 4: An ensemble of sparse random generators of Markov processes

The results of this chapter have mostly appeared in [301]

G. Nakerst, S. Denisov, and M. Haque, Random sparse generators of Markovian evolution and their spectral properties, *Phys. Rev. E* **108**, 014102 (2023).

In Chapter 4, we introduce and study an ensemble of random generators \mathcal{K} of CTMCs with adjustable sparsity. This sparsity is controlled by a parameter φ denoting the number of non-zero elements per row and column of \mathcal{K} . In the graph framework, \mathcal{K} is the negative Laplacian of a φ -regular, directed graph with D vertices and $2\varphi D$ edges and random, iid edge weights. For $\varphi = D - 1$, the ensembles of dense random Markov generators, introduced in Section 1.3.3, are recovered. For typical physical CTMCs, φ is constant in D for single-body systems, while φ increases logarithmically with D for many-body systems (e.g. ASEP).

We study the effects of sparsity on the spectrum of the generator matrix \mathcal{K} . We present results for the bulk of the spectrum, the spectral gap and correlations of eigenvalues. Concerning the bulk spectrum, we show that the first moment of the eigenvalue distribution scales as $\sim \varphi$, and the standard deviation as $\sim \sqrt{\varphi}$. This implies that the bulk diverges from the stationary eigenvalue 0, whenever φ increases with D . For the spectral gap, we show that its well-approximated by the smallest diagonal element of \mathcal{J} . Using extreme value theory, we demonstrate how the spectral gap is related to the tails of the edge weight distribution. For common distributions, the spectral gap closes as a power-law in D for constant φ (single-body), is constant (up to $\log D$ corrections) for $\varphi \sim \log D$ (many-body) and diverges, whenever φ increases substantially faster than logarithmically with D . Consequently, sparsity closes the large spectral gap, which is characteristic of dense random generators. Eigenvalue correlations are analyzed through complex spacing ratio (CSR) statistics. We find that starting already at $\varphi \geq 2$, the CSR distribution agrees with the RMT prediction, while the extreme case $\varphi = 1$ is anomalous.

Chapter 5: The spectral boundary of the ASEP

The results of this chapter have appeared in [302]

G. Nakerst, T. Prosen, and M. Haque, The spectral boundary of the asymmetric simple exclusion process: Free fermions, Bethe ansatz, and random matrix theory, *Phys. Rev. E* **110**, 014110 (2024).

In Chapter 5, we analyze the \mathcal{K} -generator spectrum of the Asymmetric Simple Exclusion Process (ASEP); particularly, the spectral boundary. We examine finite chains of length L , under periodic (pbc) and open boundary conditions (obc). Notably, the spectral boundary exhibits L spikes for pbc and $L+1$ spikes for obc. We investigate the origin of these spikes from several points of view. We map the generator \mathcal{K} to interacting non-Hermitian fermions and extend this model to have adjustable interaction U . In the non-interacting case ($U = 0$), the analytically computed many-body spectrum shows a spectral boundary with prominent spikes for both pbc and obc. For pbc, we use the coordinate Bethe ansatz to interpolate between the non-interacting model ($U = 0$) to the ASEP generator ($U = 1$). We show that spectral boundary spikes stem from clustering of Bethe roots. We apply RMT by relating the ASEP generator to random graphs with a distinct cycle structure. In these graphs, all cycle lengths are divisible by L ($L+1$ for obc). The corresponding adjacency matrices have higher-order trace correlations, akin to the random matrices following the hypotrochoidic law discussed in Section 1.1.2. The spectral boundaries of the adjacency matrices and Laplacians of the random graph ensemble show L ($L+1$ for obc) spikes, resembling those of ASEP and of matrices obeying the hypotrochoidic law.

Results not included in this thesis

As outlined above, parts of this thesis are based on the publications [299–301] and the preprint [302]. The author of this thesis has additionally contributed to the publications and preprints [303–305]:

- [303] G. Nakerst, J. Brennan, and M. Haque, Gradient descent with momentum — to accelerate or to super-accelerate? (2020), arXiv:2001.06472.
- [304] P. C. Burke, G. Nakerst, and M. Haque, Assigning temperatures to eigenstates, *Phys. Rev. E* **107**, 024102 (2023).
- [305] P.C. Burke, G. Nakerst, and M. Haque, Structure of the Hamiltonian of mean force, *Phys. Rev. E* **110**, 014111 (2023).

The content of these works is not part of this thesis. The preprint [303] is not related to RMT. The work in Refs. [304, 305] can be put into the framework of thermalization of closed quantum systems, which has some relations to RMT. But the contribution of RMT results in these works is minor compared to Refs. [299–302] and therefore has not been incorporated in this thesis.

Chapter 2

“Eigenstate thermalization” in the classical limit

The content of this chapter has appeared as part of [299]:

G. Nakerst, and M. Haque, Eigenstate thermalization scaling in approaching the classical limit, *Phys. Rev. E* **103**, 042109 (2021).

In this chapter, we explore the fluctuations of diagonal operator elements $A_{\alpha\alpha}$ in the basis of Bose-Hubbard eigenstates. According to the ETH, these fluctuations decrease with increasing Hilbert space size D as $D^{-1/2}$ in the thermodynamic limit. The Bose-Hubbard model has another limit of increasing D , the classical limit of fixed system size L and increasing particle number N . One might question whether the ETH scaling of eigenstate expectation value $A_{\alpha\alpha}$ (EEV) fluctuations applies in the classical limit too. This chapter addresses that question.

In Section 2.1, we introduce the notation and outline the numerical procedure to compute EEV fluctuations. In Section 2.2, we derive analytical expressions for the EEV fluctuations corresponding to GOE eigenstates. For such states, the EEV fluctuations depend on D as a power-law $\sim D^{-e_0}$, with power $e_0 = \frac{1}{2} - \frac{1}{L-1}$. This deviation from the ETH prediction is attributed to the bandwidth of the operators A increasing with N in the classical limit. After rescaling according to the bandwidth, EEV fluctuations agree with the ETH prediction. In Section 2.3, we present a numerical analysis of EEVs for Bose-Hubbard eigenstates. We find that the EEV fluctuations depend on D as a power-law. For large system sizes L , the EEV fluctuations agree with those of GOE eigenstates. For small L , we observe discrepancies between the numerical exponent and the GOE prediction. In Section 2.4, we examine several plausible mechanisms for these deviations. We summarize and suggest possible future studies in Section 2.5.

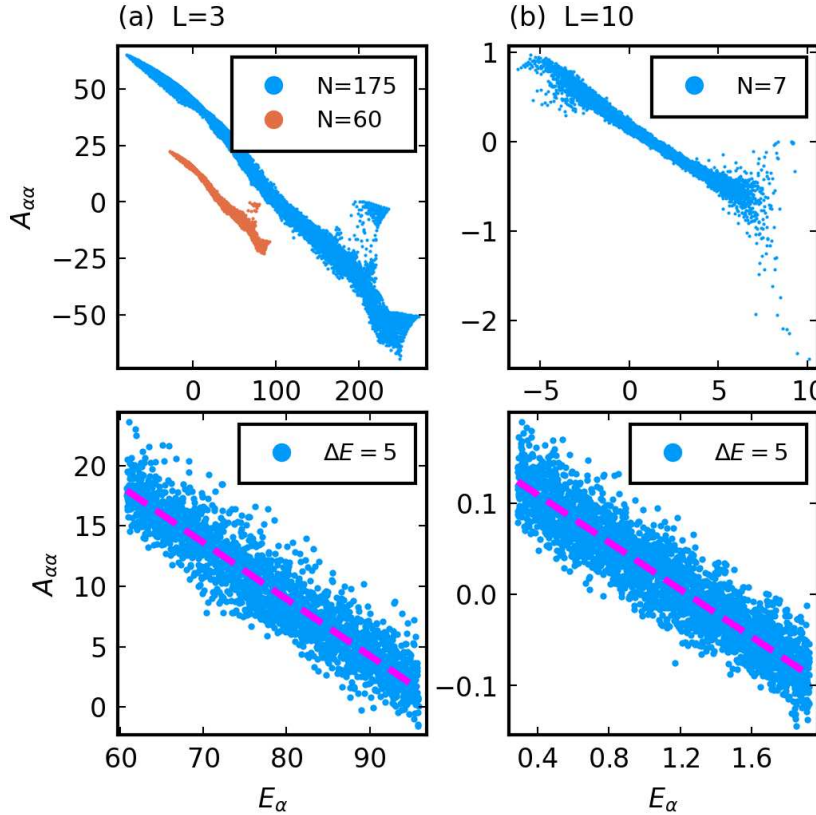


Fig. 2.1 Eigenstate expectation values $A_{\alpha\alpha}$ of the tunnel operator $A = a_2^\dagger a_1$, plotted against eigenenergies E_α , for a Bose-Hubbard chain with (a) $L = 3$ sites and (b) $L = 10$ sites. The numbers of particles N are listed in the legends. In (a), the larger cluster corresponds to $N = 175$ particles, while the smaller cluster on the left corresponds to $N = 60$ particles. The interaction parameter is $\Lambda \approx 2.477$. Top panels show full spectra. Bottom panels zoom into the 5th of ten equal-length energy intervals, as indicated by the shorthand label “ $\Delta E = 5$ ”. Dotted lines are fitted linear functions.

2.1 Eigenstate expectation value (EEV) fluctuations

In this chapter, we study the diagonal elements $A_{\alpha\alpha} = \langle E_\alpha | A | E_\alpha \rangle$ of operators A in the bases of eigenstates $|E_\alpha\rangle$ as a function of (energy) eigenvalues E_α . We refer to the $A_{\alpha\alpha}$ ’s as eigenstate expectation values (EEVs). We discuss EEVs wrt Gaussian states (GOE eigenstates) in Section 2.2, Bose-Hubbard eigenstates in Section 2.3 and other random states in Section 2.4. To visualize the quantities of interest, we present EEVs $A_{\alpha\alpha}$ for Bose-Hubbard eigenstates $|E_\alpha\rangle$ as functions of energy E_α in Figure 2.1. The EEVs are calculated numerically by exact diagonalization.

In general, EEVs $A_{\alpha\alpha}$ fluctuate with E_α . To quantify this fluctuation we express

$$A_{\alpha\alpha} = f(A, E_\alpha) + \sigma(A, E_\alpha)R_\alpha, \quad (2.1)$$

in terms of functions f and σ and a pseudo-random random variable R_α with mean 0 and unit variance. Here, f encodes the mean of $A_{\alpha\alpha}$ and σ the width of $A_{\alpha\alpha}$ around its mean. In contrast to the ETH-formula presented in Section 1.2.2, we incorporated the dependence on E_α and the magnitude of fluctuations in a single function σ . In Eq. (2.1), we do not assume that the ETH holds. If the ETH holds, f and σ are smooth functions of E_α and $\sigma \sim D^{-1/2}$.

Our main incentive in this chapter is to study the scaling of σ with D in approaching the classical limit of fixed L and increasing N . To calculate σ , we first estimate f . If f is smooth then it should be locally linear in E_α . Therefore, we divide the energy spectrum into 10 equal-length, disjoint intervals ΔE . In these intervals, we find that f is indeed linear to an excellent approximation in our cases, as seen in panels (c) and (d) of Figure 2.1. Additionally, σ as a function of E_α appears constant in ΔE . Therefore, we can estimate $\sigma(A, E_\alpha)$ by fitting linear functions $E_\alpha \rightarrow b + mE_\alpha$ on ΔE to $A_{\alpha\alpha}$ and considering the variance

$$\sigma^2(A, \Delta E) = \frac{1}{N_{\Delta E}} \sum_{E_\alpha \text{ in } \Delta E} |A_{\alpha\alpha} - b - mE_\alpha|^2. \quad (2.2)$$

Here, $N_{\Delta E}$ denotes the number of states in ΔE .

Since the ETH is expected to hold only away from the edges, we are primarily interested in mid-spectrum eigenstates. We will show data from the 5th, 6th and 7th energy intervals. In shorthand, these will be labeled as $\Delta E = 5$, $\Delta E = 6$, $\Delta E = 7$, with ΔE referring to the label and not the interval width. In Figure 2.1, we display the EEVs for the full spectrum in (a,b) and for the $\Delta E = 5$ interval in (c,d), for two different values of L . Unless indicated otherwise, we present data for an intermediate value of the interaction parameter $\Lambda = UN$ around which the systems are found to be significantly chaotic (Figure 1.7), namely, $\Lambda = 10^{13/33} \approx 2.477$. Scaling of σ with D will be investigated for a broad range of Λ and all energies in Chapter 3 for the three site Bose-Hubbard system.

The ETH generally holds for operators that are sufficiently local. In this chapter, we consider two operators: the tunnel operator $a_2^\dagger a_1$ from site 1 to site 2 and the number operator n_1 on site 1. We have checked that our results are qualitatively the same for $a_i^\dagger a_j$ with other i, j . It is noteworthy that the operator $a_2^\dagger a_1$ is non-Hermitian.

In cases where Hermiticity is required, we instead investigate the Hermitian operator $(a_2^\dagger a_1 + a_1^\dagger a_2)$. This results in an additional multiplicative factor of 2 in the fluctuations of EEVs.

2.2 EEV fluctuations for random Gaussian states

In this section, we present EEV fluctuations wrt random states, especially GOE eigenstates approximated by Gaussian states. All results are obtained analytically. The EEVs calculated for random states do not have large-scale smooth variation as a function of energy, in contrast to EEVs presented in Figure 2.1. Thus, the statistical standard deviation of EEVs can be directly compared with our measurement of EEV fluctuations for physical eigenstates. The assumption of eigenstates being effectively random has been previously used to derive scaling properties of EEVs in the thermodynamic limit [131, 135, 97]. Here, we provide explicit expressions for σ in terms of trace properties of the operator matrix, and then specialize to both thermodynamic and classical limits.

2.2.1 General trace expressions

Let A be a $D \times D$ square matrix representing the operator of interest, and $|Z\rangle$ be a D -dimensional, multivariate random state with iid coefficients Z_i , each with mean 0. Then the statistical variance of $A_Z = \langle Z|A|Z\rangle$ can be expressed as

$$\sigma^2(A_Z) = \sum_{i,j,i',j'=1}^D A_{i,j} A_{i',j'} \text{cov}(Z_i Z_j, Z_{i'} Z_{j'}), \quad (2.3)$$

where $\text{cov}(Z_i Z_j, Z_{i'} Z_{j'})$ denotes the covariance between the random variables $Z_i Z_j$ and $Z_{i'} Z_{j'}$. Its given by

$$\begin{aligned} \text{cov}(Z_i Z_j, Z_{i'} Z_{j'}) &= \langle Z_i Z_j Z_{i'} Z_{j'} \rangle - \langle Z_i Z_j \rangle \cdot \langle Z_{i'} Z_{j'} \rangle \\ &= \langle Z_i Z_j Z_{i'} Z_{j'} \rangle - \delta_{ij} \delta_{i'j'} \langle Z_i^2 \rangle^2, \end{aligned} \quad (2.4)$$

where $\langle \dots \rangle$ denotes the average wrt to the random state $|Z\rangle$ and δ_{ij} denotes the Kronecker symbol. By the independence of Z_i, Z_j for $i \neq j$, $\langle Z_i Z_j Z_{i'} Z_{j'} \rangle$ is only non-zero if there is no index i, j, i', j' different to the other three. The only possibilities

for this are

$$\begin{aligned}
& i = j = i' = j' \\
& i = j \text{ and } i' = j' \\
& i = i' \text{ and } j = j' \\
& i = j' \text{ and } j = i',
\end{aligned} \tag{2.5}$$

so

$$\begin{aligned}
\langle Z_i Z_j Z_{i'} Z_{j'} \rangle &= \delta_{ij} \delta_{i'i} \delta_{ij'} \langle Z_i^4 \rangle \\
&+ (1 - \delta_{ij} \delta_{i'i} \delta_{ij'}) \left[\delta_{ij} \delta_{i'j'} \langle Z_i^2 \rangle^2 + \delta_{ii'} \delta_{jj'} \langle Z_i^2 \rangle^2 + \delta_{ij'} \delta_{ji'} \langle Z_i^2 \rangle^2 \right].
\end{aligned} \tag{2.6}$$

Thus, the variance of A_Z can be expressed as

$$\begin{aligned}
\sigma^2(A_Z) &= \langle Z_1^4 \rangle \sum_i A_{ii}^2 + \langle Z_1^2 \rangle^2 \left[\sum_{i \neq i'} A_{ii} A_{i'i'} + \sum_{i \neq j} A_{ij}^2 + \sum_{i \neq j} A_{ij} A_{ji} \right] - \langle Z_1^2 \rangle^2 \sum_{i, i'} A_{ii} A_{i'i'} \\
&= (\langle Z_1^4 \rangle - \langle Z_1^2 \rangle^2) \sum_i A_{ii}^2 + \langle Z_1^2 \rangle^2 \left[\sum_{i \neq j} A_{ij}^2 + \sum_{i \neq j} A_{ij} A_{ji} \right] \\
&= (\langle Z_1^4 \rangle - 3\langle Z_1^2 \rangle^2) \sum_i A_{ii}^2 + \langle Z_1^2 \rangle^2 \left[\text{tr}(A^2) + \text{tr}(AA^\dagger) \right].
\end{aligned} \tag{2.7}$$

This rather general result, does not assume a particular distribution of the coefficients, only that they should be independent and identically distributed and have mean 0.

Eq. (2.7) simplifies by specializing to the case of GOE eigenstates. As outlined in Section 1.2.1, these are generically considered as reasonable models for the behavior of mid-spectrum eigenstates of chaotic Hamiltonians. As discussed in Section 1.1.4, in the large D limit, GOE eigenstate coefficients are to good approximation independently Gaussian distributed with mean 0 and variance D^{-1} . Their second and fourth moments are given by $\langle Z_i^2 \rangle = D^{-1}$ and $\langle Z_i^4 \rangle = 3D^{-2}$. For such Gaussian states $|Z\rangle$, Eq. (2.7) simplifies to

$$\begin{aligned}
\sigma^2(A_Z) &= \left(\frac{3}{D^2} - \frac{3}{D^2} \right) \sum_i A_{ii}^2 + \frac{1}{D^2} \left[\text{tr}(A^2) + \text{tr}(AA^\dagger) \right] \\
&= \frac{1}{D^2} \left[\text{tr}(A^2) + \text{tr}(AA^\dagger) \right].
\end{aligned} \tag{2.8}$$

The second of the two traces, $\text{tr}(AA^\dagger)$, is the squared Hilbert-Schmidt norm or the Frobenius norm of the operator. For Hermitian A the two trace terms are equal,

$\text{tr}(A^2) = \text{tr}(AA^\dagger)$. In this case, we recover Eq. (1.33) from the introduction. Expressions equivalent or analogous to Eq. (2.8) have appeared in Refs. [306–309, 124]. As $\text{tr}(A^2)$ and $\text{tr}(AA^\dagger)$ are invariant under a basis change, so is the variance Eq. (2.8). In contrast, Eq. (2.7) is not basis-invariant, due to the first term.

2.2.2 Quadratic observables

In the subsequent analysis, we compute the trace expressions $\text{tr}(A^2) + \text{tr}(AA^\dagger)$ for quadratic bosonic observables denoted by A . These observables can be represented as linear combinations of the form $a_j^\dagger a_i$. For such operators A , the terms A^2 and $A^\dagger A$ can be expressed as summations over $a_j^\dagger a_i a_{j'}^\dagger a_{i'}$. Our aim is to determine $\text{tr}(a_j^\dagger a_i a_{j'}^\dagger a_{i'})$.

Let us consider a basis state defined as $|\mathbf{n}\rangle = |n_1, \dots, n_k\rangle$, where n_j denotes the number of particles at site j . Consequently, we can represent

$$a_j^\dagger a_i |\mathbf{n}\rangle = \delta_{ij} n_i |\mathbf{n}\rangle + (1 - \delta_{ij}) \sqrt{n_j + 1} \sqrt{n_i} |\dots, n_i - 1, n_j + 1, \dots\rangle. \quad (2.9)$$

By applying Eq. (2.9) twice we get

$$\langle \mathbf{n} | a_j^\dagger a_i a_{j'}^\dagger a_{i'} | \mathbf{n} \rangle = \delta_{i'j'} \delta_{ij} n_{i'} n_i + (1 - \delta_{i'j'}) (1 - \delta_{ij}) \delta_{ij'} \delta_{ji'} (n_{j'} + 1) n_{i'}. \quad (2.10)$$

First let $i = j = i' = j'$. Given that there are $\binom{N-l+L-2}{L-2}$ states with l particles on site i , we deduce

$$\text{tr}(n_i^2) = \sum_{l=0}^N l^2 \binom{N-l+L-2}{L-2}. \quad (2.11)$$

Writing l^2 in terms of binomial coefficients and invoking an upper index Vandermonde identity, namely

$$\sum_{l=0}^n \binom{l}{c_1} \binom{n-l}{c_2} = \binom{n+1}{c_1 + c_2 + 1}, \quad (2.12)$$

for constants n , c_1 and c_2 , we derive

$$\text{tr}(n_i^2) = \frac{N(2N+L-1)}{L(L+1)} D. \quad (2.13)$$

Now let $i = j$ and $i' = j'$ but $i \neq i'$. There are $\binom{N-l-s+L-3}{L-3}$ many states with l particles on site i and s particles on site i' , so

$$\text{tr}(n_i n_{i'}) = \sum_{l=0}^N \sum_{s=0}^{N-l} l s \binom{N-l-s+L-3}{L-3}. \quad (2.14)$$

Applying the Vandermonde identity, as defined in Eq. (2.12), twice we infer

$$\mathrm{tr}(n_i n_{i'}) = \frac{N(N-1)}{(L+1)L} D. \quad (2.15)$$

For the case $i \neq j$ and $i' \neq j'$, but $j = i'$ and $i = j'$, the computation mirrors the scenario when $i = j$ and $i' = j'$ but $i \neq i'$. Applying Eq. (2.12) twice on

$$\mathrm{tr}(a_j^\dagger a_i a_i^\dagger a_j) = \sum_{l=0}^N \sum_{s=0}^{N-l} (l+1)s \binom{N-l-s+L-3}{L-3} \quad (2.16)$$

yields

$$\mathrm{tr}(a_j^\dagger a_i a_i^\dagger a_j) = \frac{N(N+L)}{L(L+1)} D. \quad (2.17)$$

Particularly, for operators $A = a_i^\dagger a_j$ the traces are given by

$$\mathrm{tr}(A^2) + \mathrm{tr}(AA^\dagger) = \frac{N(N+L)}{L(L+1)} D \quad i \neq j, \quad (2.18a)$$

$$\mathrm{tr}(A^2) + \mathrm{tr}(AA^\dagger) = \frac{2N(2N+L-1)}{L(L+1)} D \quad i = j. \quad (2.18b)$$

In the thermodynamic limit where the ratio N/L remains constant and both N and L tend towards infinity, the coefficient preceding D is $O(D^0)$ in both cases. Consequently, this results in a relationship $\sigma^2 \approx \frac{D}{D^2} = D^{-1}$, thereby implying the standard $\sigma \sim D^{-1/2}$ scaling for EEV fluctuations in the thermodynamic limit.

2.2.3 Scaling in the classical limit

We now turn our attention to the classical limit, $L \ll N$. We denote by A a linear combination of terms such as $a_j^\dagger a_i$. From the previous analysis we infer

$$\mathrm{tr}(A^2) + \mathrm{tr}(AA^\dagger) \sim N^2 D. \quad (2.19)$$

Since $N \sim D^{1/(L-1)}$ in the classical limit, the variance scales as

$$\sigma^2(A_Z) \sim \frac{D \cdot D^{2/(L-1)}}{D^2} = D^{-2e_0}, \quad (2.20)$$

where

$$e_0 = e_0(L) = \frac{1}{2} - \frac{1}{(L-1)} \quad (2.21)$$

is the scaling exponent announced previously. When $L \gg 1$ but still $L \ll N$, the second term in Equation (2.21) becomes negligible, leading to a scaling behavior of $\sigma \sim D^{-1/2}$ similar to the thermodynamic limit.

For systems with a moderate number of sites, it’s important to note that the scaling of EEV fluctuations for two-point operators of the form $a_j^\dagger a_i$ or their linear combinations differs between the classical limit and the thermodynamic limit. Mathematically, this difference can be attributed to the operators A scaling with N . By normalizing A to $\bar{A} = A/N$, the traces in Equation (2.19) scale as D rather than $N^2 D$, resulting in scaling of the variance for all L as

$$\sigma^2(\bar{A}_Z) \sim \frac{D}{D^2} = D^{-1}. \quad (2.22)$$

To summarize, in the classical limit, the EEV fluctuation scaling is $\sim D^{-1/2}$ for normalized operators $\bar{A} = A/N$ for all L , and also for unnormalized operators A in the $L \gg 1$ limit. This is the same exponent $e_0 = \frac{1}{2}$ familiar from the thermodynamic limit [135, 97]. However, for moderate L and for the operator A , the scaling is according to the exponent $e_0 = \frac{1}{2} - \frac{1}{(L-1)}$.

2.3 EEV fluctuations for Bose-Hubbard eigenstates

In this section, we present numerical results of the scaling of EEV fluctuations for Bose-Hubbard eigenstates. In Figure 2.2, we show σ of the EEVs for different energy windows near the middle of the spectrum, plotted against D . Each panel shows a different (fixed) number of sites L ; in each case the classical limit is approached by increasing N . Generally, the sequences follow clear power-law dependencies, $\sigma \sim D^{-e}$. The power-law behavior sets in at relatively small values of D already.

It is clear from the $L = 3$ data, panel (a), that the exponent e does not match the value predicted for Gaussian states, Eq. (2.21), which is $e_0 = 0$ for $L = 3$. The EEV fluctuation for the system eigenstates *increases* with a positive exponent ($e < 0$) instead of being flat as a function of D . Similarly, for the 4-site chain the exponent e is seen to be slightly negative (σ increases slowly with system size), whereas the predicted value is $e_0 = +1/6$.

The calculations rely on full numerical diagonalization, and hence are limited by the Hilbert space size D . Our limit was $D \lesssim 10^5$. For each L , we increased the particle number N as far as possible such that D did not exceed 100,000. For small L , this provides a satisfactory number of available N values, and extracting the exponent e

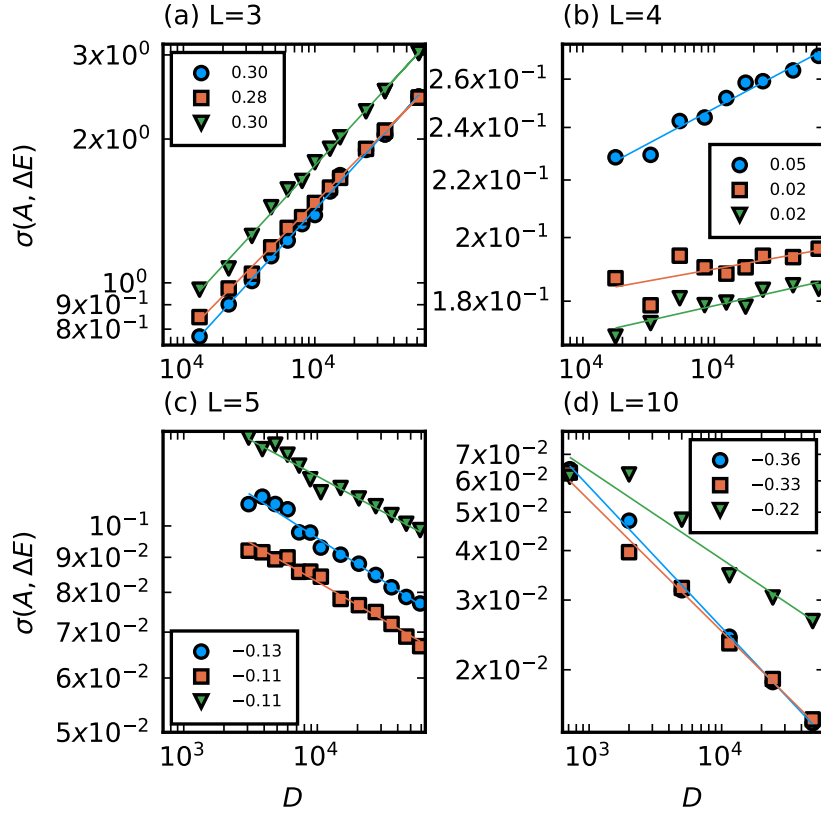


Fig. 2.2 EEV fluctuations σ of the operator $A = a_2^\dagger a_1$ against Hilbert space size D for various chain lengths L . Data shown for eigenstates in energy windows $\Delta E = 5$ (blue circles), 6 (red squares), 7 (green inverted triangles). The σ vs D data sequences are arranged reasonably linearly in all cases in the log-log plots, suggesting $\sigma \sim D^{-e}$ behavior. The slopes of fitted lines (i.e., numerical estimates of $-e$) are given in the legends. The Gaussian predictions e_0 for the exponents are 0 , $\frac{1}{6} \approx 0.1667$, 0.25 , and $\frac{7}{18} \approx 0.3889$ respectively for $L = 3, 4, 5$, and 10 .

from a fit to $\sigma \sim D^{-e}$ is quite reliable. For large L , only a few N values are available. For the largest lattice ($L = 15$), only three data points ($N = 4$, $N = 5$, and $N = 6$) were used. This means a large uncertainty in the estimation of e (Figure 2.3 inset). It also means that the regime $N \gg L$ is not reached.

In Figure 2.3, we present the exponents e extracted from the numerical data. In addition to the exponents for the operator $a_2^\dagger a_1$ (corresponding to Figure 2.2), we also show the exponents for the operator n_1 . For small L , the numerically observed exponents e fall significantly below the Gaussian case, for both operators. For larger L values, the Bose-Hubbard systems show EEV fluctuations closer to the Gaussian case, at least for $\Delta E = 5, 6$. (The $\Delta E = 7$ window shows larger deviation, presumably

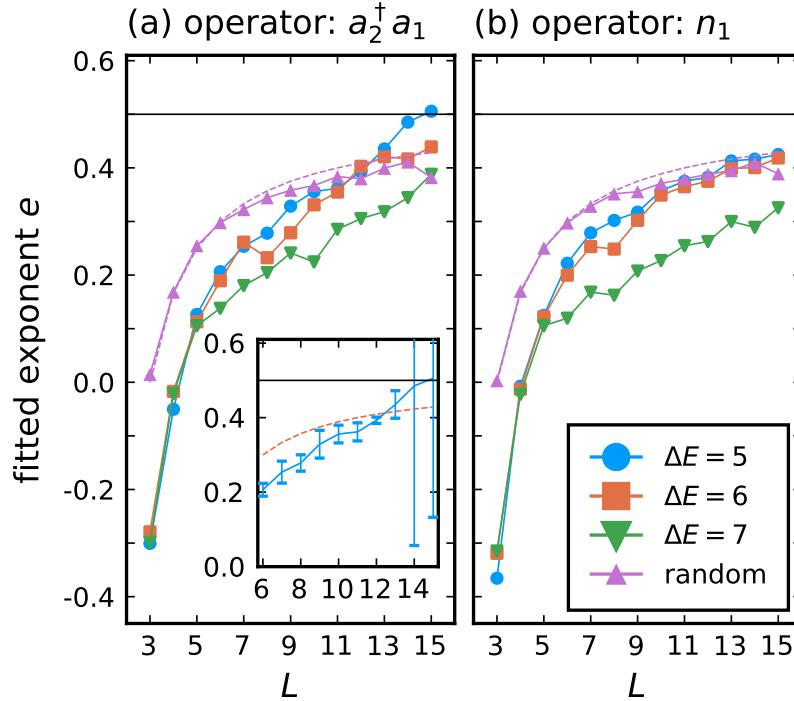


Fig. 2.3 The exponent e versus the chain length L for Bose-Hubbard eigenstates in different energy windows, and for Gaussian states. The pink dashed curve is the predicted formula for exponents, e_0 , which tends to $1/2$ (solid horizontal line) for large L . Inset to left panel shows the error bars for the estimation of e from $\Delta E = 5$ data. The error bars are omitted elsewhere and will be omitted in later figures. In general, error bars are small for $L < 14$.

because it is closer to the edges of the spectrum.) We interpret this as a signature of the large- L Bose-Hubbard systems being more chaotic, so that mid-spectrum eigenstates are better approximated by Gaussian states. The deviation for small L represents the mixed nature of the few-site Bose-Hubbard Hamiltonians.

Figure 2.3 also shows numerically calculated exponents for EEV fluctuations in Gaussian (pink triangles), and compares with the $L \ll N$ prediction, Eq. (2.21) (pink dashed curve). The agreement is good for all L and excellent for small L . At larger L , computer memory limitations prevent our calculations from reaching particle numbers $N \gg L$. This explains the (minor) deviation of the numerical exponents from the $N \gg L$ prediction.

One can view the same effects through the fluctuations of the normalized (\bar{A}) operators $a_2^\dagger a_1/N$ and n_1/N . For these operators, the predicted exponent is $1/2$ for all L . We present the numerical exponents for such operators in Figure 2.4. However,

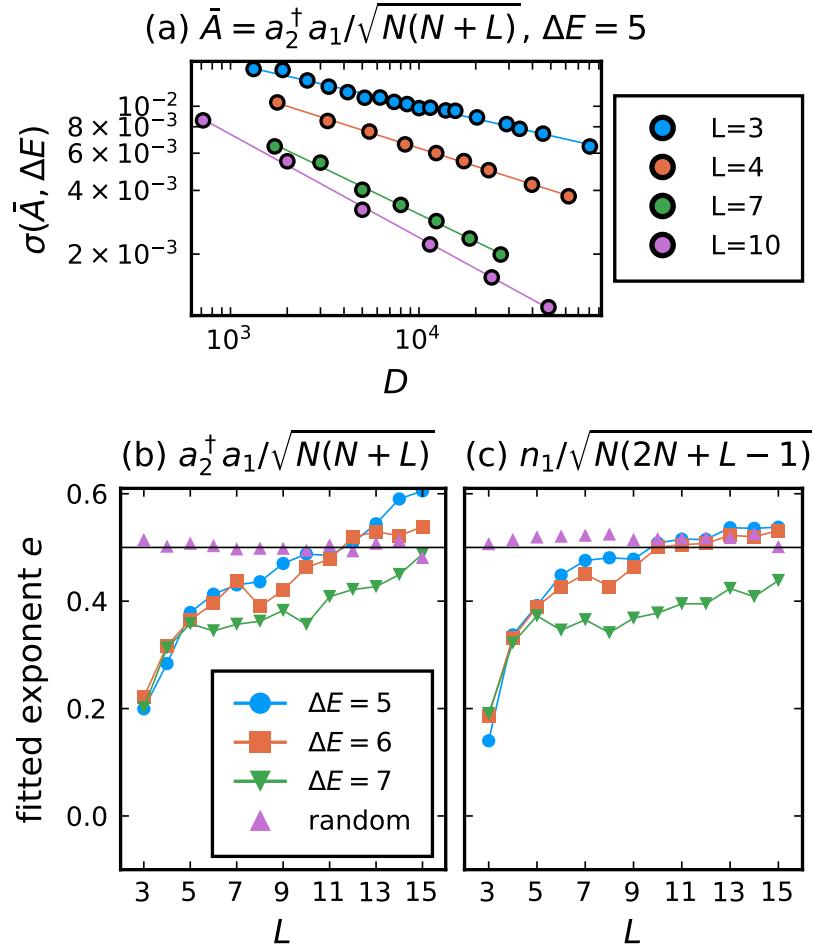


Fig. 2.4 Similar data as in Figures 2.2 and 2.3 but with normalized operators \bar{A} . The operators are normalized by factors $\sim N$; the precise factors are explained in the text. (a) Points and fits are from top to bottom $L = 3$, $L = 4$, $L = 7$ and $L = 10$.

we normalize by factors slightly different from N . The prediction $e_0 = 1/2$ was obtained in the previous section by assuming $N \gg L$. In the trace expressions of Eq. (2.18), this led to $N(N+L) \approx N^2$ and $2N(2N+L-1) \approx 4N^2$. In our numerical calculations, for larger L we do not have access to N values in this regime. Therefore, we normalize the operators by the factor $\sqrt{N(N+L)}$ for $A = a_i^\dagger a_j$ with $i \neq j$ and by the factor $\sqrt{N(2N+L-1)}$ for $i = j$. With this modification, the numerically calculated exponents using Gaussian states (pink triangles) do not deviate systematically from $1/2$ at large L , even though the $N \gg L$ regime is not reached. The observed physical exponents (for Bose-Hubbard eigenstates) are significantly different from the predicted $e_0 = 1/2$ for small L , but approach this value as L is increased.

Summarizing our numerical findings: power-law dependence of EEV fluctuations on D is seen for all L . The exponent at larger L (more fully chaotic systems) matches well the Gaussian prediction. For smaller L (mixed systems), there are significant deviations from the Gaussian prediction. Remarkably, for small L , the departure of the eigenstates from Gaussian behavior does not destroy the power-law dependence of EEV fluctuations with D but changes the exponent substantially. In fact, for the smallest sizes ($L = 3$ and $L = 4$) the numerically measured exponent e even turns negative for unnormalized operators, so fluctuations of EEVs actually *grow* with N .

In the following section, we will examine possible explanations for this phenomenon.

2.4 Non-reasons for anomalous scaling

The discrepancy between observed and theoretically predicted EEV fluctuation scaling for small L can be attributed to the eigenstates of Bose-Hubbard systems with few sites deviating from the canonical Gaussian states. In this section, we investigate multiple forms of deviation from the Gaussian framework and eliminate several tenable hypotheses for the observed anomalous scaling.

First, it is plausible to assume that the eigenstates may occupy a restricted portion of the full Hilbert space, in contrast to a Gaussian random state, and that this portion exhibits sublinear scaling wrt D . This proposition can be tested through evaluation of the participation ratio P_α , which is the inverse of the IPR, introduced in Section 1.1.4. In Section 2.4.1, we show that a scaling behavior of $P_\alpha \sim D^1$ leads to EEV fluctuations scaling as derived in Section 2.2. We verify $P_\alpha \sim D^1$ for eigenstates of the $L = 3$ and $L = 6$ systems. This excludes reduced Hilbert space occupancy as the underlying cause for the anomalous EEV scaling exponents.

Another hypothesis one might consider is that the anomalous behavior of the scaling exponents arises from the eigenstate coefficients not adhering to an identical distribution. In Section 2.4.2, we present numerical data that excludes this as the mechanism behind the anomalous scaling in EEV fluctuations.

These results lead us to conclude that non-Gaussian scaling phenomena stem from correlations among eigenstates. In Section 2.4.3, we examine two-point correlations of eigenstate coefficients. Surprisingly, we find that these two-point correlations do not fully explain the observed anomalous scaling. Thus, we infer that the anomalous scaling exponents of EEV fluctuations arise from more complex, higher-order correlations of eigenstate coefficients.

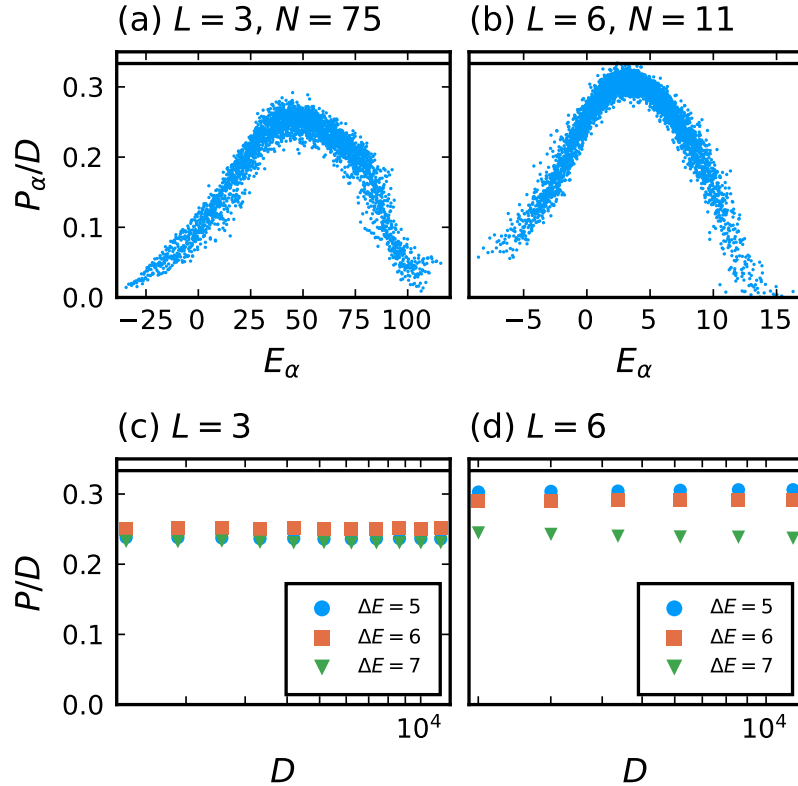


Fig. 2.5 Participation ratio in the basis of eigenstates of the operator $a_2^\dagger a_1 + a_1^\dagger a_2$. Horizontal lines indicate the Gaussian expectation ($= \frac{1}{3}$). In (a,b), normalized participation ratio P_α/D of energy eigenstates, versus corresponding energy eigenvalues. In (c,d), average normalized participation ratio P for different energy intervals as function of Hilbert space dimension D , for fixed chain length L and increasing particle number N .

2.4.1 Participation ratios

For this section it will be convenient to consider the operator A to be Hermitian. We expand the eigenstates $|E_\alpha\rangle$ of the Hamiltonian in the eigenstate basis $|\phi_\gamma\rangle$ of the operator A

$$|E_\alpha\rangle = \sum_\gamma c_\gamma^{(\alpha)} |\phi_\gamma\rangle, \quad (2.23)$$

where $c_\gamma^{(\alpha)} = \langle \phi_\gamma | E_\alpha \rangle$. If we denote the eigenvalues of A as a_γ , then the EEVs can be written as

$$A_{\alpha\alpha} = \sum_{\gamma=1}^D |c_\gamma^{(\alpha)}|^2 a_\gamma. \quad (2.24)$$

We treat the coefficients $c_\gamma^{(\alpha)}$ as stochastic variables, with each eigenstate index (α) signifying an independent realization from a common underlying distribution. The distribution is assumed to be the same for every γ . It is noteworthy that this model does not account for large-scale dependencies of EEVs $A_{\alpha\alpha}$ on the corresponding energies E_α , which is acceptable given our focus on fluctuation characteristics.

The variance of the EEVs $A_{\alpha\alpha}$ wrt to the random coefficients $c_\gamma^{(\alpha)}$ is

$$\text{var}(A_{\alpha\alpha}) = \sum_{\gamma=1}^D \text{var}(|c_\gamma^{(\alpha)}|^2) a_\gamma^2 = \text{var}(|c_\gamma^{(\alpha)}|^2) \text{tr}(A^2). \quad (2.25)$$

The variance of $|c_\gamma^{(\alpha)}|^2$ can be written as

$$\text{var}(|c_\gamma^{(\alpha)}|^2) = \langle |c_\gamma^{(\alpha)}|^4 \rangle - (\langle |c_\gamma^{(\alpha)}|^2 \rangle)^2 = \frac{1}{DP_\alpha} - \frac{1}{D^2}, \quad (2.26)$$

where we have used the definition of the participation ratio to be

$$P_\alpha = \left(\sum_{\gamma=1}^D |c_\gamma^{(\alpha)}|^4 \right)^{-1} = (D \times \langle |c_\gamma^{(\alpha)}|^4 \rangle)^{-1}. \quad (2.27)$$

Eq. (2.27) is the inverse of the IPR introduced in Section 1.1.4. By denoting $P = P(\Delta E)$ as the average of P_α over an energy window ΔE , we arrive at the prediction for the EEV variance

$$\sigma^2 = \left(\frac{1}{DP} - \frac{1}{D^2} \right) \text{tr}(A^2) = \left(\frac{1}{DP} - \frac{1}{D^2} \right) \text{tr}(AA^\dagger). \quad (2.28)$$

For Gaussian states, where $P = D/3$, this variance expression simplifies to Eq. (2.8). More generally, provided the participation ratio P scales linearly with D , the factor in brackets scales as $\sim 1/D^2$, so that we obtain the same scaling as for Gaussian states. For states characterized by $P \sim D^K$ with $K < 1$, the first term in brackets becomes dominant, leading to a distinct scaling behavior.

In Figure 2.5, we show the behavior of the participation ratio in the eigenbasis of $(a_2^\dagger a_1 + a_1^\dagger a_2)$. For highly chaotic systems (with larger L), the mid-spectrum P_α approximates the Gaussian expectation closely. However, for $L = 3$, there is a significant deviation from Gaussian behavior ($P = D/3$). In both scenarios, the scaling of P_α with the Hilbert space dimension D remains predominantly linear (as evident in the lower panels).

Consequently, Hilbert space occupancy fails to account for the observed anomalous scaling in EEV fluctuations.

2.4.2 Non-identical distribution of eigenstate coefficients

The analysis in Section 2.2 is based on the assumption that eigenstate coefficients are iid. One may inquire whether the anomalous scaling of EEV fluctuations for small L values results from non-identical eigenstate coefficient distributions.

To explore this hypothesis, we relax the assumption of identically distributed coefficients, while maintaining independence. In Figure 2.6, we present the EEV fluctuations derived from an estimation of such underlying distributions of Bose-Hubbard eigenstates. We assume that these distributions are identical within the same energy interval ΔE but vary across different ΔE . Within a given energy interval ΔE , states are sampled from the corresponding distribution on a coefficient-by-coefficient basis. For each coefficient a Bose-Hubbard eigenstate is selected randomly within ΔE and the corresponding entry of this eigenstate is used. The EEV fluctuations based on such sampled states are denoted as “independent” in Figure 2.6. The results match well with the EEV fluctuations obtained from Gaussian states but fail to align with the EEV fluctuations in the actual physical systems for small L .

We conclude that models that assume eigenstates with independent coefficients are insufficient in explaining the observed anomalous scaling for small L . Put differently, the root of the anomaly cannot be traced back to non-identical or non-Gaussian distributions of the eigenstate coefficients, nor can it be attributed to insufficient occupancy of the Hilbert space. Rather, the crux of the matter lies in the fact that the eigenstate coefficients are not truly independent.

2.4.3 Eigenstate correlations

Continuing our effort to identify what feature of small- L eigenstates is responsible for the anomalous ETH scaling, we assume that eigenstates are drawn independently from a multivariate distribution Z , with two-point correlations between coefficients. Such correlations are quantified by the covariance matrix Σ . The covariance matrix of eigenstates can be estimated by regarding the eigenstates within a specific energy interval as different samples of a common Z . It is reasonable to assume that the mean of all coefficients of Z is zero, as coefficients of mid-spectrum eigenstates generally have

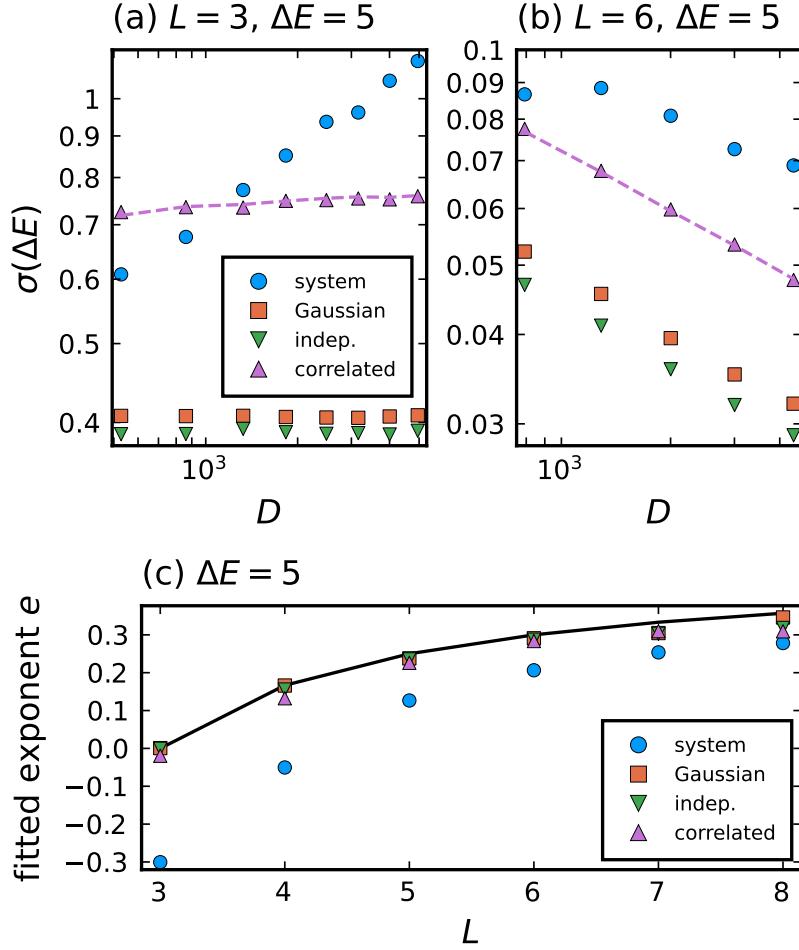


Fig. 2.6 The operator in all plots is $a_2^\dagger a_1$. Blue dots: eigenstates of physical Bose-Hubbard system. Red squares: Gaussian states with i.i.d. coefficients. Green down triangles: vectors with independent but non-identically distributed coefficients, each coefficient sampled from system eigenstates. Purple up triangles: multivariate Gaussian states with covariance matrix estimated from system eigenstates. **(a,b)** EEV fluctuations. The dashed purple line is the prediction by Eq. (2.32). **(c)** The exponent e , such that $\sigma \sim D^{-e}$, versus the number of sites L for the same distributions as in **(a,b)**.

zero mean. In this case, an estimate of Σ is given by

$$\Sigma = N_{\Delta E}^{-1} \sum_{E_\alpha \text{ in } \Delta E} |E_\alpha\rangle \langle E_\alpha|, \quad (2.29)$$

where E_α and $|E_\alpha\rangle$ denote eigenvalues and eigenstates, respectively, and $N_{\Delta E}$ is the number of eigenstates in the energy window ΔE . Eq. (2.29) follows directly from the

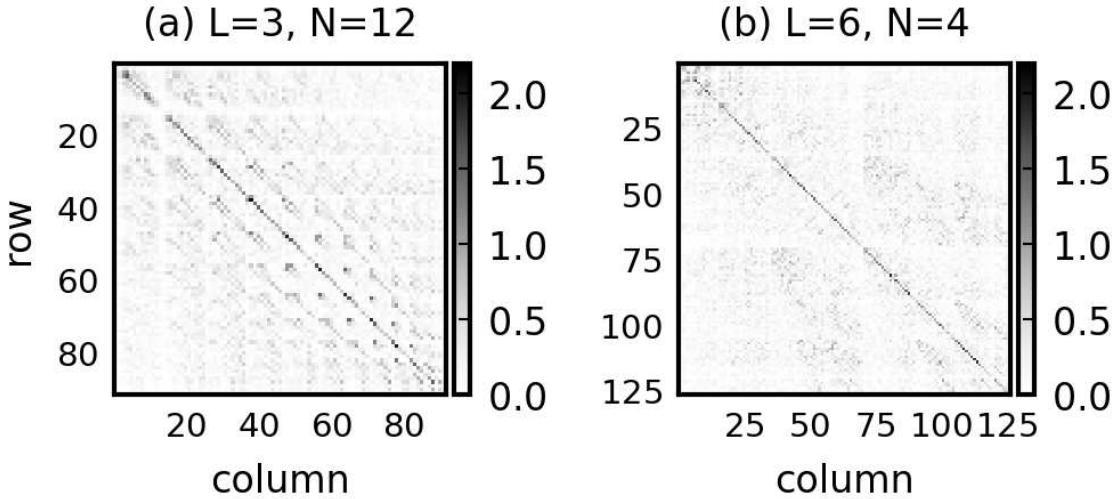


Fig. 2.7 Normalized estimated covariance matrix $D\Sigma$ of mid-spectrum eigenstates (energy window $\Delta E = 5$) for Bose-Hubbard chains with L sites and N particles. The estimate Σ is defined in Eq. (2.29). The absolute values of matrix entries, $|D \cdot \Sigma_{ij}|$, corresponding to the basis \mathcal{B} described in text, are shown. The tick labels are row and column indices, e.g. in the top left is the entry $|D \cdot \Sigma_{11}|$. N had to be chosen significantly smaller than in the rest of this chapter to visualize the patterns without zooming. The patterns are stable for increasing N .

definition of the sample covariance matrix of Z , where the samples are the eigenstates $|E_\alpha\rangle$.

In Figure 2.7, we show the estimated covariance matrices for $L = 3$ and $L = 6$. For a multivariate distribution with uncorrelated entries, the off-diagonal elements of the covariance matrix are all zero (white in Figure 2.7). The $L = 3$ case is seen to have significant off-diagonal elements, arranged in intriguing patterns (black). The $L = 6$ case has still significant, but less pronounced off-diagonal elements than the $L = 3$ case. Hence, for small L , eigenstate coefficients appear to be two-point correlated. The deviation of the covariance matrix from a diagonal matrix suggests that mid-spectrum states, expected to be significantly chaotic states, deviate from infinite-temperature states. This is consistent with Refs. [96, 95, 98, 99, 310, 311, 159, 104, 97].

The covariance matrices are basis-dependent. In Figure 2.7, the chosen basis \mathcal{B} is the computational basis. Its elements are the mutual eigenstates of the number operators n_j . Interpreted as $(N + 1)$ -adic numbers, the elements of \mathcal{B} are arranged in descendant order. For example, for $L = 3$ and $N = 2$, the computational basis is

ordered from left to right as

$$\mathcal{B} = (|0, 0, 2\rangle, |0, 1, 1\rangle, |0, 2, 0\rangle, |1, 0, 1\rangle, |1, 1, 0\rangle, |2, 0, 0\rangle). \quad (2.30)$$

By assuming that the coefficients of the multivariate distribution Z have mean zero and estimating a covariance matrix Σ , we have fixed the first two moments of Z . It is natural to assume that higher moments are generic. Hence, we model eigenstates by a multivariate Gaussian distribution Z with mean 0 and covariance matrix Σ .

In Figure 2.6, the EEV fluctuations obtained from such sampled states are marked as “correlated”. The values of the corresponding fluctuations are larger than those obtained from the independent-coefficient random states, and more comparable to the fluctuations obtained from the physical eigenstates. In the chaotic cases (large L), all of these cases have the same scaling. However, in the $L = 3$ case, the scaling exponent is close to the Gaussian case and does not reproduce the anomalous scaling at all. This is seen in panel (a) of Figure 2.6, and also in panel (c) where the fitted exponents are plotted. The fitted exponent is slightly off the Gaussian value for small L , but far from the anomalous values of the physical system.

These results show that the deviation of the physical system from expected Gaussian behavior is only partially captured by the two-point correlations between the eigenstate coefficients. This suggests that the small- L eigenstates deviate from randomness in some more drastic manner, which does not seem easy to quantify.

In addition to the direct numerical verification discussed above, we argue (non-rigorously) that the inclusion of reasonable two-point correlations in the model of random states should not change the EEV fluctuation scaling exponent. For this, we decompose Z into $Z = RX$, where X is a vector whose independent coefficients are Gaussian-distributed with mean zero and variance 1, and R is the Cholesky root of the non-random matrix Σ , i.e $\Sigma = RR^t$. The statistical variance of the EEVs wrt Z is given by

$$\begin{aligned} \text{var}(A_Z) &= \text{var}((RX)^t A R X) = \text{var}(X^t R^t A R X) \\ &= \text{var}(1/\sqrt{D} X^t D R^t A R 1/\sqrt{D} X). \end{aligned} \quad (2.31)$$

Since the coefficients of $1/\sqrt{DX}$ are normally distributed with mean 0 and variance $1/D$, we can make use of Eq. (2.8) with A replaced by $R^t AR$,

$$\begin{aligned}\text{var}(A_Z) &= \frac{1}{D^2}(\text{tr}(D^2(R^t AR)^2) + \text{tr}(D^2 R^t AR(R^t AR)^t)) \\ &= \frac{1}{D^2}(\text{tr}((D\Sigma A)^2) + \text{tr}(D\Sigma A D\Sigma A^t)).\end{aligned}\quad (2.32)$$

This is Eq. (2.8) with the change $A \rightarrow D\Sigma A$. The variance of the wavefunction coefficients is not fixed by normalization of the eigenstates any more. But it is reasonable to assume that it still scales as $\sim 1/D$, and we have checked numerically that this scaling holds for the mid-spectrum eigenstates of all our physical systems, including $L = 3$. Since the variances of the wavefunction coefficients are the diagonal entries of Σ , the diagonals of $D\Sigma$ scale (at most) as constant in D . By the Cauchy-Schwartz theorem the off-diagonal terms of Σ are bounded by the diagonal, so every coefficient of $D\Sigma$ is (at most) constant in D .

Without making assumptions about the detailed structure of Σ , we cannot derive rigorously the scaling of the traces in Eq. (2.32), which was possible for Eq. (2.18) or (2.19). However, since $D\Sigma$ is elementwise at most $\sim D^0$, and assuming Σ is not too exotic, one can argue that the derivation in Section 2.2 should hold for this case as well. In other words, for “reasonable” Σ , one expects the same scaling as in the case of independent Gaussian eigenstates. This is consistent with Figure 2.6, where the matrix Σ is estimated numerically from the physical eigenstates.

2.5 Discussion

In this chapter, we studied the ETH in the scaling sense, but considered increasing Hilbert space dimensions along the classical limit rather than the usual thermodynamic limit. This has led to a characterization of the distinctive properties of few-site Bose-Hubbard systems in terms of anomalous scaling exponents.

Summary of analytic results. For GOE eigenstates, akin to Gaussian states, we have derived trace expressions for the EEV fluctuation σ , Eq. (2.8). For operators of the type $A = a_j^\dagger a_i$, the trace operators can be expressed as Eq. (2.18). Based on these main expressions, we are able to predict ideal scaling behaviors of EEV fluctuations in the classical limit, for both unnormalized operators of the type A and normalized operators $\bar{A} = A/N$. Of course, the usual ETH scaling of the thermodynamic limit also follows from these expressions.

In the classical limit $N \gg L$, the EEV fluctuations are found for such idealized eigenstates to behave as $\sigma \sim D^{-e_0}$, with $e_0 = \frac{1}{2} - \frac{1}{(L-1)}$ for unnormalized A operators and $e_0 = 1/2$ for normalized \bar{A} operators.

In addition, we have presented expressions for σ for a number of related cases, e.g., for i.i.d. distributed eigenstate coefficients with the distribution not assumed to be Gaussian, Eq. (2.7), in terms of the participation ratio, Eq. (2.28), and for the more general case where the eigenstate coefficients are allowed to be correlated according to a covariance matrix, Eq. (2.32).

Summary of numerical results. We have explored the scaling exponent for various lattice lengths L , increasing the boson number N with fixed L to approach the classical limit. At larger L , the exponent matches the RMT eigenstate prediction. At small L , the fluctuation appears to have power-law dependence $\sigma \sim D^{-e}$ on the Hilbert space dimension D , i.e., e is well-defined, but the value of e differs markedly from the RMT prediction. Through a series of additional numerical tests, we have shown that this anomalous scaling is not explained by two-point correlations between eigenstate coefficients. The small-size Bose-Hubbard systems thus have mid-spectrum eigenstates which violate the usual randomness approximation.

Deviation from RMT. The deviation of quantum many-body systems from RMT has been the subject of interest from multiple viewpoints in recent years. In many-body systems that are nominally chaotic, mid-spectrum states are largely well-modeled by random states, but small or subleading deviations have been observed in various properties [310, 95, 96, 311, 98, 97, 99, 159, 104]. However, *scaling* properties in these systems generally follow RMT predictions. In the small- L Bose-Hubbard systems, we have shown a striking exception: a system which is not integrable or many-body localized, but nevertheless violates the usual scaling behavior expected in chaotic systems.

The present work opens up a number of new questions deserving investigation:

(1) We have found that the small- L Bose-Hubbard systems display EEV fluctuations scaling with exponents that appear numerically well-defined but very clearly different from the random-state prediction. An analytic explanation for these observed new exponents is currently not available, and remains an open question. The anomalous scaling is related to the insufficient chaoticity of few-site systems. Hence, a tempting conjecture is that some property measuring the degree of chaos in the classical limit might explain the exponents. A first step in this direction is conducted in Chapter 3, where we compare the EEV fluctuation exponent e to other measures of quantum and classical chaos.

(2) Our analytic results have focused on essentially infinite-temperature (mid-spectrum) states. It would be interesting to develop trace expressions for finite temperatures. This is likely not possible to do in complete generality without making assumptions on the system Hamiltonian, but perhaps some results can be derived with minimal assumptions, such as locality of the Hamiltonian.

(3) Bose-Hubbard systems are, of course, not the only quantum systems with a classical limit. It remains to be discovered how generic our findings are. Candidate systems have been mentioned in Section 1.2.1. Studying the behavior of EEV fluctuations in such systems when approaching the classical limit would provide interesting characterizations of ergodicity, e.g., of how well RMT approximations work.

(4) As part of our effort to address the anomalous scaling at small L , we have briefly examined the covariance matrix of eigenstates, treating each eigenstate as a sample drawn from the distribution of eigenstates, according to Eq. (2.29). Studying the so-defined covariance matrix might be fruitful for various quantum systems, as the departure of this matrix from the identity matrix tells us how different the eigenstates are from infinite-temperature states. A further significance of this covariance matrix is that the same object is the microcanonical density matrix, and hence its structure should provide insights into the connection between quantum eigenstates and thermodynamics. In Ref. [304], some initial work has been done in this direction.

Chapter 3

Classical and quantum chaos in a mixed many-body system

The content of this chapter has appeared as part of [300]:

G. Nakerst, and M. Haque, Chaos in the three-site Bose-Hubbard model: Classical versus quantum, *Phys. Rev. E* **107**, 024210 (2023).

In this chapter, we will compare the classical limit of the Bose-Hubbard system (the discrete non-linear Schrödinger equation (DNLS) or Gross-Pitaevskii equation) with the quantum model by different chaos measures. In the previous chapter, we encountered remarkable deviations from RMT in Bose-Hubbard systems with a few sites, related to the fact that these systems are of “mixed” type (neither integrable nor strongly chaotic). This motivated us to focus on such mixed systems in our classical-quantum comparison, presented in this chapter.

Our study will cover various chaos measures. In the classical model, we calculate Lyapunov exponents and compare these with quantum chaos indicators like eigenvalue and eigenstate statistics, and fluctuations in eigenstate expectation values (EEVs). To connect the classical and the quantum model, the classical phase space is refined into energy manifolds and compared with eigenvalues and eigenstates of the quantum Hamiltonian in the corresponding energy ranges.

The main result of this chapter is a qualitative comparison of chaos measures as a function of energy and interaction strength for the three site Bose-Hubbard model. These results are presented in Section 3.1 and summarized in Figure 3.1. We find the overall agreement of the chaotic regions depicted by different chaos measures striking. In the remainder of this chapter, we detail the chaos measures shown in Figure 3.1 and present related numerical results. In Section 3.2, we focus on Lyapunov exponents of

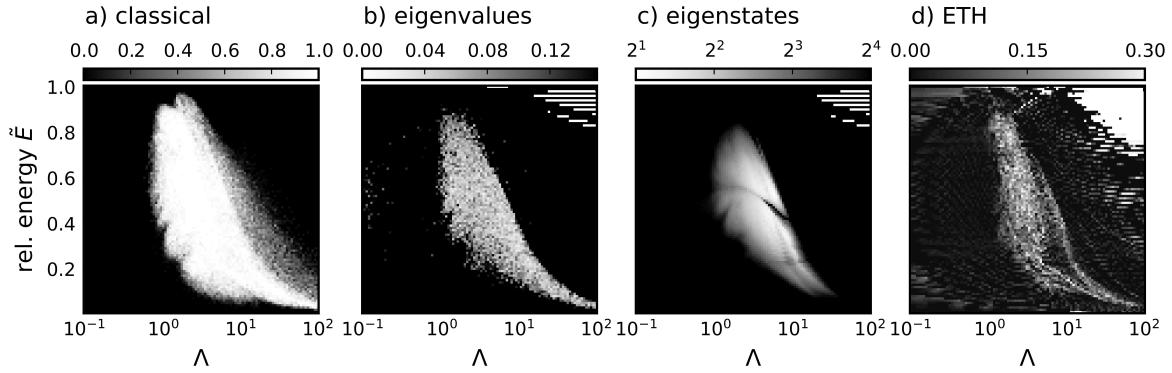


Fig. 3.1 Heatmap of (a) classical chaos indicator and (b-d) quantum chaos indicators. Relative energy 0 corresponds to the minimal (ground state) energy while 1 corresponds to the maximal energy. Λ is the onsite interaction strength. Lighter color corresponds to stronger chaos. (a) Fraction of states with positive largest Lyapunov exponent. (b) Kullback-Leibler divergence of level ratios from GOE level ratios; capped at 0.15. (c) Excess kurtosis of eigenstates; capped at 2^4 . (d) Exponent of EEV fluctuations, clipped between 0 and 0.3.

the classical model. We analyze those for the three site Bose-Hubbard model in detail and explain the data of Figure 3.1(a). We present results for more chaotic cases of larger system sizes and explore alternate ways to Figure 3.1(a) of using the Lyapunov exponent to demarcate chaotic and non-chaotic regions. In Section 3.3, we investigate the eigenvalues of the quantum model leading to the results shown in Figure 3.1(b). We present the average level ratio as function of energy and interaction strength for the three site case, which extends the discussion in Section 1.2.3. In Section 3.4, the eigenstates of the Bose-Hubbard model are compared to GOE eigenstates and the numerical derivation of Figure 3.1(c) is explained. In Section 3.5, we quantify chaos using EEV scaling exponents and explain how Figure 3.1(d) is obtained. The EEV scaling exponents have been analyzed in detail for intermediate interaction strengths Λ in Chapter 2. In Section 3.6, we conclude and provide suggestions for future studies.

3.1 Main results for the three site Bose-Hubbard model

This chapter centers on contrasting classical Lyapunov exponents with quantum chaos metrics, such as level statistics, eigenstate statistics, and EEV fluctuations. Chaos in classical mechanics manifests in the sensitivity to initial conditions of the classical

motion and will be measured by the largest Lyapunov exponent λ_{\max} . It is generically not possible to calculate the largest Lyapunov exponents analytically or exactly. Hence, we will estimate them numerically by integrating classical motion up to a finite time, the finite-time Lyapunov exponents (FTLEs). We will use the terms “Lyapunov exponents” and “FTLEs” interchangeably. It is to be understood that all presented data for λ_{\max} are the best available numerical estimates and that analytically exact values are generally not available.

Figure 3.1 provides an overview of the results. Here we show chaoticity as a function of interaction parameter Λ and relative energy. Chaos is visualized as grayscale heatmaps, where the intensity indicates how chaotic that region is — the lighter the more chaotic.

Figure 3.1(a) shows chaos of the *classical* Bose-Hubbard model, while panels (b-d) show chaos measures of the *quantum* system. In (a) we show the fraction of positive FTLEs of the classical model. We consider a FTLE as positive if it is greater than 10^{-4} , and zero otherwise. In (b) we show the deviation of level statistics of the quantum model from the RMT prediction measured by the Kullback-Leibler divergence. In (c) we show how much eigenstates of the quantum model deviate from Gaussian states via the kurtosis. The kurtosis obtained from the eigenstate coefficients in two different bases are combined — the larger of the two is used at every point of the heatmap. In (d) we show the exponent in the size-dependence of the fluctuations of EEVs. The data in panels (b) and (c) are for $N = 150$ bosons, while the exponents in (d) are obtained by fitting EEV fluctuations between $N = 90$ and $N = 170$. Overall, we have found these quantum results to be broadly independent of N .

Figure 3.1(a) reveals features of the classical phase space, i.e., the phase space of the three-site DNLS. For $\Lambda \lesssim 1$ all FTLEs are close to 0. For $\Lambda > 1$ regions with a non-zero fraction of positive Lyapunov exponents emerge at intermediate energies. At $\Lambda \approx 3$ there are positive largest FTLEs at most energies, except for smallest and largest energies. For $\Lambda > 3$ the region of non-zero fractions of positive Lyapunov exponents shrinks and shifts to lower energies, where it survives even for the largest $\Lambda = 100$ we investigated. These results highlight the mixed nature of the classical phase space. In particular, zero and non-zero Lyapunov exponents exist at the same energy for the same Λ . This is explained in more detail in Section 3.2.

The same shape of the heatmap in Figure 3.1(a) is observed in (b-d) as well. The white bars at the top right of the quantum plots do not show chaotic regions; these are finite size defects (gaps in the spectra which are larger than the energy windows used to compile the heatmaps). The exact measures used in these panels and the subtleties

encountered for the quantum cases will be detailed in Sections 3.3, 3.4 and 3.5, which focus respectively on level statistics, panel (b), on eigenstate coefficient statistics, panel (c), and on EEV scaling, panel (d).

The overall visual agreement between classical chaos regions, panel (a), and quantum chaos regions, panels (b-d), is striking. Chaotic energy regions of the classical phase space correspond generally to chaotic regions of the spectrum of the quantum Hamiltonian. Even fine structures in the heatmaps show some agreement. For $1 < \Lambda < 3$ small bulbs appear at the chaotic-regular boundary in the classical spectrum (a), which can be recognized in the level statistics (b) as well as in the kurtosis of eigenstates (c). We conclude that overall there is a close correspondence of chaotic and non-chaotic regions of the classical model and the quantum model. There are, of course, some discrepancies, also among the various quantum measures, and various artifacts due to the particular measures used. These issues will be discussed in the remainder of this chapter.

Relative energy and energy intervals

Our classical-quantum comparison is energy-resolved. For each Λ , we compare the degree of chaos in individual energy regions of the classical system with the degree of chaos in corresponding energy regions of the quantum system.

Numerically, for each interaction Λ the possible energies are divided into 100 evenly spaced energy intervals. We also rescale and shift the energy for each Λ to define the relative energy

$$\tilde{E} = \frac{E - E_{\min}}{E_{\max} - E_{\min}} \quad (3.1)$$

which takes values in the range $[0, 1]$. For the classical system, E_{\min} and E_{\max} are the lowest and highest possible classical energies. For the quantum system, they are respectively the lowest eigenenergy (ground state energy) and the highest eigenenergy. Each energy interval corresponds to an interval of \tilde{E} having width 0.01. When we refer to the interval at relative energy \tilde{E} , we mean the interval $[\tilde{E} - 0.01, \tilde{E}]$.

For the classical calculation (Figure 3.1(a)), Lyapunov exponents are collected for phase space points whose energy is in the desired interval. For the quantum eigenvalue statistics (Figure 3.1(b)), the spacing between eigenvalues within the desired interval is analyzed. For quantum measures based on eigenstates (Figure 3.1(c) and (d)), all eigenstates whose eigenvalues lie in the interval are considered.

3.2 Classical Lyapunov exponents

This section discusses Lyapunov exponents, particularly their finite time estimates (FTLE), for the classical Bose-Hubbard model. We start by introducing Lyapunov exponents in Section 3.2.1, followed by numerically calculated FTLEs for the highly mixed three-site model in Section 3.2.2. FTLEs for larger chains with $L > 3$ are explored in Section 3.2.3. We conclude with chaos indicators, incorporating FTLE magnitudes, in Section 3.2.4.

3.2.1 Preliminaries

In the following, we introduce Lyapunov exponents, focusing on the largest Lyapunov exponent, λ_{\max} . The subsequent derivations are either straightforward or detailed in Refs. [312, 313].

Throughout this chapter, Lyapunov exponents are denoted by λ . This notation should not be confused with the eigenvalues of matrices in Chapters 1, 4 and 5. The eigenvalues of the only matrices considered here, the quantum Bose-Hubbard Hamiltonians, are denoted by E .

Intuitively, the largest Lyapunov exponent λ_{\max} captures the sensitivity of trajectories to perturbations of initial values. Consider two “close by” initial states ψ_0 and $\tilde{\psi}_0$. (Throughout this chapter, subscripts ≥ 1 to ψ are used as site indices. But there should be no confusion with the use of the subscript 0 for initial values.) The states $\psi(t)$ and $\tilde{\psi}(t)$ are time-evolved states with initial values ψ_0 and $\tilde{\psi}_0$, respectively. In the classical Bose-Hubbard model, the time-evolution is via the equations of motion, Eqs. (1.43), introduced in Chapter 1. The largest Lyapunov exponent is informally given by

$$e^{t\lambda_{\max}} \approx \frac{\|\tilde{\psi}(t) - \psi(t)\|}{\|\tilde{\psi}_0 - \psi_0\|}, \quad (3.2)$$

where t denotes a large time point. Eq. (3.2) implies that if the largest Lyapunov exponent λ_{\max} is positive the two states ψ and $\tilde{\psi}$ separate exponentially, while a zero largest Lyapunov exponent $\lambda_{\max} = 0$ means an at most polynomial spread.

Formally, Lyapunov exponents are defined through a linearization of Eq. (3.2). This involves representing the time-evolution of the dynamical system, governed by Hamilton’s equations of motion, as

$$\Phi(t, \psi_0) = \psi(t), \text{ where } \psi(0) = \psi_0. \quad (3.3)$$

The dynamical system Φ obeys the (semi-group) property $\Phi(t+s, x_0) = \Phi(s, \Phi(t, x_0))$ for all times t and s . Consequently, Eq. (3.2) can be reformulated using Φ and $\phi_0 = \psi_0 - \tilde{\psi}_0$ as follows:

$$e^{t\lambda_{\max}} \approx \frac{\|\Phi(t, \psi_0 + \phi_0) - \Phi(t, \psi_0)\|}{\|\phi_0\|}. \quad (3.4)$$

By linearizing Eq. (3.4) we obtain the largest Lyapunov exponent as

$$\lambda_{\max} = \lim_{t \rightarrow \infty} \frac{1}{t} \log \left\| \partial_\psi \Phi(t, \psi) \Big|_{\psi=\psi_0} \cdot \frac{\phi_0}{\|\phi_0\|} \right\|. \quad (3.5)$$

Note that $\partial_\psi \Phi$ is in general a matrix, so the product \cdot denotes the matrix-vector product. The existence of the above limit is ensured by Oseledelets theorem [314]. The largest Lyapunov exponent is independent of the choice of the norm, as long as the phase space is finite-dimensional. This is a consequence of the equivalence of norms in finite dimensional vector spaces.

One can show that $\partial_\psi \Phi$ evolves in time according to so called variational equations

$$i \frac{d}{dt} \partial_\psi \Phi(t, \psi) = \partial_\psi \partial_{\psi^*} \mathcal{H}(\psi(t)) \cdot \partial_\psi \Phi(t, \psi), \quad (3.6)$$

where $\partial_\psi \partial_{\psi^*} \mathcal{H}$ denotes the Hessian of the Hamiltonian \mathcal{H} in the variables ψ and ψ^* and the initial condition is $\partial_\psi \Phi(0, \psi_0) = \text{Id}$. In Eq. (3.5), the knowledge of the full matrix $\partial_\psi \Phi$ is not required. Only the deviation vector $\phi(t) = \partial_\psi \Phi(t, \psi) \Big|_{\psi=\psi_0} \phi_0 / \|\phi_0\|$ is needed. The deviation vector evolves according to the variational equations (3.6) as well. The largest Lyapunov exponent is related to the largest eigenvalue of the deviation matrix $\partial_\psi \Phi(t, \psi)$ in Eq. (3.5). The other eigenvalues of $\partial_\psi \Phi(t, \psi)$ give rise to other Lyapunov exponents.

For the L -site Bose-Hubbard system, because there are $2L$ real equations of motion, $\partial_\psi \Phi(t, \psi)$ is a $2L \times 2L$ -matrix. Thus, there are in total $2L$ Lyapunov exponents $\lambda_{\max} = \lambda_1 \geq \dots \geq \lambda_{2L}$. For Hamiltonian systems Lyapunov exponents come in pairs of equal magnitude and opposite sign, which is a consequence of Liouville's theorem. Consequently, the largest Lyapunov exponent λ_{\max} is at least 0. Two pairs of Lyapunov exponents are zero because of the conservation of energy and the conservation of norm, as implied by Eq. (1.46). Thus, at most $L - 2$ exponents can be positive. For $L = 3$, which we will focus on, there is at most one positive Lyapunov exponent, which is λ_{\max} .

Numerical calculation of FTLEs

To numerically compute the largest Lyapunov exponent, λ_{\max} , a straightforward approach might involve selecting two initially close states and evaluating the right-hand side of Eq. (3.2) over long time periods t . However, this method is ineffective for systems with bounded state magnitudes, as is the case for the Bose-Hubbard model. In these scenarios, the right-hand side of the equation is also bounded and consequently does not exhibit exponential growth for large t .

Instead, one evolves Hamilton's equations together with the variational equations to obtain $\phi(t)$ for some large time t and determines λ_{\max} via Eq. (3.5). Some care has to be taken when λ_{\max} is positive. In this case the norm of $\phi(t)$ will blow up exponentially and will quickly be unmanageable by finite precision. This is circumvented by renormalizing $\phi(t)$ and restarting the time evolution, whenever it becomes too large.

Accurately estimating Lyapunov exponents in imperfectly chaotic systems, such as the Bose-Hubbard model on few sites poses a significant numerical challenge, requiring extensive time evolution. In this work, the FTLEs are computed by evolving the systems for up to one million time units.

Sampling states

The continuous nature of the classical phase space precludes the calculation of Lyapunov exponents for every initial state ψ_0 . One strategy to obtain representative results is to sample states uniformly across this space. Given the total norm conservation implied by Eq. (1.46), the classical phase space is limited to the sphere S^{2L-1} within \mathbb{R}^{2L} . Uniform sampling on S^{2L-1} is achieved by selecting the $2L$ coefficients of states from a Gaussian distribution and normalizing the resultant state.

However, this uniform sampling approach on S^{2L-1} tends to under-represent states at lower and higher energies. To ensure uniform energy distribution, we divide the energy spectrum into 100 equally spaced segments and employ the rejection method for uniform state sampling within these segments. This involves initially sampling states uniformly on S^{2L-1} and retaining only those whose energy falls within a specified interval. In this way, for each interaction strength Λ , we obtain up to 10^4 states uniformly distributed in energy and numerically calculate the corresponding FTLE.

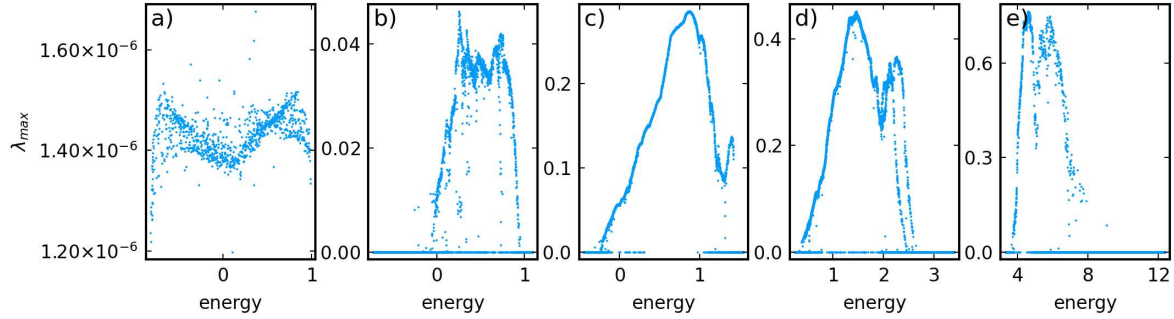


Fig. 3.2 FTLE estimates for the largest Lyapunov exponent λ_{\max} for the classical limit, Eq. (1.43). The numerical estimates for λ_{\max} are plotted against energy, for several different values of the interaction parameter Λ . From left to right Λ is (a) $\Lambda = 0.43$, (b) $\Lambda = 0.93$, (c) $\Lambda = 2.48$, (d) $\Lambda = 6.58$ and (e) $\Lambda = 24.77$. The variational equations were evolved up time $t = 10^6$.

3.2.2 The three site case

In Figure 3.2, we show FTLEs of sampled states against the energy of these states for several interaction parameters Λ . Only estimates of the largest Lyapunov exponent λ_{\max} are presented — the other LEs are either zero or the negative of λ_{\max} .

For $\Lambda = 0$, the model is integrable and hence $\lambda_{\max} = 0$. Figure 3.2(a) shows the numerical estimates for λ_{\max} for non-zero but still small Λ ($\Lambda \approx 0.43$). The numerical estimates for all six Lyapunov exponents have the same order of magnitude, 10^{-6} . This implies that λ_{\max} is either zero or vanishingly small up to some finite value of the interaction.

For larger Λ , panels (b-e), we find cases of λ_{\max} being unambiguously zero, together with cases of the FTLE being smaller than the cutoff 10^{-4} , which we interpret as λ_{\max} being zero. In each of these panels, there are low-energy and high-energy regimes where there are only zero λ_{\max} , and a central energy regime with non-zero positive λ_{\max} . For smaller Λ , the positive- λ_{\max} behavior is concentrated at higher energies (there is an extended $\lambda_{\max} = 0$ range of low energies), panel (b). For large Λ , the converse is true: $\lambda_{\max} > 0$ is seen at lower energies, panel (d),(e).

In general, when there are non-zero exponents, they coexist with zero exponents at the same energy, i.e., the λ_{\max} vs energy function is multi-valued. The only exception is in the intermediate-interaction panel (c), $\Lambda \approx 2.48$, for which an energy window with a single non-zero branch is seen. In fact, for any $\Lambda \gtrsim 1$, there appears always to be some energy window where λ_{\max} is multi-valued — we did not see any exceptions.

The coexistence of zero and non-zero λ_{\max} is a peculiar manifestation of the mixed nature of the system. This is in contrast to integrable systems (for which λ_{\max} is always zero except a measure zero set) and to strongly chaotic systems (for which λ_{\max} is always positive except a measure zero set). To highlight this contrast, we give examples of systems with stronger chaos, the same Hamiltonian on $L = 4$ sites and $L = 7$ sites, in the next section.

In a fully chaotic system, the largest Lyapunov exponent is a smooth single valued function of energy. We showed that λ_{\max} is not a single valued function, but rather often has two branches. One can ask whether each branch is smooth. There are some noisy features in the plots, especially in panels (a), (b) and (e). Presumably, these are finite-time effects, and each branch would resolve into smooth lines if we could integrate up to infinite times. While this conjecture could not be verified conclusively, we observed that integrating up to longer times generally reduces the noisy aspect.

In one case, panel (d), λ_{\max} even appears to have three branches (one zero and two non-zero). We have not seen any indication that this is a finite-time effect, although we cannot rule it out. The data suggests that the mixed nature of the system even allows for three λ_{\max} values. Apparently, the same fixed-energy region of phase space can consist of a regular (non-chaotic) sub-manifold as well as two different sub-manifolds with different non-zero λ_{\max} .

In Figure 3.1(a), we used as an indicator of chaos the fraction of λ_{\max} which are non-zero. The same measure has been used in Ref. [83].

3.2.3 More chaotic cases

The arguably most remarkable signature of mixedness in the $L = 3$ case is the multi-branched behavior of the Lyapunov exponents, as presented in Figure 3.2. In fully chaotic Hamiltonian systems, λ_{\max} depends solely on the single conserved quantity, the energy and is therefore single-branched. In Figure 3.3 we present, for comparison, FTLEs calculated for the 4-site chain and the 7-site chain. The systems are increasingly more chaotic with increasing L . For the $L = 4$ case some multi-valued signature can be seen at small and large energies, Figure 3.3(a). In the $L = 7$ case, Figure 3.3(b), which is much more chaotic, the FTLE appears to be smooth and single-valued.

Obtaining good estimates for the Lyapunov exponents is more challenging for mixed systems. Comparing Figure 3.2 and the two panels of Figure 3.3, we see cleaner (less noisy) data for larger L , for the same time of propagation, even though there are more variables ($2L$) to be evolved for larger L .

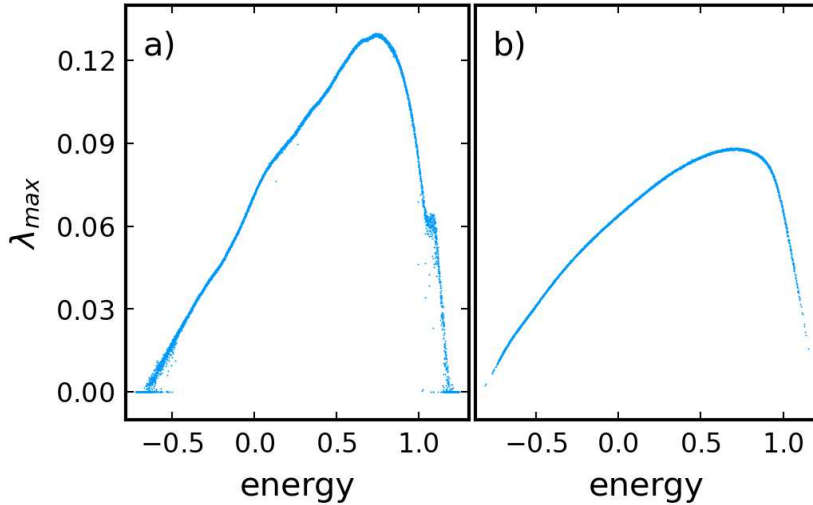


Fig. 3.3 FTLE estimates for the classical largest Lyapunov exponent λ_{\max} plotted against energy, for the classical limits of Bose-Hubbard chains with $L = 4$ (left) and $L = 7$ (right) sites. The interaction parameter is $\Lambda = 1.52$. The variational equations were evolved to time $t = 10^6$.

3.2.4 Magnitudes of Lyapunov exponents as chaos indicator

The procedure of using the fraction of non-zero λ_{\max} 's to characterize chaos neglects the magnitudes of λ_{\max} altogether. One could also make use of the magnitude as a chaos indicator. This raises the issue of comparing values of λ_{\max} for systems with different interactions Λ . We consider two ways of rescaling the λ_{\max} values. The resulting heatmaps in Figure 3.4 show reasonable agreement with that in Figure 3.4(a).

The magnitude of λ_{\max} depends on the timescales of the dynamics of the system. From Eq. (1.43) one could expect that the dominant timescale will be given by the inverse of the maximum of the Hamiltonian parameters, J and Λ . We fixed $J_{12} = 1.5$ and $J_{23} = 1$, so $\max(J, \Lambda) = \max(1.5, \Lambda)$. In Figure 3.4(a), we show the average largest Lyapunov exponent $\bar{\lambda}_{\max}$ per energy interval, rescaled by

$$\beta_{\Lambda} = \max(1.5, \Lambda). \quad (3.7)$$

The resulting heatmap in Figure 3.4(a), by construction, shows chaos in the same region as in Figure 3.1(a). But Figure 3.4(a) shows more detail as it encapsulates the information about the magnitude of λ_{\max} as well. We observe the highest intensities in the mid of the spectrum for $1 < \Lambda < 10$. From there it falls off in all directions. At

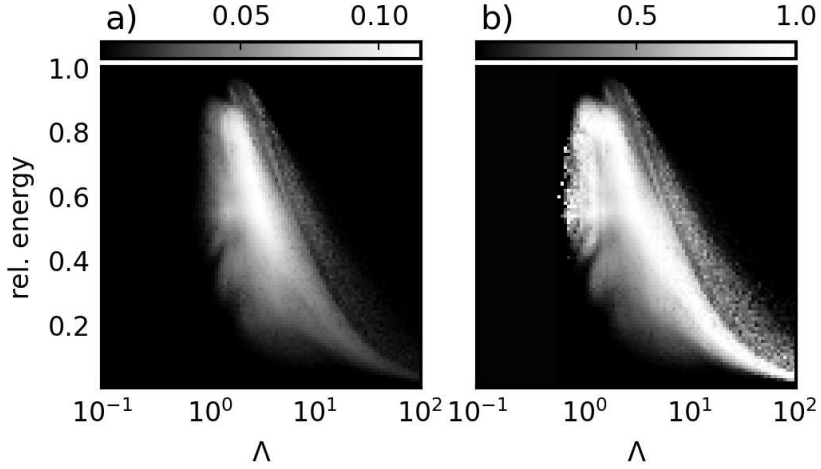


Fig. 3.4 Average largest Lyapunov exponent $\bar{\lambda}_{\max}$ per relative energy interval renormalized by (a) β_{Λ} given by Eq. (3.7) and (b) γ_{Λ} given by Eq. (3.8).

the top end of Figure 3.4(a) we observe a dip in intensity and a sudden increase again, before $\bar{\lambda}_{\max}$ becomes zero. These reflect the dips seen in Figure 3.2(c) and (d).

Another approach is to rescale all largest Lyapunov exponents in a system with fixed interaction Λ by the maximal largest Lyapunov exponent λ_{\max} in that specific system. A problem occurs when all largest Lyapunov exponents are close to zero, as for Bose-Hubbard systems with $\Lambda \ll 1$. In these systems there is simply no significantly positive λ_{\max} . Therefore, we choose the cutoff 10^{-4} by which all Lyapunov exponents are minimally divided. The rescaling parameter is

$$\gamma_{\Lambda} = \max(10^{-4}, \max_{\psi} \lambda_{\max}(\psi)), \quad (3.8)$$

where the maximum runs over all states ψ in the phase space and $\lambda_{\max}(\psi)$ denotes the corresponding largest Lyapunov exponent. A heatmap of the average largest Lyapunov exponent $\bar{\lambda}_{\max}$ with this rescaling is shown in Figure 3.4(b).

The overall features are the same as in panel 3.4(a). There are some artifacts at the boundary between chaotic and non-chaotic regions, around $\Lambda \approx 0.7$ in panel (b), presumably because of numerical uncertainties when λ_{\max} is around 10^{-4} . The intensity of the heatmap does not decrease with Λ beyond $\Lambda \approx 10$, unlike panel (a) where this decrease is built into the scaling function β_{Λ} .

3.3 Eigenvalue statistics

In this section, we will investigate energy-eigenvalue correlations via the distribution of the level ratios, which was introduced in Section 1.1.3.

We will characterize the degree of chaos at different energies. Hence, we compare the distributions obtained from the energy levels within each of the 100 energy intervals described in Section 3.1 to the level spacing distributions of the GOE and independent random variables (Poisson). Such energy-resolved comparisons of level statistics have appeared in Refs. [315, 103]. To compare with GOE or Poisson distributions, we use a common measure of the difference between two distributions, namely the Kullback-Leibler (KL) divergence [316]. The KL divergence between an observed distribution $P(x)$ and a reference distribution $Q(x)$ is

$$D_{\text{KL}}(P|Q) = \int_{-\infty}^{\infty} P(x) \log \frac{P(x)}{Q(x)} dx. \quad (3.9)$$

This quantity vanishes if $P(x)$ is identical to $Q(x)$. Generally, a larger KL divergence indicates stronger deviation of $P(x)$ from $Q(x)$. In this section, $P(x)$ will be the ratio distribution obtained from the Bose-Hubbard energy levels within each energy interval. We will use either the GOE or the Poisson ratio distribution, denoted in the introduction by Eq. (1.23) or (1.27), as the reference $Q(x)$.

3.3.1 Level spacing ratio distribution

In Figures 3.5(a-c), we show the observed ratio distributions for three different combinations of relative energy \tilde{E} and interaction parameter Λ . Since these distributions are estimated from a finite number of energy eigenvalues within the respective energy windows, they are shown as histograms. The data here is extracted from calculations with $N = 150$ bosons. The histograms are expected to converge to a smooth distribution in the limit $N \rightarrow \infty$. For visual guidance, the parameters (Λ, \tilde{E}) corresponding to the panels in Figure 3.5 are marked with respective symbols in Figure 3.6(a).

The distribution in panel 3.5(a) is visually seen to be close to the Poisson case. Hence we expect the KL divergence from the Poisson distribution (D^{Poi}) to be small and the KL divergence from the GOE (D^{GOE}) to be large. The situation in panel 3.5(b) is the opposite (close to GOE), while panel 3.5(c) shows an intermediate case.

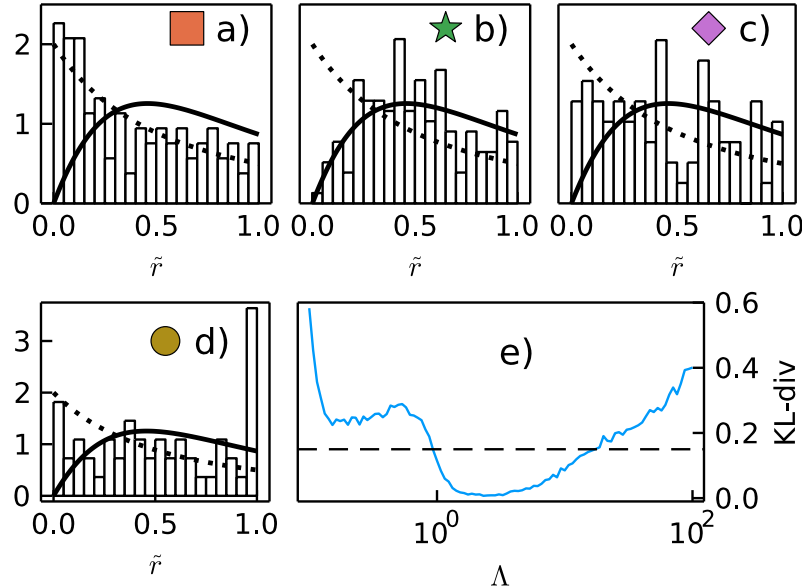


Fig. 3.5 **(a-d)** Level ratio distributions for combinations of interaction Λ and relative energy \tilde{E} . **(a)** $\Lambda \approx 0.28$ and $\tilde{E} = 0.25$, **(b)** $\Lambda \approx 2.48$ and $\tilde{E} = 0.4$, **(c)** $\Lambda \approx 12.33$ and $\tilde{E} = 0.65$ and **(d)** $\Lambda \approx 0.28$ and $\tilde{E} = 0.13$. Solid and dashed lines are the Wigner-like surmises $P_{\text{GOE}}(\tilde{r})$ and $P_{\text{Poi}}(\tilde{r})$, respectively. **(e)** KL divergence of the distribution of the level ratios over the full spectrum from the GOE distribution.

These expectations are in line with the calculated KL divergences:

$$\begin{aligned}
 \text{a)} \quad D^{\text{Poi}} &\approx 0.05, \quad D^{\text{GOE}} \approx 0.4; \\
 \text{b)} \quad D^{\text{Poi}} &\approx 0.22, \quad D^{\text{GOE}} \approx 0.06; \\
 \text{c)} \quad D^{\text{Poi}} &\approx 0.16, \quad D^{\text{GOE}} \approx 0.29.
 \end{aligned}$$

In Figure 3.1(b), we used D^{GOE} as a quantifier of chaos and presented its values in the entire (Λ, \tilde{E}) plane as a heatmap. We capped the values at 0.15, meaning that values $D^{\text{GOE}} > 0.15$ are considered fully non-chaotic and are not distinguished. There is some arbitrariness in the exact choice of this value, but the main results — the overall shape in Figure 3.1(b) and its close correspondence with the classical case, Figure 3.1(a) — are not strongly affected by the use of a cutoff. In Figure 3.5(e), we show D^{GOE} for the complete energy spectrum as a function of Λ , to provide a visual sense of the role of the cutoff in separating chaotic from non-chaotic parameter values.

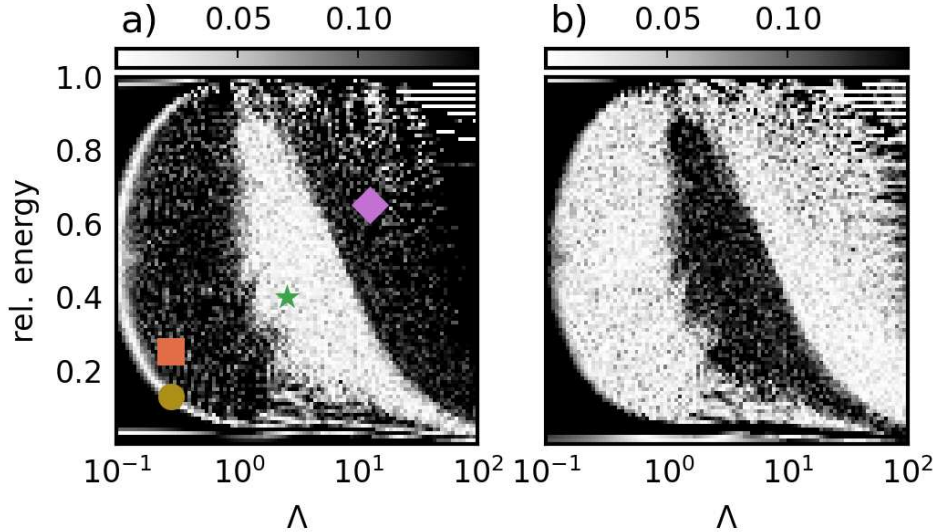


Fig. 3.6 Distance of the mean of the level ratios $\langle \tilde{r} \rangle$ from (a) the GOE level ratio mean $\langle \tilde{r} \rangle_{\text{GOE}}$ and (b) the Poisson level ratio mean $\langle \tilde{r} \rangle_{\text{Poisson}}$. The markers in (a) indicate the systems shown in Figure 3.5. The square corresponds to Figure 3.5(a), the star to (b), the rhombus to (c) and the circle to (d).

3.3.2 Average of level spacing ratios

Often only the first moment (average) of the level ratio distribution is used as a measure of closeness to GOE or Poisson level statistics. An example was provided in the introduction to this thesis, Section 1.2.3. In this section, we use the average level spacing ratio as alternate chaos measure to the KL divergence.

The average level spacing ratio for the GOE is $\langle \tilde{r} \rangle_{\text{GOE}} \approx 0.54$ and for Poisson values $\langle \tilde{r} \rangle_{\text{Poi}} \approx 0.39$. In the previous cases (a), (b) and (c), the means are 0.39, 0.51, and 0.44. They are, respectively, close to $\langle \tilde{r} \rangle_{\text{Poi}}$, close to $\langle \tilde{r} \rangle_{\text{GOE}}$, and intermediate, as expected.

In Figure 3.6, we present the absolute distance from (a) $\langle \tilde{r} \rangle_{\text{GOE}}$ and from (b) $\langle \tilde{r} \rangle_{\text{Poisson}}$. Compared to Figure 3.1(b), we see that the same information is captured; a more chaotic region at intermediate Λ and intermediate \tilde{E} is clearly visible in both these cases. Overall, the mean of level ratios is closer to $\langle \tilde{r} \rangle_{\text{GOE}}$ inside this region and closer to $\langle \tilde{r} \rangle_{\text{Poi}}$ outside. Even the fine structures at the boundary between the two regions, previously seen in the classical case in Figure 3.1(a), are visible.

However, there are some artifacts. The most prominent is the arc at the left (small Λ) region, in Figure 3.6(a). The reason is that, at small Λ , the spectrum shows features specific to the free-boson case, deviating from the Poisson model of completely uncorrelated values. We can see this in Figure 3.5(d), which corresponds to a (Λ, \tilde{E})

combination falling on the arc of Figure 3.6(a). The distribution is neither Poisson-like nor GOE-like: it is non-zero for $\tilde{r} \rightarrow 0$ and has a pronounced peak at $\tilde{r} \approx 1$. Together, these lead to an average $\langle \tilde{r} \rangle \approx 0.52$ which is coincidentally close to $\langle \tilde{r} \rangle_{\text{GOE}}$. The deviation from Poisson at very small Λ is also seen in panel 3.6(b), in the form of a darker region at the very left of the heatmap.

Summarized, the chaos-regular demarcation in the (Λ, \tilde{E}) plane can also be visualized using the mean $\langle \tilde{r} \rangle$, modulo some artifacts.

3.4 Eigenstate statistics

In this section, we will compare eigenstates of the Bose-Hubbard system to eigenstates of random matrices, specifically random matrices of the GOE. As discussed in Section 1.1.4, eigenstates of the GOE have real entries and are uniformly distributed on the $(D - 1)$ dimensional unit sphere $S^{D-1} \subset \mathbb{R}^D$. For large D , the GOE eigenstates are well approximated by a D -dimensional Gaussian distribution with independent entries and mean zero and variance $1/D$. Consequently, we will compare the coefficients of Bose-Hubbard eigenstates against states with iid Gaussian distributed entries.

To compare distributions of eigenstate coefficients, we use the excess kurtosis, κ , of the set of coefficients. The kurtosis is the fourth standardized moment and was introduced in Section 1.1.4. The excess kurtosis of a distribution is the difference between the kurtosis of that distribution and the kurtosis of a Gaussian distribution, which is 3. Thus, large values of κ represent larger deviations from Gaussianity and hence from RMT/chaotic behavior, whereas small values represent more chaotic behavior. When we report values of the kurtosis, we always mean the excess kurtosis κ , even when the word “excess” is omitted.

The deviation of many-body eigenstates from Gaussianity could also be measured using the KL divergence, as in Ref. [96], or using the inverse participation ratio (IPR) or multifractal exponents, as in Refs. [105, 310, 98, 99, 317, 103, 202]. We expect these measures to provide very similar overall pictures as the one we present using the kurtosis. As discussed in Section 1.1.4, when the average of the eigenstate coefficients is negligible (which is true for most eigenstates excepting some at the spectral edges), the kurtosis is proportional to the IPR.

Eigenstate coefficients are defined with respect to a basis. We will investigate eigenstates of the Bose-Hubbard system with respect to three bases:

1. the computational basis, which is given by the mutual eigenstates of the number operators n_i ;

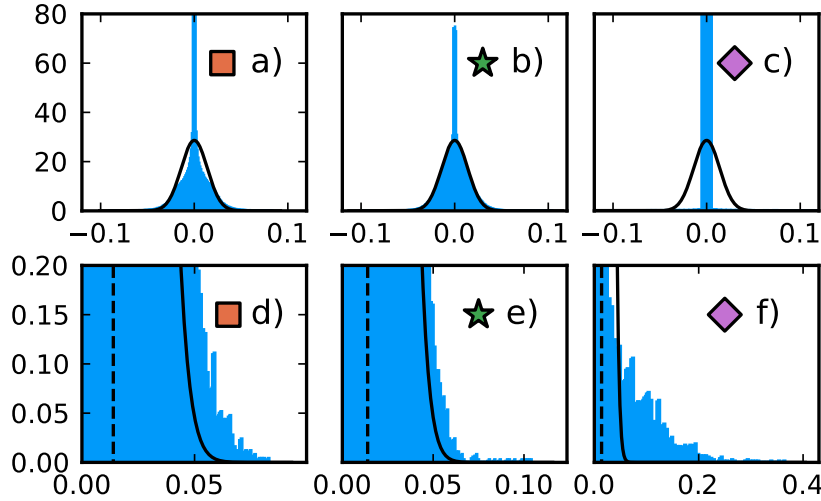


Fig. 3.7 Histograms of eigenstate coefficients of Bose-Hubbard systems with $N = 100$ particles, in the computational basis. In (a-c), the interaction and energy intervals, (Λ, \tilde{E}) , are the same as those used in Figure 3.5(a-c). Panels (d-f) are zoomed into the right tails of (a-c). The black dashed line indicates the standard deviation. The black solid line is a Gaussian density with mean 0 and standard deviation $1/D$. The excess kurtosis is (a) $\kappa_1 \approx 1.6$, (b) $\kappa_1 \approx 0.8$, (c) $\kappa_1 \approx 122$.

2. the mutual eigenbasis of the hopping operators $a_i^\dagger a_j$, i.e., the eigenbasis of the non-interacting (free) system;
3. the eigenbasis of a perturbed free system with hopping terms $J_{ij} = 1$ for all i, j and small on-site perturbing potentials $\sum_i \epsilon_i n_i$ with values $\epsilon_1 = -0.01$, $\epsilon_2 = 0.02$ and $\epsilon_3 = -0.03$ on the three sites.

We name the kurtosis of the coefficients in the three bases as κ_1 , κ_2 , κ_3 respectively. In Figure 3.1(c), the quantity presented is obtained from a combination of the first and third choices above, namely $\max(\kappa_1, \kappa_3)$.

We assume that the distributions underlying the eigenstate coefficients of two eigenstates close in energy are similar. As before, we divide the energy spectrum of each Bose-Hubbard system with interaction strength Λ into 100 equally spaced intervals and refer to them by their relative energy \tilde{E} . We compute the kurtosis κ for every eigenstate and average the calculated kurtosis over each energy interval. If the mean is zero, the averaged kurtosis in an energy interval equals the kurtosis of all coefficients of all eigenstates in that energy interval.

In Figures 3.7(a-c), we show the eigenstate coefficient distributions in the computational (n_i) basis, for the three (Λ, \tilde{E}) combinations used previously in Figure 3.5.

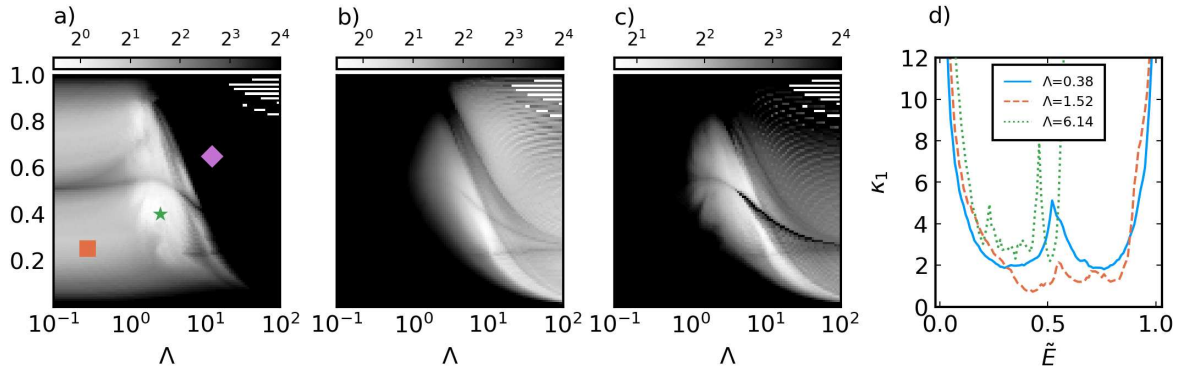


Fig. 3.8 Heatmaps of kurtosis of eigenstate coefficients, for three different bases, listed in the text. The kurtosis is cut off at 2^4 in each case. Markers in (a) indicate the (Λ, \tilde{E}) values for which histograms are shown in Figure 3.7. The kurtosis heatmap shown in Sec. 3.1, Figure 3.1(b), is a combination of panels (a) and (c) here — for each (Λ, \tilde{E}) , the larger of the two values is chosen in Figure 3.1(b). Panel (d) shows vertical slices of panel (a) for values of Λ denoted in the legend of panel (d).

Visual guidance to these three parameter combinations is provided in Figure 3.6(a) and 3.8(a) using corresponding symbols. The calculated excess kurtosis for these cases are respectively $\kappa_1 \approx 1.6$, $\kappa_1 \approx 0.8$ and $\kappa_1 \approx 122$. The case (b) is thus closest to Gaussian, followed by (a), while case (c) is very far from Gaussian. This is consistent with the visual appearance of the full distributions. It is also consistent with the comparison of the tails of the distributions against the tails of the Gaussian distribution, as shown in (d-f).

We note in Figure 3.7(b) that the coefficient distribution, although closest to Gaussian, has a large peak near zero. Even in the most chaotic region of the (Λ, \tilde{E}) plane, the eigenstates depart considerably from the random-matrix case. We attribute this feature to the mixedness of the three-site Bose-Hubbard system.

In Figure 3.8(a) we show the kurtosis κ_1 for eigenstates in the computational basis as a heatmap in the (Λ, \tilde{E}) plane. Comparing with previous sections, we see that small κ_1 correlates with non-zero Lyapunov exponents and GOE level statistics, while intermediate and large κ_1 correlates with zero Lyapunov exponents and non-GOE level statistics. The shape of the small- κ_1 region matches the more chaotic region identified previously using classical Lyapunov exponents or using level statistics. Even subtle features from the heatmaps in the previous sections, such as the bulges around $\Lambda \approx 1$ and $\tilde{E} \approx 0.5$ are visible.

For small Λ , the kurtosis in the computational basis in Figure 3.8(a) shows intermediate rather than large kurtosis, thus failing to fully capture the highly non-chaotic

nature of the system in this region. The reason is probably that the small- Λ eigenstates are so different from the computational basis states (which are $\Lambda \rightarrow \infty$ eigenstates) that they have overlap with a large number of the basis states, leading to a small IPR (hence small kurtosis).

A complementary view is obtained via κ_2 in Figure 3.8(b), where $\Lambda = 0$ eigenstates have been used as basis. Because of the large degeneracy at $\Lambda = 0$, there is some computational arbitrariness in the choice of this basis. This basis now has the opposite problem — it fails to show the non-chaotic nature of large- Λ region. The problem is partially alleviated by choosing as basis the eigenstates of a non-interacting Hamiltonian with small on-site perturbing potentials; the resulting excess kurtosis κ_3 is shown in Figure 3.8(c).

For random-matrix eigenstates, one expects Gaussian behavior with respect to almost any basis. In Figure 3.8, the high-chaos region is marked by low kurtosis in all three basis choices, consistent with the idea of basis-independence. The other regions appear more or less Gaussian-like depending on the basis choice. To demarcate the highly chaotic region from less chaotic regions, we can use a combination of kurtosis calculations, taking the larger one from the kurtosis obtained in the first and third basis, i.e., $\max(\kappa_1, \kappa_3)$. This is what we did in Figure 3.1(b).

3.5 Scaling of EEV fluctuations

In Chapter 2, we investigated the dependence of the magnitude σ of EEV fluctuations on the Hilbert space dimension D and found that for renormalized local operators \bar{A} , σ depends on D as a power-law $\sigma(\bar{A}) \sim D^{-e}$ with exponent e .

In Figure 3.1(d), we have presented a heatmap of the exponents e , determined numerically, for each energy window \tilde{E} and interaction parameter Λ . The operator was chosen as $\bar{A} = a_2^\dagger a_1/N$. The exponents are determined by fitting $\sigma(\bar{A})$ vs D , for system sizes ranging from $N = 90$ to $N = 170$ in steps of 10, i.e., D ranging from $\approx 4,000$ to $\approx 15,000$. The numerically observed exponent e ranges from 0 in the regular regions to ≈ 0.3 in the most chaotic regions of the (Λ, \tilde{E}) plane. The exponent $e = 0$ in the regular regions coincides with the ETH exponent for integrable models. In agreement with the results of Chapter 2, even in the most chaotic regions, e is smaller than the RMT exponent $\frac{1}{2}$. The resulting heatmap, Figure 3.1(d), is noisier and less sharp than those obtained from the other measures discussed in previous sections. But the overall demarcation of chaotic and non-chaotic regimes is clearly visible.

3.6 Discussion

In this chapter, we considered a quantum many-body model that has a classical limit and is well-known to be “mixed”, the Bose-Hubbard model on three sites. We compared the classical Lyapunov exponents of the classical limit against quantum measures of chaos obtained from eigenvalues (statistics of level spacing ratios) and eigenstates (coefficient statistics, EEV fluctuations). Overall, the agreement in the chaos-regular demarcation between the classical case and the various quantum measures is very good.

This reflects the general agreement of chaos measures between quantum systems and their classical limit, when such a limit exists, observed computationally in many different Hamiltonian systems.

For classical systems, it is common in the literature to demarcate chaotic and non-chaotic regimes using Poincaré sections [71, 318, 319, 91, 211, 182, 79, 80, 86, 87]. We have focused instead on the Lyapunov exponent, and presented it as a multi-branched function of energy. Inspired by Ref. [83], we have used the fraction of Lyapunov exponents which are positive as a chaos measure, and compared it with other ways of exploiting the FTLE results to demarcate highly chaotic and less chaotic behaviors. It is clear that, if the phase space at fixed energy is separated into regular and chaotic regions, then the Lyapunov exponent plotted against energy (with many phase space points sampled in each energy window) will have to be a multi-valued plot. We hope that explicitly presenting and analyzing this multi-valued dependence will contribute to the intuition available on mixed systems.

For quantum systems, we used several measures: (1) the statistics of level spacing ratios based on eigenvalues alone; (2) the coefficients of eigenstates, based on eigenstates expressed in different bases; (3) the scaling of EEV fluctuations, based on eigenstate properties. Level spacing statistics and eigenstate coefficients have been considered and used as chaos measures for several decades. The EEV fluctuation scaling is based on understanding that has emerged in recent years, motivated by studies of thermalization and the ETH.

Of course, there are other interesting measures of quantum chaos that could be considered for comparison. A candidate is the out-of-time-ordered correlator (OTOC) whose initial growth defines a quantum Lyapunov exponent for chaotic systems. For our mixed system, we were unable to unambiguously identify or rule out exponential regimes in the dynamics, for the parameter combinations we attempted. It remains unclear to us whether the OTOC is a useful measure for numerically demarcating more-chaotic parameter regimes from less-chaotic and non-chaotic parameter regimes in mixed systems. Another measure of chaos is the fractal dimension of eigenstates,

which was presented in Refs. [103, 202] for a quantum Bose-Hubbard chain, not in the classical (fixed L , large N) limit but rather for parameters relevant to the thermodynamic (large L , fixed N/L) limit. The authors found a similar chaotic region for intermediate Λ and \tilde{E} .

There are some peculiar features in both the eigenvalue and eigenstate statistics, whose origins remain unclear and might be clarified in future studies. In Figure 3.6(a), the arc in the small- Λ part of the heatmap is due to the level spacing having peculiar statistics, as shown in Figure 3.5(d), due to a significant number of successive equal spacings. In the eigenvector statistics, there are some mid-spectrum states that are highly non-Gaussian, even at intermediate Λ , as seen through the dark nearly horizontal line in Figure 3.8(a) at intermediate energies, and the dark curved line in Figure 3.1(c), running through the more-chaotic light-colored region at intermediate energies. Presumably, such peculiar features are less likely to appear in more fully chaotic systems, such as the Bose-Hubbard system with larger number of sites.

Chapter 4

An ensemble of sparse random generators of Markov processes

The content of this chapter has appeared as part of [301]:

G. Nakerst, S. Denisov, and M. Haque, Random sparse generators of Markovian evolution and their spectral properties, *Phys. Rev. E* **108**, 014102 (2023).

In this chapter, we discuss an ensemble of random Kolmogorov generators for continuous-time Markov chains (CTMCs) with adjustable sparsity. This ensemble aims to address the unrealistic large spectral gaps seen in dense random Kolmogorov operators (introduced in Section 1.3.3), which result in long, less physical relaxation times. The discrepancy between the spectral gaps of dense random generators and non-random generators of physical models is highlighted in Figure 4.1.

The ensemble of random Kolmogorov generators, introduced in this chapter, is characterized by φ non-zero off-diagonal elements per row and column. For small φ these operators are sparse, while for large φ they become denser. The dense random generator case is recovered for $\varphi = D - 1$, with D denoting the matrix size, or equivalently, the size of the state space. For typical physical CTMCs, φ is constant in D for single-body systems, while φ increases logarithmically with D for many-body systems.

In Section 4.1, we discuss how dense random Kolmogorov generators ($\varphi = D - 1$) differ from typical physical generators. In Section 4.2, we introduce the ensemble of sparse random Kolmogorov operators. The bulk spectrum is analyzed in Section 4.3. We show that whenever φ increases with D the bulk spectrum is shifted away from the stationary value 0, independent of the distribution of non-zero elements of the generator matrix. In Section 4.4, we address the spectral gap. In contrast to the bulk, the gap

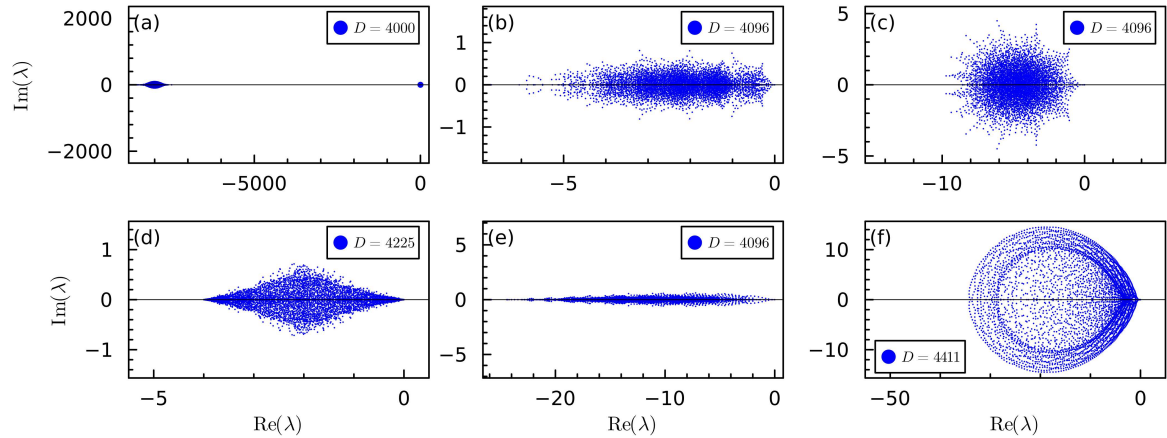


Fig. 4.1 Spectra of CTMC generators. (a) Dense (non-sparse) random generator with χ^2 edge weight distribution, (b) TASEP on a ring with staggered hopping probabilities [52], (c) ASEP on a chain with open boundary conditions and next nearest neighbor terms, (d) a process of particle hopping on an open boundary grid with random hopping probabilities, (e) a 1D contact process, (f) a gene transcription model from Ref. [239]. In each plot the real and imaginary axes have the same scale. Further details of the models are presented in an appendix in Section 4.7.3.

depends on the distribution of non-zero matrix elements, particularly on the left tail. For typical distributions, we show using extreme value theory that the gap decreases as a power-law in D for constant φ (single-body), is constant (up to logarithmic corrections) for $\varphi \sim \log D$ (many-body), and increases whenever φ increases substantially faster than $\log D$. In Section 4.5, we discuss correlations between eigenvalues in terms of complex spacing ratios (CSRs). We show that already for $\varphi \geq 2$, CSRs agree with the GinOE, while the extreme case $\varphi = 1$ is anomalous. We conclude with a summary of our results in Section 4.6 and highlight open questions. An appendix in Section 4.7 contains details of the models whose spectra are presented in Figure 4.1 and the details of analytical derivations.

4.1 Motivation

In this section, we contrast the spectra of physical Markov process generators with those of dense random generators, discussed in Section 1.3.3. The observation that dense random generators exhibit significantly larger spectral gaps than physical generators motivates us to explore sparse generators in this chapter.

In Figure 4.1(a) we present the spectrum of a random dense \mathcal{K} -generator. Similar to Figure 1.11(a) from the introduction, the spectral bulk is well separated from the stationary eigenvalue 0. The Kolmogorov operator \mathcal{K} in Figure 4.1(a) has χ_2^2 -distributed elements. As discussed in Section 1.3.3, the spectrum of such generators is independent of the specific matrix element distribution, provided the distributions are non-exotic and have similar mean and variance.

In contrast to panel (a), panels (b-f) show the spectrum of physical CTMC generators. These are non-random matrices which emerge from microscopic laws. Panel (b) shows the spectrum of a modified TASEP according to Ref. [52], (c) the ASEP with obc and next-nearest neighbor hopping terms, (d) a single particle hopping on a distorted two-dimensional grid, (e) a contact process modeling epidemic spread, and (f) a biological model describing the accumulation and release of mechanical strain of DNA during transcription. Further information and details of these models are presented in Section 4.7.3.

The large gap of dense random generators implies rapid convergence from any generic initial probability vector to the steady state. The relaxation time, which is the inverse of the spectral gap, decreases inversely in the state space size D . In contrast, physical generators of CTMCs in general exhibit spectral gaps and relaxation times that depend on D in ways that are not simply (anti-)linear. For example, the ASEP on a 1D chain with L sites shows a spectral gap vanishing as $O(L^{-3/2})$.

Our preference for sparse random generators in modeling physical generators stems from the observation that, in many established models, the corresponding \mathcal{K} -generators are inherently sparse. This sparsity typically arises due to locality, which limits permissible transitions within the state spaces of the models. In systems involving multiple components or particles, a generic generator matrix element often represents simultaneous changes in several (or all) components. For example in the ASEP, a generic matrix element corresponds to correlated hopping of many particles. However, such processes are typically absent in models that are motivated by physical, biological, economic, or other considerations. This results in a predominance of zero elements in the \mathcal{K} -matrices.

The inability of dense random generators to reasonably model the spectral gap and relaxation times of physical generators, combined with the inherent sparsity of these physical generators, motivates us to refine the RMT approach to Kolmogorov operators by incorporating sparsity.

4.2 Defining the ensemble

In this section, we define an ensemble of random sparse Kolmogorov operators. As discussed in Section 1.3.1, every Kolmogorov operator can be decomposed into

$$\mathcal{K} = \mathcal{M} - \mathcal{J}, \quad (4.1)$$

where \mathcal{M} is a matrix with non-negative entries and \mathcal{J} is a diagonal matrix, with its diagonal elements formed by column sums of \mathcal{M} . In the following, we will describe how to randomly generate \mathcal{M} as a sparse matrix. By Eq. (4.1) the associated Kolmogorov operator \mathcal{K} will be sparse, too.

The matrix \mathcal{M} can be considered as the adjacency matrix of a random directed graph with positive, iid edge weights, without self-loops, and with fixed vertex degree equal to φ . Therefore, the Kolmogorov operator \mathcal{K} is the negative combinatorial Laplacian associated with the graph.

In this chapter, we will consider directed graphs which in general makes \mathcal{M} and so \mathcal{K} non-symmetric and their spectra complex. We focus on φ -regular graphs, characterized by each vertex having φ outgoing and incoming edges, with φ denoting the vertex degree. Such graphs possess exactly $2D\varphi$ edges. This regularity ensures that the adjacency matrix \mathcal{M} contains precisely φ non-zero elements in every row and column. For simplicity, we do not allow self-loops that are edges with the same starting and ending vertex. This ensures that the adjacency matrix \mathcal{M} has zero diagonal and the Kolmogorov operator \mathcal{K} has exactly $\varphi + 1$ non-zero elements in every column and row (including the negative diagonal element). The sparsity of the random graphs is controlled by the vertex degree φ , which is bounded by $1 \leq \varphi \leq D - 1$. For small φ the graph and the adjacency matrix \mathcal{M} are very sparse while for larger φ they become denser. The fully connected graphs are recovered for maximal $\varphi = D - 1$.

The adjacency matrix \mathcal{M} is uniformly drawn from the set of all graphs with the above properties. Said differently, \mathcal{M} is uniformly distributed on the set of φ -regular directed graphs on D vertices without self-loops. Sampling such a graph begins with a graph on D vertices and no edges. Then, each vertex is connected to φ other vertices iteratively, while rejecting edges if the corresponding vertex already has φ incoming edges. For the final vertices, it may not be possible to connect to other vertices without violating the constraint of φ incoming edges for each vertex. In such cases, the entire process is restarted. To mitigate the risk of restarting the procedure, we reduce the probability of connecting to a vertex that already has a high degree. Following this

approach, we find that we rarely need to restart the algorithm for the matrix sizes and vertex degrees φ examined in this chapter.

So far we have not specified the non-zero elements of \mathcal{M} . In un-weighted graphs the non-zero elements of the adjacency matrix are typically 1. Here, we consider the more general framework of weighted graphs. In these graphs the edges and the non-zero elements of \mathcal{M} have weights different from 1. Because all entries of \mathcal{M} have to be non-negative the weight distributions we consider are all non-negative. Explicit results in the following sections are mostly derived for uniform and χ_2^2 distributions. (The χ_k^2 distribution is the sum of k squared, independent standard Gaussians.) However, our results can be adapted to other weight distributions.

The sparse graph ensemble considered here is quite generic. For example, the graph corresponding to the \mathcal{K} -generator of a single particle hopping on a d -dimensional hypercubic lattice with periodic boundary conditions and random hopping rates is a particular (to the nearest-neighbor connections) realization of the ensemble with $\varphi = 2d$. Figure 4.1(d) shows an example spectrum for $d = 2$.

The regularity of the graphs ensures that, with probability $1 - O(D^{-\varphi-1})$, they are strongly connected as long as $\varphi \geq 2$ [320]. As discussed in Section 1.1.5, strongly connected means that by traversing along the edges of the graph every vertex can be reached from every other vertex. Strong connectivity is a desirable feature for a minimal random \mathcal{K} -generator model. It implies that the matrix \mathcal{K} is not of block-diagonal structure and the state space is not partitioned into disconnected subsets. Additionally, strong connectivity implies that the multiplicity of the zero eigenvalue is one, which makes the steady state unique. Finally, every state in the state space is reachable from every other state. Therefore, the steady state has all states populated. All physical models motivating this study and presented in Figure 4.1 are - except for the contact process - all strongly connected. The contact process is only effectively strongly connected, with one exceptional state. In the following sections, we will focus on sparse generators with $\varphi \geq 2$. The case $\varphi = 1$ will be discussed in Section 4.5.

The physical models presented in Figure 4.1 motivate us to focus on two types of dependencies of φ on the matrix size D , namely $\varphi = \text{const}$ and $\varphi \sim \log D$. For generators of single particle hopping models - an example is shown in Figure 4.1(d) - the average number of non-zero elements per column and row is constant and independent of D . In many-body hopping models such as the ASEP or the contact process, Figure 4.1(b), (c), and (e), it increases logarithmically with D . There is no simple dependence of φ on D in the gene transcription model, Figure 4.1(f), as the matrix size D is controlled by multiple parameters.

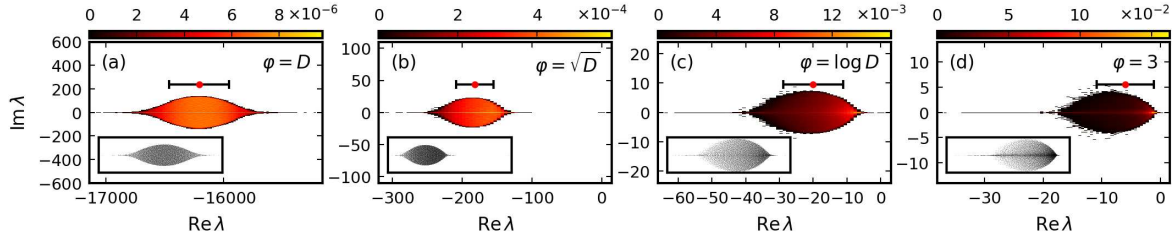


Fig. 4.2 Spectral densities of random Kolmogorov operators with χ^2 weight distribution. The matrix size is $D \approx 8000$ and the densities are estimated with 100 samples. White areas contain no eigenvalues. (a) Dense matrix without the zero eigenvalue, (b) sparse matrix with $\varphi = \sqrt{D}$ non-zero elements per row and column, (c) $\varphi = \log D$ and (d) $\varphi = 3$. The insets show spectra of single realizations. In each plot, the real and imaginary axes have the same scale. The red dots mark the location of $\mu(\lambda)$, given by Eq. (4.2), and the intervals shown in black are $[\mu(\lambda) - \sigma(\lambda), \mu(\lambda) + \sigma(\lambda)]$, where $\sigma(\lambda)$ is given by Eq. (4.4).

A similar setup to the one presented here was studied in Ref. [295], where an ensemble of oriented Erdős-Rényi graphs [321] was used. In these graphs, edges between vertices are present with a probability $p(D)$. Hence, the vertex degrees are binomial-distributed [321] and not constant as in our case. However, one might expect similar behavior in the $D \rightarrow \infty$ limit with the correspondence $p(D) = \varphi/D$. The authors of Ref. [295] considered the regime $Dp(D) \gg (\log D)^6$, which they found to have the same universal properties as in the non-sparse case. In this work, we consider sparsity beyond this limit, including specifically $\varphi \sim D^0$ (vertex degree not growing with D) and $\varphi \sim \log D$.

4.3 Bulk spectrum

In this section, we analyze the dependence of the position and horizontal width of the bulk of the spectrum on the sparsity parameter φ and the matrix dimension D . We first provide (Sections 4.3.1 and 4.3.2) expressions and bounds for the position and the width, characterized respectively by the mean $\mu(\lambda)$ of all eigenvalues and the standard deviation $\sigma(\text{Re } \lambda)$ of the real parts of the eigenvalues. These results are expressed in terms of the mean and standard deviation of the weight distribution (distribution of non-zero elements of the Kolmogorov operator \mathcal{K}), denoted by μ_0 and σ_0 , respectively.

Since the most prominent effect of sparsity is to reduce the parametrically large gap seen in the full random case, it is instructive to analyze the ratio $\alpha = |\mu(\lambda)|/\sigma(\text{Re } \lambda)$. This quantity provides insight into the distance of the bulk of the spectrum from the

origin, relative to the size of the bulk. Section 4.3.3 is devoted to an analysis of the ratio α .

Numerical results presented in this section are obtained by sampling edge weights from the χ_2^2 and the standard uniform distribution.

The spectrum of dense generators ($\varphi = D - 1$) consists of two distinct parts - an eigenvalue $\lambda_1 = 0$ and the rest of the eigenvalues forming the spectral bulk away from the imaginary axis, as shown in Figure 4.1 (a) and Figure 4.2 (a). In contrast, the bulk of the spectrum is much closer to the imaginary axis for $\varphi \ll D$, as seen in Figure 4.2 for (b) $\varphi = \sqrt{D}$, (c) for $\varphi = \log D$ and (d) for $\varphi = 3$. For $\varphi = \sqrt{D}$, the bulk of the spectrum is visibly separated from zero, as in the dense case. In fact, the spectral boundary has the same spindle-like form as the dense case $\varphi = D - 1$. Whether the spectral distribution is separated from zero for $\varphi = \log D$ and $\varphi = 3$ is difficult to say with certainty from the available numerical data ($D \approx 8000$).

4.3.1 Position

The position of the spectral bulk of \mathcal{K} can be identified with the estimated mean $\mu(\lambda)$ of the eigenvalues λ_i of \mathcal{K} ,

$$\mu(\lambda) = \left\langle \frac{1}{D} \sum_{i=1}^D \lambda_i \right\rangle, \quad (4.2)$$

where the average $\langle \dots \rangle$ is taken over the ensemble of random Kolmogorov operators described in Section 4.2. Because the eigenvalues are either real or come in complex conjugate pairs, the mean of the spectral bulk is real, $\mu(\lambda) = \mu(\text{Re } \lambda)$.

A simple calculation shows that $\mu(\lambda)$ can be expressed as

$$\mu(\lambda) = \left\langle \frac{1}{D} \text{tr}(\mathcal{K}) \right\rangle = \frac{1}{D} \sum_{j=1}^D \langle K_{jj} \rangle = -\varphi \mu_0. \quad (4.3)$$

The averaging $\langle \dots \rangle$ over the matrix ensemble in Eq. (4.2) and Eq. (4.3) is, in principle, not needed since self-averaging is expected, i.e., for large enough D , a single sample will display all the spectral features of the ensemble. This is because the quantity $\frac{1}{D} \text{tr}(\mathcal{K})$ is concentrated around its average $\left\langle \frac{1}{D} \text{tr}(\mathcal{K}) \right\rangle$ for increasing D , which we show in an appendix in Section 4.7.1.

For the four different dependencies of φ on D shown in Figure 4.2, Eq. (4.3) implies the following: For $\varphi = \text{const}$, the mean is independent of the matrix size D . For $\varphi = \log D$ ($\varphi = \sqrt{D}$) the mean decreases logarithmically with D (as $\sim \sqrt{D}$) and for $\varphi = D$ the mean decreases linearly with D as is expected for the dense generators [294].

In Figure 4.2, the location $\mu(\lambda)$ of generator matrices \mathcal{K} is indicated with a red dot in each panel. The real part of the dot resides in the bulk of the spectrum for every dependence of φ on D shown in Figure 4.2.

4.3.2 Horizontal width

In Section 4.3.1, we investigated the bulk location of the spectrum in the complex plane. In this section, we will analyze the width of the distribution, particularly the horizontal width.

We characterize the width of the bulk spectrum, both in the real and imaginary directions, $\text{Re } \lambda$ and $\text{Im } \lambda$, using the estimated variances

$$\sigma^2(\text{Re } \lambda) = \left\langle \frac{1}{D} \sum_{i=1}^D \left(\text{Re } \lambda_i - \frac{1}{D} \sum_{j=1}^D \lambda_j \right)^2 \right\rangle \quad (4.4)$$

$$\sigma^2(\text{Im } \lambda) = \left\langle \frac{1}{D} \sum_{i=1}^D (\text{Im } \lambda_i)^2 \right\rangle, \quad (4.5)$$

where we used the fact that $\sum_{j=1}^D \lambda_j$ is real. Since eigenvalues are real or appear in complex conjugate pairs, $\sigma^2(\text{Re } \lambda)$ and $\sigma^2(\text{Im } \lambda)$ are related to the estimated complex pseudo-variance via

$$\begin{aligned} \sigma^2(\lambda) &= \left\langle \frac{1}{D} \sum_{i=1}^D \left(\lambda_i - \frac{1}{D} \sum_{j=1}^D \lambda_j \right)^2 \right\rangle \\ &= \sigma^2(\text{Re } \lambda) - \sigma^2(\text{Im } \lambda). \end{aligned} \quad (4.6)$$

The estimated pseudo variance lower bounds the estimated variance of the real parts of the eigenvalues, $\sigma^2(\lambda) \leq \sigma^2(\text{Re } \lambda)$.

The complex pseudo variance can be analytically calculated for the ensemble of random generator matrices as

$$\begin{aligned} \sigma^2(\lambda) &= \left\langle \frac{1}{D} \text{tr}(\mathcal{K}^2) \right\rangle - \left\langle \frac{1}{D^2} \text{tr}(\mathcal{K})^2 \right\rangle \\ &= \varphi \left(\sigma_0^2 + \frac{\varphi}{D} \mu_0^2 - \frac{1}{D} \sigma_0^2 \right). \end{aligned} \quad (4.7)$$

Details of the calculation are provided in an appendix in Section 4.7.1. The bound of the estimated real variance by the pseudo variance together with Eq. (4.7) leads to the asymptotic lower bound of $\sigma(\text{Re } \lambda)$ in terms of the sparsity parameter φ . As $1 \leq \varphi \leq D$, the estimated horizontal width of the bulk spectrum cannot grow asymptotically slower

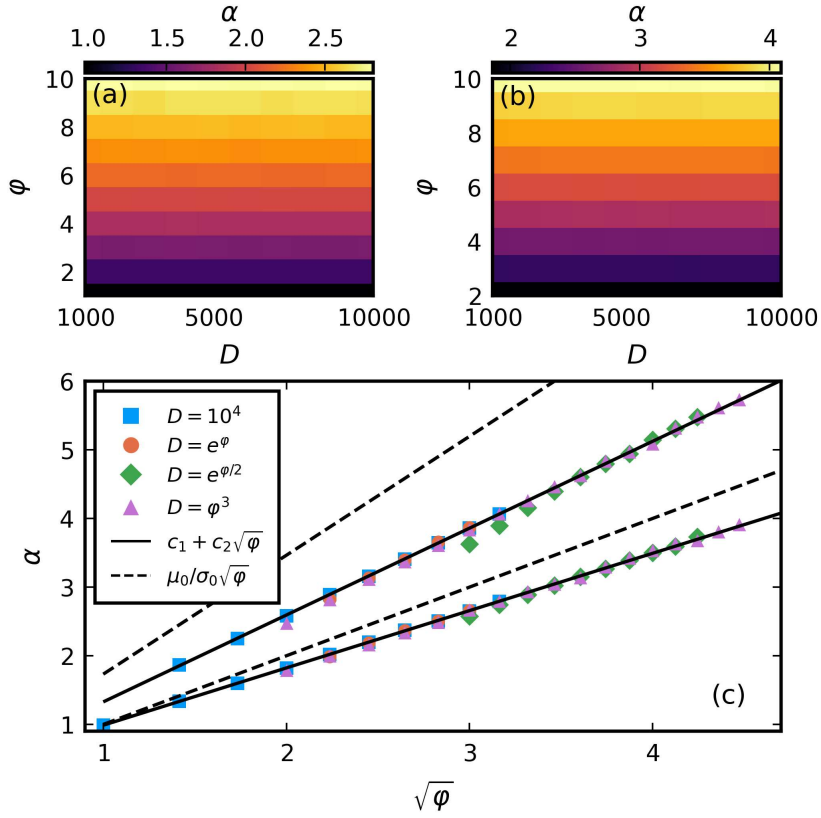


Fig. 4.3 Ratio α of mean $\mu(\text{Re } \lambda)$ and horizontal width $\sigma(\text{Re } \lambda)$ of the bulk of the spectrum of sparse random Kolmogorov operators with (a) χ^2_2 and (b) standard uniform weight distributions. In (c) α as a function of $\sqrt{\varphi}$. The bottom markers correspond to χ^2_2 and the top to uniform distribution. Dependencies of φ on D are $\varphi \equiv \text{constant}$, $\varphi = \log D$, $\varphi = 2 \log D$, and $\varphi = D^{1/3}$. The black solid lines correspond to $\alpha = c_1 + c_2\sqrt{\varphi}$ ($c_{1,2}$ given in the main text) and the dashed lines denote $\alpha = \mu_0/\sigma_0\sqrt{\varphi}$.

than $\sqrt{\varphi}$,

$$\sigma(\text{Re } \lambda) \gtrsim \sqrt{\varphi}. \quad (4.8)$$

Numerically, we find that the bound in Eq. (4.8) is asymptotically sharp for $\varphi \ll D$, as shown in Figure 4.3 through the ratio α of mean $\mu(\text{Re } \lambda)$ and width $\sigma(\text{Re } \lambda)$. The collapse of the data points in Figure 4.3(c) implies that $\sigma(\text{Re } \lambda) \sim \sqrt{\varphi}$.

4.3.3 Ratio of mean and horizontal width

In this section, we combine the information of the location of the spectrum given by Eq. (4.2) and the horizontal width of the bulk given by Eq. (4.4) into the ratio

$$\alpha = \frac{|\mu(\operatorname{Re} \lambda)|}{\sigma(\operatorname{Re} \lambda)}. \quad (4.9)$$

This quantifies how close the bulk spectrum is, relative to its size, to the stationary value $\lambda_1 = 0$. i.e., to the imaginary axis. For $\alpha = O(1)$ the estimated width of the bulk is of the same order as the estimated mean, thus the spectrum is located close to 0. For $\alpha \gg 1$ the estimated mean is much bigger than the horizontal width of the bulk and the bulk of the spectrum is far away from 0.

The analytical result for the estimated mean of the spectrum, Eq. (4.3), together with the asymptotic bound on the standard deviation of the real parts of the spectrum, Eq. (4.7), imply the following asymptotic bound on α

$$\alpha \lesssim \sqrt{\varphi}. \quad (4.10)$$

Numerically, we observe that the bound in Eq. (4.10) is asymptotically tight for $\varphi \ll D$, i.e.

$$\alpha \approx c_1 + c_2 \sqrt{\varphi}, \quad (4.11)$$

for constants c_1 and c_2 . Since $\mu(\lambda)$ scales linearly with φ , this behavior is consistent with $\sigma(\operatorname{Re} \lambda) \sim \sqrt{\varphi}$, stated previously. The constants are found to be $c_1 \approx 0.15$ (≈ 0.1) and $c_2 \approx 0.84$ (≈ 1.3) for the χ_2^2 (uniform) distribution.

Numerical results for α are summarized in Figure 4.3. For each combination of φ and D , α is averaged over n samples of random generators such that $nD = 50,000$. The weight distribution is the χ_2^2 distribution in (a) and in the lower part of (c), and is the uniform distribution in $[0, 1]$ in (b) and in the upper part of Figure 4.3(c). We have found that these results are qualitatively the same for exponentially distributed edge weights.

In Figure 4.3(a,b), we show the value of α as a function of D and φ . On the x -axis D varies in steps of 10^3 between 10^3 and 10^4 . We observe that α increases with φ and is independent of D , as predicted by Eq. (4.11). In Figure 4.3(c) we show α as a function of φ for different dependencies of φ on D . In all the cases, values of α collapse onto the black solid line given by Eq. (4.11).

For $\varphi \sim D$, the ratio α scales as $\sim \sqrt{D}$, thus recovering the parametrically large gap in the non-sparse case. For constant φ , the location of the bulk relative to its size

is constant and independent of D , i.e, if measured relative to the size of the bulk, the bulk does not move away from the imaginary axis with increasing D . We have thus quantified how sparsity cures one of the less physical aspects of the non-sparse random model of Markov generators.

4.4 Spectral gap

In this section, we will consider the spectral gap γ_* of \mathcal{K} ,

$$\gamma_* = \min\{|\operatorname{Re} \lambda_i| : \operatorname{Re} \lambda_i < 0\}. \quad (4.12)$$

The spectral gap γ_* is asymptotically, approximately bounded by the right extent of the bulk $|\mu(\lambda)| - \sigma(\lambda)$, which depends on φ as $\sim \varphi - \sqrt{\varphi} \sim \varphi$. So for constant φ , the spectral gap is bounded from above, while for φ increasing with D the spectral gap can increase with D .

In this section, the edge weights are distributed according to the χ_2^2 and the standard uniform distributions. We first demonstrate numerically that, for $\varphi = \text{const}$, the average spectral gap $\langle \gamma_* \rangle$ decreases as $D^{-1/\varphi}$, while $\langle \gamma_* \rangle$ is constant if φ increases logarithmically with D . We then show that the spectral gap is well approximated by the smallest (in magnitude) diagonal term of $\mathcal{J}(\mathcal{K})$ and use the theory of extreme values (EVT) to underpin the numerical observations. The results are then generalized to weight distributions with power-law left tails in that for constant φ the average spectral gap decreases as a power-law in D and the crossover from decreasing to increasing $\langle \gamma_* \rangle$ happens when $\varphi \sim \log D$.

4.4.1 Numerical results

In Figure 4.4, we show the average spectral gap $\langle \gamma_* \rangle$ for edge weights distributed as χ_2^2 (a-c) and according to the standard uniform distribution (d-f). For every combination of φ and D , the average of the spectral gap is estimated with 100 samples. In Figure 4.4(a) and (d) we show $\langle \gamma_* \rangle$ as a function of D for different dependencies of φ on D . The average spectral gaps for constant $\varphi = 3, 5, 8, 13$ (presented with colored circles) clearly follow a power-law scaling with D .

In Figure 4.4(b) and (e), we show the average spectral gap $\langle \gamma_* \rangle$ as a function of φ and D . The black dashed lines are contour lines of constant $\langle \gamma_* \rangle$. They are straight lines to a very good approximation, showing that for a logarithmic increase of φ in D the spectral gap is constant.

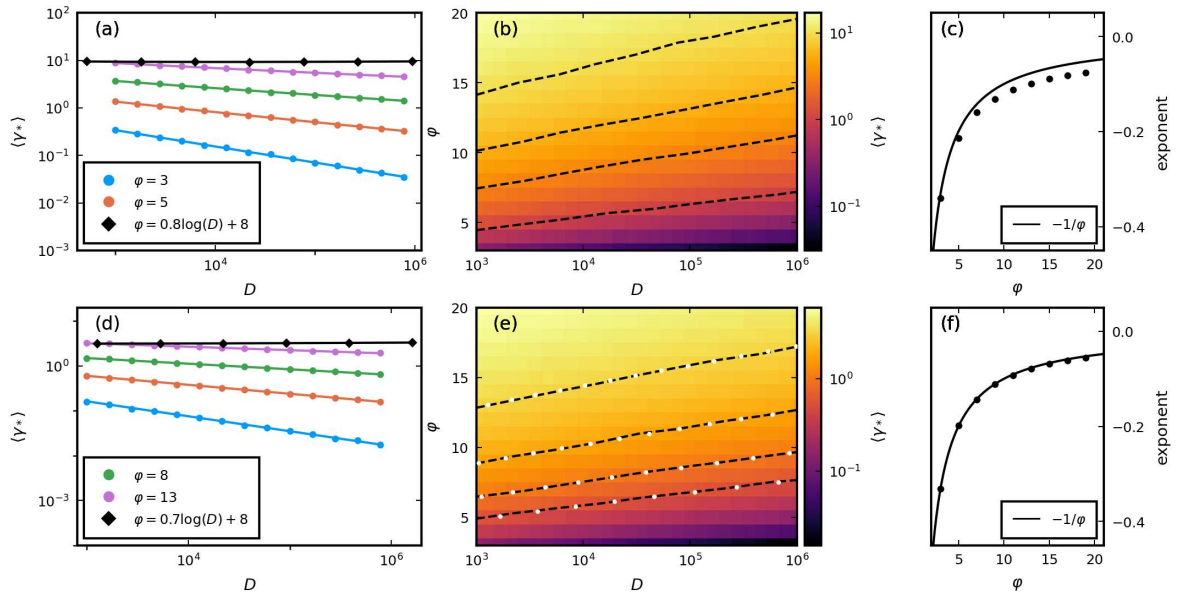


Fig. 4.4 The average spectral gap $\langle \gamma_* \rangle$ with χ^2_2 (top) and standard uniform (bottom) weight distributions. Solid lines in the log-log plots are analytical predictions from Eq. (4.21) in (a) and Eq. (4.24) in (d). Black dashed lines in the heatmaps denote contours of constant gap. White circles in the heatmap in (e) are given by Eq. (4.26).

We show the average spectral gap $\langle \gamma_* \rangle$ as a function of D for $\varphi = \frac{4}{5} \log D + 8$ in Figure 4.4(a) and $\varphi = \frac{7}{10} \log D + 8$ in (d) as black diamonds. These dependencies of φ on D agree well with the top dashed contour lines in (b) and (e), respectively. The average spectral gap of φ depending logarithmically on D is constant in Figure 4.4(a) and (d).

4.4.2 Gap as the minimum of the diagonal

Let us assume for a moment that the generator matrix \mathcal{K} is Hermitian with eigenvalues $\lambda_D \leq \dots \leq \lambda_2 < \lambda_1 = 0$. Then $\mathbb{1} = (1, \dots, 1)^t$ is the eigenvector with eigenvalue 0 and all other eigenvectors are orthogonal to it. By the Courant-Fischer theorem [322]

$$\gamma_* = -\lambda_2 = \min_{|v|=1, v \perp \mathbb{1}} v^t (-\mathcal{K}) v, \quad (4.13)$$

where the minimum runs over all vectors $v \in \mathbb{R}^D$, which have Euclidean norm $|v| = 1$ and are perpendicular to $\mathbb{1}$. Choosing $1 \leq l \leq D$ arbitrarily and v as (see the appendix

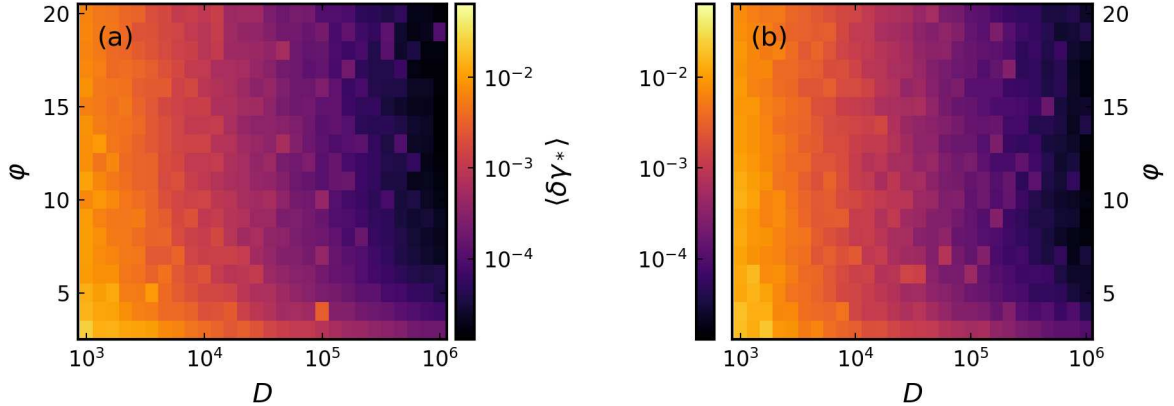


Fig. 4.5 The average relative error (Eq. (4.19)) between the spectral gap and the minimal value of \mathcal{J} . Weight distributions are the χ_2^2 distribution in (a) and the standard uniform distribution in (b). Averages are over 100 samples.

in Section 4.7.2 for more details)

$$v_i = \begin{cases} \sqrt{1 - \frac{1}{D}} & i = l \\ -\frac{1}{\sqrt{D(D-1)}} & i \neq l, \end{cases} \quad (4.14)$$

together with a simple calculation shows that

$$\gamma_* \leq \left(1 + \frac{1}{D-1}\right) \min_{1 \leq l \leq D} J_{ll}. \quad (4.15)$$

Similarly, by using the Courant-Fisher theorem for the eigenvalue with largest magnitude λ_D we find

$$-\lambda_D = \max_{|v|=1} v^t (-\mathcal{K}) v, \quad (4.16)$$

and with v as the l -th vector of the standard basis of \mathbb{R}^D

$$-\lambda_D \geq \max_{1 \leq l \leq D} J_{ll}. \quad (4.17)$$

Under some mild conditions on random weights K_{ij} , a result from Ref. [323] shows that the inequality Eq. (4.17) becomes an equality in the large D limit with probability approaching 1. Motivated by this observation and the bound from Eq. (4.15), we expect a similar asymptotic tightness for Eq. (4.15). However, it is an open question whether the result from Ref. [323] applies to the bound of the spectral gap, Eq. (4.15). Further, the proof presented in Ref. [323] makes use of the Central Limit Theorem for

the diagonal elements J_{ll} of \mathcal{J} , and so the corresponding result does not apply to the case of constant or logarithmically increasing (with D) sparsity parameter φ .

Nevertheless, the above arguments allow us to conjecture that in the limit of large D and $\varphi \ll D$ the spectral gap γ_* is well approximated by the minimum of the diagonal of \mathcal{J} ,

$$\gamma_* \approx \min_{1 \leq l \leq D} J_{ll}, \quad (4.18)$$

for general, non-hermitian random generator matrices \mathcal{K} , with iid and non-exotic edge weight distributions. We support our conjecture with numerical data presented in Figures 4.5(a) and (b). We quantify the approximation in Eq. (4.18) by the relative error between the spectral gap γ_* and the minimum $\min_{1 \leq l \leq D} J_{ll}$ of the diagonal of \mathcal{J} ,

$$\delta\gamma_* = \frac{|\gamma_* - \min_{1 \leq l \leq D} J_{ll}|}{\gamma_*}. \quad (4.19)$$

Figure 4.5 shows $\langle \delta\gamma_* \rangle$ as a function of φ and D for the χ^2_2 distribution and the standard uniform distribution. The average relative error is at least two orders of magnitude smaller than the average spectral gap shown in Figure 4.4(b) and (e). For increasing D , the approximation in Eq. (4.18) improves. We conclude that the approximation in Eq. (4.18) works well in the case $\varphi \ll D$.

4.4.3 Extreme value theory

The distribution of the right-hand side of Eq. (4.18) can be tackled with EVT. As all non-zero entries of \mathcal{M} (edge weights) are iid distributed random variables, so are the diagonal entries of \mathcal{J} . Let the cumulative distribution function (CDF) of the diagonal entries J_{ll} of \mathcal{J} be denoted by F and its probability density function by $f(x) = \frac{d}{dx}F(x)$. If the edge weights are distributed according to a χ^2 distribution (or any gamma distribution) the CDF F of J_{ll} is a gamma distribution function; if the edge weights are uniformly distributed, F is an Irwin-Hall distribution function [296]. The expected value of $\min_{1 \leq l \leq D} J_{ll}$ is given in terms of F (and f) by

$$\left\langle \min_{1 \leq l \leq D} J_{ll} \right\rangle = D \int dx x f(x) (1 - F(x))^{D-1}. \quad (4.20)$$

Eq. (4.18) and Eq. (4.20) imply that

$$\langle \gamma_* \rangle \approx D \int dx x f(x) (1 - F(x))^{D-1}. \quad (4.21)$$

We demonstrate the validity of Eq. (4.21) with Figure 4.4(a), where the solid lines, given by Eq. (4.21), perfectly match numerically sampled average spectral gap $\langle \gamma_* \rangle$. In the remainder of this section, we will use EVT to approximate the integral in Eq. (4.21) by elementary functions of φ and D .

Power-law tail distributions

Let us consider first the case $\varphi = \text{const}$ and increasing D . By the Fisher-Tippet-Gnedenko or extreme value theorem [324], $\min_{1 \leq l \leq D} J_{ll}$ converges in law, under some mild assumptions on the distribution of J_{ll} and proper renormalization, to the Weibull distribution. The Weibull CDF is given by $\Psi_\beta(x) = e^{-x^\beta}$, where $\beta > 0$ and the support is on the positive real line.

The specifics of the convergence type are less critical for the outcomes of this chapter. Convergence in law, a weak form of convergence in probability theory, is often used in extreme value analysis. We will proceed under the assumption that moments of the distributions converge as well and concentrate on the asymptotic behavior of the integral in Eq. (4.21). Our approximations are supported by numerical results, which validate sufficient accuracy. While the details of the convergence type present a mathematical interest, they are not the focus here.

For distributions of J_{ll} with power-law left tail, the renormalization of $\min_{1 \leq l \leq D} J_{ll}$ for convergence to the Weibull distribution is well known, see e.g. Theorem 3.3.2, page 137 in Ref. [324]. We use a version modified to our case. Let a positive random variable X have CDF F with β -power left tail, i.e.

$$F(x) = Cx^\beta \quad \text{for } 0 \leq x \leq C^{1/\beta}, \quad (4.22)$$

where $C > 0$ is a constant. Further, let $m_D = \min_{1 \leq l \leq D} X_l$, where the X_l are iid copies of X . Then

$$(DC)^{1/\beta} m_D \rightarrow \Psi_\beta \quad \text{in law.} \quad (4.23)$$

The Irwin-Hall distribution has a left power-law tail given by $F(x) = \frac{x^\varphi}{\varphi!}$ for $0 \leq x \leq 1$. The constants for the Irwin-Hall distribution are listed in Table 4.1.

We assume that the convergence in Eq. (4.23) is not only in distribution but that the renormalized moments of m_D converge as well. If the convergence of the moments is sufficiently fast, then Eq. (4.23) together with Eq. (4.18) imply

$$\langle \gamma_* \rangle \approx \langle m_D \rangle \approx \Gamma \left(1 + \frac{1}{\varphi} \right) (\varphi!)^{1/\varphi} D^{-1/\varphi}, \quad (4.24)$$

off-diag. $\mathcal{K} = M_{ij}$	χ_k^2	uniform
diag. $\mathcal{K} = J_{ll}$	gamma($\frac{k\varphi}{2}, 2$)	Irwin-Hall
C	$\frac{2^\varphi}{\varphi!}^*$	$\frac{1}{\varphi!}$
β	$\frac{k}{2}\varphi^*$	φ

Table 4.1 The distributions of the off-diagonal elements M_{ij} of \mathcal{K} (edge weights) and the corresponding distributions of the diagonal elements J_{ll} of \mathcal{K} and the corresponding constants C and β for the convergence of J_{ll} to the Weibull distribution Ψ_β in Eq. (4.23). (*) constants obtained by a power-law approximation of the left tail of the gamma distribution.

whenever the weight distribution (distribution of non-zero off-diagonal elements of \mathcal{K}) is such that the diagonal of \mathcal{J} has a power-law left tail and the coefficients C and β are given by $C = 1/\varphi!$ and $\beta = \varphi$.

Finally, we consider the case that the weight distribution is uniform. We observe that the approximation in Eq. (4.24) works very well in this case. The solid lines in Figure 4.4(d) are given by the right-hand side of Eq. (4.24) and they match the numerically calculated average spectral gap.

Eq. (4.24) implies for $\varphi = \text{const}$ and increasing D that the average spectral gap decreases as

$$\langle \gamma_* \rangle \sim D^{-1/\varphi}. \quad (4.25)$$

In Figure 4.4(f) we show that the numerically retrieved power-law exponents of the average spectral gap, Figure 4.4(d), match the scaling in Eq. (4.25).

We find that the large deviation result is not only valid for constant φ and increasing D but also for φ increasing logarithmically with D ; see Figure 4.4(d). This allows us to estimate the crossover from decreasing to increasing spectral gap. Let c denote a constant and let $\langle \gamma_* \rangle = c$. Then by Eq. (4.24)

$$D \approx \left[\frac{\Gamma\left(1 + \frac{1}{\varphi}\right)}{c} \right]^\varphi \varphi!. \quad (4.26)$$

In Figure 4.4(e) the contour lines of constant average spectral gap c perfectly line up with the functional dependence of D on φ through Eq. (4.26) shown as white dots.

To find φ as a function of D such that the average spectral gap is constant, we assume that φ is reasonably large and approximate $\Gamma\left(1 + \frac{1}{\varphi}\right) \approx 1$ and by Stirling's

formula $(\varphi!)^{1/\varphi} \approx \frac{\varphi}{e}$. Denoting $y = \log \frac{\varphi}{ce}$ and rearranging Eq. (4.26) gives us

$$\frac{\log D}{ce} \approx ye^y, \quad (4.27)$$

which can be inverted by the Lambert W function. Resubstituting $\varphi = ce e^y$ we arrive at

$$\varphi \approx ce \cdot e^{W\left(\frac{\log D}{ce}\right)}, \quad (4.28)$$

which for $\log D \geq ce^2$ behaves as [325]

$$\varphi \approx \frac{\log D}{(\log \log D - \log c - 1)^{1-\eta(D)}}, \quad (4.29)$$

where $\eta(D) \rightarrow 0$ slowly, as $\eta(D) \sim (\log \log D)^{-1}$. So in the limit $1 \ll \varphi \ll D$ the crossover from decreasing to increasing spectral gap happens at $\varphi \sim \log D$ with corrections of the order $\log \log D$. This confirms our numerical observations that the average spectral gap $\langle \gamma_* \rangle$ appears to be constant for $\varphi \sim \log D$ in the range of matrix sizes D we considered.

Approximate power-law distributions

If the weight distribution is a χ^2 or exponential distribution, the diagonal elements of \mathcal{J} are distributed according to a Gamma distribution, see Table 4.1. The left tail of the Gamma distribution only follows approximately a power-law. Approximating the left tail by a Taylor expansion, we obtain constants C and β presented in Table 4.1. Especially, for the χ_2^2 distribution, the power-law approximation of the gamma distribution and the large deviation result in the previous subsection suggest that the average spectral gap $\langle \gamma_* \rangle$ decreases for constant φ and increasing D as a power in D with exponent given $-1/\varphi$.

In Figure 4.4(c), we present the numerically calculated exponents of the power-law decrease of $\langle \gamma_* \rangle$, for χ_2^2 weight distribution, with D and compare it to the prediction $-1/\varphi$. We find excellent agreement for small $\varphi \leq 5$. For larger φ the deviation between the numerical exponent and $-1/\varphi$ is visible, but the agreement is still good.

A quantitative comparison between the numerically calculated spectral gap $\langle \gamma_* \rangle$ and the EVT prediction by a power-law approximation of the left tail of the gamma distribution resulted in poor agreement. As the expected minimum value of the diagonal of \mathcal{J} perfectly agrees with $\langle \gamma_* \rangle$, we attribute the disagreement to the power-

law approximation of the left tail and slow convergence of Eq. (4.23) for diagonal elements of \mathcal{J} distributed according to the gamma distribution.

4.4.4 Summary

We presented numerical and analytical arguments that, for the weight distributions considered, the average spectral gap decreases as a power-law for constant φ and increasing D with exponent given (approximately) by $-1/\varphi$. The crossover between decreasing and increasing spectral gap happens at $\varphi \sim \log D$, with $\log \log D$ corrections, for uniform weight distribution. For χ_2^2 distributed edge weights the crossover was observed at $\varphi \sim \log D$. If φ increases with D faster than $\log D$ then the average spectral gap increases.

The presented results generalize. Let us assume that the spectral gap is well approximated by the smallest diagonal element of \mathcal{J} , at least in the regime of large D and $\varphi \ll D$. Then the distribution of the spectral gap is given by the limiting extreme value distribution of the diagonal elements of \mathcal{J} . Consequently, the classification of functional dependencies of the spectral gap on φ and D with respect to weight distributions reduces to the classification of extreme value distributions. Extensive research has been conducted in this field [326, 324]. Therefore, the presented approach allows the calculation of the distribution of the spectral gap for broad classes of weight distributions.

4.5 Complex spacing ratios

So far we considered the marginal distribution of eigenvalues of sparse random generator matrices. But correlations between the eigenvalues are also of interest.

In Section 1.1.3 of the introduction, we presented the complex spacing ratio r (CSR) distribution as a measure of eigenvalue correlations. As discussed there, uncorrelated eigenvalues λ have uniform CSR density, while eigenvalues of random matrices typically have a CSR density, which vanishes at $r = 0$ and $r = 1$. The random generators considered in this chapter have real entries, so they should be compared to real Ginibre matrices (GinOE).

In Figure 4.6, we show the CSR densities of (a) GinOE members (with Gaussian entries) and (b-d) sparse random generators with χ_2^2 distributed edge weights and $\varphi = 1, 2, 3$. The densities are estimated from 100 samples for $D = 10,000$. We also checked that the obtained densities are independent of the weight distribution. As

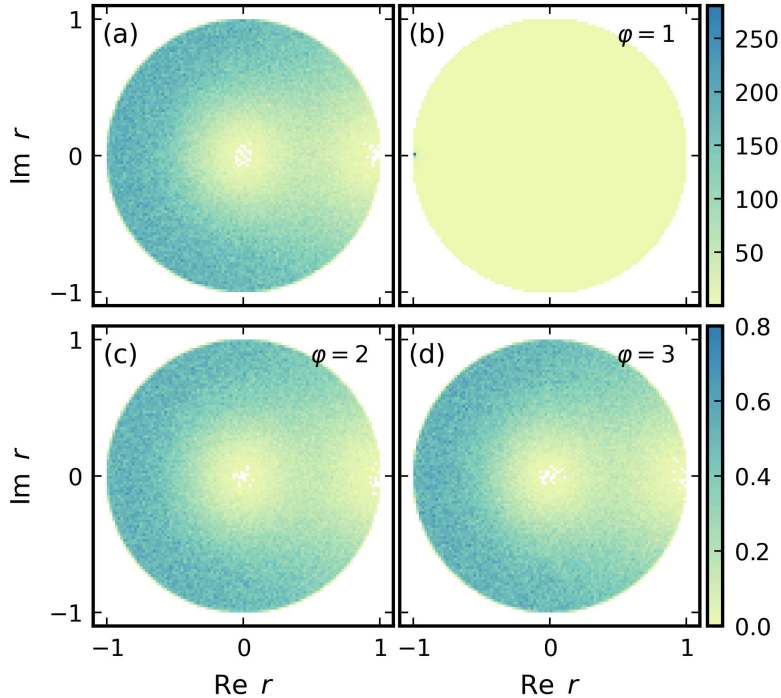


Fig. 4.6 Density of complex spacing ratios (CSRs) r for (a) GinOE and (b-d) sparse Kolmogorov operators with $\varphi = 1, 2, 3$. The number of states $D = 10,000$ and densities are obtained from 100 samples. Edge weights are distributed according to the χ^2 distribution. The color range is from 0 to 0.8 in (a), (c), and (d) and from 0 to 260 in (b).

suggested in Ref. [52], we avoid eigenvalues close to the real line (by excluding all eigenvalues from the strip $\text{Im } \lambda < 10^{-14}$) when sampling CSR densities.

The CSR density of GinOE matrices shown in Figure 4.6(a) exhibits typical depletion at $r = 0$ and $r = 1$, similar to the CSRs of the GinUE presented in Figure 1.5(a) in Section 1.1.3. In Ref. [260], it was shown that the CSR density obtained for dense random Kolmogorov operators agrees well with the distribution shown in Figure 4.6(a). The CSR density of sparse generators with sparsity $\varphi \geq 2$ (c,d) agrees remarkably well with the GinOE case.

The CSR density for $\varphi = 1$ is anomalous, as observed in Figure 4.6(b). It has an extremely high density around $r = -1$ while being nearly flat on the rest of the unit disk. This anomalous CSR density is a consequence of the graph of Kolmogorov operators with $\varphi = 1$ fragmenting into a set of disjoint (distorted) cycle graphs. The spectra of each of these fragments are approximately arranged on (distorted) circles, as observed in Figure 4.7. Consequently, the CSRs of the fragments are likely close to

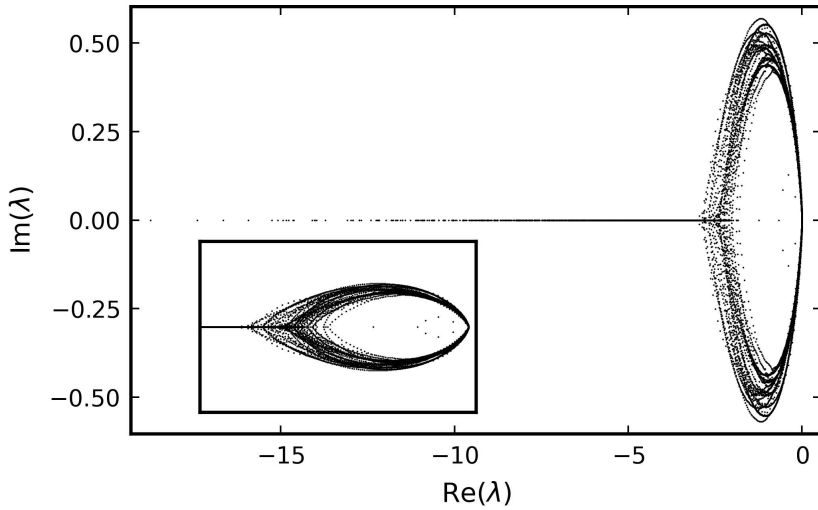


Fig. 4.7 Spectrum of a random Kolmogorov operator with $\varphi = 1$ and χ^2_2 weight distribution. The matrix size is $D = 1,000$. Inset: same data plotted with both axes having the same scale.

	GinOE	$\varphi = 1$	$\varphi = 2$	$\varphi = 3$
$-\langle \cos \theta \rangle$	0.7379	0.7871	0.7359	0.7372
$\langle r \rangle$	0.2347	0.3516	0.2225	0.2284

Table 4.2 Mean and angle of spacing ratio distributions obtained with 100 samples of random $D \times D$ -matrices with $D = 10,000$ rounded to the 4th digit. The matrix ensembles correspond to the ones shown in Figure 4.6.

$r = -1$. The independence of the fragments implies the flatness of the CSR density away from $r = -1$, akin to the CSRs of independent random variables.

To quantify the difference between CSR distributions, we use the average length $\langle |r| \rangle$ and the average cosine of the angle $-\langle \cos \theta \rangle$ of spacing ratios, where $\langle \dots \rangle$ again denotes the average over the random matrix ensemble [52]. We numerically estimate $\langle |r| \rangle_{\text{GinOE}} \approx 0.7379$ and $-\langle \cos \theta \rangle_{\text{GinOE}} \approx 0.2347$ for 100 $D \times D$ -matrices with $D = 10,000$. These agree well with $\langle |r| \rangle$ and $-\langle \cos \theta \rangle$ for $\varphi = 2$ and $\varphi = 3$, as shown in Table 4.2. We found similar results for $\varphi > 3$ (not shown). In contrast, the corresponding quantities for $\varphi = 1$ deviate substantially from $\langle |r| \rangle_{\text{GinOE}}$ and $-\langle \cos \theta \rangle_{\text{GinOE}}$, as also shown in Table 4.2. We conclude that, for $\varphi \geq 2$, correlations between eigenvalues of sparse random Kolmogorov operators agree with correlations of eigenvalues of GinOE matrices.

4.6 Discussion

Summary of results

Motivated by the inability of dense random Kolmogorov operators to reasonably model the spectral gap of physical Markov processes we introduced and analyzed an ensemble of sparse random Kolmogorov operators. We showed that, if the number of non-zero elements per column (and row) φ increases with the matrix size D , the bulk of the spectrum is shifted away from the stationary eigenvalue 0 in the limit of large matrix size D . This is independent of the weight distribution, i.e. of the distribution of the non-zero matrix elements.

In contrast, the spectral gap depends on the tails of the weight distribution. These tails determine, together with φ , the tails of the diagonal elements of generator matrices. We numerically showed that the spectral gap is well approximated by the minimum of the diagonal elements. From extreme value theory it follows that for diagonal distributions with power-law left tails (this includes among others edge weights being uniform, exponential, χ^2 , gamma or beta distributed), the average spectral gap decreases as a power-law in D for fixed φ , is constant for $\varphi \sim \log D$ and increases, whenever φ increases with D substantially faster than $\log D$.

Additionally, we showed that CSR distributions of generator matrices with $\varphi \geq 2$ follow the distribution typical of the GinOE, while there is a strong anomaly for $\varphi = 1$.

Open questions

(1) We have introduced sparsity to model \mathcal{K} -generators of physical Markov processes, and have used the sparsity to tune spectral features of the generators. There are other ways of providing random matrices with a structure that models physical constraints (e.g., locality). For example, one could consider banded matrices [32–35, 38–41, 59, 42] or matrices with decaying off-diagonal terms [36, 37, 59] or temperature based models [327]. These are alternate routes to tuning spectral features. To the best of our knowledge, generators of continuous-time Markov processes with such structures have not yet been considered.

(2) The application of extreme value theory to find the limiting distribution of the spectral gap relied on the observation that the spectral gap is well approximated by the minimum of the diagonal of the generator matrix. For symmetric generators, the Courant-Fisher theorem implies that the extremes of the diagonal are upper and lower bounds for the gap and the largest eigenvalue in magnitude, respectively. In this case, a concentration of the largest eigenvalue in magnitude around the maximum of

the diagonal was shown in [323]. An analytical treatment of general non-symmetric generators and the spectral gap is to the best of our knowledge not known. We hope that our results motivate a rigorous investigation of the connection between the spectral gap and the diagonal of the generator matrix.

(3) Kolmogorov generators have real entries and thus their eigenvalues are real or come in complex conjugate pairs. In the investigation of correlations between eigenvalues, we left out real eigenvalues. The appearance of a large number of real eigenvalues in the spectrum of non-Hermitian matrices is a phenomenon of wide interest [22, 328–332, 294, 333, 53, 334, 335]. For real Ginibre matrices, the average number of real eigenvalues is $\sim D^{-1/2}$ [328–330] while for dense generators, it is substantially larger [294]. We observed that the fraction of real eigenvalues is larger for small φ and smaller for larger φ (not presented). Understanding of the functional dependence of the number of real eigenvalues for sparse generators is an interesting problem.

(4) We focused on the location and extent of the bulk spectrum as well as the spectral gap. One could inquire about other features of the spectral distribution as a function of sparsity, e.g., about the envelope of the spectral distribution. Following Ref. [260], the spectral density of dense random Kolmogorov operators emerges as convolution of an asymptotically free matrix and a diagonal Gaussian matrix. This lead to the prominent spindle shape of the spectral boundary. Free probability arguments break down for sparse random Kolmogorov generators. Analytical tools which have been employed to calculate the spectral density of sparse, random matrices include replica tricks [336–340], single defect and effective medium approximations [341–343], supersymmetry-based techniques [30, 344] and the cavity approach [345–347, 340]. Spectral properties of symmetric, sparse, random Kolmogorov generators have been investigated with the cavity method [348–350] and with supersymmetric approaches [344]. Investigations of the spectral density of non-symmetric sparse, random Kolmogorov operators with the above methods might be an interesting objective.

(5) In this chapter, we have considered sparse generators based on strongly connected, sparse random graphs. It is an open question whether our results can be generalized to other sparse graph ensembles. One potential avenue to explore are directed Erdős-Rényi (dER) graphs. In dER graphs, the probability of an edge connecting any two vertices is $0 < p \leq 1$. For a dER graph to be strongly connected with a high probability, the value of p must exceed $\sim \log D/D$ [351, 352]. As a result, the average degree of the vertices must increase logarithmically with D to ensure strong connectivity. Consequently, the range of constant average vertex degree and increasing vertex number D is excluded. Nonetheless, modifying the dER graph by enforcing a minimum (in- and out-) degree

≥ 2 guarantees strong connectivity with high probability [320]. Exploring the spectral properties of Kolmogorov generators based on dER graphs may represent a promising next step towards generalizing our results.

4.7 Appendix

4.7.1 Analytical results for the bulk spectrum

In this section, we will derive the analytical results of the estimated mean $\mu(\lambda)$ in Eq. (4.3) and the estimated pseudo-variance in Eq. (4.7) in the main text of this chapter and show that $\frac{1}{D} \sum_{j=1}^D \lambda_j$ concentrates around its average $\langle \dots \rangle$.

We denote by ι the function $\iota : \{1, \dots, \varphi\} \times \{1, \dots, D\} \rightarrow \{1, \dots, D\}^2$ with $\iota(l, j) = (i, j)$ where i is the l th non-zero index in column j in \mathcal{M} . Note that $\iota(l, j) = (i, j)$ implies $i \neq j$ and $l \rightarrow \iota(l, j)$ is injective for fixed j . Further, let in this appendix the location of the bulk be denoted as

$$\mu(\lambda) = \frac{1}{D} \sum_{j=1}^D \lambda_j = \frac{1}{D} \text{tr}(\mathcal{K})$$

and the pseudo-variance as

$$\sigma^2(\lambda) = \frac{1}{D} \sum_{j=1}^D \lambda_j^2 - \left(\frac{1}{D} \sum_{j=1}^D \lambda_j \right)^2 = \frac{\text{tr}(\mathcal{K}^2)}{D} - \frac{\text{tr}(\mathcal{K})^2}{D^2}. \quad (4.30)$$

Here we explicitly do not include the averaging over the random matrix ensemble $\langle \dots \rangle$ in contrast to the main text.

Location

The average value with respect to $\langle \dots \rangle$ of the location $\mu(\lambda)$ can then be computed as

$$\langle \mu(\lambda) \rangle = \left\langle \frac{1}{D} \text{tr}(\mathcal{K}) \right\rangle = \frac{1}{D} \sum_{j=1}^D \langle K_{jj} \rangle = \frac{1}{D} \sum_{j=1}^D \sum_{l=1}^{\varphi} \langle K_{\iota(l, j)} \rangle = -\varphi \mu_0,$$

where we used that $\langle K_{\iota(l,j)} \rangle = -\mu_0$. This is Eq. (4.3) in the main text. Similarly, it holds that

$$\begin{aligned} \langle \text{tr}(\mathcal{K})^2 \rangle &= \sum_{j_1, j_2=1}^D \sum_{l_1, l_2=1}^{\varphi} \langle K_{\iota(l_1, j_1)} K_{\iota(l_2, j_2)} \rangle \\ &= \sum_{j=1}^D \left[\sum_{l=1}^{\varphi} \langle K_{\iota(l, j)}^2 \rangle + \sum_{l_1 \neq l_2} \langle K_{\iota(l_1, j)} K_{\iota(l_2, j)} \rangle \right] + \sum_{j_1 \neq j_2} \sum_{l_1, l_2=1}^{\varphi} \langle K_{\iota(l_1, j_1)} K_{\iota(l_2, j_2)} \rangle. \end{aligned}$$

Although the off-diagonal elements of \mathcal{K} are weakly dependent because of the constraint that the number of non-zero elements per row and column has to equal φ , the non-zero elements $K_{\iota(l,j)}$ are independent. Hence, $\langle K_{\iota(l_1, j)} K_{\iota(l_2, j)} \rangle = \langle K_{\iota(l_1, j)} \rangle \langle K_{\iota(l_2, j)} \rangle$ and $\langle K_{\iota(l_1, j_1)} \rangle \langle K_{\iota(l_2, j_2)} \rangle$, so

$$\begin{aligned} \langle \text{tr}(\mathcal{K})^2 \rangle &= D\varphi(\sigma_0^2 + \mu_0^2) + D\varphi(\varphi - 1)\mu_0^2 + D(D - 1)\varphi^2\mu_0^2 \\ &= D\varphi\sigma_0^2 + (D\varphi\mu_0)^2, \end{aligned}$$

where we used that the second moment $\langle K_{\iota(l,j)}^2 \rangle$ equals $\sigma_0^2 + \mu_0^2$. This implies that

$$\langle \mu(\lambda)^2 \rangle - \langle \mu(\lambda) \rangle^2 = \left\langle \frac{\text{tr}(\mathcal{K})^2}{D^2} \right\rangle - \left\langle \frac{\text{tr}(\mathcal{K})}{D} \right\rangle^2 = \frac{\varphi\sigma_0^2}{D}.$$

The right-hand side vanishes for increasing D and φ growing slower with D than linearly. Relatively to $\langle \mu(\lambda) \rangle$ the typical deviation of $\mu(\lambda)$ from its average value always vanishes for either increasing D or φ , as

$$\frac{\sqrt{\langle \mu(\lambda)^2 \rangle - \langle \mu \rangle^2}}{|\langle \mu(\lambda) \rangle|} = \frac{\sigma_0}{\mu_0} (\varphi D)^{-1/2}.$$

Complex pseudo-variance

The first term in the averaged pseudo-variance given by Eq. (4.30) can be calculated as

$$\langle \text{tr}(\mathcal{K}^2) \rangle = \sum_{i,j=1}^D \langle K_{ij} K_{ji} \rangle = \sum_{i=1}^D \langle K_{ii}^2 \rangle + \sum_{i \neq j} \langle K_{ij} K_{ji} \rangle. \quad (4.31)$$

We proceed with $\sum_{i=1}^D \langle K_{ii}^2 \rangle$ in Eq. (4.31) and get

$$\begin{aligned} \sum_{i=1}^D \langle K_{ii}^2 \rangle &= \sum_{i=1}^D \left\langle \left(- \sum_{j \neq i} K_{ji} \right)^2 \right\rangle = \sum_{i=1}^D \sum_{j,l \neq i} \langle K_{ji} K_{li} \rangle \\ &= \sum_{i=1}^D \sum_{j \neq i} \langle K_{ji}^2 \rangle + \sum_{i=1}^D \sum_{j,l \neq i; j \neq l} \langle K_{ji} \rangle \langle K_{li} \rangle. \end{aligned} \quad (4.32)$$

The former sum in Eq. (4.32) is given by

$$\sum_{i=1}^D \sum_{j \neq i} \langle K_{ji}^2 \rangle = \sum_{i=1}^D \sum_{l=1}^{\varphi} \langle K_{\iota(l,i)}^2 \rangle = D\varphi(\sigma_0^2 + \mu_0^2), \quad (4.33)$$

where we used that $\langle K_{\iota(l,i)}^2 \rangle = \sigma_0^2 + \mu_0^2$. The latter sum in Eq. (4.32) is

$$\sum_{i=1}^D \sum_{j,l \neq i; j \neq l} \langle K_{ji} \rangle \langle K_{li} \rangle = \sum_{i=1}^D \sum_{k=1}^{\varphi} \sum_{n=1; \iota(n,i) \neq \iota(k,i)}^{\varphi} \langle K_{\iota(k,i)} \rangle \langle K_{\iota(n,i)} \rangle = D\varphi(\varphi-1)\mu_0^2. \quad (4.34)$$

Combining Eq. (4.33) and Eq. (4.34) we get

$$\sum_{i=1}^D \langle K_{ii}^2 \rangle = D\varphi(\sigma_0^2 + \mu_0^2) + D\varphi(\varphi-1)\mu_0^2 = D\varphi\sigma_0^2 + D\varphi^2\mu_0^2.$$

Now, we are left with calculating $\sum_{i \neq j} \langle K_{ij} K_{ji} \rangle$, the second term in Eq. (4.31),

$$\sum_{i \neq j} \langle K_{ij} K_{ji} \rangle = \sum_{i=1}^D \sum_{l=1}^{\varphi} \left\langle K_{\iota(\bar{l},i)} M_{\iota(l,i)} \right\rangle,$$

where \bar{l} denotes swapping the first and second component, $\bar{l}(l,i) = \iota(i,l)$. Note that $K_{\iota(\bar{l},i)}$ is not necessarily a non-zero entry of \mathcal{K} , hence $K_{\iota(\bar{l},i)}$ and $K_{\iota(l,i)}$ depend weakly on each other. In the large D limit, we can assume that the dependence is sufficiently weak and we treat $K_{\iota(\bar{l},i)}$ and $K_{\iota(l,i)}$ as independent, thus $\langle K_{\iota(\bar{l},i)} K_{\iota(l,i)} \rangle = \mu_0 \langle K_{\iota(\bar{l},i)} \rangle$. By the assumed independence the mean of *every* entry in the i th row, except the diagonal, is $\langle K_{\iota(\bar{l},i)} \rangle = \frac{\varphi}{D}\mu_0$. Hence,

$$\sum_{i \neq j} \langle K_{ij} K_{ji} \rangle = \sum_{i=1}^D \frac{1}{D} \varphi^2 \mu_0^2 = \varphi^2 \mu_0^2.$$

Collecting the above results we arrive at

$$\langle \text{tr}(\mathcal{K}^2) \rangle = D\varphi\sigma_0^2 + D\varphi^2\mu_0^2 + \varphi^2\mu_0^2 = D\varphi\sigma_0^2 + (D+1)\varphi^2\mu_0^2.$$

The second term of the averaged pseudo-variance in Eq. (4.30) is

$$\langle \text{tr}(\mathcal{K})^2 \rangle = D\varphi\sigma_0^2 + (D\varphi\mu_0)^2.$$

Finally, we can evaluate

$$\begin{aligned} \langle \sigma^2(\lambda) \rangle &= \left\langle \frac{\text{tr}(\mathcal{K}^2)}{D} \right\rangle - \left\langle \frac{\text{tr}(\mathcal{K})^2}{D^2} \right\rangle = \varphi\sigma_0^2 + \varphi^2\mu_0^2 + \frac{1}{D}\varphi^2\mu_0^2 - \frac{1}{D}\varphi\sigma_0^2 - \varphi^2\mu_0^2 \\ &= \varphi \left(\sigma_0^2 + \frac{\varphi}{D}\mu_0^2 - \frac{1}{D}\sigma_0^2 \right), \end{aligned}$$

which is Eq. (4.7) in the main text.

4.7.2 Bound of the spectral gap for symmetric generators

In this section, we present the proof of Eq. (4.15). Let $\mathcal{K} = \mathcal{M} - \mathcal{J}$ be a symmetric generator matrix. According to Eq. (4.13), we have to show that $v^t(-\mathcal{K})v \leq \left(1 + \frac{1}{D-1}\right) \min_{1 \leq l \leq D} J_{ll}$ for the vector v defined as

$$v_i = \begin{cases} \sqrt{1 - \frac{1}{D}} & i = l \\ -\frac{1}{\sqrt{D(D-1)}} & i \neq l, \end{cases}$$

where $1 \leq l \leq D$ is arbitrary. Let us fix any $1 \leq l \leq D$. It is easy to see that $|v|^2 = 1$ and v is orthogonal to $\mathbb{1} = (1, \dots, 1)^t$. So we proceed with

$$\begin{aligned} \gamma_* &\leq v^t(\mathcal{J} - \mathcal{M})v = \sum_{i,j=1}^D v_i v_j (\mathcal{J} - \mathcal{M})_{ij} = \sum_{i=1}^D v_j^2 J_{jj} - \sum_{i,j=1}^D v_i v_j M_{ij} \\ &= \sum_{i,j=1}^D v_j^2 M_{ij} - \sum_{i,j=1}^D v_i v_j M_{ij} = \sum_{i,j=1}^D v_j M_{ij} (v_j - v_i). \end{aligned} \quad (4.35)$$

Note that any summand in Eq. (4.35) where either $i = j$ or $i \neq l$ and $j \neq l$ is zero. Therefore, by using the symmetry of \mathcal{M} and the definition of v we get

$$\begin{aligned}\gamma_* &\leq \sum_{i \neq l} v_l M_{il} (v_l - v_i) + \sum_{j \neq l} v_j M_{lj} (v_j - v_l) = \sum_{i \neq l} M_{il} [v_l (v_l - v_i) + v_i (v_i - v_l)] \\ &= \sum_{i \neq l} M_{il} (v_i - v_l)^2 = \left(1 + \frac{1}{D-1}\right) \sum_{i \neq l} M_{il} = \left(1 + \frac{1}{D-1}\right) J_{ll}.\end{aligned}\quad (4.36)$$

Since the index l was chosen arbitrarily, we get

$$\gamma_* \leq \left(1 + \frac{1}{D-1}\right) \min_{1 \leq l \leq D} J_{ll},$$

which is Eq. (4.15) in the main text.

4.7.3 Stochastic systems presented in Figure 4.1

In this section we present physical Markov processes, whose generator spectra have been depicted in Figure 4.1.

Modified TASEP

Figure 4.1(b) illustrates an adapted version of the TASEP on a ring, consisting of $L = 12$ sites with alternating hopping amplitudes. The matrix \mathcal{M} can be expressed as [52]

$$\mathcal{M} = \frac{1}{2} \sigma_1^+ + \frac{1}{2} \sigma_1^- + \sum_{j=1}^L p_j \sigma_j^- \sigma_{j+1}^+, \quad (4.37)$$

where the hopping amplitude p_j is assigned a value of 1 for even indices j and 0.2 for odd indices. Contrasting with the ASEP presented in Section 1.3.2, which was Bethe-integrable, this particular version of TASEP is non-integrable.

Single particle system

The random hopping of a single particle on a two-dimensional lattice constitutes a CTMC. The corresponding \mathcal{M} matrix for this process can be expressed as

$$\mathcal{M} = \sum_{\langle (i,j), (i',j') \rangle} p_{(i,j) \rightarrow (i',j')} \sigma_{i,j}^- \sigma_{i',j'}^+, \quad (4.38)$$

where $\langle \dots \rangle$ indicates a summation over nearest neighbors. The spin-up state represents the particle present, while a spin-down state indicates absence of any particle. The

transition probabilities $p_{(i,j) \rightarrow (i',j')}$ from site (i,j) to site (i',j') are chosen randomly within the range of 0 to 1, subject to the constraint $p_{(i,j) \rightarrow (i',j')} = 1 - p_{(i',j') \rightarrow (i,j)}$.

Figure 4.1(d) illustrates the spectrum of a single particle moving on a 65×65 grid with pbc and uniformly random hopping amplitudes. While the model in Eq. (4.38) can be extended to multiple particles, we present the single-particle sector.

Contact Process

The contact process [247, 220, 255] is another fundamental model in the study of non-equilibrium statistical mechanics, particularly in the context of phase transitions and critical phenomena [353–355]. Originating from the field of interacting particle systems, it serves as a prototypical example for understanding the dynamics of spreading phenomena, such as infection spread in epidemiology or growth of bacterial colonies [356–358].

At its core, the contact process is a stochastic model defined on a lattice where each site can be in one of two states: active (infected) or inactive (healthy). The dynamics are governed by two primary processes: the spontaneous recovery of an active site to an inactive state, and the infection of neighboring inactive sites by an active site.

The matrix \mathcal{M} for the contact process, characterized by a recovery rate μ and an infection rate λ , can be represented as

$$\mathcal{M} = -\mu \sum_i \sigma_i^- - \lambda \sum_{\langle i,j \rangle} n_i \sigma_j^+, \quad (4.39)$$

where n_i signifies the spin-up state ($n_i = 1$) or spin-down state ($n_i = 0$) at site i . The first term models the recovery process at infected sites, while the second term, summing over adjacent site pairs $\langle i,j \rangle$, accounts for the infection of inactive sites.

In Figure 4.1(e), we show the spectrum of a contact process on a one-dimensional chain with $L = 12$ sites and obc as well as $\mu = \lambda = 1$.

Gene transcription model

Finally, in Figure 4.1(f) we show the spectrum of the generator matrix \mathcal{K} of a gene transcription model taken from [239]. The following master equations model the accumulation and release of mechanical strain of DNA during transcription. The parameters chosen are the mRNA transcription rate $r = 2$ and decay rate $\lambda = 0.05$, the maximum number of transcripts until no further strain can be put on the DNA $m_c = 10$, the relaxation rate of the DNA string $g = 0.05$ and a maximum number of

transcription events $m_{\max} = 400$ to make the generator matrix M finite. By m we denote the number of current transcripts and by α the number of transcripts made since the last relaxation event. Then for $0 \leq m \leq m_{\max}$ and $1 \leq \alpha \leq m_c - 1$ the master equation reads

$$\frac{d}{dt}P_\alpha = -(r + g + \lambda m)P_\alpha(m, t) + \lambda(m + 1)P_\alpha(m + 1, t) + rP_{\alpha-1}(m - 1, t) \quad (4.40)$$

while for $\alpha = 0$ we have

$$\frac{d}{dt}P_0 = -(r + g + \lambda m)P_0(m, t) + \lambda(m + 1)P_0(m + 1, t) + g \sum_{\alpha=0}^{m_c} P_\alpha(m, t) \quad (4.41)$$

and for $\alpha = m_c$

$$\frac{d}{dt}P_{m_c} = -(g + \lambda m)P_{m_c}(m, t) + \lambda(m + 1)P_{m_c}(m + 1, t) + rP_{m_c-1}(m - 1, t). \quad (4.42)$$

These dynamical equations are collected into a Kolmogorov generator \mathcal{K} such that $\frac{d}{dt}P(t) = \mathcal{K}P(t)$ with $P = (P_0(0, t), \dots, P_0(m, t), P_1(0, t), \dots, P_{m_c}(m, t))$. The corresponding spectrum is presented in Figure 4.1(f).

Chapter 5

The spectral boundary of the ASEP

The content of this chapter has appeared as part of [302]:

G. Nakerst, T. Prosen, and M. Haque, The spectral boundary of the Asymmetric Simple Exclusion Process (ASEP) – free fermions, Bethe ansatz and random matrix theory (2024), arXiv:2402.00662.

In this chapter, we investigate the spectrum of the ASEP with focus on the spectral boundary. This boundary is characterized by pronounced spikes: L spikes for pbc and $L + 1$ spikes for obc. We analyze the emergence of the spikes in the spectral boundary from several points of view.

We start in Section 5.1 by rewriting the generator matrices of ASEP, formulated in terms of spin-1/2 operators in Section 1.3.2, as interacting fermions. The presence of single Pauli matrices in the obc generator makes this a nontrivial task. The emergence of spikes in the spectral boundary is then elucidated in three ways. First, in Sections 5.2 and 5.3, we present results of the non-interacting ASEP with pbc and obc, respectively. In these cases, the spikes in the spectral boundary emerge since many-body eigenvalues are sums of circular/elliptic single-body eigenvalues. We analytically derive a parametrization of the spectral boundary of the non-interacting ASEP. This parametrization is similar to the hypotrochoidic curve enclosing non-Hermitian random matrices with correlated entries, presented in Section 1.1.2. Second, in Section 5.4, we reintroduce the interactions and study the TASEP with pbc using the coordinate Bethe ansatz. In this case, many-body eigenvalues are sums of Bethe roots. We demonstrate a sufficient clustering of Bethe roots, which in turn leads to a spiky spectral boundary. Third, in Section 5.5, we compare the TASEP to random graphs. These graphs are similar to the graphs in Section 1.1.2, which followed the hypotrochoidic law. In the graphs resembling the TASEP, all cycle lengths are integer multiples of L ($L + 1$ for

obc). We show that the spectral boundaries of the corresponding adjacency matrices and Laplacians have an identical number of pronounced spikes, similar to the TASEP. In Section 5.6, we provide a summary and present open questions.

5.1 The generator as interacting fermions

In this chapter, we investigate the spectrum of Kolmogorov generators of the ASEP. As discussed in Section 1.3.1 of the introduction, every Kolmogorov generator \mathcal{K} can be expressed as

$$\mathcal{K} = \mathcal{M} - \mathcal{J}, \quad (5.1)$$

where \mathcal{M} is a matrix with zero diagonal entries and \mathcal{J} is a diagonal matrix, containing the column sums of \mathcal{M} as diagonal elements. One way to gain insight into the spectrum of \mathcal{K} is to study the spectrum of \mathcal{M} . An advantage of studying \mathcal{M} is that, in the case of ASEP, we can obtain its spectrum analytically. To extend results of \mathcal{M} to \mathcal{K} , we generalize Eq. (5.1) to

$$\mathcal{K} = \mathcal{M} - U\mathcal{J}, \quad (5.2)$$

with $0 \leq U \leq 1$. The generator in Eq. (5.1) is recovered for $U = 1$. We note that for general $U \neq 1$, the matrix \mathcal{K} is not a generator of a CTMC, as its column sums are non-zero. For ASEP, \mathcal{J} can be expressed as a 4-point (2-body) fermion interaction. Therefore, we refer to U as “interaction strength”.

In the remainder of this section, we express \mathcal{M} in terms of fermions and present spectra of \mathcal{M} and \mathcal{K} .

5.1.1 Periodic boundary conditions (pbc)

In Section 1.3.2, we showed that the matrices \mathcal{M} and \mathcal{J} for pbc can be expressed in terms of Pauli spin-1/2 matrices as

$$\mathcal{M} = \sum_{j=1}^L \left(p\sigma_{j+1}^+ \sigma_j^- + q\sigma_j^+ \sigma_{j+1}^- \right), \quad (5.3)$$

$$\mathcal{J} = -\frac{1}{4} \sum_{j=1}^L \left(\sigma_j^z \sigma_{j+1}^z - 1 \right). \quad (5.4)$$

The matrices \mathcal{M} and \mathcal{J} (and so \mathcal{K}) can be written in terms of spinless fermions by a Jordan-Wigner transformation

$$c_j = \left(\prod_{l=1}^{j-1} (-\sigma_l^z) \right) \sigma_j^-, \quad c_j^\dagger = \left(\prod_{l=1}^{j-1} (-\sigma_l^z) \right) \sigma_j^+, \quad (5.5)$$

where c_j and c_j^\dagger are fermionic annihilation and creation operators, respectively. In terms of these fermionic operators, \mathcal{M} and \mathcal{J} are given by

$$\mathcal{M} = \sum_{j=1}^{L-1} (pc_{j+1}^\dagger c_j + qc_j^\dagger c_{j+1}) + (-1)^{N+1} (pc_1^\dagger c_L + qc_L^\dagger c_1), \quad (5.6)$$

$$\mathcal{J} = - \sum_{j=1}^L c_j^\dagger c_j c_{j+1}^\dagger c_{j+1} + N. \quad (5.7)$$

Therefore, \mathcal{M} represents non-Hermitian free fermions with a possible, N -dependent, twist in the boundary conditions, while \mathcal{J} denotes a quartic fermion interaction.

5.1.2 Open boundary conditions (obc)

In the case of obc, it was shown in Section 1.3.2 that the matrix \mathcal{M} can be expressed as

$$\mathcal{M} = \sum_{j=1}^{L-1} (p\sigma_{j+1}^+ \sigma_j^- + q\sigma_j^+ \sigma_{j+1}^-) + \alpha\sigma_1^+ + \gamma\sigma_1^- + \beta\sigma_L^- + \delta\sigma_L^+, \quad (5.8)$$

and the diagonal \mathcal{J} as

$$\begin{aligned} \mathcal{J} = & -\frac{1}{4} \sum_{j=1}^{L-1} (\sigma_j^z \sigma_{j+1}^z - 1) - \frac{1}{2} \left[\left(\frac{p-q}{2} - \alpha + \gamma \right) \sigma_1^z + \left(\frac{q-p}{2} - \delta + \beta \right) \sigma_L^z \right] \\ & + \frac{1}{2} [\alpha + \beta + \gamma + \delta]. \end{aligned} \quad (5.9)$$

Similar to the pbc case, \mathcal{M} and \mathcal{J} can be reformulated in terms of fermions, where \mathcal{M} is non-Hermitian and quadratic in these fermions, while the diagonal \mathcal{J} contains terms, which are quartic in fermions. In the following, we will express \mathcal{M} in terms of fermions. A similar approach is applicable to \mathcal{J} .

The single spin operators at the end of the chain on site 1 and L hinder a straightforward application of a Jordan-Wigner transformation. Instead, we will treat the reservoirs as an additional site. For this, we enlarge the chain of length L by adding a site $L+1$. The matrix \mathcal{M} in terms of σ -operators acts trivially on this site. Consequently, the multiplicity of every eigenvalue of \mathcal{M} acting on $L+1$ sites is doubled

compared to \mathcal{M} acting on the original L -site chain. The incorporation of an additional site allows us to apply the Kramers-Wannier duality transformation [359]

$$\sigma_j^x \rightarrow \prod_{l=1}^j \sigma_l^z, \quad \sigma_j^y \rightarrow - \left(\prod_{l=1}^{j-1} \sigma_l^z \right) \sigma_j^y \sigma_{j+1}^x, \quad \sigma_j^z \rightarrow \sigma_j^x \sigma_{j+1}^x. \quad (5.10)$$

Application of this transformation to \mathcal{M} , followed by the Jordan-Wigner transformation

$$w_j = \left(\prod_{l=1}^{j-1} (-\sigma_l^z) \right) \sigma_j^-, \quad w_j^\dagger = \left(\prod_{l=1}^{j-1} (-\sigma_l^z) \right) \sigma_j^+, \quad (5.11)$$

and rewriting in terms of Majorana “real” and “imaginary” parts of the Dirac fermions w, w^\dagger ,

$$\gamma_{j,1} = w_j^\dagger + w_j, \quad \gamma_{j,2} = i(w_j^\dagger - w_j), \quad (5.12)$$

implies that \mathcal{M} in terms of the Majorana γ -fermions is given by

$$\begin{aligned} \mathcal{M} = & \sum_{j=1}^{L-1} \left[\frac{p+q}{4} (i\gamma_{j+1,1}\gamma_{j+1,2} - i\gamma_{j,2}\gamma_{j+2,1}) + \frac{p-q}{4} (\gamma_{j+1,1}\gamma_{j+2,1} + \gamma_{j,2}\gamma_{j+1,2}) \right] \\ & + \frac{1}{2} [(\alpha + \gamma)i\gamma_{1,1}\gamma_{1,2} + (\alpha - \gamma)\gamma_{1,1}\gamma_{2,1}] \\ & + \frac{1}{2} \left(\prod_{j=1}^{L+1} i\gamma_{j,1}\gamma_{j,2} \right) [(\delta + \beta)i\gamma_{L+1,1}\gamma_{L+1,2} - (\delta - \beta)\gamma_{L,2}\gamma_{L+1,2}]. \end{aligned} \quad (5.13)$$

The string of Majoranas, $\prod_{j=1}^{L+1} (i\gamma_{j,1}\gamma_{j,2}) = (-1)^{L+1} \mathcal{P}_w$, equals, up to a sign, the parity operator \mathcal{P}_w of Dirac w -fermions,

$$\mathcal{P}_w = (-1)^{\sum_{j=1}^{L+1} w_j^\dagger w_j}. \quad (5.14)$$

This parity operator commutes with \mathcal{M} . Thus, restricted to the subspaces of constant parity, \mathcal{M} is quadratic. Note that \mathcal{M} in terms of the Majorana γ -fermions acts non-trivially on the additional site $L+1$.

To keep the algebra simpler we restrict to the TASEP case $p = 1$ and $q = \gamma = \delta = 0$, leaving α and β as free parameters. The following calculations can be straightforwardly generalized to arbitrary p, q, γ, δ . Thus, \mathcal{M} in terms of the Majorana γ -fermions

simplifies to

$$\begin{aligned} \mathcal{M} = & \frac{1}{2}\alpha[i\gamma_{1,1}\gamma_{1,2} + \gamma_{1,1}\gamma_{2,1}] + \frac{1}{4}\sum_{j=1}^{L-1} \left[(\gamma_{j,2}, \gamma_{j+1,1}) \begin{pmatrix} 1 & -i \\ i & 1 \end{pmatrix} \begin{pmatrix} \gamma_{j+1,2} \\ \gamma_{j+2,1} \end{pmatrix} \right] \\ & + \frac{1}{2}(-1)^{L+1}\mathcal{P}_w\beta[i\gamma_{L+1,1}\gamma_{L+1,2} + \gamma_{L,2}\gamma_{L+1,2}]. \end{aligned} \quad (5.15)$$

The eigenvalues of the 2×2 -matrix are 0 and 2, while the eigenvectors are $(1, -i)^t$ and $(1, i)^t$, respectively. Thus the following pairing of Majorana fermions

$$c_j^\dagger = \frac{1}{2}(\gamma_{j,2} - i\gamma_{j+1,1}), \quad c_j = \frac{1}{2}(\gamma_{j,2} + i\gamma_{j+1,1}), \quad (5.16)$$

into Dirac c -fermions simplifies the bulk term. Note that this pairing differs from the pairing of γ -Majoranas into Dirac w -fermions. By identifying $\gamma_{L+2,1} = \gamma_{1,1}$, the pairing in Eq. (5.16) turns the chain into a ring, connecting site 1 and $L + 1$. The matrix \mathcal{M} is given in terms of c -fermions as

$$\mathcal{M} = \alpha(c_{L+1} - c_{L+1}^\dagger)c_1^\dagger + \sum_{j=1}^{L-1} [c_j c_{j+1}^\dagger] + (-1)^L \mathcal{P}_c \beta c_L(c_{L+1} + c_{L+1}^\dagger), \quad (5.17)$$

where \mathcal{P}_c denotes the parity of the Dirac c -fermions,

$$\mathcal{P}_c = (-1)^{\sum_{j=1}^{L+1} c_j^\dagger c_j} = (-1)_c^N, \quad (5.18)$$

and N_c denotes the number of c -fermions. The parity is conserved by \mathcal{M} . Restricted to a fixed parity sector, \mathcal{M} is quadratic. The corresponding spectrum is the same for each parity sector leading to the aforementioned doubling of the spectral multiplicity. This follows from results presented in Section 5.3.2.

Summarized, the non-interacting TASEP \mathcal{M} on L sites with obc can be written as a quadratic, non-Hermitian fermion model on $L + 1$ sites, with twisted pbc and super-conducting terms $c_{L,1}^{(\dagger)} c_{L+1}^{(\dagger)}$ connecting to the additional site $L + 1$. The reservoirs at the ends of the original chain are converted into an additional site on the chain. The superconducting terms connecting site 1 and L with the additional site $L + 1$ relate to the entry and exit of particles from the reservoirs.

5.1.3 Spectrum

Figure 5.1 presents the \mathcal{K} -spectrum of the TASEP on a lattice with $L = 11$ sites. The spectral boundary shows L spikes for pbc ($N = 5$ particles) for $U = 1$ in (a) and

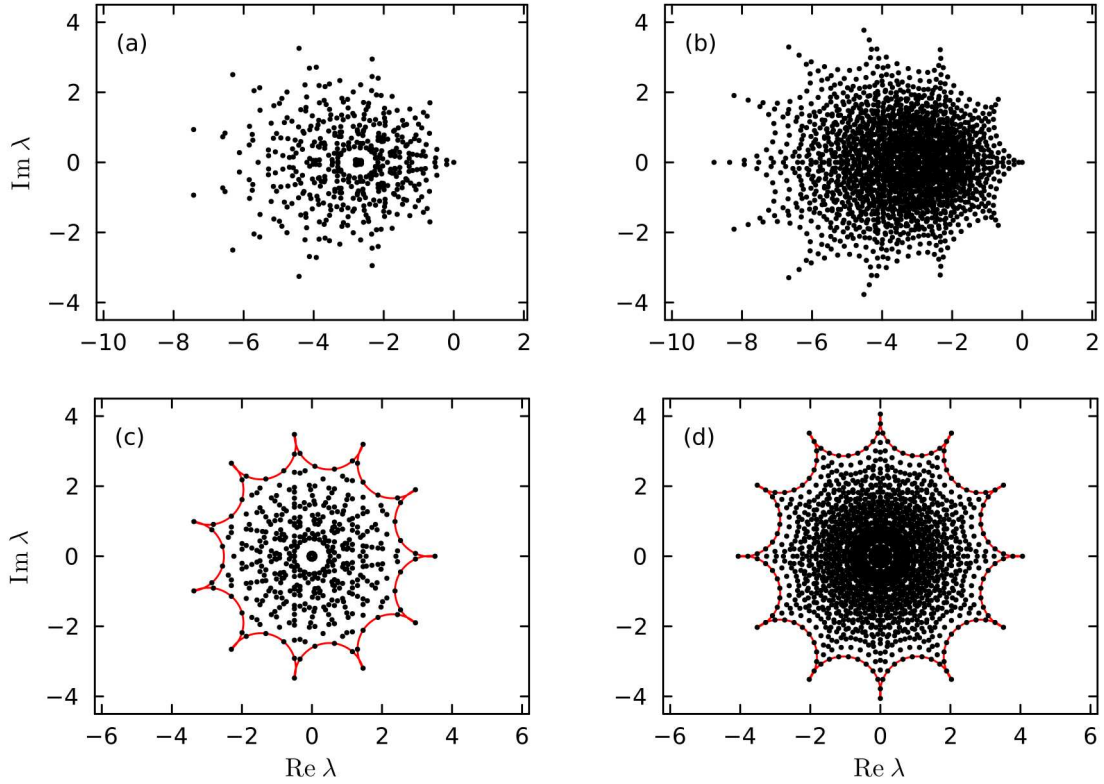


Fig. 5.1 Spectrum of the generator matrix \mathcal{K} of TASEP **(a,b)** and the interaction free TASEP **(c,d)** on $L = 11$ sites. The spectrum shows L spikes in **(a,c)** for pbc with $N = 5$ particles and $L + 1$ spikes in **(b,d)** for obc. Red solid lines in **(c,d)** denote the spectral boundary according to Eq. (5.30).

$U = 0$ in **(c)** and $L + 1$ spikes for obc and $U = 1$ in **(b)** and $U = 0$ in **(d)**. For obc the parameters corresponding to the reservoirs are chosen as $\alpha = \beta = 1$ and $\gamma = \delta = 0$. The remainder of this chapter is dedicated to elucidating the nature of the spikes observed in the spectral boundary of the ASEP.

Panels **(c)** and **(d)** of Figure 5.1 reveal a highly structured spectrum for the non-interacting TASEP \mathcal{M} , exhibiting rotational invariance at angles $2\pi/L$ for pbc and $2\pi/(L + 1)$ for obc. This characteristic stems from a “quasi-symmetry” of \mathcal{M} , which will be presented in Sections 5.2 and 5.3.

For TASEP with obc, the spectral boundary spikes are always prominent, as illustrated for the non-interacting TASEP in Sec. 5.3. However, this is not the case for pbc. In Fig. 5.3(a) the spectrum of the pbc TASEP ($U = 1$) and in (b) its non-interacting variant ($U = 0$) are presented for $L = 40$ sites and $N = 2$ particles, without any noticeable spikes in the spectral boundary. In Section 5.2, we will demonstrate

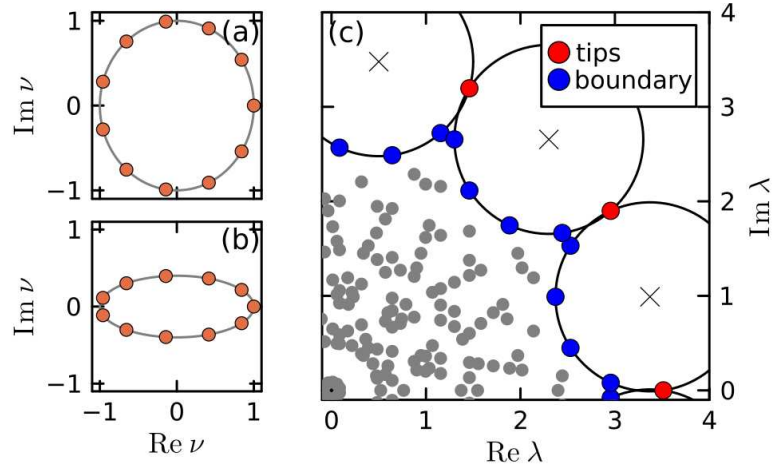


Fig. 5.2 Spectrum of \mathcal{M} on $L = 11$ sites with pbc. Single-body eigenvalues with $p = 1$ and $q = 0$ in (a) and $p = 0.7$ and $q = 0.3$ in (b). In (c) we show part of the many-body spectrum with $N = 5$ particles highlighting the tips of the spikes (red) and other boundary eigenvalues (blue). All boundary eigenvalues are located on circles of radius 1, with crosses marking the midpoints.

that, technically, the spectral boundary of the non-interacting TASEP has $L = 40$ spikes, but their distinctiveness fades in the dilute limit where $\rho = N/L \rightarrow 0$.

5.2 The “non-interacting” ASEP with pbc

In this section, we investigate the spectrum of the non-interacting ASEP \mathcal{M} for pbc given by Eq. (5.3) and Eq. (5.6). Section 5.2.1 is devoted to the calculation of the single-body eigenvalues of \mathcal{M} . In Section 5.2.2, we show the rotational invariance of the many-body spectrum and in Section 5.2.3, we discuss how the spiky spectral boundary emerges. We quantify the prominence of the spikes in Section 5.2.4 and comment on whether they survive in the limit of large L .

5.2.1 Single-body spectrum

The matrix \mathcal{M} represents non-Hermitian free fermions. Its (many-body) eigenvalues are therefore expressible as sums of single-body eigenvalues ν . In the following, we will present these single-body eigenvalues ν . Due to the dependence of the boundary conditions in Eq. (5.6) on $(-1)^N$, the single-particle spectrum for even and odd N differs slightly. Let us consider the totally asymmetric case $p = 1$ and $q = 0$ first. Then

ν are the roots of a polynomial,

$$\nu^L + (-1)^N = 0, \quad (5.19)$$

which in turn are given by $\nu = \omega^j$, where $\omega = e^{i\pi/L}$ and $0 \leq j < 2L$ runs over all even (odd) integers when N is odd (even). Thus, the single-body spectrum is evenly spaced on the unit circle. In Figure 5.2(a), the single-body spectrum for $p = 1$ and $q = 0$ and $L = 11$ and odd N is shown together with the unit circle.

For arbitrary values of p and q , the single-body eigenvalues ν are

$$\nu = p\omega^j + q\omega^{-j}, \quad (5.20)$$

with j defined as previously. This spectrum, as described by Eq. (5.20), forms an ellipse with foci at $\pm 2\sqrt{pq}$ and semi-major axis $p + q$ and semi-minor axis $p - q$,

$$\{(p + q)\cos(t) + i(p - q)\sin(t) : 0 \leq t \leq 2\pi\}. \quad (5.21)$$

Figure 5.2 (b) illustrates the single-body spectrum for $p = 0.7$ and $q = 0.3$, alongside the ellipse defined by Eq. (5.21).

The structure of the single-body spectrum for general p, q suggests a straightforward relation with the totally asymmetric case $q = 0$. By rescaling the imaginary part while keeping the real part constant,

$$z \rightarrow \operatorname{Re} z + i \frac{p+q}{p-q} \operatorname{Im} z, \quad (5.22)$$

we can map the single-body eigenvalues for general p, q values to the totally asymmetric case. This transforms the ellipse into a circle of radius $p + q$. Without loss of generality, we restrict ourselves to $p = 1$ and $q = 0$ for the remainder of this section.

5.2.2 Rotational invariance

With $p = 1$ and $q = 0$, the single-body spectrum remains unchanged under complex plane rotations of $2\pi/L$. This rotational invariance also applies to the many-body spectrum, which consists of sums of single-body eigenvalues.

Furthermore, this symmetry of the spectrum is related to a “quasi-symmetry” of \mathcal{M} . Transforming $c_j \rightarrow e^{-i2\pi j/L} c_j = \tilde{c}_j$ and $c_j^\dagger \rightarrow e^{i2\pi j/L} c_j^\dagger = \tilde{c}_j^\dagger$, or in terms of spin operators $\sigma_j^\pm \rightarrow e^{\pm i2\pi j/L} \sigma_j^\pm = \tilde{\sigma}_j^\pm$, results in $e^{i2\pi/L} \mathcal{M} = \tilde{\mathcal{M}}$. Here, $\tilde{\mathcal{M}}$ is constructed like \mathcal{M} , but using the modified operators $\tilde{c}, \tilde{c}^\dagger$ ($\tilde{\sigma}^\pm$). Since these altered operators

maintain their respective (anti-)commutation relations, the spectra of \mathcal{M} and $\tilde{\mathcal{M}}$ are identical. Consequently, the spectrum of \mathcal{M} is invariant under $2\pi/L$ rotations.

5.2.3 Spectral boundary

The structure of the many-body spectrum as observed in Figure 5.1(c) is now a consequence of the relation of single-body to many-body eigenvalues and the rotational symmetry. For ease of notation, we define $\nu_j = \omega^{2j}$ when N is odd, and $\nu_j = \omega^{2j+1}$ for even N . The many-body eigenvalues correspond uniquely to configurations $s = (s_1, \dots, s_L) \in \{0, 1\}^L$, where $\sum_j s_j = N$, and are given by

$$\lambda = \sum_{j=1}^L s_j \nu_j. \quad (5.23)$$

The many-body eigenvalues λ_t , which form the spike tips, have the largest absolute values and are derived from configurations s with contiguous non-zero s_j entries. Specifically, each of the L tips $\lambda_t(j_0)$ is linked to an index $1 \leq j_0 \leq L$ and a configuration $s = s_t(j_0)$ with

$$s_j = \begin{cases} 1 & j_0 \leq j \leq j_0 + N - 1 \\ 0 & \text{otherwise.} \end{cases} \quad (5.24)$$

Here, $j \equiv j - L$ is applied for $j > L$. The eigenvalues $\lambda_t(j_0)$ are calculated as

$$\lambda_t(j_0) = \sum_{j=j_0}^{j_0+N-1} \nu_j. \quad (5.25)$$

Configurations s that lead to spike tips are termed “domain wall configurations”. The many-body eigenvalues λ_t are depicted as red circles in Figure 5.2(c).

Boundary eigenvalues in the many-body spectrum arise from “interpolating” between configurations of adjacent spike tips. These configurations consist of exactly two domain walls, each separated by one site. The interpolation process involves moving a single particle (or executing a single spin flip). Specifically, boundary configurations $s = s_b(j_0, l_0)$ are associated with indices $1 \leq j_0 \leq L$ and $j_0 \leq l_0 \leq j_0 + N$, defined as

$$s_j = \begin{cases} 1 & j_0 \leq j \leq j_0 + N \text{ and } j \neq l_0 \\ 0 & j = l_0 \\ 0 & \text{otherwise.} \end{cases} \quad (5.26)$$

Again, $j \equiv j - L$ is used for $j > L$. The corresponding boundary eigenvalues $\lambda_b(j_0, l_0)$ are expressible as

$$\lambda_b(j_0, l) = \sum_{j=j_0; j \neq l}^{j_0+N} \nu_j. \quad (5.27)$$

When $l_0 = j_0$ or $l_0 = j_0 + N$ (indicating a single domain wall), the boundary eigenvalue matches a spike tip, $\lambda_b(j_0, j_0) = \lambda_t(j_0 + 1)$ or $\lambda_b(j_0, j_0 + N) = \lambda_t(j_0)$, respectively. The boundary eigenvalues $\lambda_b(j_0, l)$ for $j_0 < l < j_0 + N$ are those many-body eigenvalues located “between” the spike tips $\lambda_t(j_0)$ and $\lambda_t(j_0 + 1)$, depicted as blue circles in Figure 5.2(c).

Eq.(5.27) can be reformulated as

$$\lambda_b(j_0, l) = \sum_{j=j_0}^{j_0+N} \nu_j - \nu_l. \quad (5.28)$$

Given $|\nu_l| = 1$ and the independence of the sum from l , all boundary eigenvalues are on L circles of radius 1. For $N \leq L/2$, the circle midpoints are the many-body spectrum tips $\lambda_t^{(N+1)}(j_0)$ with $N + 1$ particles. The tips $\lambda_t^{(N)}$ intersect two adjacent circles. This is illustrated in Figure 5.2(c) with circles as black lines and midpoints as gray crosses.

According to Eq. (5.25), all tips reside on a circle, centered at 0 with radius R , defined as

$$R = \left| \frac{1 - e^{i2\pi N/L}}{1 - e^{i2\pi/L}} \right| = \frac{\sin(\pi N/L)}{\sin(\pi/L)}. \quad (5.29)$$

This radius, combined with the circular pattern of the boundary eigenvalues, enables us to establish a continuous boundary for the many-body spectrum. It is formed by the intersection of all circles of radius 1 with the disc of radius R from Eq. (5.29). The boundary can be parameterized by

$$z_B(t) = e^{-if(t)} \left(\gamma_1 + \gamma_2 e^{ig(kt)} \right), \quad (5.30)$$

with $\gamma_1 = \frac{\sin(\pi\rho)}{\sin(\pi/L)}$ and $\gamma_2 = 1$, while the function f is piece-wise constant,

$$f(t) = \frac{\pi}{L} \left(2 \left\lfloor \frac{Lt}{2\pi} \right\rfloor - 1 \right), \quad (5.31)$$

and g is piece-wise the identity,

$$g(t) = \pi(1 - \rho) + \rho(t \bmod 2\pi). \quad (5.32)$$

The continuous boundary $z_B(t)$ is illustrated in Figure 5.1(c) as a red curve for $L = 11$ and $N = 5$.

The spectral boundary of the non-interacting TASEP is intentionally parameterized as in Eq. (5.30). It underlines the similarity to the spectral boundary of random matrices with higher-order cyclic correlations and adjacency matrices of random graphs with dominant cycle lengths, introduced in Section 1.1.2. The spectral boundary of such matrices adheres to the hypotrochoidic law, which can be parametrized as in Eq. (5.30) by setting $f(t) = g(t) = t$. The similarity between the functions f and g of the non-interacting TASEP and random matrices adhering to the hypotrochoidic law indicates a relation between the spectral boundary of the non-interacting TASEP and RMT. In Section 5.5, one possible link will be investigated in detail.

5.2.4 Quantification of spikes

This section aims to measure the sharpness of the spectral boundary of \mathcal{M} , focusing on whether spikes persist in large system sizes and, if so, how. For simplicity, we consider particle densities $0 \leq \rho \leq 1/2$. As the spectrum of \mathcal{M} is invariant under changing $\rho \rightarrow 1 - \rho$ this comes with no loss of generality.

To assess the spikiness of the spectral boundary, we examine the ratio between two distances: d_t , the distance between spike tips, and d_b , the maximum extension of the spectral boundary beyond a circle of radius R , given by Eq. (5.29). This circle of radius R represents the smallest enclosing disk for the \mathcal{M} -spectrum. d_b measures how far the circles with radius 1, carrying the boundary eigenvalues, reach into the enclosing circle. A larger d_b relative to d_t indicates that the circles with radius 1 extend more into the enclosing circle. Therefore, the ratio $2d_b/d_t$ quantifies the spikiness of the spectral boundary. A value close to 1 suggests a spiky boundary, while a significantly smaller ratio implies a less spiky boundary. The factor of two arises because d_t relates to the diameter of the boundary circles, whereas d_b is compared to their radius.

Following some simple trigonometry one finds that the distances d_t and d_b are given by

$$d_t = 2 \sin(\pi\rho) \tag{5.33}$$

and

$$d_b = 1 - \frac{\cos(\pi\rho + \pi/(2L))}{\cos(\pi/(2L))}. \tag{5.34}$$

The fraction $2d_b/d_t$ then simplifies to

$$\frac{2d_b}{d_t} = \tan(\pi\rho/2) + \tan(\pi/(2L)). \quad (5.35)$$

Eq. (5.35) shows a monotonic increase with ρ , indicating that the spectral boundary becomes more spiky at higher ρ values. Due to the invariance of the spectrum under the transformation $\rho \rightarrow 1 - \rho$, the boundary reaches its maximum spikiness at $\rho = 1/2$.

In examining the large L limit, we will explore two scenarios: the “thermodynamic” limit, where both N and L increase to infinity while maintaining a fixed ρ , and the few-particle (dilute) limit, where N remains constant and only L approaches infinity.

“Thermodynamic” limit

In the thermodynamic limit, the distance d_t remains constant, whereas d_b approaches $1 - \cos(\pi/\rho)$. Consequently, the ratio $2d_b/d_t$ tends towards $\tan(\pi\rho/2)$. This implies that for any non-zero ρ , the spiky structure of the spectral boundary is preserved in the thermodynamic limit, becoming more pronounced with increasing ρ .

Fig. 5.1(c) presents the many-body spectrum of the non-interacting TASEP for $L = 11$ and $N = 5$, with Fig. 5.2(c) offering a closer view of the spectral boundary. Here, $\rho \approx 0.45$ and $2d_b/d_t \approx 1.01$ indicate pronounced spikes of the spectral boundary, as evident.

Regarding the length scales at which these spikes are observable, consider the following: The radius R of the spectrum scales as $O(L)$, necessitating a rescaling of the spectrum by $1/L$ to ensure a well-defined spectral density in the thermodynamic limit. At an infinite L , this rescaled spectrum densely fills the unit circle. For finite L , the tips of the spikes are spaced at a distance of $d_t = O(1/L)$, and the distance d_b of the spectral boundary from the unit circle is also $O(1/L)$. Therefore, at the length scale of $1/L$, the spiky nature of the spectral boundary is distinctly visible.

Dilute limit (large L , constant N)

In the scenario where N is fixed and L increases, both distances d_t and d_b decrease, scaling as $O(1/L)$ and $O(1/L^2)$, respectively. Consequently, the ratio $2d_b/d_t$ tends towards 0, as indicated by Eq. (5.35). Therefore, in this limit, the spiky structure of the spectral boundary does not persist.

In Fig. 5.3, we present the many-body spectrum of the TASEP for $L = 40$ and $N = 2$, representative of the dilute limit. We show both a TASEP case ($U = 1$) in (a) and a non-interacting TASEP case \mathcal{M} ($U = 0$) in (b). The non-interacting case has a

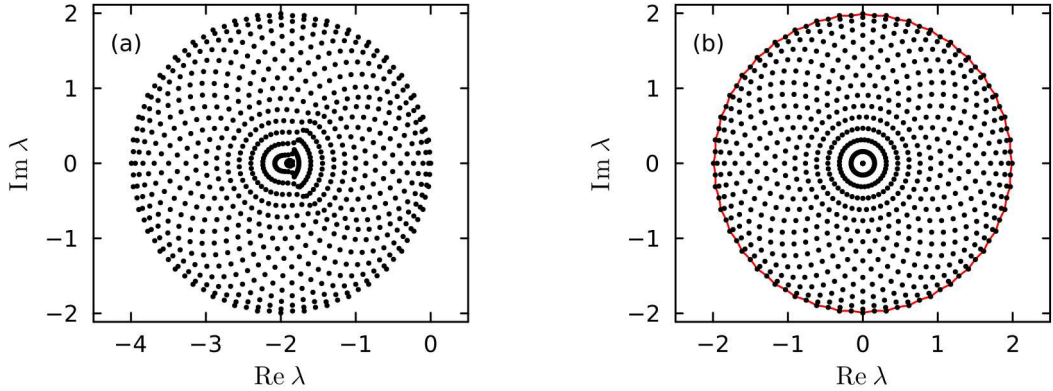


Fig. 5.3 Spectrum of the generator matrix \mathcal{K} of (a) TASEP and (b) the “non-interacting” TASEP on $L = 40$ sites with $N = 2$ particles (dilute limit). The red solid line in (b) denotes the spectral boundary according to Eq. (5.30). The spectral boundary appears smooth and non-spiky in both panels.

$2d_b/d_t$ ratio of ≈ 0.01 . Thus, the spectral boundary (red curve) is not spiky but barely distinguishable from a circle.

5.3 The “non-interacting” TASEP with obc

In this section, we will present the analytical derivation of the spectrum of the non-interacting TASEP \mathcal{M} with obc, specifically for $p = 1$ and $q = \gamma = \delta = 0$. We expect our results to extend to general p, q, γ, δ .

In Section 5.3.1, we establish the rotational invariance of the \mathcal{M} -spectrum. In Section 5.3.2, we derive single-particle eigenvalues of \mathcal{M} and demonstrate the relation to the spectrum of \mathcal{M} . In Section 5.3.3, we demonstrate that the spectral boundary of \mathcal{M} is, as for pbc, defined by the intersection of circles with a disk, featuring $L + 1$ spikes. In the limit of large L , this boundary is similar to the pbc case with density $\rho = 1/2$.

5.3.1 Rotational symmetry

The spectrum of the non-interacting TASEP \mathcal{M} is invariant under rotations of angle $\frac{2\pi}{L+1}$. Similar to the pbc case, consider the change of operators $c_j^\dagger \rightarrow e^{i\frac{2\pi}{L+1}j} c_j^\dagger = \tilde{c}_j^\dagger$ and $c_j \rightarrow e^{-i\frac{2\pi}{L+1}j} c_j = \tilde{c}_j$ or, equivalently, $\sigma_j^\pm \rightarrow e^{\pm i\frac{2\pi}{L+1}j} \sigma_j^\pm = \tilde{\sigma}^\pm$. This change implies that $e^{i\frac{2\pi}{L+1}} \mathcal{M} = \tilde{\mathcal{M}}$, where $\tilde{\mathcal{M}}$ is \mathcal{M} with c, c^\dagger (σ) replaced by the tilde operators. As the tilde operators fulfill the canonical (anti-)commutation relations of fermion

operators (Pauli matrices), the spectrum of the non-interacting TASEP is invariant under rotations of angle $\frac{2\pi}{L+1}$.

5.3.2 Single- and many-body spectrum

Before we diagonalize \mathcal{M} , let's specify the parity sector as $s = (-1)^L \mathcal{P}_c$. To simplify the following arguments, we will abuse notation and not distinguish between \mathcal{M} and \mathcal{M} restricted to a subspace of constant parity. At the end of this subsection, we will take the difference into account properly.

Let us collect the Dirac fermion operators c, c^\dagger into a $(2L + 2)$ -dimensional vector $\mathbf{c} = (c_1, \dots, c_{L+1}, c_1^\dagger, \dots, c_{L+1}^\dagger)^t$. We express \mathcal{M} given by Eq. (5.17) as

$$\mathcal{M} = \frac{1}{2} \mathbf{c}^\dagger \begin{pmatrix} A & B \\ C & -A^t \end{pmatrix} \mathbf{c} = \frac{1}{2} \mathbf{c}^\dagger M_c \mathbf{c} \quad (5.36)$$

where the $(L + 1) \times (L + 1)$ -matrices A, B and C are given by

$$\begin{aligned} A_{ij} &= -\delta_{i,j+1 \bmod (L+1)} \\ &\quad + (1 - \beta s) \delta_{i,L+1} \delta_{j,L} + (1 - \alpha) \delta_{i,1} \delta_{j,L+1}, \end{aligned} \quad (5.37)$$

$$B_{ij} = \alpha (\delta_{i,1} \delta_{j,L+1} - \delta_{i,L+1} \delta_{j,1}), \quad (5.38)$$

$$C_{ij} = \beta s (\delta_{i,L} \delta_{j,L+1} - \delta_{i,L+1} \delta_{j,L}), \quad (5.39)$$

and δ denotes the Kronecker symbol. The matrix A is, up to deformations in the $(1, L + 1)$ th and $(L + 1, L)$ th entries, a circulant matrix. The matrices B and C only contain two non-zero entries. Thus, the solutions ν and \mathbf{u} to the eigenvalue problem

$$M_c \mathbf{u} = \nu \mathbf{u}, \quad (5.40)$$

are closely related to the eigen-decomposition of circulant matrices, which in turn are given by Fourier transforms. In terms of $\mathbf{u} = (u_1, \dots, u_{L+1}, u'_1, \dots, u'_{L+1})$ the eigenvalue

equation reads

$$\nu u_1 = -\alpha(u_{L+1} - u'_{L+1}) \quad (5.41)$$

$$\nu u_2 = -u_1 \quad (5.42)$$

...

$$\nu u_{L-1} = -u_{L-2} \quad (5.43)$$

$$\nu u_L = -u_{L-1} \quad (5.44)$$

$$\nu u_{L+1} = -s\beta u_L - \alpha u'_1 \quad (5.45)$$

and

$$\nu u'_1 = u'_2 \quad (5.46)$$

$$\nu u'_2 = u'_3 \quad (5.47)$$

...

$$\nu u'_{L-1} = u'_L \quad (5.48)$$

$$\nu u'_L = \beta s(u_{L+1} + u'_{L+1}) \quad (5.49)$$

$$\nu u'_{L+1} = -\beta s u_L + \alpha u'_1. \quad (5.50)$$

Combining Eqs. (5.42)-(5.44) with u_1, \dots, u_L and Eqs. (5.46)-(5.48) with u'_1, \dots, u'_L recursively we get for $2 \leq j \leq L$

$$u_j = -\nu^{-1} u_{j-1} = \dots = (-\nu)^{-j+1} u_1 \quad (5.51)$$

and

$$u'_j = \nu u'_{j-1} = \dots = \nu^{j-1} u'_1. \quad (5.52)$$

Especially, the following holds

$$u_L = (-\nu)^{-L+1} u_1 \quad (5.53)$$

$$u'_L = \nu^{L-1} u'_1. \quad (5.54)$$

By substituting Eq. (5.53) and Eq. (5.54) into Eq. (5.45) and Eq. (5.50), respectively, we get the following self-consistent set of equations

$$u_1 = \alpha\nu^{-1}(-u_{L+1} + u'_{L+1}) \quad (5.55)$$

$$u_{L+1} = \beta s(-\nu)^{-L}u_1 - \alpha\nu^{-1}u'_1 \quad (5.56)$$

$$u'_1 = \nu^{-L}\beta s(u_{L+1} + u'_{L+1}) \quad (5.57)$$

$$u'_{L+1} = \beta s(-\nu)^{-L}u_1 + \alpha\nu^{-1}u'_1. \quad (5.58)$$

Adding and subtracting Eq. (5.56) and Eq. (5.58), respectively, leads to

$$u_{L+1} + u'_{L+1} = 2\beta s(-\nu)^{-L}u_1 \quad (5.59)$$

$$-u_{L+1} + u'_{L+1} = 2\alpha\nu^{-1}u'_1, \quad (5.60)$$

which in turn implies that

$$u'_1 = 2(-1)^L\nu^{-2L}\beta^2u_1 \quad (5.61)$$

$$u_1 = 2\alpha^2\nu^{-2}u'_1, \quad (5.62)$$

by using Eqs. (5.55) and (5.57). Combining the last two equations leads to

$$u_1 = 4(\alpha\beta)^2(-1)^L\nu^{-2L-2}u_1, \quad (5.63)$$

which implies, for $u_1 \neq 0$,

$$\nu^{2(L+1)} = (-1)^L4(\alpha\beta)^2. \quad (5.64)$$

The roots of this polynomial, and therefore the eigenvalues of M_c are given by

$$\nu = (2\alpha\beta)^{\frac{1}{L+1}} \begin{cases} \exp\left(\frac{i\pi}{2L+2}2k\right) & L \text{ even,} \\ \exp\left(\frac{i\pi}{2L+2}(2k-1)\right) & L \text{ odd,} \end{cases} \quad (5.65)$$

where $k = 1, \dots, 2L+2$. Especially, the eigenvalues ν are independent of the parity sector s and appear in pairs of $\pm\nu$.

The matrix \mathcal{M} in Eq. (5.17) is non-Hermitian, preventing the direct application of the (Hermitian) Bogoliubov-de-Gennes formalism for linking the eigenvalues of M_c to the many-body spectrum of \mathcal{M} . Hence, we will pursue an alternative method. We

proceed as in [360] and express c, c^\dagger in terms of Majorana fermions

$$\phi_{j,1} = \frac{1}{\sqrt{2}}(c_j + c_j^\dagger), \quad \phi_{j,2} = \frac{1}{i\sqrt{2}}(c_j - c_j^\dagger). \quad (5.66)$$

The column vector ϕ , defined as $\phi = (\phi_{1,1}, \phi_{1,2}, \dots, \phi_{L+1,1}, \phi_{L+1,2})^t$, encapsulates the Majorana fermions $\phi_{j,l}$. Utilizing this vector, the matrix \mathcal{M} can be reformulated as

$$\mathcal{M} = \frac{1}{2}\phi^t M_\phi \phi, \quad (5.67)$$

where M_ϕ represents a complex and anti-symmetric $(2L + 2) \times (2L + 2)$ -matrix. The transformation of Majorana fermions ϕ to Dirac fermions c via Eq. (5.66) is unitary, making M_ϕ and M_c unitarily equivalent and, consequently, they have the same eigenvalues.

As M_ϕ is anti-symmetric, it can be factorized [360] as

$$M_\phi = \frac{1}{2}V\Lambda JV^t \quad (5.68)$$

where

$$V^t V = J = \text{Id}_{L+1} \otimes \begin{pmatrix} 0 & 1 \\ 1 & 0 \end{pmatrix}, \quad (5.69)$$

Id_{L+1} denotes the $(L+1) \times (L+1)$ identity matrix and Λ is a diagonal matrix containing the eigenvalues of M_ϕ (M_c). The anti-symmetry of M_ϕ implies that its eigenvalues come in pairs $\pm\nu$, which is consistent with the solutions of Eq. (5.64). The diagonal of Λ is ordered as $\nu_1, -\nu_1, \dots, \nu_{L+1}, -\nu_{L+1}$. We fix the choice between ν_j and $-\nu_j$ by requiring $\text{Re } \nu_j \geq 0$.

Let us define another type of Dirac fermions b, b' as

$$(b_1, b'_1, \dots, b_{L+1}, b'_{L+1})^t = (V^t \phi). \quad (5.70)$$

These fulfill the usual anti-commutation relations of Dirac fermions [360], but b' is in general not the Hermitian adjoint of b . Nevertheless, \mathcal{M} becomes diagonal in terms of b, b' ,

$$\mathcal{M} = \sum_{j=1}^{L+1} \nu_j b'_j b_j - \frac{1}{2} \sum_{j=1}^{L+1} \nu_j. \quad (5.71)$$

The eigenstates of \mathcal{M} are given by creation operators b'_j acting on the vacuum $|0\rangle_b$, which are 2^{L+1} in total. But not all eigenstates correspond to an eigenvalue of \mathcal{M} given by Eq. (5.17). We have to take into account that the Dirac fermions b, b' are only

defined on fixed parity subspaces. We numerically find that the parity operator \mathcal{P}_b of the b, b' fermions obeys

$$\mathcal{P}_b = -s\mathcal{P}_c, \quad (5.72)$$

where \mathcal{P}_c denotes the parity operator of the c fermions. In the beginning of this section, we set $s = (-1)^L \mathcal{P}_c$. Thus, the admissible b' -fermion states must have b -parity $\mathcal{P}_b = -(-1)^L = (-1)^{L+1}$. Especially, the parity of the admissible b -states does not depend on s . Consequently, both parity sectors give rise to the same many-body spectrum of \mathcal{M} in Eq. (5.71).

Summarized, the spectrum of \mathcal{M} , subject to a global shift in the complex plane, consists of sums of the $L + 1$ roots from Eq. (5.64) with positive real parts. These are scaled roots of ± 1 with magnitude proportional to $(\alpha\beta)^{1/(L+1)}$. Depending on whether L is odd or even, an even or odd number of summands, respectively, are included in the sums.

5.3.3 Spectral boundary

The relation of the \mathcal{M} -spectrum to single-particle eigenvalues for obc follows a similar principle to the pbc case, discussed in Section 5.2: both consist of sums of (scaled) roots of ± 1 . In the following, we want to show how the spiky spectral boundary emerges for obc. Especially, we will show that, similar to pbc, the spectral boundary lies on $L + 1$ circles with radius $(2\alpha\beta)^{1/(L+1)}$.

We discuss the spectral boundary associated with the most negative real parts. This is illustrated in Figure 5.4, where the eigenvalues of the relevant sectors are marked with blue and red circles. The rotational symmetry of the spectrum implies that the structure of the boundary is a repetitive pattern reflecting the shape of sectors with the smallest real parts. Hence, the restriction to sectors with the most negative real part eigenvalues comes with no loss of generality.

Let us first consider even L . In this case the many-body spectrum is given by sums of an odd number of positive real part roots of the polynomial in Eq. (5.64). Let us denote the $L + 1$ roots with non-negative real part by ν_1, \dots, ν_{L+1} . The $L + 1$ many-body eigenvalues λ with the smallest real parts are eigenvalues lying on the spectral boundary and given by

$$\lambda_b = \nu_j - \frac{1}{2} \sum_{l=1}^{L+1} \nu_l. \quad (5.73)$$

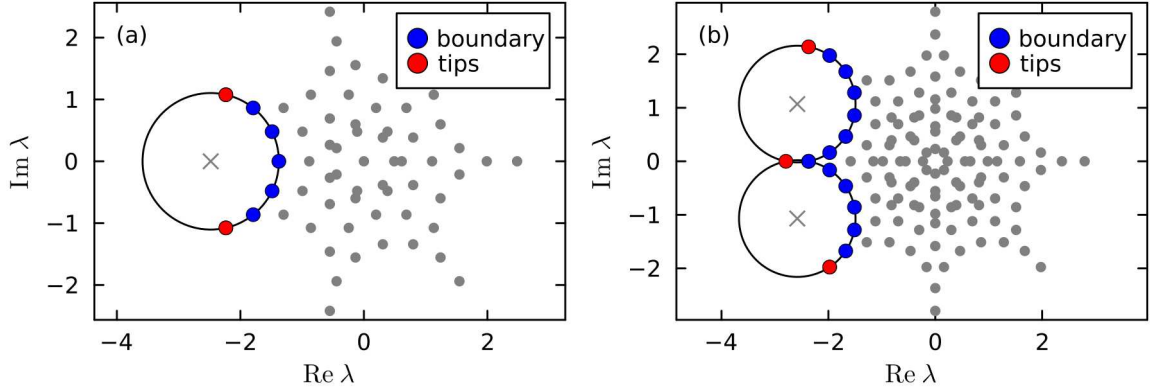


Fig. 5.4 Many-body spectrum of the non-interacting TASEP with obc on (a) $L = 6$ and (b) $L = 7$ sites. Similar to pbc in Fig. 5.2, all boundary eigenvalues lie on circles, with midpoints denoted by crosses.

If we label ν_l by increasing angle with branch-cut on the negative imaginary axis then the tips λ_t of the sector are given by the indices $j = 1$ and $j = L + 1$. In Figure 5.4(a), we show the spectrum of the non-interacting TASEP with obc on $L = 6$ sites. The spectrum shows $L + 1 = 7$ spikes. The boundary and tips according to Eq. (5.73) are shown as blue and red markers, respectively. The markers lie on a circle with midpoint $-\frac{1}{2} \sum_{l=1}^{L+1} \nu_l$ and radius $|\nu_j| = (2\alpha\beta)^{1/(L+1)}$.

Let us now consider the case of odd L . In Figure 5.4(b) we show the many-body spectrum on $L = 7$ sites. The tip λ_t of the spectral edge with the smallest real part is given by an “empty” sum of ν_l ’s and thus is $\lambda_t = -\frac{1}{2} \sum_{l=1}^{L+1} \nu_l$. The boundary eigenvalues λ_b are given by the (shifted) sum of two single-particle eigenvalues,

$$\lambda_b = \nu_j + \nu_{1,L+1} - \frac{1}{2} \sum_{l=1}^{L+1} \nu_l, \quad (5.74)$$

where $2 \leq j \leq L$; ν_1 corresponds to the lower spectral boundary in Figure 5.4(b) while ν_{L+1} corresponds to the upper part. The midpoints of the circles are given by $\nu_{1,L+1} - \frac{1}{2} \sum_{l=1}^{L+1} \nu_l$ and the radius again by $|\nu_j| = (2\alpha\beta)^{1/(L+1)}$.

Similar to the pbc case, we can establish a continuous boundary for the many-body spectrum, parametrized by Eq. (5.30). In the obc case the constants $\gamma_{1,2}$ are given by

$$\gamma_1 = (2\alpha\beta)^{1/(L+1)} \frac{1}{2 \sin(\pi/(2L+2))} \quad (5.75)$$

$$\gamma_2 = (2\alpha\beta)^{1/(L+1)}, \quad (5.76)$$

while the piece-wise constant f and the piece-wise identify function g are given by

$$f(t) = \frac{\pi}{L} \left(2 \left\lfloor \frac{Lt}{2\pi} \right\rfloor - 1 \right), \quad (5.77)$$

$$g(t) = \pi \frac{L+2}{2L+2} + \frac{L}{2L+2} (t \bmod 2\pi). \quad (5.78)$$

The continuous boundary $z_B(t)$ with the above parameters is illustrated in Figure 5.1(d) as a red curve for $L = 11$.

The parametrization of the spectral boundary for obc shows a clear link to the spectral boundary for pbc. Specifically, in the large L limit with constant α, β , the obc spectral boundary aligns with the pbc case at $\rho = 1/2$. This relation is immediately evident for γ_2 , f , and g . For γ_1 , a series expansion in the large L limit reveals that the leading term, $\gamma_1 = L/\pi + O(1)$, is identical in both cases, with differences emerging only at $O(1)$. Consequently, in the large L limit, the spiky spectral boundary in the obc case remains pronounced, as does the spectral boundary for pbc in the thermodynamic limit.

5.4 The TASEP with pbc by Bethe ansatz

In Section 5.2, we showed that in the non-interacting TASEP ($U = 0$) with pbc, the spiky boundary of the many-body spectrum emerges essentially as sums of circularly arranged single-body eigenvalues ν_1, \dots, ν_L . This section expands that concept to interaction strengths $0 < U$. Employing the coordinate Bethe ansatz, we generalize the single-body framework to Bethe roots, which tend to cluster close to ν_1, \dots, ν_L . This clustering, combined with TASEP many-body eigenvalues being sums of Bethe roots, results in a spiky spectrum boundary for any interaction strength $0 \leq U \leq 1$.

This section focuses on $\rho \approx 1/2$, where the most prominent spectral boundary spikes in the non-interacting ASEP were observed. In the low-density limit (ρ approaching zero), we anticipate a spectral boundary for the usual ASEP similar to the non-interacting case, characterized by a smooth, circular boundary without spikes. Fig. 5.3 partly supports this, showing similar many-body spectra for TASEP with $U = 1$ (a) and $U = 0$ (b), both featuring smooth, non-spiky spectral boundaries.

In Section 5.4.1, we derive the coordinate Bethe ansatz for arbitrary U , while numerical solution methods are detailed in Section 5.4.2. In Section 5.4.3, we demonstrate the clustering of solutions to the Bethe equations and in Section 5.4.4, we establish how this clustering results in a spiky spectral boundary.

5.4.1 Coordinate Bethe ansatz

In this section, we determine the eigenvalues of \mathcal{K} for arbitrary U by application of the coordinate Bethe ansatz. Readers familiar with Bethe ansatz techniques can skip to the end of this section. For ASEP, the eigenvalues λ in terms of the Bethe roots z_j are given by Eq. (5.89), with z_j fulfilling the recurrent relations in Eq. (5.88). For the specific case of TASEP, simplified versions are given by Eq. (5.90) and Eq. (5.91). We follow the derivation of the $U = 1$ case in Refs. [276, 254], but present derivations in much more detail.

Bethe equations for ASEP with general U

We denote the state of N particles at positions x_1, \dots, x_N by $|x_1, \dots, x_N\rangle$, with $x_1 < \dots < x_N$ up to an overall shift in the indices. A state $|\psi\rangle$ in the basis of $|x_1, \dots, x_N\rangle$ is

$$|\psi\rangle = \sum_{x_1 < \dots < x_N} \psi(x_1, \dots, x_N) |x_1, \dots, x_N\rangle,$$

where $\psi(x_1, \dots, x_N)$ denotes the coefficient of $|\psi\rangle$ wrt $|x_1, \dots, x_N\rangle$. In the following, $|\psi\rangle$ is an eigenstate of \mathcal{K} with eigenvalue λ , i.e. $\mathcal{K}|\psi\rangle = \lambda|\psi\rangle$. The matrix \mathcal{K} in terms of spin matrices is given by

$$\mathcal{K} = \sum_{i=1}^L (p\sigma_i^- \sigma_{i+1}^+ + q\sigma_i^+ \sigma_{i+1}^-) + \frac{U}{4} \sum_{i=1}^L (\sigma_i^z \sigma_{i+1}^z - 1). \quad (5.79)$$

The spin-up state is interpreted as a particle present, while the spin-down state is interpreted as particle absent.

First, let us consider the action of the off-diagonal term in Eq. (5.79) on $|x_1, \dots, x_N\rangle$. It follows that

$$\begin{aligned} \sum_{i=1}^{L-1} \sigma_i^- \sigma_{i+1}^+ |x_1, \dots, x_N\rangle &= \sum_{j=1}^{N-1} (1 - \delta(x_{j+1} - x_j, 1)) |x_1, \dots, x_j + 1, \dots, x_N\rangle, \\ \sum_{i=1}^{L-1} \sigma_i^+ \sigma_{i+1}^- |x_1, \dots, x_N\rangle &= \sum_{j=2}^N (1 - \delta(x_j - x_{j-1}, 1)) |x_1, \dots, x_j - 1, \dots, x_N\rangle, \end{aligned}$$

where $\delta(x, y) = 1$ whenever $x = y$ and is zero otherwise. The boundary terms are determined as follows. If $x_N \neq L$ then $\sigma_L^- \sigma_1^+ |x_1, \dots, x_N\rangle = 0$, so let $x_N = L$. Then

$$\begin{aligned} \sigma_L^- \sigma_1^+ |x_1, \dots, x_N\rangle &= (1 - \delta(x_1, 1)) |1, x_1, \dots, x_{N-1}\rangle \\ &= (1 - \delta(x_1 - x_N \bmod L, 1)) |x_1, \dots, x_{N-1}, x_N + 1\rangle \end{aligned}$$

by identifying $|x_1, \dots, x_{N-1}, L+1\rangle = |1, x_1, \dots, x_{N-1}\rangle$. On the other hand, whenever $x_1 \neq 1$ we have $\sigma_L^+ \sigma_1^- |x_1, \dots, x_N\rangle = 0$, while for $x_1 = 1$ we get

$$\begin{aligned}\sigma_L^+ \sigma_1^- |x_1, \dots, x_N\rangle &= (1 - \delta(x_N, L)) |x_2, \dots, x_N, L\rangle \\ &= (1 - \delta(x_1 - x_N \bmod L, 1)) |x_1 - 1, x_2, \dots, x_N\rangle,\end{aligned}$$

where we identified $|0, x_2, \dots, x_N\rangle = |x_2, \dots, x_N, L\rangle$. Taking everything together we have

$$\begin{aligned}\sum_{i=1}^L \sigma_i^- \sigma_{i+1}^+ |x_1, \dots, x_N\rangle &= \sum_{j=1}^N (1 - \delta(x_{j+1} - x_j \bmod L, 1)) |x_1, \dots, x_j + 1, \dots, x_N\rangle, \\ \sum_{i=1}^L \sigma_i^+ \sigma_{i+1}^- |x_1, \dots, x_N\rangle &= \sum_{j=1}^N (1 - \delta(x_j - x_{j-1} \bmod L, 1)) |x_1, \dots, x_j - 1, \dots, x_N\rangle,\end{aligned}$$

where we additionally identified $x_{L+1} = x_1$ and $x_0 = x_L$.

Before calculating the action of the diagonal term in Eq. (5.79) on $|x_1, \dots, x_N\rangle$, let us denote $n_i = \frac{1}{2}(\sigma_i^z + 1)$, such that $n_i = 1$ for a particle (spin-up) at position i and $n_i = 0$ otherwise. Then it follows that

$$\frac{1}{4} \sum_{i=1}^L (\sigma_i^z \sigma_{i+1}^z - 1) = \frac{4}{4} \sum_{i=1}^L n_i n_{i+1} - \frac{2}{4} \sum_{i=1}^L n_i - \frac{2}{4} \sum_{i=1}^L n_{i+1} = \left[\sum_{i=1}^L n_i n_{i+1} \right] - N.$$

Thus, the diagonal term in Eq. (5.79) is acting on $|x_1, \dots, x_N\rangle$ as

$$\begin{aligned}\frac{1}{4} \sum_{i=1}^L (\sigma_i^z \sigma_{i+1}^z - 1) |x_1, \dots, x_N\rangle &= \sum_{j=1}^{N-1} (\delta(x_{j+1} - x_j, 1) + \delta(x_1 - x_N, 1 - L) - 1) |x_1, \dots, x_N\rangle \\ &= \sum_{j=1}^N (\delta(x_{j+1} - x_j \bmod L, 1) - 1) |x_1, \dots, x_N\rangle.\end{aligned}$$

Summarized, the action of \mathcal{K} on $|x_1, \dots, x_N\rangle$ is

$$\begin{aligned}\mathcal{K}|x_1, \dots, x_N\rangle &= p \sum_{j=1}^N (1 - \delta(x_{j+1} - x_j \bmod L, 1)) |x_1, \dots, x_j + 1, \dots, x_N\rangle \\ &\quad + q \sum_{j=1}^N (1 - \delta(x_j - x_{j-1} \bmod L, 1)) |x_1, \dots, x_j - 1, \dots, x_N\rangle \\ &\quad - U \sum_{j=1}^N (1 - \delta(x_{j+1} - x_j \bmod L, 1)) |x_1, \dots, x_N\rangle.\end{aligned}\quad (5.80)$$

Next, we consider the eigenvalue equation $\mathcal{K}|\psi\rangle = \lambda|\psi\rangle$,

$$\mathcal{K}|\psi\rangle = \sum_{x_1 < \dots < x_N} \psi(x_1, \dots, x_N) \mathcal{K}|x_1, \dots, x_N\rangle = \sum_{x_1 < \dots < x_N} \psi(x_1, \dots, x_N) \lambda |x_1, \dots, x_N\rangle.$$

First, we concentrate on the term in Eq. (5.80) proportional to p ,

$$p \sum_{j=1}^N \sum_{x_1 < \dots < x_N} \psi(x_1, \dots, x_N) (1 - \delta(x_{j+1} - x_j \bmod L, 1)) |x_1, \dots, x_j + 1, \dots, x_N\rangle.$$

After a change of variables $\tilde{x}_i = x_i$ for $i \neq j$ and $\tilde{x}_j = x_j + 1$ the above equation reads

$$p \sum_{j=1}^N \sum_{\tilde{x}_1 < \dots < \tilde{x}_N} \psi(\tilde{x}_1, \dots, \tilde{x}_j - 1, \dots, \tilde{x}_N) (1 - \delta(\tilde{x}_j - \tilde{x}_{j-1} \bmod L, 1)) |\tilde{x}_1, \dots, \tilde{x}_N\rangle.$$

Second, we consider the term in Eq. (5.80) proportional to q . One finds with the change $\tilde{x}_j = x_j - 1 < x_{j+1} - 1 = \tilde{x}_{j+1} - 1$, thus $\tilde{x}_{j+1} - \tilde{x}_j > 1$ and $\tilde{x}_{j-1} = x_{j-1} < x_j - 1 = \tilde{x}_j$, that this term equals

$$q \sum_{\tilde{x}_1 < \dots < \tilde{x}_N} \psi(\tilde{x}_1, \dots, \tilde{x}_j + 1, \dots, \tilde{x}_N) (1 - \delta(\tilde{x}_{j+1} - \tilde{x}_j \bmod L, 1)) |\tilde{x}_1, \dots, \tilde{x}_N\rangle,$$

where the first constraint is realized via the delta term and the second constraint by the summation. By orthogonality of $|x_1, \dots, x_N\rangle$ the eigenvalue equation $\mathcal{K}|\psi\rangle = \lambda|\psi\rangle$

turns into $\binom{L}{N}$ equations for the coefficients $\psi(x_1, \dots, x_N)$,

$$\begin{aligned} & p \sum_{j=1}^N [1 - \delta((x_j - x_{j-1}) \bmod L, 1)] (\psi(x_1, \dots, x_j - 1, \dots, x_N) - U\psi(x_1, \dots, x_N)) \\ & + q \sum_{j=1}^N [1 - \delta((x_{j+1} - x_j) \bmod L, 1)] (\psi(x_1, \dots, x_j + 1, \dots, x_N) - U\psi(x_1, \dots, x_N)) \\ & = \lambda\psi(x_1, \dots, x_N). \end{aligned} \quad (5.81)$$

Now, we make the ansatz for the coefficients $\psi(x_1, \dots, x_N)$,

$$\psi(x_1, \dots, x_N) = \sum_{\tau \in S_N} A(\tau) \prod_{j=1}^N z_{\tau(j)}^{x_j}, \quad (5.82)$$

where S_N denotes the symmetric group. Its elements τ are permutations of $\{1, \dots, N\}$. The z_j 's are the Bethe roots and, together with $A(\tau)$, complex numbers.

Let us consider a configuration $x_1 < \dots < x_N$ where all particles have at least distance 1, so no particle is adjacent to any other particle. Additionally, we assume that $x_1 \neq 1$ and $x_N \neq N$, so we do not have to consider the pbc. Then Eq. (5.81) reduces to

$$\begin{aligned} & p \sum_{j=1}^N \psi(x_1, \dots, x_j - 1, \dots, x_N) + q \sum_{j=1}^N \psi(x_1, \dots, x_j + 1, \dots, x_N) - UN\psi(x_1, \dots, x_N) \\ & = \lambda\psi(x_1, \dots, x_N). \end{aligned} \quad (5.83)$$

Plugging the ansatz into the term proportional to p results in

$$\begin{aligned} \sum_{j=1}^N \psi(x_1, \dots, x_j - 1, \dots, x_N) &= \sum_{j=1}^N \sum_{\tau \in S_N} A(\tau) z_{\tau(j)}^{x_j-1} \prod_{l=1; l \neq j}^N z_{\tau(l)}^{x_l} \\ &= \sum_{\tau \in S_N} A(\tau) \prod_{l=1}^N z_{\tau(l)}^{x_l} \sum_{j=1}^N z_{\tau(j)}^{-1} \\ &= \sum_{j=1}^N z_j^{-1} \psi(x_1, \dots, x_N), \end{aligned}$$

where the sum over j is independent of τ since τ is a permutation of $\{1, \dots, N\}$. Similarly, one gets the analogous expression for the term proportional to q with the

change $z_j^{-1} \rightarrow z_j$. Consequently, Eq. (5.81) reduces to

$$\lambda = \sum_{j=1}^N (qz_j + pz_j^{-1} - U). \quad (5.84)$$

Eq. (5.84) relates the Bethe-ansatz eigenvalue λ of \mathcal{K} to the Bethe roots z_j . Next, we derive recurrent relations for the Bethe roots. For this, we replace λ in Eq. (5.81) with the right-hand side of Eq. (5.84).

We consider a configuration $x_1 < \dots < x_N$ with exactly two particles adjacent to each other, $x_{k+1} = x_k + 1$. To avoid dealing with the boundary conditions, we consider $x_1 \neq 1$ and $x_N \neq L$. For this configuration, Eq. (5.81) is

$$\begin{aligned} & p \sum_{j \neq k+1} \psi(\dots, x_j - 1, \dots) + q \sum_{j \neq k} \psi(\dots, x_j + 1, \dots) - U(N-1)\psi(x_1, \dots, x_N) \\ &= p \sum_j \psi(\dots, x_j - 1, \dots) + q \sum_j \psi(\dots, x_j + 1, \dots) - UN\psi(x_1, \dots, x_N) \end{aligned}$$

and therefore

$$p\psi(\dots, x_{k+1} - 1, \dots) + q\psi(\dots, x_k + 1, \dots) + U\psi(x_1, \dots, x_N) = 0.$$

By considering the chosen configuration, this equation reads in terms of the Bethe ansatz

$$\sum_{\tau \in S_N} A(\tau) \left(\prod_{l \neq k, k+1} z_{\tau(l)}^{x_l} \right) z_{\tau(k)}^{x_k} z_{\tau(k+1)}^{x_k} (p + qz_{\tau(k)}z_{\tau(k+1)} - Uz_{\tau(k+1)}) = 0. \quad (5.85)$$

Requiring that the last term in Eq. (5.85) vanishes for every τ is too restrictive. We note that the Bethe roots in Eq. (5.85) are invariant under swapping $\tau(k)$ with $\tau(k+1)$. Therefore, Eq. (5.85) can be fulfilled by letting

$$A(\tau) (p + qz_{\tau(k)}z_{\tau(k+1)} - Uz_{\tau(k+1)}) = -A(\tau') (p + qz_{\tau(k)}z_{\tau(k+1)} - Uz_{\tau(k)}), \quad (5.86)$$

where τ' differs from τ by swapping $\tau(k) \leftrightarrow \tau(k+1)$.

Next, we derive restrictions on A implied by the pbc. For a particle hopping across the boundary, we identified $\psi(0, x_2, \dots, x_N) = \psi(x_2, \dots, x_N, L)$. In terms of the Bethe ansatz, this expression reads

$$\sum_{\tau \in S_N} A(\tau) z_{\tau(1)}^0 z_{\tau(2)}^{x_2} \dots z_{\tau(N)}^{x_N} = \sum_{\tau \in S_N} A(\tau) z_{\tau(1)}^{x_2} \dots z_{\tau(N-1)}^{x_N} z_{\tau(N)}^L.$$

This equation can be fulfilled by letting

$$A(\tau) = A(\tau\sigma)z_{\tau(1)}^L, \quad (5.87)$$

for the permutation $\sigma \in S_N$ which shifts all indices by one, $\sigma(j) = j + 1$ and $\sigma(N) = 1$.

Combining Eq. (5.86) and Eq. (5.87) leads to the Bethe equations

$$z_j^L = \prod_{k=1; k \neq j}^N \left(-\frac{p + qz_j z_k - U z_j}{p + qz_j z_k - U z_k} \right). \quad (5.88)$$

Summarized, the Bethe ansatz eigenvalues λ for arbitrary U are given by

$$\lambda = \sum_{j=1}^N (p z_j^{-1} + q z_j - U), \quad (5.89)$$

where z_j are the so-called Bethe roots, which in turn are solutions of the recurrent relations given in Eq. (5.88).

By construction of the Bethe ansatz, all solutions (z_1, \dots, z_L) of Eq. (5.88) give rise to an eigenvalue λ of \mathcal{K} via Eq. (5.89). Numerical data indicates that in small systems, each eigenvalue is a sum of Bethe roots, but a formal proof of the completeness of the Bethe ansatz is lacking [361, 362]. However, in our finite ASEP system investigations, all eigenvalues conformed to the Bethe ansatz.

Bethe equations for TASEP with general U

In the case of TASEP with $q = 1$ and $p = 0$, the eigenvalues λ expressed in terms of Bethe roots simplify to

$$\lambda = \frac{1}{2} \sum_{j=1}^N (Z_j - U), \quad (5.90)$$

with

$$Z_j = 2z_j - U$$

representing scaled, shifted Bethe roots. We refer to the z_j 's and the Z_j 's as Bethe roots. The Bethe Eqs. (5.88) simplify to

$$z_j^L = \prod_{k=1; k \neq j}^N \left(-\frac{z_j z_k - U z_j}{z_j z_k - U z_k} \right) = \frac{z_j^N}{(z_j - U)^N} (-1)^{N-1} \prod_{k=1}^N \frac{z_k - U}{z_k},$$

so

$$z_j^{L-N} (z_j - U)^N = (-1)^{N-1} \prod_{k=1}^N \frac{z_k - U}{z_k}.$$

In terms of Z_k they are

$$(U + Z_j)^{L-N} (U - Z_j)^N = -2^L \prod_{k=1}^N \frac{Z_k - U}{Z_k + U}. \quad (5.91)$$

In Eqs. (5.91), the main simplification from the general p, q case is the independence of the right-hand side from j , which makes the solutions Z_j roots of the polynomial

$$P(z) = (U + z)^{L-N} (U - z)^N - Y, \quad (5.92)$$

with Y given by the right-hand side of Eq. (5.91). This not only simplifies the numerical computation of the Bethe roots Z_j , but also ensures their continuity in U [363]. Consequently, we will focus on the TASEP case for the remainder of Section 5.4.

5.4.2 Solving the Bethe equations numerically

In this section, we outline the numerical procedure for solving the TASEP Bethe equations. Solutions are obtained by self-consistently iterating Eqs. (5.91), similar to Ref. [257]. The challenge lies not in identifying a single solution to the Bethe equations but in systematically finding all $\binom{L}{N}$ solutions.

In the following, Y will denote an arbitrary complex number and the right-hand side of Eq. (5.91) will be referred to as

$$\tilde{Y}(Z_1, \dots, Z_N) = 2^L \prod_{k=1}^N \frac{Z_k - U}{Z_k + U}.$$

Then every solution Z_1, \dots, Z_N of Eq. (5.91) consists of roots of the polynomial P with $Y = \tilde{Y}(Z_1, \dots, Z_N)$.

To find solutions of the Bethe equations numerically one can proceed as follows. First, calculate the roots $Z_1^{(1)}, \dots, Z_L^{(1)}$ of P for an initial $Y^{(1)}$. Of these L roots of P choose N roots, $Z_1^{(1)}, \dots, Z_N^{(1)}$, and evaluate the next $Y^{(2)} = \tilde{Y}(Z_1^{(1)}, \dots, Z_N^{(1)})$. Again, the roots $Z_1^{(2)}, \dots, Z_L^{(2)}$ of P with $Y = Y^{(2)}$ are calculated and N roots $Z_1^{(1)}, \dots, Z_N^{(1)}$ are chosen to evaluate the next $Y^{(3)} = \tilde{Y}(Z_1^{(2)}, \dots, Z_N^{(2)})$. This procedure is then iterated until convergence all of the N chosen roots is reached, $Z_j^{(l)} \approx Z_j^{(l+1)}$ for all $1 \leq j \leq N$.

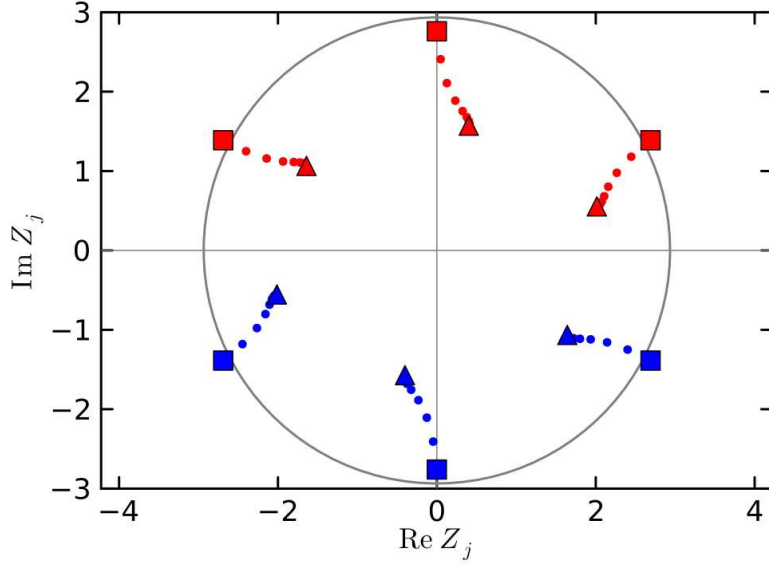


Fig. 5.5 Visualization of solving the Bethe Eqs. (5.91) of TASEP (pbc) for $L = 6$ and $N = 3$. All markers are roots of the polynomial P , given by Eq. (5.92), for different Y . The outer (square) markers are the roots for initial $Y^{(1)} = 10 \times 2^L$, the inner (triangles) markers for Y converged, and the circles denote roots of P for intermediate Y . Red markers (upper complex plane) are chosen to calculate the next Y . The gray circle has a radius of $|Y^{(1)}|^{1/L}$.

The convergence of this procedure presupposes consistency of the choice of the N roots out of L roots of the polynomial P [364, 289]. The first choice of $Z_1^{(1)}, \dots, Z_N^{(1)}$ out of $Z_1^{(1)}, \dots, Z_L^{(1)}$ is arbitrary. Subsequent roots $Z_1^{(l)}, \dots, Z_N^{(l)}$ are chosen to be closest to the previous roots

$$Z_j^{(l)} = \underset{Z_k^{(l)}: 1 \leq k \leq L}{\operatorname{argmin}} |Z_k^{(l)} - Z_j^{(l-1)}|, \quad (5.93)$$

where the minimum runs over all roots $Z_1^{(l)}, \dots, Z_L^{(l)}$ of P with $Y = Y^{(l)}$. If multiple $Z_k^{(l)}$ are close to $Z_j^{(l-1)}$ we do not update $Y^{(l+1)}$ with $Z_j^{(l)}$ but with a linear combination of $Z_j^{(l)}$ and $Z_j^{(l-1)}$, i.e. $Y^{(l+1)} = \tilde{Y}(\dots, dY Z_j^{(l)} + (1 - dY) Z_j^{(l-1)}, \dots)$ where $0 < dY \leq 1$ denotes the fraction of interpolation between $Z_j^{(l)}$ and $Z_j^{(l-1)}$.

The above-described procedure typically leads to convergence of $Z_1^{(l)}, \dots, Z_N^{(l)}$ and thus to a solution of the Bethe Eqs. (5.91). In Figure 5.5 we show the roots $Z_1^{(l)}, \dots, Z_6^{(l)}$ obtained during the algorithm for $L = 6$ and $N = 3$. The square markers denote the initial $Z_1^{(1)}, \dots, Z_6^{(1)}$ with $Y^{(1)} = 10 \times 2^L$, while the triangles denote the final and converged $Z_1^{(end)}, \dots, Z_6^{(end)}$ (relative or absolute error of Eq. (5.91) $< 10^{-3}$). The circles indicate intermediate roots. Initially, the 3 red squares (upper half-plane) are

chosen as $Z_1^{(1)}, \dots, Z_3^{(1)}$, and subsequent roots (upper half-plane in red) according to their previous closest roots. For visualization purposes, dY was chosen to be $dY = 0.5$.

To find all solutions to the Bethe Eqs. (5.91) systematically we use different combinations of initial $Y^{(1)}$ and initial root choices. Namely, we typically choose $Y^{(1)}$ with $|Y^{(1)}|^{1/L} \gg U$. This ensures that the roots of P with $Y = Y^{(1)}$ are close to the circle with radius $|Y^{(1)}|^{1/L}$. In Figure 5.5 the roots of P for $Y = Y^{(1)} = 10 \times 2^6$ denoted by the square markers are close to the circle with radius $2 \times 10^{1/6} \approx 2.9$. Then we solve the Bethe equations for every combination of N roots out of L . This typically gives us almost all solutions of the Bethe Eqs. (5.91). By iterating this procedure for a handful initial $Y^{(1)}$ we found all Bethe roots for the systems we investigated (up to $L = 22$).

We note that in Ref. [289] a transformation of the TASEP Bethe Eqs. (5.91) lead to a self-consistent solution algorithm, which is less dependent on the initial condition $Y^{(1)}$.

5.4.3 Structure of the Bethe roots

To examine the spectral boundary in terms of the Bethe roots, we will consider, in the complex plane, the Bethe roots (z_j or Z_j) corresponding to each of the $\binom{L}{N}$ eigenstates. There are thus $N \times \binom{L}{N}$ Bethe roots in total, for any value of U . Such plots are shown in Figure 5.6.

For $U = 0$, the Bethe roots z_j satisfy the equation $z_j^L = (Z_j/2)^L = (-1)^{N+1}$, and agree with the single-body eigenvalues of \mathcal{M} (stated in Eq. (5.20)). Therefore, the spectrum derived via the Bethe ansatz for $U = 0$ aligns with that of the non-interacting ASEP model discussed in Section 5.2, as expected. An illustrative example of the Bethe roots $Z_j = 2z_j$ for $U = 0$ is provided in Figure 5.6(a) for $L = 8$ and $N = 4$. Here, each solution of the Bethe equations contributes $N = 4$ roots, which together describe one of the $\binom{8}{4}$ eigenstates. We plot all the $4 \times \binom{8}{4}$ roots together in a single plot. Since for $U = 0$ every solution to the Bethe equations is a subset of the 8 single-body eigenvalues of \mathcal{M} , the union of all solutions is highly degenerate and only 8 unique markers show up in Fig. 5.6(a).

For $U > 0$ the degeneracy of the $U = 0$ case is lifted and the $4 \times \binom{8}{4}$ Bethe roots Z_j become distinct, as observed in Fig. 5.6(b-d) for $U = 0.33$, 0.66 , and $U = 1$, respectively. The continuity of Bethe roots z_j in U suggests that for small U , these roots should be proximate to the L th roots of $(-1)^{N+1}$. Numerically, this is confirmed as the Bethe roots z_j tend to cluster around the L th roots of $(-1)^{N+1}$ for small U . As depicted in Figure 5.6(b) and (c) for $U = 0.33$ and $U = 0.66$ respectively, the Z_j 's distinctly form

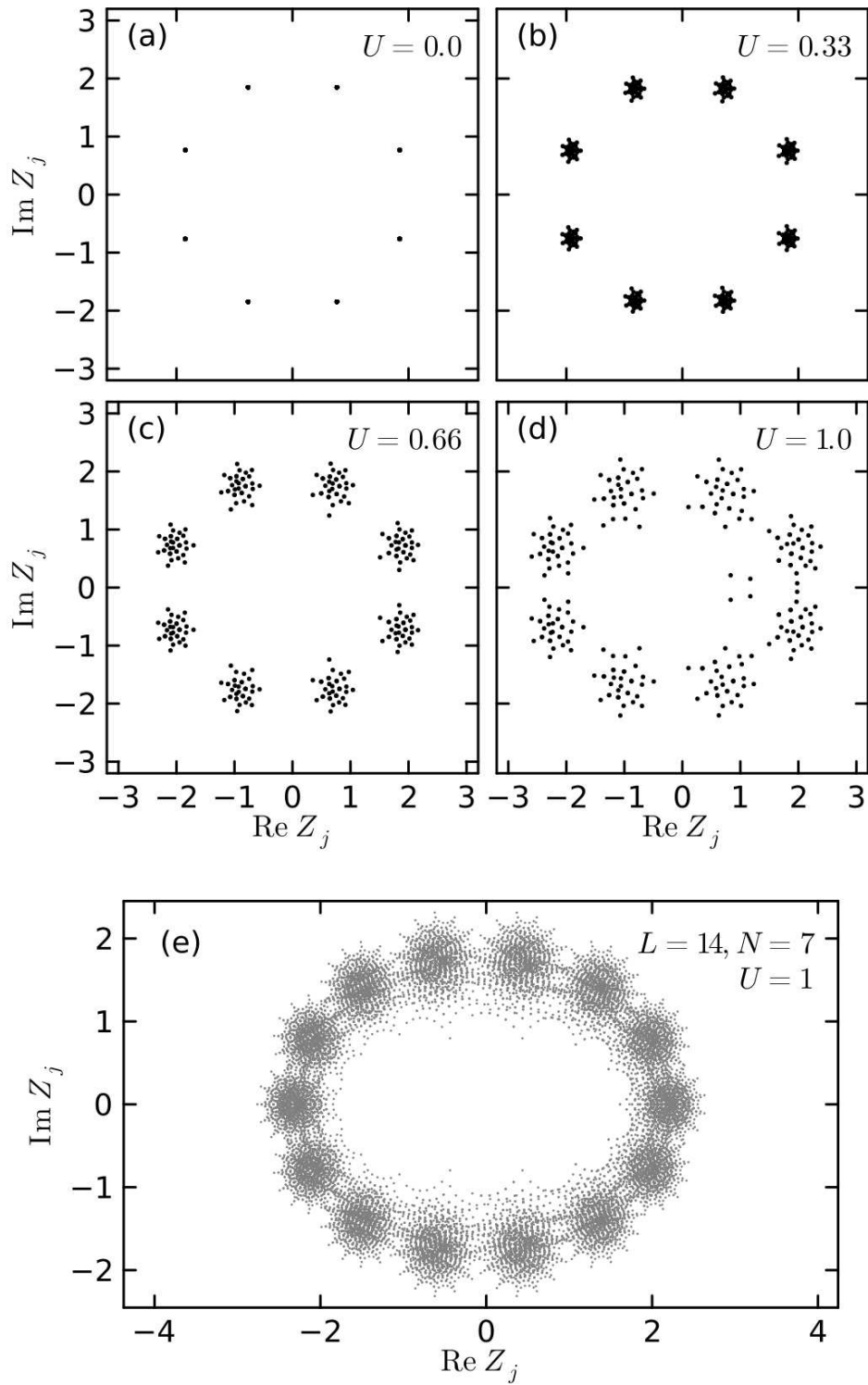


Fig. 5.6 **(a-d)** All $N \times \binom{L}{N}$ Bethe roots Z_j of the TASEP with $L = 8$ and $N = 4$ for different values of U . **(e)** Bethe roots for $L = 14$ and $N = 7$ with $U = 1$.

$L = 8$ clusters around the Bethe roots for $U = 0$. This clustering is even discernible for $U = 1$, as shown in Figure 5.6(d), where the $L = 8$ clusters remain identifiable.

For larger L , the Bethe root clusters overlap at $U = 1$, evident from Fig. 5.6(e) for $L = 14$ and $N = 7$. However, the statistical width of these clusters diminishes with larger L . This is demonstrated in Fig. 5.8, where the average cluster width decreases as $L^{-1/2}$ in the thermodynamic limit with $\rho = N/L = 1/2$ and $N, L \rightarrow \infty$.

We define the locations and widths of these clusters by fitting a Gaussian mixture model of L independent Gaussians with complex means to the Bethe roots. The Bethe root distribution is approximated as $\frac{1}{L} \sum_{j=1}^L f_j$, with f_j representing Gaussian densities. We label the Gaussians of the optimal fit as \mathcal{N}_j for $j = 1, \dots, L$, each characterized by its mean μ_j (in \mathbb{C}) and standard deviation σ_j (in $\mathbb{R}_{\geq 0}$).

5.4.4 Structure of the many-body spectrum

In this section, we demonstrate that by considering only the centers μ_j and widths σ_j of the Bethe root clusters, rather than their specific structure, it is possible to approximate a many-body spectrum that exhibits characteristics of the TASEP many-body spectrum, particularly its spiky boundary.

For $U = 0$ each many-body eigenvalue λ is a sum of N out of L single-body eigenvalues. Specifically, λ is given by

$$\lambda = \sum_{j=1}^L s_j \nu_j = \sum_{s_j \neq 0} \nu_j, \quad (5.94)$$

where $s \in \{0, 1\}^L$ is a configuration with $\sum_j s_j = N$ and ν_j are the single-particle eigenvalues determined in Section 5.2.3. According to Eq. (5.90), every many-body eigenvalue of the TASEP ($U = 1$) corresponds to a sum of N Bethe roots and by the continuation from $U = 1$ to $U = 0$ each Bethe root belongs to one of the L clusters. Instead of summing solutions of the Bethe Eqs. (5.91), we employ a statistical ansatz and consider random many-body eigenvalues of the form

$$\lambda_{rand} = \sum_{j=1}^L s_j \mathcal{N}_j = \mathcal{N}_s, \quad (5.95)$$

where \mathcal{N}_s denotes a Gaussian with mean $\mu_s = \sum_{j=1}^L s_j \mu_j$ and variance $\sigma_s^2 = \sum_{j=1}^L s_j \sigma_j^2$. We refer to \mathcal{N}_s as many-body Gaussians and denote their density by f_s . We let the random variables \mathcal{N}_s be independent for different configurations s . The full random many-body spectrum is a superposition of many-body Gaussians \mathcal{N}_s for all

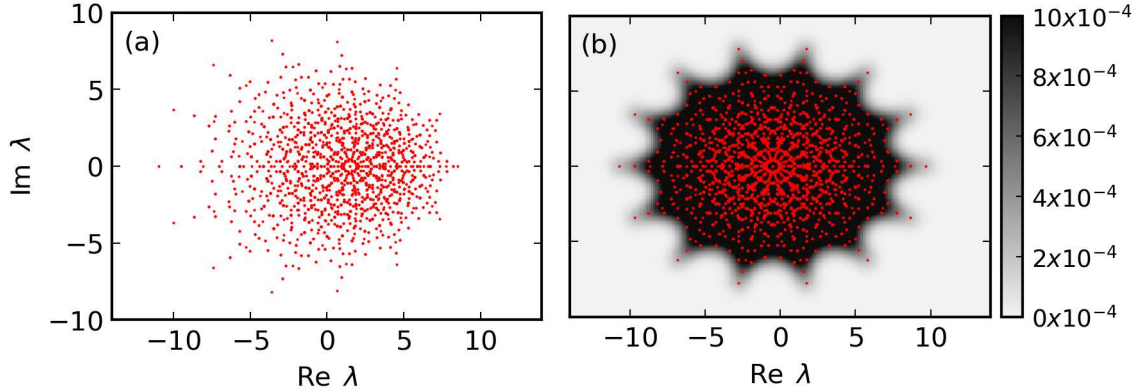


Fig. 5.7 (a) The many-body spectrum of TASEP with $L = 14$ and $N = 7$ (multiplied by 2 and shifted by N). (b) Probability density function of the many-body spectrum of the random Bethe roots Z for $L = 14$ and $N = 7$ capped at 10^{-3} . Red dots are the means of the complex Gaussians.

configurations $s \in \{0, 1\}^L$ with $\sum_j s_j = N$. The density of this many-body spectrum is given by

$$\frac{1}{\mathcal{Z}} \sum_{\substack{s \in \{0, 1\}^L \\ s_1 + \dots + s_L = N}} f_s, \quad (5.96)$$

where $\mathcal{Z} = \binom{L}{N}$ is a normalization constant. The many-body spectrum of the TASEP is a specific sample of the distribution in Eq. (5.96). For $U = 0$ the random spectrum becomes deterministic and agrees with the non-interacting many-body spectrum presented in Section 5.2.

In Figure (5.7)(b), we present the probability density from Eq. (5.96) for $L = 14$, $N = 7$, and $U = 1$, with the density capped at 10^{-3} for clarity. The red markers indicate the means μ_s of the many-body Gaussians \mathcal{N}_s . Both the discrete means and the continuous density exhibit pronounced spikes at the boundary. When these means are compared to the many-body spectrum of the TASEP shown in Figure 5.7(a), even finer details of the TASEP spectrum are discernible in the structure of the means.

The boundary of the random many-body spectrum is mainly determined by Gaussians \mathcal{N}_s , associated with domain wall configurations of one or two domain walls, separated by at most one empty site. This is a consequence of the exponential decay of Gaussian probability density functions. These configurations are identical to those defining the spectral boundary in the non-interacting case.

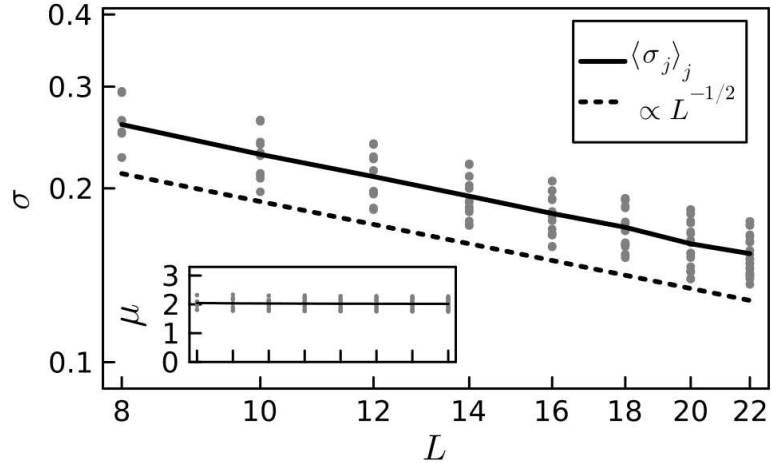


Fig. 5.8 The width σ of the complex Gaussians fitted to the clusters of the Bethe roots for $U = 1$ at half-filling $N = L/2$. The solid line denotes the average $\langle \sigma_j \rangle_j = \frac{1}{L} \sum_j \sigma_j$ of the cluster widths and the dotted line guides the eye to $L^{-1/2}$. The **inset** shows the absolute value of the centers of the complex Gaussians $|\mu|$. Black solid line indicates the average.

The random Bethe spectrum and the TASEP spectrum share a remarkably similar overall shape. However, differences do exist. The boundary of the random Bethe spectrum is not skewed towards larger negative real parts, as is the boundary of the TASEP spectrum. This is attributed to the additional structure in the Bethe root clusters seen in Figure 5.6, which is not represented by rotationally invariant Gaussians.

5.4.5 “Thermodynamic limit”

Similar to the non-interacting case with $U = 0$, we will argue that the spiky boundary persists in the thermodynamic limit as L and N increase while maintaining a fixed density $\rho = N/L$.

Let us first focus on the means μ_s of the many-body Gaussians \mathcal{N}_s , depicted as red dots in Figure 5.7. According to the inset of Figure 5.8, the absolute values of $|\mu_j|$ appear to be independent of L . This independence suggests that the non-interacting scenario, presented in Section 5.2, also applies to the many-body Gaussian centers μ_s . They scale as $\propto L$. The spiky structure of the boundary is of $O(1)$; more precisely, the tip distance (d_t) and boundary depth (d_b), investigated in Section 5.2.4, are of $O(1)$. Hence, the spiky structure of the boundary Gaussian centers is maintained in the thermodynamic limit.

However, this doesn't automatically imply that the spiky spectral boundary of the random spectrum, as defined in Eq. (5.96), persists in the thermodynamic limit. For this to hold true, the widths σ_j of the Gaussians \mathcal{N}_j in the mixture model must decrease sufficiently fast. More precisely, the widths of the corresponding many-body Gaussians \mathcal{N}_s must be (at most) of the same order as the length scale of the spike structure, which is $O(1)$.

Figure 5.8 displays the widths σ_j of \mathcal{N}_j for the TASEP case ($U = 1$) at half-filling ($N = L/2$), with L ranging from 8 to 22. The cluster widths σ_j vary. They are larger for clusters with smaller $|\text{Re } Z|$ and smaller for those with larger $|\text{Re } Z|$. This is observed in Figure 5.6(e) as well. Despite this variation, the widths σ_j are centered around their average $\langle \sigma_j \rangle_j = \frac{1}{L} \sum_{j=1}^L \sigma_j$. This average decreases approximately as $\propto L^{-1/2}$, as shown by the dashed line in Figure 5.8. Consequently, the variance $\sigma_s^2 = \sum_{j=1}^L s_j \sigma_j^2$ of the many-body Gaussians \mathcal{N}_s scales as $\propto 1$ and so does the standard deviation σ_s . The spiky structure of the statistical many-body spectrum for $U = 1$ therefore persists in the thermodynamic limit.

5.5 The random matrix picture

In the previous sections, we showed that the spectral boundary spikes of the TASEP are a consequence of the many-body spectrum being generated by summing single-particle eigenvalues or Bethe root clusters. In this section, we demonstrate that the spiky spectral boundary is characteristic for a broad range of systems, extending beyond those solvable by the (coordinate) Bethe ansatz. Specifically, this feature is typical in systems where the many-body graph exhibits a particular cycle structure, where all cycle lengths are integer multiples of the spike count.

5.5.1 From TASEP to graphs

The matrix elements of the non-interacting TASEP \mathcal{M} are either zero or one. Thus, \mathcal{M} is the adjacency matrix of a directed graph. This graph, termed the many-body graph of TASEP, has vertices representing particle configurations in the chain and edges indicating permissible transitions. For TASEP with $U = 1$, its generator matrix \mathcal{K} is the negative Laplacian of this graph.

5.5.2 Cycles of TASEP

The permissible transitions between particle configurations impose constraints on the structure of the many-body graph. Our focus is on the nature of cycles in this graph.

The cycle lengths in the TASEP many-body graph are divisible by L for pbc and by $L + 1$ for obc [288]. This is evident in cycles among configurations $s \in \{0, 1\}^L$, which only contain a single particle, $s_j = \delta_{jk}$. These cycles consist of L particle movements ($L + 1$ for obc) such that the particle arrives at its original position. For general configurations s let us restrict to the pbc case. The following argument applies to the obc case with $L + 1$ instead of L as well. Consider the sum $X(s) = \sum_{j=1}^L js_j \bmod L$ of particle positions in the configuration s [288]. This sum X partitions the many-body graph of TASEP into L subgraphs $X_j = \{s : X(s) = j\}$ for $j = 0, \dots, L - 1$. Within each X_j no two vertices are connected. The only allowed transitions are between configurations of X_j and $X_{j+1 \bmod L}$. Thus, for returning to a configuration s an integer multiple of L transitions have to be performed and cycle lengths of the many-body graph are divisible by L .

As discussed in Section 1.1.5, the number of closed walks with length k is given by $\text{tr}(\mathcal{M}^k)$. Especially, if $\text{tr}(\mathcal{M}^k) = 0$ then the graph does not contain any closed walks, thus any cycle, of length k . In Figure 5.9(e), we depict $\text{tr}(\mathcal{M}^k) + 1$ as blue squares as a function of $k = 1, \dots, 2L$ for a system of $L = 12$ sites and pbc with $N = 6$ particles. The addition of $+1$ facilitates a logarithmic scale on the y-axis. Here, $\text{tr}(\mathcal{M}^k)$ equals zero for all values of k not divisible by L , indicating the absence of cycles in the graph with length $k \bmod L \neq 0$. Similarly, for obc, $\text{tr}(\mathcal{M})^k = 0$ if and only if $k \bmod L + 1 = 0$ (not shown).

5.5.3 Random graph model

To demonstrate that the spiky spectral boundary is a generic feature, we compare the TASEP spectrum with the spectral density of a random graph ensemble. The distribution of the random graphs is the uniform distribution over all graphs with D vertices, n edges and the property that all cycle lengths are divisible by L . (We discuss the pbc case. The obc case is equivalent by changing L to $L + 1$.)

To sample a random graph from such an ensemble, one starts with a directed cycle on D vertices. Then, one randomly chooses a vertex and traverses the graph randomly along $L - 1$ edges. The vertex reached after $L - 1$ steps is connected back to the starting vertex, creating a closed walk of length L . This process is repeated until the graph contains n edges. If the length of the initial cycle on all D vertices is divisible

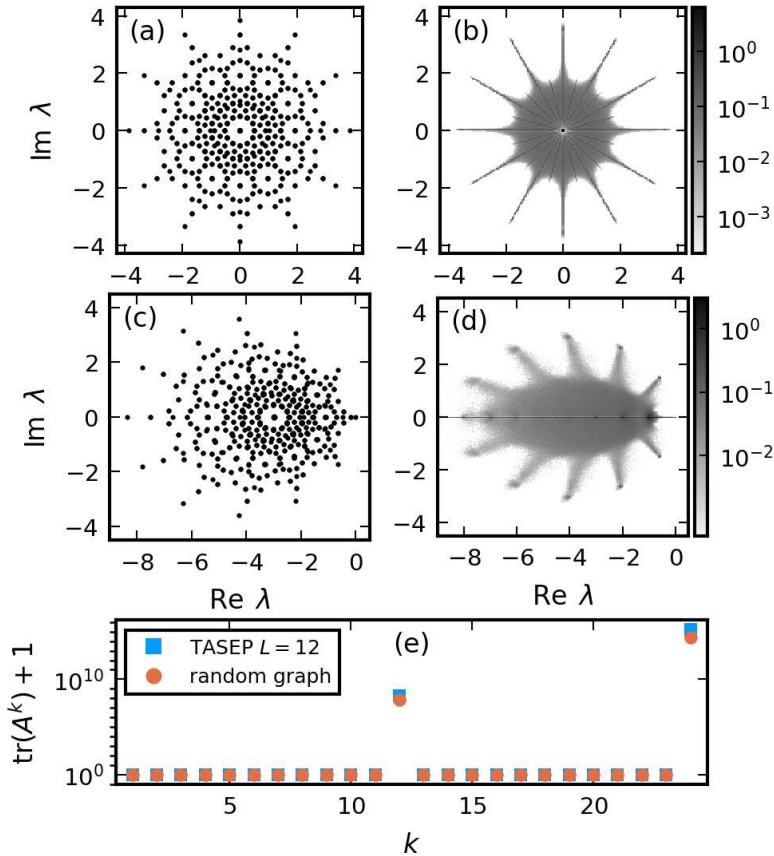


Fig. 5.9 TASEP spectrum (pbc) with $L = 12$ and $N = 6$ in (a) $U = 0$ and (c) $U = 1$. In (b,d) spectral density of random graphs with cycle length divisible by L ; in (b) of the adjacency matrix and in (d) of the negative (combinatorial) Laplacian. In (e) traces of powers of the non-interacting TASEP generator $A = \mathcal{M}$ (squares) and adjacency matrices A of random graphs (circles).

by L , then the presented procedure ensures that *all* cycle lengths are divisible by L . We expect this algorithm to sample approximately uniformly from the above described random graph ensemble.

Figure 5.9 compares the random graph ensemble to the TASEP with $L = 12$ sites and $N = 6$ particles. Quantities of the random graph ensemble are averaged over 2,000 samples. The number of vertices is $D = 924$, matching the Hilbert space dimension of the TASEP, and the number of edges was chosen accordingly.

In Figure 5.9(e), we present $\text{tr}(A^k) + 1$ as red circles, where A is the adjacency matrix of the random graphs. There, $\text{tr}(A^k)$ is zero for all k that are not integer multiple of L . Whenever k is an integer multiple of L , $\text{tr}(A^k)$ is comparable in magnitude to $\text{tr}(\mathcal{M}^k)$ for TASEP. This similarity suggests that the number of closed walks in the random graph ensemble is on par with that in the TASEP many-body graph.

Figure 5.9(a-d) show a comparison between spectra of the random graph ensemble and the TASEP. In (a) and (b), we show the spectrum of the non-interacting TASEP alongside the estimated spectral density of the adjacency matrix. Both have L distinct spikes. In Figure 5.9(c) and (d), we present the spectrum of TASEP ($U = 1$) and the spectral density of the negative graph Laplacian. Notably, the random graph Laplacian also presents L pronounced spikes. The spike patterns, particularly their “bending” towards the left, show a resemblance to the TASEP spikes. The overall shape of the Laplacian spectral density (ignoring the spikes) has a spindle-like form, characteristic of sparse random generators of continuous-time Markov chains discussed in Chapter 4.

5.6 Discussion

In this chapter, we explored the connections between the ASEP, free fermion models, and RMT, focusing on the distinctive spiky spectral boundary. We reformulated the generator of the ASEP as non-Hermitian fermionic models with a variable interaction parameter U , where $U = 1$ corresponds to the standard ASEP. We analytically demonstrated that in the non-interacting ASEP ($U = 0$), this spiky spectral boundary arises from summing single-particle eigenvalues positioned on ellipses (circles for TASEP). For pbc, we extended this concept to interacting TASEP ($U = 1$), showing that the spiky boundary remains and originates from the summation of clustered Bethe roots. Lastly, we confirmed the robustness of this spiky boundary by considering only the cycle structure in the many-body graph, revealing that corresponding random graphs exhibit a similar spiky spectral boundary.

This research opens up several questions for further exploration. We demonstrated the spiky spectral boundary in TASEP, largely attributed to Bethe roots clustering. It’s intriguing to consider whether such clustering also occurs in ASEP. The straightforward connection between TASEP and ASEP in their non-interacting forms suggests that the spiky spectral boundary might extend to standard ASEP (with $U = 1$) as well. However, it remains to be seen how introducing interactions influences Bethe roots clustering and the potential emergence of a spiky spectral boundary.

In this chapter, we concentrated on the Bethe ansatz for pbc. The ASEP with obc is also solvable via the Bethe ansatz, though the equations are more complex [280, 365–367]. A promising area for future research is to explore whether a clustering of Bethe roots in the obc case similarly results in a spiky spectral boundary.

The random graphs following the hypotrochoidic law usually lack cycles shorter than L but can have cycles longer than L . However, the random graph ensemble we

introduced in this chapter deviates from this standard hypotrochoidic law, likely due to its more restricted cycle structure, where all cycles are of lengths divisible by L . Extending the hypotrochoidic law to encompass this specific graph ensemble would be a valuable advancement.

This study concentrated on the spiky spectral boundary of the ASEP. Formation of spikes in the complex plane have been observed in the off-diagonals of reduced density matrices in the symmetric simple exclusion process [156] and the observable representation of Ising chain Glauber dynamics [368]. These observations together with the robustness of the spiky spectral boundary to perturbations make the investigation of other models, both classical and quantum, that possess a similar cycle structure in their many-body graphs or comparable trace correlations in their generator matrices, an intriguing direction for future research.

Chapter 6

Summary

The content of this thesis is placed in the broad context of studying many-body systems through the lens of random matrix theory (RMT). We focused on two types of many-body systems: quantum and stochastic many-body systems. In the quantum case we investigated a specific system — the Bose-Hubbard model. We studied several aspects of this model related to quantum chaos and the Eigenstate Thermalization Hypothesis (ETH). In the case of stochastic many-body systems we focused on generators of Markovian processes. We investigated the spectra of generic systems — an ensemble of random generator matrices — and the spectral boundary of a specific system — the Asymmetric Simple Exclusion Process (ASEP).

In Chapter 2, we investigated eigenstate-to-eigenstate fluctuations of expectation values of local observables (EEV fluctuations) in the 1D Bose-Hubbard model. The ETH predicts that in the thermodynamic limit of increasing lattice size and fixed particle density these fluctuations decrease in the Hilbert space dimension D as $D^{-1/2}$. In this thesis, we investigated EEV fluctuations in the classical limit of fixed lattice size and increasing particle density. We showed analytically that for RMT-like eigenstates, EEV fluctuations decrease as $D^{-1/2}$ after appropriate renormalization of the observables. Fluctuations of mid-spectrum Bose-Hubbard eigenstates conform to this decrease for large lattice sizes. For small lattice sizes however, EEV fluctuations decrease as a power-law in D^{-e} , but with an exponent e smaller than 1/2. We showed that this anomalous scaling is not explained by two-point correlations between eigenstates but is due to subtle higher-order correlations of eigenstate coefficients.

Partly motivated by the anomalous EEV fluctuation scaling, in Chapter 3, we studied the Bose-Hubbard model on three sites in detail. We compared the quantum model to its classical limit — the discrete nonlinear Schrödinger equation (DNLS). For three sites, the Bose-Hubbard model is known to be neither integrable nor strongly

chaotic but shows mixed behavior. We calculated several quantities used to demarcate chaos from integrability. In the quantum model we studied correlations of energy eigenvalues, statistics of eigenstates and the decrease of EEV fluctuations. In each case, the degree of adherence to RMT predictions quantifies how chaotic the quantum system is. In the DNLS, we calculated Lyapunov exponents. As a function of energy and interaction strength, we demonstrated a strong overall correspondence between all four measures of chaos.

In Chapter 4, we presented a model of random sparse generator matrices of Markovian evolution. We investigated its spectral properties, particularly, the first two moments of the eigenvalue distribution and the spectral gap, the inverse of the relaxation time. The dependence of the eigenvalue moments on the sparsity φ — number of non-zero elements per column — implied divergence of the bulk spectrum from the stationary eigenvalue, whenever φ increased with the matrix size D . However, in the limit of large D , the spectral gap decreases for constant φ (single-particle case) and is constant (up to logarithmic corrections) for $\varphi \sim \log D$ (many-body case). These results show that sparsity cures the large spectral gap, leading to unphysically long relaxation times, which is characteristic for nonsparse random generators.

In Chapter 5, we focused on the spectrum of a particular generator of Markovian evolution — the ASEP. The spectral boundary of the ASEP features characteristic spikes: L spikes for periodic boundary conditions (pbc) and $L + 1$ for open boundary conditions (obc), with L being the system size. We elucidated the emergence of these spikes in several ways. First, we expressed the generator as an interacting non-Hermitian fermion model. In the noninteracting case, the spectral boundary spikes emerged as sums of single-particle eigenvalues on ellipses. Second, by invoking Bethe ansatz techniques we interpolated between the noninteracting and the ASEP limit. In the totally ASEP (TASEP) case, the spikes stem from clustering of Bethe roots. Third, we investigated adjacency and Laplacian matrices of random graphs with cycle lengths divisible by the spike count. In the many-body graph of the TASEP all cycle lengths are divisible by L ($L + 1$ for obc). We demonstrated that the spectra of these random graphs have L ($L + 1$) prominent spikes akin to spectra of random matrices with higher-order trace correlations.

References

- [1] F. J. Dyson, J. Math. Phys. **3**, 140 (1962).
- [2] G. Livan, M. Novaes, and P. Vivo, *Introduction to Random Matrices* (Springer, 2018).
- [3] M. L. Mehta, *Random matrices* (Elsevier, 2004).
- [4] P. J. Forrester, *Log-Gases and Random Matrices* (Princeton University Press, 2010).
- [5] G. Akemann, J. Baik, and P. Di Francesco, eds., *The Oxford Handbook of Random Matrix Theory* (Oxford University Press, 2015).
- [6] A. Edelman and N. R. Rao, Acta Numerica **14**, 233 (2005).
- [7] E. P. Wigner, in *Conference on Neutron Physics by Time-of-flight* (1956) pp. 59–70.
- [8] R. L. Schilling, *Measures, Integrals and Martingales* (Cambridge University Press, 2005).
- [9] F. J. Dyson, J. Math. Phys. **3**, 1199 (1962).
- [10] M. R. Zirnbauer, in *The Oxford Handbook of Random Matrix Theory* (Oxford University Press, 2015) pp. 43–65.
- [11] J. C. Baez, Found. Phys. **42**, 819 (2012).
- [12] C. Wall, Journal für die reine und angewandte Mathematik **1964**, 187 (1964).
- [13] A. Altland and M. R. Zirnbauer, Phys. Rev. B **55**, 1142 (1997).
- [14] A. Altland, B. D. Simons, and M. R. Zirnbauer, Phys. Rep. **359**, 283 (2002).
- [15] M. R. Zirnbauer, “Symmetry classes in random matrix theory,” (2004), arXiv:math-ph/0404058 .
- [16] A. Kitaev, AIP Conf. Proc. **1134**, 22 (2009).
- [17] S. Ryu, A. P. Schnyder, A. Furusaki, and A. W. W. Ludwig, New J. Phys. **12**, 065010 (2010).
- [18] D. S. Freed and G. W. Moore, Ann. Henri Poincaré **14**, 1927 (2013).

- [19] F. J. Dyson, *J. Math. Phys.* **3**, 157 (1962).
- [20] F. J. Dyson, *J. Math. Phys.* **3**, 166 (1962).
- [21] J. Ginibre, *J. Math. Phys.* **6**, 440 (1965).
- [22] N. Lehmann and H.-J. Sommers, *Phys. Rev. Lett.* **67**, 941 (1991).
- [23] E. P. Wigner, *Annals of Mathematics* **67**, 325 (1958).
- [24] I. Dumitriu and A. Edelman, *J. Math. Phys.* **43**, 5830 (2002).
- [25] W. Buijsman, V. Cheianov, and V. Gritsev, *Phys. Rev. Lett.* **122**, 180601 (2019).
- [26] Á. L. Corps and A. Relaño, *Phys. Rev. E* **101**, 022222 (2020).
- [27] L. A. Pastur, *Theor. Math. Phys.* **10**, 67 (1972).
- [28] B. Eynard, T. Kimura, and S. Ribault, “Random matrices,” (2018), arXiv:1510.04430 .
- [29] W. Bryc, A. Dembo, and T. Jiang, *Ann. Probab.* **34**, 1 (2006).
- [30] A. D. Mirlin and Y. V. Fyodorov, *J. Phys. A: Math. Gen.* **24**, 2273 (1991).
- [31] L. Erdős, A. Knowles, H.-T. Yau, and J. Yin, *Ann. Probab.* **41**, 2279 (2013).
- [32] G. Casati, L. Molinari, and F. Izrailev, *Phys. Rev. Lett.* **64**, 1851 (1990).
- [33] G. Casati, F. Izrailev, and L. Molinari, *J. Phys. A: Math. Gen.* **24**, 4755 (1991).
- [34] Y. V. Fyodorov and A. D. Mirlin, *Phys. Rev. Lett.* **67**, 2405 (1991).
- [35] Y. V. Fyodorov and A. D. Mirlin, *Phys. Rev. B* **52**, R11580 (1995).
- [36] A. D. Mirlin, Y. V. Fyodorov, F.-M. Dittes, J. Quezada, and T. H. Seligman, *Phys. Rev. E* **54**, 3221 (1996).
- [37] Y. V. Fyodorov, A. Ossipov, and A. Rodriguez, *J. Stat. Mech.* **2009**, L12001 (2009).
- [38] S. Sodin, *Annals of Mathematics* **172**, 2223 (2010).
- [39] L. Erdős and A. Knowles, *Commun. Math. Phys.* **303**, 509 (2011).
- [40] L. Erdős, A. Knowles, H.-T. Yau, and J. Yin, *Commun. Math. Phys.* **323**, 367 (2013).
- [41] L. Erdős, A. Knowles, and H.-T. Yau, *Ann. Henri Poincaré* **14**, 1837 (2013).
- [42] P. Bourgade, in *Proceedings of the International Congress of Mathematicians: Rio de Janeiro 2018* (2018) pp. 2759–2783.
- [43] V. L. Girko, *Theory Probab. Its Appl.* **29**, 694 (1985).

- [44] T. Tao and V. Vu, *Acta Math.* **206**, 127 (2011).
- [45] V. L. Girko, *Theory Probab. Its Appl.* **30**, 677 (1986).
- [46] H. J. Sommers, A. Crisanti, H. Sompolinsky, and Y. Stein, *Phys. Rev. Lett.* **60**, 1895 (1988).
- [47] P. V. Aceituno, T. Rogers, and H. Schomerus, *Phys. Rev. E* **100**, 010302 (2019).
- [48] L. Erdős, H.-T. Yau, and J. Yin, *Probab. Theory Relat. Fields* **154**, 341 (2012).
- [49] L. Erdős, J. Ramírez, B. Schlein, T. , V. Vu, and H.-T. Yau, *Math. Res. Lett.* **17**, 667 (2010).
- [50] V. Oganesyan and D. A. Huse, *Phys. Rev. B* **75**, 155111 (2007).
- [51] Y. Y. Atas, E. Bogomolny, O. Giraud, and G. Roux, *Phys. Rev. Lett.* **110**, 084101 (2013).
- [52] L. Sá, P. Ribeiro, and T. Prosen, *Phys. Rev. X* **10**, 021019 (2020).
- [53] T. Tao and V. Vu, *Ann. Probab.* **43**, 782 (2015).
- [54] H. A. David and H. N. Nagaraja, *Order statistics* (John Wiley, 2003).
- [55] I. Pinelis, *ESAIM: PS* **19**, 24 (2015).
- [56] I. Pinelis and R. Molzon, *Electron. J. Statist.* **10**, 1001 (2016).
- [57] L. Erdős, B. Schlein, and H.-T. Yau, *Ann. Probab.* **37**, 815 (2009).
- [58] A. Knowles and J. Yin, *Probab. Theory Relat. Fields* **155**, 543 (2013).
- [59] T. Spencer, in *The Oxford Handbook of Random Matrix Theory* (Oxford University Press, 2015) pp. 470–488.
- [60] F. R. Chung, *Spectral graph theory* (American Mathematical Society, 1997).
- [61] F. Chung, *Annals of Combinatorics* **9**, 1 (2005).
- [62] S. Hoory, N. Linial, and A. Wigderson, *Bull. Amer. Math. Soc.* **43**, 439 (2006).
- [63] A. Einstein, *Verh. Deutsch. Phys. Ges.* **19**, 82 (1917).
- [64] H. Schuster and W. Just, *Deterministic Chaos: An Introduction* (Wiley, 2006).
- [65] F. Haake, *Quantum Signatures of Chaos* (Springer, 2010).
- [66] H.-J. Stöckmann, *Quantum Chaos* (Cambridge University Press, 1999).
- [67] D. Braun, *Dissipative Quantum Chaos and Decoherence* (Springer, 2001).
- [68] O. Bohigas, M. J. Giannoni, and C. Schmit, *Phys. Rev. Lett.* **52**, 1 (1984).
- [69] O. Bohigas, M. J. Giannoni, and C. Schmit, *J. Physique Lett.* **45**, 1015 (1984).

- [70] M. Berry and M. Tabor, Proc. R. Soc. Lond. A. **356**, 375 (1977).
- [71] M. Feingold and A. Peres, Physica D **9**, 433 (1983).
- [72] M. Feingold, N. Moiseyev, and A. Peres, Phys. Rev. A **30**, 509 (1984).
- [73] L. E. Ballentine, Phys. Rev. A **70**, 032111 (2004).
- [74] Y. Fan, S. Gnutzmann, and Y. Liang, Phys. Rev. E **96**, 062207 (2017).
- [75] D. Mondal, S. Sinha, and S. Sinha, Phys. Rev. E **102**, 020101 (2020).
- [76] C. Weiss and N. Teichmann, Phys. Rev. Lett. **100**, 140408 (2008).
- [77] A. R. Kolovsky, Int. J. Mod. Phys. B **30**, 1630009 (2016).
- [78] M. Rautenberg and M. Gärttner, Phys. Rev. A **101**, 053604 (2020).
- [79] M. A. Bastarrachea-Magnani, S. Lerma-Hernández, and J. G. Hirsch, Phys. Rev. A **89**, 032102 (2014).
- [80] M. A. Bastarrachea-Magnani, B. L. del Carpio, S. Lerma-Hernández, and J. G. Hirsch, Phys. Scr. **90**, 068015 (2015).
- [81] S. Ray, A. Ghosh, and S. Sinha, Phys. Rev. E **94**, 032103 (2016).
- [82] M. A. Bastarrachea-Magnani, B. López-del Carpio, J. Chávez-Carlos, S. Lerma-Hernández, and J. G. Hirsch, Phys. Rev. E **93**, 022215 (2016).
- [83] J. Chávez-Carlos, B. López-del Carpio, M. A. Bastarrachea-Magnani, P. Stránský, S. Lerma-Hernández, L. F. Santos, and J. G. Hirsch, Phys. Rev. Lett. **122**, 024101 (2019).
- [84] R. Lewis-Swan, A. Safavi-Naini, J. J. Bollinger, and A. M. Rey, Nat. Commun. **10**, 1 (2019).
- [85] A. Lerose and S. Pappalardi, Phys. Rev. A **102**, 032404 (2020).
- [86] Q. Wang and M. Robnik, Phys. Rev. E **102**, 032212 (2020).
- [87] D. Villaseñor, S. Pilatowsky-Cameo, M. A. Bastarrachea-Magnani, S. Lerma-Hernández, L. F. Santos, and J. G. Hirsch, New J. Phys. **22**, 063036 (2020).
- [88] S. Pilatowsky-Cameo, D. Villaseñor, M. A. Bastarrachea-Magnani, S. Lerma-Hernández, L. F. Santos, and J. G. Hirsch, New J. Phys. **23**, 033045 (2021).
- [89] Q. Wang and M. Robnik, Phys. Rev. E **109**, 024225 (2024).
- [90] S. Pappalardi, A. Polkovnikov, and A. Silva, SciPost Phys. **9**, 21 (2020).
- [91] D. T. Robb and L. E. Reichl, Phys. Rev. E **57**, 2458 (1998).
- [92] J. Emerson and L. Ballentine, Phys. Rev. A **63**, 052103 (2001).

- [93] S. Pappalardi, A. Russomanno, B. Žunkovič, F. Iemini, A. Silva, and R. Fazio, Phys. Rev. B **98**, 134303 (2018).
- [94] S. Ray, S. Sinha, and D. Sen, Phys. Rev. E **100**, 052129 (2019).
- [95] D. J. Luitz and Y. Bar Lev, Phys. Rev. Lett. **117**, 170404 (2016).
- [96] W. Beugeling, A. Bäcker, R. Moessner, and M. Haque, Phys. Rev. E **98**, 022204 (2018).
- [97] I. M. Khaymovich, M. Haque, and P. A. McClarty, Phys. Rev. Lett. **122**, 070601 (2019).
- [98] A. Bäcker, M. Haque, and I. M. Khaymovich, Phys. Rev. E **100**, 032117 (2019).
- [99] D. J. Luitz, I. M. Khaymovich, and Y. B. Lev, SciPost Phys. Core **2**, 6 (2020).
- [100] G. De Tomasi, I. M. Khaymovich, F. Pollmann, and S. Warzel, Phys. Rev. B **104**, 024202 (2021).
- [101] M. Srdinšek, T. Prosen, and S. Sotiriadis, Phys. Rev. Lett. **126**, 121602 (2021).
- [102] S. Sugimoto, R. Hamazaki, and M. Ueda, Phys. Rev. Lett. **126**, 120602 (2021).
- [103] L. Pausch, E. G. Carnio, A. Rodríguez, and A. Buchleitner, Phys. Rev. Lett. **126**, 150601 (2021).
- [104] M. Haque, P. A. McClarty, and I. M. Khaymovich, Phys. Rev. E **105**, 014109 (2022).
- [105] A. D. Luca and A. Scardicchio, EPL **101**, 37003 (2013).
- [106] A. I. Larkin and Y. N. Ovchinnikov, Sov. Phys. JETP **28**, 1200 (1969).
- [107] J. Maldacena, S. H. Shenker, and D. Stanford, J. High Energ. Phys. **2016**, 106 (2016).
- [108] D. Stanford, J. High Energ. Phys.. **2016**, 9 (2016).
- [109] B. Swingle, Nature Phys. **14**, 988 (2018).
- [110] J. Rammensee, J. D. Urbina, and K. Richter, Phys. Rev. Lett. **121**, 124101 (2018).
- [111] B. Craps, M. De Clerck, D. Janssens, V. Luyten, and C. Rabideau, Phys. Rev. B **101**, 174313 (2020).
- [112] N. Kolganov and D. A. Trunin, Phys. Rev. D **106**, 025003 (2022).
- [113] B. Dóra and R. Moessner, Phys. Rev. Lett. **119**, 026802 (2017).
- [114] J. von Neumann, Eur. Phys. J. H **35**, 201 (2010).
- [115] I. Bloch, J. Dalibard, and W. Zwerger, Rev. Mod. Phys. **80**, 885 (2008).

- [116] J. M. Deutsch, Phys. Rev. A **43**, 2046 (1991).
- [117] M. Srednicki, Phys. Rev. E **50**, 888 (1994).
- [118] M. Srednicki, J. Phys. A: Math. Gen. **29**, L75 (1996).
- [119] M. Srednicki, J. Phys. A: Math. Gen. **32**, 1163 (1999).
- [120] M. Rigol, V. Dunjko, and M. Olshanii, Nature **452**, 854 (2008).
- [121] A. Polkovnikov, K. Sengupta, A. Silva, and M. Vengalattore, Rev. Mod. Phys. **83**, 863 (2011).
- [122] M. Rigol and M. Srednicki, Phys. Rev. Lett. **108**, 110601 (2012).
- [123] J. Eisert, M. Friesdorf, and C. Gogolin, Nature Phys. **11**, 124 (2015).
- [124] L. D'Alessio, Y. Kafri, A. Polkovnikov, and M. Rigol, Advances in Physics **65**, 239 (2016).
- [125] M. Rigol, Phys. Rev. Lett. **103**, 100403 (2009).
- [126] G. Biroli, C. Kollath, and A. M. Läuchli, Phys. Rev. Lett. **105**, 250401 (2010).
- [127] M. Rigol and L. F. Santos, Phys. Rev. A **82**, 011604 (2010).
- [128] L. F. Santos and M. Rigol, Phys. Rev. E **82**, 031130 (2010).
- [129] G. Roux, Phys. Rev. A **81**, 053604 (2010).
- [130] A. Motohashi, Phys. Rev. A **84**, 063631 (2011).
- [131] C. Neuenhahn and F. Marquardt, Phys. Rev. E **85**, 060101 (2012).
- [132] G. P. Brandino, A. De Luca, R. M. Konik, and G. Mussardo, Phys. Rev. B **85**, 214435 (2012).
- [133] R. Steinigeweg, J. Herbrych, and P. Prelovšek, Phys. Rev. E **87**, 012118 (2013).
- [134] H. Kim, T. N. Ikeda, and D. A. Huse, Phys. Rev. E **90**, 052105 (2014).
- [135] W. Beugeling, R. Moessner, and M. Haque, Phys. Rev. E **89**, 042112 (2014).
- [136] S. Sorg, L. Vidmar, L. Pollet, and F. Heidrich-Meisner, Phys. Rev. A **90**, 033606 (2014).
- [137] R. Steinigeweg, A. Khodja, H. Niemeyer, C. Gogolin, and J. Gemmer, Phys. Rev. Lett. **112**, 130403 (2014).
- [138] W. Beugeling, R. Moessner, and M. Haque, Phys. Rev. E **91**, 012144 (2015).
- [139] K. R. Fratus and M. Srednicki, Phys. Rev. E **92**, 040103 (2015).
- [140] R. Nandkishore and D. A. Huse, Annu. Rev. Condens. Matter Phys. **6**, 15 (2015).

- [141] A. Khodja, R. Steinigeweg, and J. Gemmer, Phys. Rev. E **91**, 012120 (2015).
- [142] R. Mondaini, K. R. Fratus, M. Srednicki, and M. Rigol, Phys. Rev. E **93**, 032104 (2016).
- [143] A. Chandran, M. D. Schulz, and F. J. Burnell, Phys. Rev. B **94**, 235122 (2016).
- [144] R. Mondaini and M. Rigol, Phys. Rev. E **96**, 012157 (2017).
- [145] J. Sonner and M. Vielma, J. High Energ. Phys. **2017**, 149 (2017).
- [146] Z. Lan and S. Powell, Phys. Rev. B **96**, 115140 (2017).
- [147] T. Yoshizawa, E. Iyoda, and T. Sagawa, Phys. Rev. Lett. **120**, 200604 (2018).
- [148] A. Dymarsky, N. Lashkari, and H. Liu, Phys. Rev. E **97**, 012140 (2018).
- [149] N. Hunter-Jones, J. Liu, and Y. Zhou, J. High Energ. Phys. **2018**, 142 (2018).
- [150] M. Haque and P. A. McClarty, Phys. Rev. B **100**, 115122 (2019).
- [151] D. Jansen, J. Stolpp, L. Vidmar, and F. Heidrich-Meisner, Phys. Rev. B **99**, 155130 (2019).
- [152] M. Mierzejewski and L. Vidmar, Phys. Rev. Lett. **124**, 040603 (2020).
- [153] C. Schönle, D. Jansen, F. Heidrich-Meisner, and L. Vidmar, Phys. Rev. B **103**, 235137 (2021).
- [154] S. Ziraldo and G. E. Santoro, Phys. Rev. B **87**, 064201 (2013).
- [155] T. N. Ikeda, Y. Watanabe, and M. Ueda, Phys. Rev. E **87**, 012125 (2013).
- [156] V. Alba, Phys. Rev. B **91**, 155123 (2015).
- [157] S. Nandy, A. Sen, A. Das, and A. Dhar, Phys. Rev. B **94**, 245131 (2016).
- [158] J. M. Magán, Phys. Rev. Lett. **116**, 030401 (2016).
- [159] T. LeBlond, K. Mallayya, L. Vidmar, and M. Rigol, Phys. Rev. E **100**, 062134 (2019).
- [160] F. Alet and N. Laflorencie, C. R. Phys. **19**, 498 (2018).
- [161] H. Bernien, S. Schwartz, A. Keesling, H. Levine, A. Omran, H. Pichler, S. Choi, A. S. Zibrov, M. Endres, M. Greiner, V. Vuletić, and M. D. Lukin, Nature **551**, 579 (2017).
- [162] C. J. Turner, A. A. Michailidis, D. A. Abanin, M. Serbyn, and Z. Papić, Nature Phys. **14**, 745 (2018).
- [163] M. Serbyn, D. A. Abanin, and Z. Papić, Nature Phys. **17**, 675 (2021).
- [164] R. Hamazaki and M. Ueda, Phys. Rev. Lett. **120**, 080603 (2018).

- [165] V. Khemani, C. R. Laumann, and A. Chandran, Phys. Rev. B **99**, 161101 (2019).
- [166] M. Brenes, T. LeBlond, J. Goold, and M. Rigol, Phys. Rev. Lett. **125**, 070605 (2020).
- [167] M. P. A. Fisher, P. B. Weichman, G. Grinstein, and D. S. Fisher, Phys. Rev. B **40**, 546 (1989).
- [168] T. D. Kühner and H. Monien, Phys. Rev. B **58**, R14741 (1998).
- [169] M. Greiner, O. Mandel, T. Esslinger, T. W. Hänsch, and I. Bloch, Nature **415**, 39 (2002).
- [170] A. Trombettoni and A. Smerzi, Phys. Rev. Lett. **86**, 2353 (2001).
- [171] A. Smerzi, A. Trombettoni, P. G. Kevrekidis, and A. R. Bishop, Phys. Rev. Lett. **89**, 170402 (2002).
- [172] A. Smerzi and A. Trombettoni, Phys. Rev. A **68**, 023613 (2003).
- [173] P. Kevrekidis, *The Discrete Nonlinear Schrödinger Equation: Mathematical Analysis, Numerical Computations and Physical Perspectives* (Springer, 2009).
- [174] T. Engl, J. Dujardin, A. Argüelles, P. Schlagheck, K. Richter, and J. D. Urbina, Phys. Rev. Lett. **112**, 140403 (2014).
- [175] T. Engl, *A semiclassical approach to many-body interference in Fock-space*, Ph.D. thesis, Regensburg (2015).
- [176] J. Rammensee, *Semiclassical Treatment of Interference Phenomena in Bosonic Quantum Many-Body Systems*, Ph.D. thesis, Regensburg (2019).
- [177] A. Polkovnikov, Phys. Rev. A **68**, 053604 (2003).
- [178] K. W. Mahmud, H. Perry, and W. P. Reinhardt, Phys. Rev. A **71**, 023615 (2005).
- [179] M. Hiller, T. Kottos, and T. Geisel, Phys. Rev. A **73**, 061604 (2006).
- [180] S. Mossmann and C. Jung, Phys. Rev. A **74**, 033601 (2006).
- [181] E. M. Graefe and H. J. Korsch, Phys. Rev. A **76**, 032116 (2007).
- [182] F. Trimborn, D. Witthaut, and H. J. Korsch, Phys. Rev. A **79**, 013608 (2009).
- [183] A. C. Cassidy, D. Mason, V. Dunjko, and M. Olshanii, Phys. Rev. Lett. **102**, 025302 (2009).
- [184] A. Polkovnikov, Annals of Physics **325**, 1790 (2010).
- [185] K. Pawłowski, P. Ziń, K. Rzażewski, and M. Trippenbach, Phys. Rev. A **83**, 033606 (2011).
- [186] L. Simon and W. T. Strunz, Phys. Rev. A **86**, 053625 (2012).

- [187] L. Simon and W. T. Strunz, Phys. Rev. A **89**, 052112 (2014).
- [188] H. Veksler and S. Fishman, New J. Phys. **17**, 053030 (2015).
- [189] T. Engl, J. D. Urbina, and K. Richter, Phys. Rev. E **92**, 062907 (2015).
- [190] T. Engl, J. D. Urbina, and K. Richter, Phil. Trans. R. Soc. A **374**, 20150159 (2016).
- [191] S. Ray, P. Ostmann, L. Simon, F. Grossmann, and W. T. Strunz, J. Phys. A: Math. Theor. **49**, 165303 (2016).
- [192] R. Dubertrand and S. Müller, New J. Phys. **18**, 033009 (2016).
- [193] R. A. Kidd, M. K. Olsen, and J. F. Corney, “Finite-time Lyapunov exponents in chaotic Bose-Hubbard chains,” (2017), arXiv:1707.00393 .
- [194] S. Tomsovic, P. Schlagheck, D. Ullmo, J.-D. Urbina, and K. Richter, Phys. Rev. A **97**, 061606 (2018).
- [195] S. Tomsovic, Phys. Rev. E **98**, 023301 (2018).
- [196] R. A. Kidd, M. K. Olsen, and J. F. Corney, Phys. Rev. A **100**, 013625 (2019).
- [197] P. Schlagheck, D. Ullmo, J. D. Urbina, K. Richter, and S. Tomsovic, Phys. Rev. Lett. **123**, 215302 (2019).
- [198] K. Nemoto, C. A. Holmes, G. J. Milburn, and W. J. Munro, Phys. Rev. A **63**, 013604 (2000).
- [199] T. F. Viscondi and K. Furuya, J. Phys. A: Math. Theor. **44**, 175301 (2011).
- [200] B. Gertjerenken and C. Weiss, Phys. Rev. A **88**, 033608 (2013).
- [201] C. Heinisch and M. Holthaus, Zeitschrift für Naturforschung A **71**, 875 (2016).
- [202] L. Pausch, E. G. Carnio, A. Buchleitner, and A. Rodríguez, New J. Phys. **23**, 123036 (2021).
- [203] E. R. Castro, J. Chávez-Carlos, I. Roditi, L. F. Santos, and J. G. Hirsch, Quantum **5**, 563 (2021).
- [204] Z. Wang, Y. Wang, and B. Wu, Phys. Rev. E **103**, 042209 (2021).
- [205] V. Z. Enol'skii, M. Salerno, N. A. Kostov, and A. C. Scott, Phys. Scr. **43**, 229 (1991).
- [206] J. Links and K. E. Hibberd, SIGMA **2**, 95 (2006).
- [207] G. Santos, C. Ahn, A. Foerster, and I. Roditi, Physics Letters B **746**, 186 (2015).
- [208] A. R. Kolovsky and A. Buchleitner, EPL **68**, 632 (2004).

[209] C. Kollath, G. Roux, G. Biroli, and A. M. Läuchli, *J. Stat. Mech.* **2010**, P08011 (2010).

[210] J. de la Cruz, S. Lerma-Hernández, and J. G. Hirsch, *Phys. Rev. E* **102**, 032208 (2020).

[211] M. Hiller, T. Kottos, and T. Geisel, *Phys. Rev. A* **79**, 023621 (2009).

[212] G. Arwas, A. Vardi, and D. Cohen, *Phys. Rev. A* **89**, 013601 (2014).

[213] A. Vardi, *Rom. Rep. Phys.* **67**, 67 (2015).

[214] X. Han and B. Wu, *Phys. Rev. A* **93**, 023621 (2016).

[215] R. Bürkle and J. R. Anglin, *Phys. Rev. A* **99**, 063617 (2019).

[216] A. A. Bychek, P. S. Muraev, D. N. Maksimov, E. N. Bulgakov, and A. R. Kolovsky, *AIP Conf. Proc.* **2241**, 020007 (2020).

[217] K. Wittmann W., E. R. Castro, A. Foerster, and L. F. Santos, *Phys. Rev. E* **105**, 034204 (2022).

[218] E. R. Castro, K. W. W., J. Chávez-Carlos, I. Roditi, A. Foerster, and J. G. Hirsch, *Phys. Rev. A* **109**, 032225 (2024).

[219] A. V. Varma, A. Vardi, and D. Cohen, “Characterization of hybrid quantum eigenstates in systems with mixed classical phasespace,” (2024), arXiv:2403.06212

[220] T. M. Liggett, *Interacting Particle Systems* (Springer, 1985).

[221] A. T. Bharucha-Reid, *Elements of the Theory of Markov Processes and their Applications* (Courier Corporation, 1997).

[222] W. J. Anderson, *Continuous-Time Markov Chains* (Springer, 1991).

[223] N. Van Kampen, *Stochastic Processes in Physics and Chemistry* (Elsevier Science, 2007).

[224] T. Lux, *IFAC Proceedings Volumes* **28**, 409 (1995).

[225] M. R. Grasselli and P. X. Li, *Journal of Network Theory in Finance* **4**, 47 (2018).

[226] J. Hofbauer and K. Sigmund, *The Theory of Evolution and Dynamical Systems. Mathematical Aspects of Selection*. (Cambridge University Press, 1988).

[227] G. Szabó and G. Fáth, *Phys. Rep.* **446**, 97 (2007).

[228] D. A. McQuarrie, *Journal of Applied Probability* **4**, 413 (1967).

[229] J. Schnakenberg, *Rev. Mod. Phys.* **48**, 571 (1976).

[230] M. J. Pilling and S. H. Robertson, *Annu. Rev. Phys. Chem.* **54**, 245 (2003).

- [231] D. T. Gillespie, *Annu. Rev. Phys. Chem.* **58**, 35 (2007).
- [232] D. F. Anderson and T. G. Kurtz, in *Design and Analysis of Biomolecular Circuits: Engineering Approaches to Systems and Synthetic Biology* (Springer, 2011) pp. 3–42.
- [233] P. Lecca, *Biophys. Rev.* **5**, 323 (2013).
- [234] H. Ge and H. Qian, in *Encyclopedia of Systems Biology* (Springer, 2013) pp. 396–399.
- [235] H. D. Jong, *J. Comput. Biol.* **9**, 67 (2002).
- [236] M. Hegland, C. Burden, L. Santoso, S. MacNamara, and H. Booth, *Journal of Computational and Applied Mathematics* **205**, 708 (2007).
- [237] H. S. Booth, C. J. Burden, M. Hegland, and L. Santoso, in *Mathematical Modeling of Biological Systems, Volume I: Cellular Biophysics, Regulatory Networks, Development, Biomedicine, and Data Analysis* (Birkhäuser, 2007) pp. 71–81.
- [238] O. Lipan, in *Molecular Life Sciences: An Encyclopedic Reference* (Springer, 2021) pp. 1–9.
- [239] S. A. Sevier, D. A. Kessler, and H. Levine, *Proc. Natl. Acad. Sci.* **113**, 13983 (2016).
- [240] J. E. Carroll, *Rate Equations in Semiconductor Electronics* (Cambridge University Press, 1986).
- [241] D. Vorberg, W. Wustmann, R. Ketzmerick, and A. Eckardt, *Phys. Rev. Lett.* **111**, 240405 (2013).
- [242] P. Prelovšek, J. Bonča, and M. Mierzejewski, *Phys. Rev. B* **98**, 125119 (2018).
- [243] M. Mierzejewski, P. Prelovšek, and J. Bonča, *Phys. Rev. Lett.* **122**, 206601 (2019).
- [244] M. P. Liul and S. N. Shevchenko, *Low Temp. Phys.* **49**, 96 (2023).
- [245] J. Knebel, M. F. Weber, T. Krüger, and E. Frey, *Nat. Commun.* **6**, 6977 (2015).
- [246] C. E. Overton, M. Broom, C. Hadjichrysanthou, and K. J. Sharkey, *J. Theor. Biol.* **468**, 45 (2019).
- [247] T. E. Harris, *Ann. Probab.* **2**, 969 (1974).
- [248] J. Marro and R. Dickman, *Nonequilibrium Phase Transitions in Lattice Models* (Cambridge University Press, 1999).
- [249] M. Henkel, *Non-Equilibrium Phase Transitions* (Springer, 2008).
- [250] F. Spitzer, *Advances in Mathematics* **5**, 246 (1970).

- [251] M. R. Evans and T. Hanney, J. Phys. A: Math. Gen. **38**, R195 (2005).
- [252] H. Spohn, *Large Scale Dynamics of Interacting Particles* (Springer, 1991).
- [253] G. Schütz and E. Domany, J. Stat. Phys. **72**, 277 (1993).
- [254] B. Derrida, Phys. Rep. **301**, 65 (1998).
- [255] T. M. Liggett, *Stochastic Interacting Systems: Contact, Voter and Exclusion Processes* (Springer, 1999).
- [256] G. M. Schütz, Phase Transitions Crit. Phenom. **19**, 1 (2001).
- [257] O. Golinelli and K. Mallick, J. Phys. A: Math. Gen. **39**, 12679 (2006).
- [258] T. Chou, K. Mallick, and R. K. P. Zia, Rep. Prog. Phys. **74**, 116601 (2011).
- [259] G. A. Pavliotis, *Stochastic Processes and Applications: Diffusion Processes, the Fokker-Planck and Langevin Equations* (Springer, 2014).
- [260] W. Tarnowski, I. Yusipov, T. Laptyeva, S. Denisov, D. Chruściński, and K. Życzkowski, Phys. Rev. E **104**, 034118 (2021).
- [261] J. Keizer, J. Stat. Phys. **6**, 67 (1972).
- [262] S. A. Gershgorin, Bull. Acad. Sc. Leningrad **6**, 749 (1931).
- [263] O. Perron, Mathematische Annalen **64**, 248 (1907).
- [264] G. Frobenius, Sitzungsber. Königl. Preuss. Akad. Wiss. (1912).
- [265] K. Mallick, Phys. A **418**, 17 (2015).
- [266] C. T. MacDonald, J. H. Gibbs, and A. C. Pipkin, Biopolymers **6**, 1 (1968).
- [267] C. T. MacDonald and J. H. Gibbs, Biopolymers **7**, 707 (1969).
- [268] D. Chowdhury, L. Santen, and A. Schadschneider, Phys. Rep. **329**, 199 (2000).
- [269] D. Helbing, Rev. Mod. Phys. **73**, 1067 (2001).
- [270] P. C. Bressloff and J. M. Newby, Rev. Mod. Phys. **85**, 135 (2013).
- [271] I. Neri, N. Kern, and A. Parmeggiani, Phys. Rev. Lett. **110**, 098102 (2013).
- [272] X. Fang, K. Kruse, T. Lu, and J. Wang, Rev. Mod. Phys. **91**, 045004 (2019).
- [273] P. Meakin, P. Ramanlal, L. M. Sander, and R. C. Ball, Phys. Rev. A **34**, 5091 (1986).
- [274] M. Kardar, G. Parisi, and Y.-C. Zhang, Phys. Rev. Lett. **56**, 889 (1986).
- [275] J. Krug and H. Spohn, in *Solids far from equilibrium* (Cambridge University Press, 1991) p. 479.

- [276] L. H. Gwa and H. Spohn, Phys. Rev. A **46**, 844 (1992).
- [277] B. Derrida, M. R. Evans, V. Hakim, and V. Pasquier, J. Phys. A: Math. Gen. **26**, 1493 (1993).
- [278] S. Sandow, Phys. Rev. E **50**, 2660 (1994).
- [279] R. A. Blythe and M. R. Evans, J. Phys. A: Math. Theor. **40**, R333 (2007).
- [280] J. de Gier and F. H. L. Essler, Phys. Rev. Lett. **95**, 240601 (2005).
- [281] J. de Gier and F. H. L. Essler, J. Stat. Mech. **2006**, P12011 (2006).
- [282] B. Derrida and K. Mallick, J. Phys. A: Math. Gen. **30**, 1031 (1997).
- [283] J. Krug, Phys. Rev. Lett. **67**, 1882 (1991).
- [284] A. Parmeggiani, T. Franosch, and E. Frey, Phys. Rev. Lett. **90**, 086601 (2003).
- [285] D. Kim, Phys. Rev. E **52**, 3512 (1995).
- [286] O. Golinelli and K. Mallick, J. Phys. A: Math. Gen. **37**, 3321 (2004).
- [287] O. Golinelli and K. Mallick, J. Phys. A: Math. Gen. **38**, 1419 (2005).
- [288] S. Prolhac, J. Phys. A: Math. Theor. **46**, 415001 (2013).
- [289] S. Prolhac, J. Stat. Mech. **2015**, P11028 (2015).
- [290] H. Bethe, Zeitschrift für Physik **71**, 205 (1931).
- [291] R. I. Nepomechie, J. Phys. A: Math. Gen. **37**, 433 (2003).
- [292] R. I. Nepomechie, J. Stat. Phys. **111**, 1363 (2003).
- [293] J. Cao, H.-Q. Lin, K.-J. Shi, and Y. Wang, Nucl. Phys. B **663**, 487 (2003).
- [294] C. Timm, Phys. Rev. E **80**, 021140 (2009).
- [295] C. Bordenave, P. Caputo, and D. Chafaï, Communications on Pure and Applied Mathematics **67**, 621 (2014).
- [296] N. L. Johnson, S. Kotz, and N. Balakrishnan, *Continuous Univariate Distributions* (Wiley, 1994).
- [297] T. Tao, Probab. Theory Relat. Fields **155**, 231 (2013).
- [298] S. Denisov, T. Laptyeva, W. Tarnowski, D. Chruściński, and K. Życzkowski, Phys. Rev. Lett. **123**, 140403 (2019).
- [299] G. Nakerst and M. Haque, Phys. Rev. E **103**, 042109 (2021).
- [300] G. Nakerst and M. Haque, Phys. Rev. E **107**, 024210 (2023).
- [301] G. Nakerst, S. Denisov, and M. Haque, Phys. Rev. E **108**, 014102 (2023).

[302] G. Nakerst, T. Prosen, and M. Haque, “The spectral boundary of the asymmetric simple exclusion process (ASEP) – free fermions, Bethe ansatz and random matrix theory,” (2024), arXiv:2402.00662 .

[303] G. Nakerst, J. Brennan, and M. Haque, “Gradient descent with momentum — to accelerate or to super-accelerate?” (2020), arXiv:2001.06472 .

[304] P. C. Burke, G. Nakerst, and M. Haque, Phys. Rev. E **107**, 024102 (2023).

[305] P. C. Burke, G. Nakerst, and M. Haque, “Structure of the Hamiltonian of mean force,” (2023), arXiv:2311.10427 .

[306] P. Reimann, Phys. Rev. Lett. **99**, 160404 (2007).

[307] P. Reimann, J. Stat. Phys. **132**, 921 (2008).

[308] J. Gemmer, M. Michel, and G. Mahler, *Quantum Thermodynamics: Emergence of Thermodynamic Behavior Within Composite Quantum Systems* (Springer, 2009).

[309] S. Lloyd, “Pure state quantum statistical mechanics and black holes,” (2013), arXiv:1307.0378 .

[310] W. Beugeling, A. Andreeanov, and M. Haque, J. Stat. Mech. **2015**, P02002 (2015).

[311] C. Liu, X. Chen, and L. Balents, Phys. Rev. B **97**, 245126 (2018).

[312] G. Benettin, L. Galgani, A. Giorgilli, and J.-M. Strelcyn, Meccanica **15**, 9 (1980).

[313] G. Benettin, L. Galgani, A. Giorgilli, and J.-M. Strelcyn, Meccanica **15**, 21 (1980).

[314] V. I. Oseledets, Tr. Mosk. Mat. Obs. **19**, 179 (1968).

[315] D. J. Luitz, N. Laflorencie, and F. Alet, Phys. Rev. B **91**, 081103 (2015).

[316] S. Kullback and R. A. Leibler, The Annals of Mathematical Statistics **22**, 79 (1951).

[317] G. De Tomasi and I. M. Khaymovich, Phys. Rev. Lett. **124**, 200602 (2020).

[318] O. Bohigas, S. Tomsovic, and D. Ullmo, Phys. Rep. **223**, 43 (1993).

[319] H. R. Dullin, P. H. Richter, and A. Wittek, Chaos **6**, 43 (1996).

[320] B. Pittel, Random Struct. Alg. **53**, 3 (2018).

[321] B. Bollobás, *Random Graphs* (Cambridge University Press, 2001).

[322] R. A. Horn and C. R. Johnson, *Matrix Analysis* (Cambridge University Press, 1985).

- [323] A. S. Bandeira, Found. Comput. Math. **18**, 345 (2018).
- [324] P. Embrechts, C. Klüppelberg, and T. Mikosch, *Modelling Extremal Events* (Springer, 1997).
- [325] A. Hoorfar and M. Hassani, J. Inequal. Pure and Appl. Math **9**, 5 (2008).
- [326] L. De Haan and A. Ferreira, *Extreme Value Theory: An Introduction* (Springer, 2006).
- [327] F. Mosam, D. Vidaurre, and E. D. Giuli, Phys. Rev. E **104**, 024305 (2021).
- [328] A. Edelman, E. Kostlan, and M. Shub, J. Amer. Math. Soc. **7**, 247 (1994).
- [329] A. Edelman, Journal of Multivariate Analysis **60**, 203 (1997).
- [330] E. Kanzieper and G. Akemann, Phys. Rev. Lett. **95**, 230201 (2005).
- [331] P. J. Forrester and T. Nagao, Phys. Rev. Lett. **99**, 050603 (2007).
- [332] H.-J. Sommers and W. Wieczorek, J. Phys. A: Math. Theor. **41**, 405003 (2008).
- [333] B. A. Khoruzhenko, H.-J. Sommers, and K. Życzkowski, Phys. Rev. E **82**, 040106 (2010).
- [334] W. Tarnowski, Phys. Rev. E **105**, L012104 (2022).
- [335] S.-S. Byun, N.-G. Kang, J. O. Lee, and J. Lee, International Mathematics Research Notices **2023**, 2243 (2023).
- [336] A. J. Bray and G. J. Rodgers, Phys. Rev. B **38**, 11461 (1988).
- [337] G. J. Rodgers and A. J. Bray, Phys. Rev. B **37**, 3557 (1988).
- [338] A. Cavagna, I. Giardina, and G. Parisi, Phys. Rev. Lett. **83**, 108 (1999).
- [339] R. Kühn, J. Phys. A: Math. Theor. **41**, 295002 (2008).
- [340] V. A. R. Susca, P. Vivo, and R. Kühn, SciPost Phys. Lect. Notes **33**, 33 (2021).
- [341] G. Biroli and R. Monasson, J. Phys. A: Math. Gen. **32**, L255 (1999).
- [342] G. Semerjian and L. F. Cugliandolo, J. Phys. A: Math. Gen. **35**, 303 (2002).
- [343] S. N. Dorogovtsev, A. V. Goltsev, J. F. F. Mendes, and A. N. Samukhin, Phys. Rev. E **68**, 046109 (2003).
- [344] P. Akara-pipattana and O. Evnin, J. Phys. A: Math. Theor. **56**, 295001 (2023).
- [345] T. Rogers, I. P. Castillo, R. Kühn, and K. Takeda, Phys. Rev. E **78**, 031116 (2008).
- [346] T. Rogers and I. P. Castillo, Phys. Rev. E **79**, 012101 (2009).

- [347] V. A. R. Susca, P. Vivo, and R. Kühn, *J. Phys. A: Math. Theor.* **52**, 485002 (2019).
- [348] R. G. Margiotta, R. Kühn, and P. Sollich, *J. Stat. Mech.* **2019**, 093304 (2019).
- [349] D. Tapias, E. Paprotzki, and P. Sollich, *J. Stat. Mech.* **2020**, 093302 (2020).
- [350] D. Tapias and P. Sollich, *Phys. Rev. E* **105**, 054109 (2022).
- [351] I. Palásti, *Studia Sci. Math. Hungar.* **1**, 205 (1966).
- [352] A. J. Graham and D. A. Pike, *Atl. Electron. J. Math.* **3**, 1 (2008).
- [353] R. Dickman and I. Jensen, *Phys. Rev. Lett.* **67**, 2391 (1991).
- [354] I. Jensen and R. Dickman, *J. Stat. Phys.* **71**, 89 (1993).
- [355] H. Hinrichsen, *Advances in Physics* **49**, 815 (2000).
- [356] D. Mollison, *J. R. Statist. Soc. B* **39**, 283 (1977).
- [357] P. Grassberger, *Math. Biosci.* **63**, 157 (1983).
- [358] J.-T. Kuhr, M. Leisner, and E. Frey, *New J. Phys.* **13**, 113013 (2011).
- [359] J. B. Kogut, *Rev. Mod. Phys.* **51**, 659 (1979).
- [360] T. Prosen, *New J. Phys.* **10**, 043026 (2008).
- [361] R. P. Langlands and Y. Saint-Aubin, in *Strings and Symmetries*, Vol. 447 (Springer, 1995) pp. 40–53.
- [362] E. Brattain, N. Do, and A. Saenz, “The completeness of the Bethe ansatz for the periodic ASEP,” (2017), arXiv:1511.03762 .
- [363] D. R. Brillinger, *Mathematics Magazine* **39**, 145 (1966).
- [364] K. Motegi, K. Sakai, and J. Sato, *Phys. Rev. E* **85**, 042105 (2012).
- [365] D. Simon, *J. Stat. Mech.* **2009**, P07017 (2009).
- [366] N. Crampé, E. Ragoucy, and D. Simon, *J. Stat. Mech.* **2010**, P11038 (2010).
- [367] N. Crampé, E. Ragoucy, and D. Simon, *J. Phys. A: Math. Theor.* **44**, 405003 (2011).
- [368] B. Gaveau, L. S. Schulman, and L. J. Schulman, *J. Phys. A: Math. Gen.* **39**, 10307 (2006).

Versicherung

Hiermit versichere ich, dass ich die vorliegende Arbeit ohne unzulässige Hilfe Dritter und ohne Benutzung anderer als der angegebenen Hilfsmittel angefertigt habe; die aus fremden Quellen direkt oder indirekt übernommenen Gedanken sind als solche kenntlich gemacht. Die Arbeit wurde bisher weder im Inland noch im Ausland in gleicher oder ähnlicher Form einer anderen Prüfungsbehörde vorgelegt.

Die vorliegende Dissertation wurde am Institut für Theoretische Physik der Technischen Universität Dresden unter der wissenschaftlichen Betreuung von Dr. Masudul Haque angefertigt. Ich erkenne die Promotionsordnung des Bereichs Mathematik und Naturwissenschaften der Technischen Universität Dresden vom 23.02.2011 an.

Goran Nakerst
19.04.2024